Engineering, 2010, 2, 205-305
Published Online April 2010 in SciRes (http://www.SciRP.org/journal/eng/)

TABLE OF CONTENTS

Volume 2 Number 4 April 2010

Engineering

Journal Information

SUBSCRIPTIONS

Engineering (Online at Scientific Research Publishing, www.SciRP.org) is published monthly by Scientific Research Publishing, Inc., USA.

Subscription rates:

Print: $50 per issue.
To subscribe, please contact Journals Subscriptions Department, E-mail: sub@scirp.org

SERVICES

Advertisements
Advertisement Sales Department, E-mail: service@scirp.org

Reprints (minimum quantity 100 copies)
Reprints Co-ordinator, Scientific Research Publishing, Inc., USA.
E-mail: sub@scirp.org

COPYRIGHT

PRODUCTION INFORMATION

For manuscripts that have been accepted for publication, please contact:
E-mail: eng@scirp.org

Engineering, 2010, 2, 205-211
doi:10.4236/eng.2010.24030 Published Online April 2010 (http://www.SciRP.org/journal/eng)

A Finite Element Study of Elastic-Plastic Hemispherical Contact Behavior against a Rigid Flat under Varying Modulus of Elasticity and Sphere Radius

Prasanta Sahoo*, Biplab Chatterjee
Department of Mechanical Engineering, *Jadavpur University*, *Kolkata*, *India*
E-mail: *psjume@gmail.com*
Received November 18, 2009; *revised January* 28, 2010; *accepted February* 4, 2010

Abstract

The present study considers a finite element analysis of elastic-plastic axi-symmetric hemispherical contact for a frictionless deformable sphere pressed by a rigid flat. The material of the sphere is modeled as elastic perfectly plastic. Analysis is carried out to study the effect of varying modulus of elasticity and sphere radius in wide range of dimensionless interference until the inception of plasticity as well as in plastic range. Results are compared with previous elastic-plastic models. It is found that materials with Young's modulus to yield strength (E/Y) ratio less than and greater than 300 show strikingly different contact phenomena. The dependency of E on dimensionless interference at which the plastic region fully covers the surface is observed. However with different radius, finite element study exhibits similar elastic-plastic phenomena.

Keywords: Elastic-plastic Contact, Sphere against Flat, ANSYS, Modulus of Elasticity, Sphere Radius

1. Introduction

Contact is necessary in any engineering application to transfer force and power hence it is almost an indispensable field of study. The elastic-plastic contact of a hemisphere with a rigid surface is a fundamental problem to study the major characteristics like localized deformation, the variation in the contact area, the contact force, displacement and the stress distribution in the deformable body. Much interest is devoted in the literature to the reverse case of indentation loading where a rigid sphere penetrates an elasto-plastic half space. It is worthy to emphasize that indentation and hemispherical deformation (this work) are significantly different in the elasto-plastic and fully plastic regimes. One of the earliest models of elastic asperity contact is that of Greenwood and Williamson [1]. This model uses the solution of the frictionless contact of an elastic hemisphere and a rigid flat plane, otherwise known as the Hertz contact solution [2]. Some works are restricted to pure plastic deformation of the contacting sphere, based on Abbott and Firestone [3]. The works on either pure elastic or pure plastic deformation of the contacting sphere overlook a wide intermediate range of interest where elastic-plastic contact prevails. An attempt to bridge this gap was made by Chang *et al*. [4]. Zhao *et al*. [5] used mathematical manipulation to smooth the transition of the contact load and contact area expressions between the elastic and elastic-plastic deformation regimes. Mathematical models are replaced using finite element model (FEM) concepts recently. Kogut and Etsion (KE) [6] used FEM concept and analyzed the evolution of the elastic-plastic contact with increasing interference revealing three distinct stages that ranges from fully elastic, elastic-plastic up to fully plastic ($0 < \omega^* \le 110$). The model provides dimensionless expression for contact area, contact load and mean contact pressure covering a large range of interference values. They inferred that their analysis is normalized in such a way that allowed a general solution, which is independent of specific material and radius of the sphere. A change in the behavior of the mean contact pressure was observed in their analysis at $\omega^* = 6$, which marks the elastic limit of the contact area. To generalize their solution, the numerical solutions were normalized with respect to their corresponding critical values at yielding inception, ω_c. The validity of this normalization was tested by solving the problem for several different material properties ($100 < E/Y < 1000$, $\nu = 0.3$) and sphere radii ($0.1 \text{ mm} < R < 10 \text{ mm}$). Their results show that the entire contact zone is plastic when the dimensionless interference ratio ($\omega/\omega_c = \omega^*$) is 68 and the rate of its radial expansion increases substantially.

Moreover when ω/ω_c = 110, the dimensionless mean contact pressure (p/Y) approaches the value of 2.8. This is identical to the ratio between the hardness and yield strength found experimentally for many materials as indicated by Tabor [7].

Kogut and Etsion [8] studied the maximum tangential load that can be supported by a normally preloaded elastic perfectly plastic spherical contact at the inception of sliding using an approximate semi analytical solution. Sliding inception was interpreted as a failure of the contact. They found that when the normal load is less than the Hertzian critical load the failure occurs on the contact surface. If the normal load exceeds that critical one, the failure occurs below the contact surface. Brizmer *et al.* [9] analyzed and compared the ductile material yielding inception and the brittle material failure inception for two different contact conditions between a smooth elastic sphere and rigid flat and the effect of contact condition and material properties on the termination of elasticity. Jackson and Green (JG) [10] extended the KE model to account for the geometry and the material effects in the analysis. They used finer mesh than the KE model and solved for five different yield strengths. Their analysis showed markedly different behavior for the materials with different strengths in the transition from elastic-plastic to fully plastic deformations. For calculating the critical interference, they used material yield strength (Y) directly in their expressions. Their results show that the dimensionless mean contact pressure does not reach 2.8 for most of the yield strength values. The JG solution used E/Y ratio of 952.4, 356.6, 219, 158.1 and 137.74 by varying the values of 'Y' with constant E = 200 GPa. They also analyzed the interference when plastic deformation first reaches the contacting surface at the far right end and the contact surface first becomes entirely plastic for yield strength of 1.619, 1.2653, 0.9115 GPa. Quicksall *et al.* [11] have taken five hypothetical material properties and studied the error of formulation for KE and JG models. The first test generated contact area and contact force data for five hypothetical metals with Poisson's ratio, yield strength and elastic modulus typical of aluminum, bronze, copper, titanium and malleable cast iron. Non-dimensional interference between ω^* = 5 and ω^* = 250 were used to generate data in both the elastic-plastic and the plastic regimes except for aluminum at ω^* = 250 and malleable cast iron above ω^* = 10. Second set of tests generated non-dimensional contact area and contact force data for a generic material in which the elastic modulus and Poison's ratio were independently varied with yield strength held constant at 200 MPa. Firstly Poisson's ratio was varied between 0.28 and 0.36 with the elastic modulus held constant at 200 GPa. Then the elastic modulus was varied between 160 and 240 GPa with Poisson's ratio held constant at 0.32. The dimensionless interference was set at ω^* = 20, 80 and 250 for each test iteration. Jackson *et al*. [12] used the mesh size same as that of JG model and presented results for a range of normalized interference ω^*, from 0.571 to 171. Then the contact force, stress tensor, von mises stresses and the displacement in both the radial and axial directions were recorded. After loading conditions had been simulated; the solution was then restarted and unloaded completely to simulate the residual stresses and the displacements. In order to measure the effect of the material properties on the hemispherical deformation, both aluminum and steel sphere unloaded from ω^* = 135; they inferred that the deformation of the hemisphere is dependent on the properties of the material and the interference.

Shankar and Mayuram (SM) [13] studied the evolution of elastic core and the plastic region within the asperity for different Y/E ratios. They varied the yield strength from 250 N/mm^2 to 2250 N/mm^2. E equals to 2.07×10^5 N/mm^2. The range of E/Y is from 83.333 to 500. It was revealed from their analysis that higher dimensionless interference, ω^* is required for the plastic region to just touch the contact surface when E/Y > 166.66 and this ω^* is varied with E/Y ratio. For E/Y < 166.667, this ω^* is constant and equals to 6. Same trend was observed for the entire contact surface to be in plastic. For E/Y > 166.66, the value of ω/ω_c decreases with decrease of E/Y ratio. When E/Y ratio is less than 166.66, the fully plastic contact condition exists at a constant interference ratio of 54. They studied the variation of mean contact pressure (p/Y) as a function of dimensionless interference ratio and observed that materials having low yield strength (*i.e.* when E/Y > 300) produces results similar to the KE model but p/Y ratio never reaches 2.8. Malayalamurti and Marappan (MM) [14] analyzed the elastic-plastic behavior of a sphere loaded against a rigid flat in two regions. One is when E/Y > 300, another when E/Y < 300. They observed that when E/Y < 300, the fully plastic average contact pressure or hardness is not constant. However, the hardness and interference at the inception of fully plastic condition are constant for materials with E/Y > 300. The present work aims to study the qualitative and quantitative contact characteristics of single asperity contact using commercial FEM software ANSYS. Analysis is carried out to study the effect of varying modulus of elasticity and sphere radius in wide range of dimensionless interference until the inception of plasticity as well as in plastic range.

2. Finite Element Model and Procedure

To improve upon the efficiency of computation, an axi-symmetric 2-D model is used. The present study utilizes the commercial program ANSYS. The hemisphere is modeled by a quarter of a circle, due to its axisymmetry. A line models the rigid flat. The model re-

fines the element mesh near the region of contact to allow the hemisphere's curvature to be captured and accurately simulated during deformation. The model uses quadrilateral, four node elements to mesh the hemisphere. The resulting ANSYS mesh is presented in **Figure 1.** The nodes on the axis of symmetry are fixed in radial direction. Likewise the nodes on the bottom of the hemisphere are fixed in both axial and radial direction. This boundary condition is valid for the modeling of asperity contacts for two reasons: first, the asperities are connected to a much larger bulk material at the base; second, since the high stress region occurs near the contact, the boundary condition at the base of the hemisphere will not greatly affect the solution because of Saint Venant's principle. The bilinear isotropic hardening (BISO) option in the ANSYS program is chosen to account the elastic-plastic material response for the single asperity model. The rate independent plasticity algorithm incorporates the von Mises criterion. Tangent modulus is assumed as zero for validating the results with other elastic perfectly plastic models. The KE model uses a maximum of 2944 nodes and JG model uses a constant of 11,101 elements for their analysis. However the present work uses a maximum of 11069 elements for the radius of 1 mm. The mesh density is iteratively increased until the contact force and contact area differed by less than 1% between iterations. In addition to mesh convergence, the model also compares well with the Hertz elastic solution at interferences below the critical interference. The contact force of the model differs from the Hertzian solution by no more than 2% while the contact radius differs by less than 10%. The smaller error in the contact force is due to overall force balance enforced by ANSYS. But, the contact radius is obtained from a discrete mesh which has a finite resolution. Apart from this, the magnitude of the contact element stiffness also has some effect on such contact radii, although not on the overall force balance. This work uses Lagrangian multiplier method. The tolerance of current work is set to 1% of the element width.

There are two ways to simulate the contact problem. The first applies a force to the rigid body and then computes the resulting displacement. The second applies a displacement and then computes the resulting contact force. In both methods, the displacement, stress, and strain can be determined as well as the contact pressure. In this work the latter approach is used. This method is used because the resulting solution converges more rapidly than the former. In this work contact parameters are normalized using the JG model's expression for critical interference (ω_c), critical load (P_c) and critical contact area (A_c) to form dimensionless parameters. The critical interference (ω_c) is expressed as [10]

$$\omega_c = (\pi CY/2E')^2 R \quad (1)$$

where $C = 1.295 \exp(0.736\nu)$. The Poisson's ratio, ν, to be used here is that of the material which yields first. The critical load, P_c, is then may be calculated as [10]

$$P_c = (4/3)(R/E')^2 \cdot (C\pi Y/2)^3 \quad (2)$$

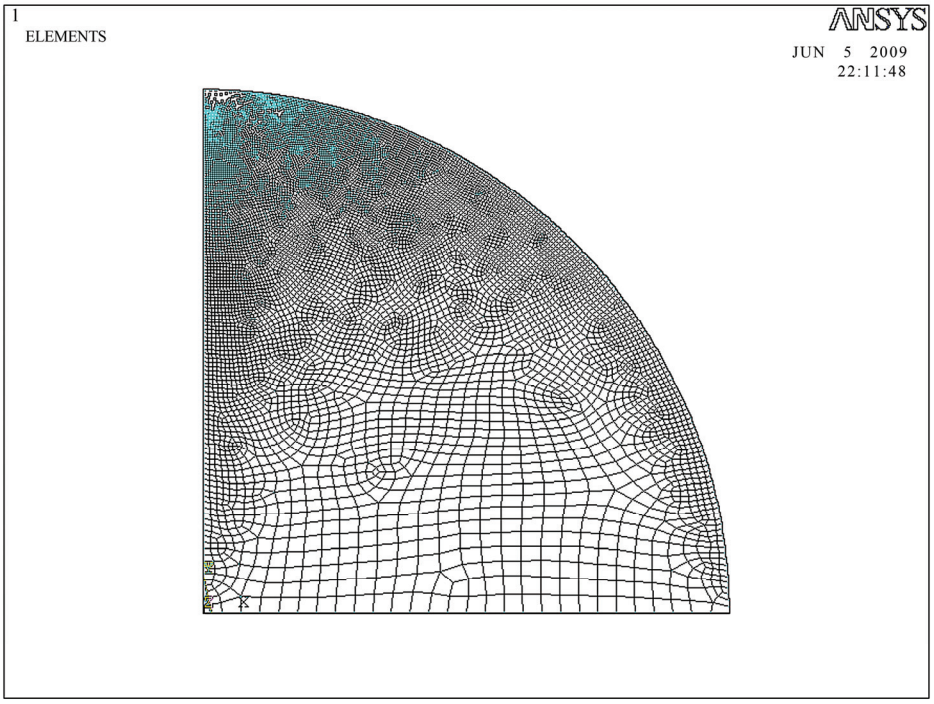

Figure 1. Finite element mesh of a sphere generated by ANSYS.

Similarly, the critical contact area is calculated as [10]

$$A_c = \pi^3 (CYR/2E^{/})^2 \quad (3)$$

In these expressions, $E^{/}$ is defined as

$$1/E^{/} = (1-\nu_1^2)/E_1 + (1-\nu_2^2)/E_2 \quad (4)$$

where E_1, E_2, and ν_1, ν_2, are Young's moduli and Poisson's ratios of the two materials, respectively. In case of the rigid flat, $E_2 \to \infty$. These critical values predict analytically the onset of plasticity. These values are, therefore, used to normalize the results. The dimensionless parameters are as follows: $\omega^* = \omega/\omega_c$, $P^* = P/P_c$, $A^* = A/A_c$.

3. Numerical Results and Discussion

The results of the finite element model are presented for a variety of interferences. The materials selected cover steel, grey cast iron and aluminum used in engineering applications. While yield strength and Poisson's ratio are held constant, four different values of elastic modulus (E) are chosen. These are 70, 80, 103, 200 GPa.

Figure 2 represents the results of the mean contact pressure to yield strength ratio (p/Y) as a function of dimensionless interference ratio (ω/ω_c) obtained from the finite element analysis. Here the study is made with constant yield strength (Y) and Poison's ratio (ν). The values of which are taken as 0.21 GPa and 0.32 respectively. With the variation of elastic modulus different E/Y ratios are obtained. Thus the E/Y ratios are 333.31, 380.95, 490.476 and 952.4 for the elastic modulus of 70, 80, 103, 200 GPa respectively. The range of ω/ω_c is from 100 to above 500. It is revealed from **Figure 2** that when E/Y > 300; the trend obtained is similar to the JG [10] model with small changes in magnitude. JG inferred that a material with higher Y has less mean contact pressure in plastic range. Here material with higher E has higher

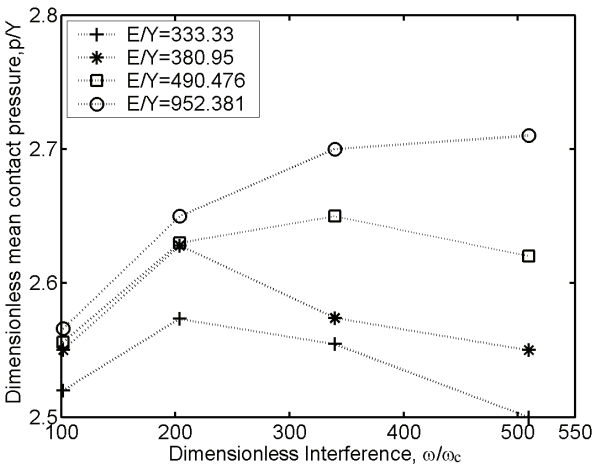

Figure 2. Dimensionless mean contact pressure versus dimensionless interference for E/Y > 300.

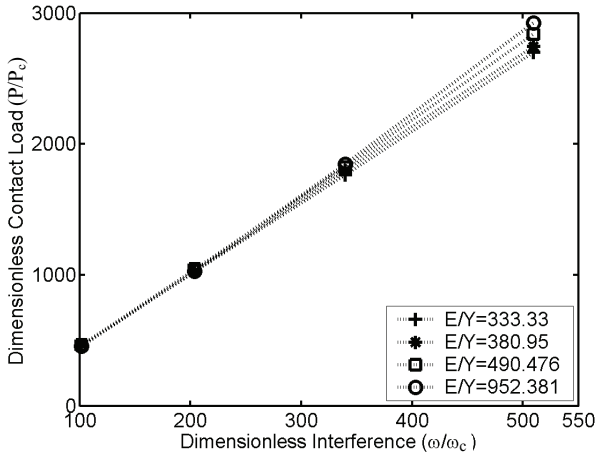

Figure 3. Dimensionless contact load as a function of dimensionless interference for E/Y > 300.

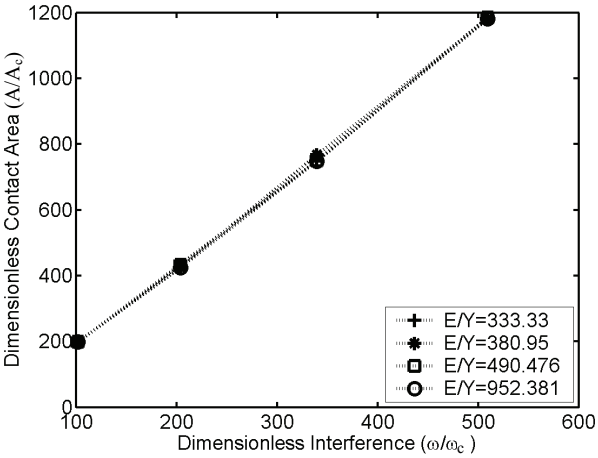

Figure 4. Dimensionless contact area as a function of dimensionless interference for E/Y > 300.

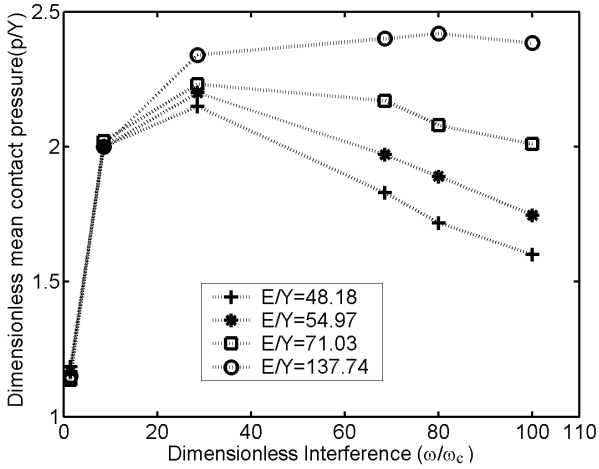

Figure 5. Dimensionless mean contact pressure as a function of dimensionless interference for E/Y < 300.

mean contact pressure as the dimensionless interference increases in the plastic range. MM [14] concluded the material independent behavior for E/Y > 300. They hadtaken the average results of four materials. Moreover they modeled the material of the sphere as an elastic linear hardening material. A 1% linear hardening was selected for their work. The present work modeled the material of the sphere as an elastic perfectly plastic material and the results entirely deviate from their result as mean contact pressure to yield strength ratio (p/Y) never reaches 2.8. **Figure 3** shows the variation of dimensionless contact load as a function of dimensionless interference, when E/Y is greater than 300. The result indicates the similarity with Quicksall *et al.* [11] findings. With the increased modulus of elasticity (E), the value of dimensionless load increases in the plastic range.

Dimensionless contact area as a function of ω^* (dimensionless interference) is plotted in **Figure 4**. The values for dimensionless contact area continue to increase with interference even past fully plastic condition. For the contact area, all the models follow the same general trend, but they differ only in magnitude. The result shows that the dimensionless contact area is independent of E when E/Y > 300.

Study is also made for the materials of E/Y < 300. For this case Y is taken as 1.619 GPa, with constant Poisson's ratio of 0.32.With four E values of 70, 80, 103 and 200 GPa the corresponding E/Y ratios are 48.178, 54.972, 71.0315 and 137.739 respectively. These values are well below 300. The behaviors of these materials in elastic as well as in elastic-plastic ranges are also analyzed. The average contact pressure to yield strength ratio is plotted in **Figure 5** as a function of dimensionless interference (ω^*). It is clearly evident from the plot that dimensionless mean contact pressure does not reach the value of 2.8 even if for steel with E = 200 GPa. There is a decrease in mean contact pressure after reaching its peak value, though the peak value is dependent on E. As the value of E increases, peak mean contact pressure also increases. There is a similarity of the trend with the findings of MM [14]. But MM inferred that peak value would reach after the dimensionless interference of 90 only. Present work observed that the peak value of mean contact pressure in all the cases occurred well below the dimensionless interference of 90. It can be seen from **Figure 5,** the location at which the mean pressure attain its peak value and its magnitude is entirely dependent on modulus of elasticity (E) of the material.

Figure 6 represents the plot of dimensionless load (P^*) versus ω^*. It is clear from the figure that for different value of E up to the inception of fully plastic contact the trend is linear with marginal change in magnitude. This is similar to the prediction of KE [6]. This trend is not observed in higher interference ratio. **Figure 7** represents the plot of dimensionless contact area with ω^* when E/Y < 300. The FEM results from this study indicate that dimensionless contact area decreases slightly with increased elastic modulus of elasticity. Same trend was observed by Quicksall *et al.* [11].

When interference increases, the elastic core completely disappears and the fully plastic region reaches the contact surface as shown in **Figure 8**, thus the transition to the fully plastic state occurs. KE model predicted this transition limited to specific dimensionless ratio of 68. JG [10] and SM [13] predicted that this ratio at which this transition occurs is not constant. In the present work it is observed that this ratio is dependent on E. As the value of E increases the dimensionless ratio at which the transition occurs is also increasing. There is no indication of constant value for the present four E/Y ratio though SM also observed a constant value of 54 when E/Y < 166.66. **Figure 9** is the plot of ω^* versus E/Y where it is clear that in the present domain of work SM overestimates the interferences marginally. The present work also studied the values of dimensionless contact load,

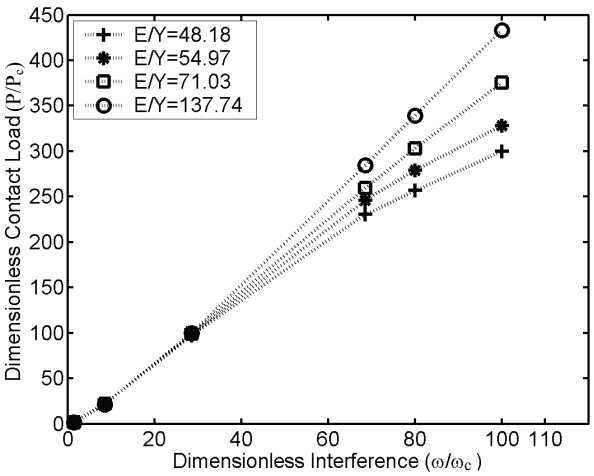

Figure 6. Dimensionless contact load versus dimension- less interference for E/Y < 300.

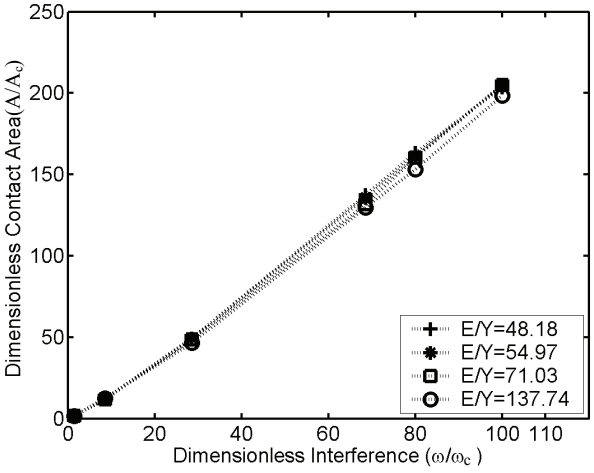

Figure 7. Dimensionless contact area versus dimension-less interference for E/Y < 300.

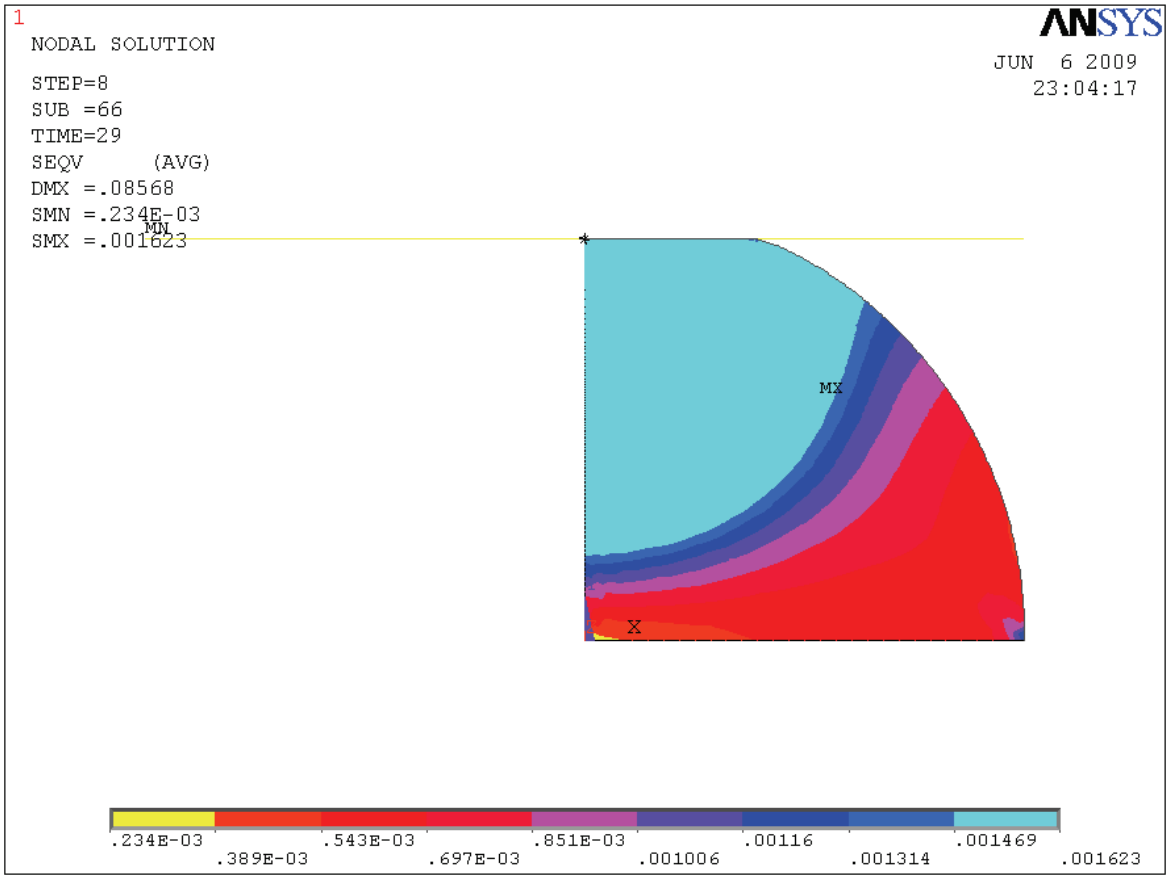

Figure 8. Inception of fully plastic contact.

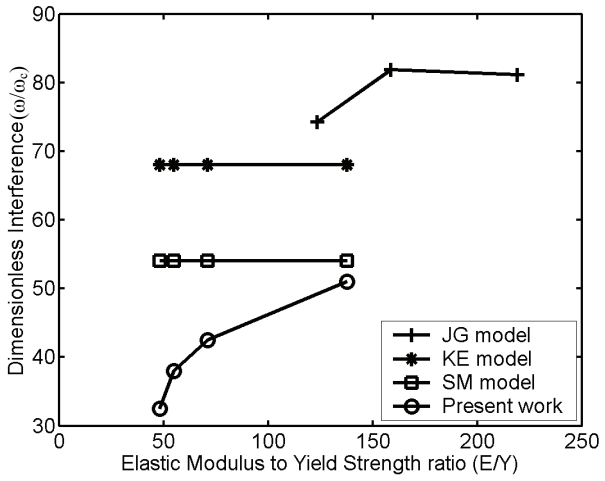

Figure 9. End of elastic-plastic region based on the disappearance of elastic core.

contact area and mean contact pressure with different sphere radii, the study is made with radii of 1, 2, and 3 mm. No significant deviation is observed. Thus it can be inferred that earlier mentioned dimensionless contact characteristics are independent of the sphere radius.

4. Conclusions

The present work considers 2D axi-symmetric finite element model of an elastic perfectly plastic hemisphere in contact with a rigid flat surface. A comparison is also made with other existing models. The material is modeled as elastic perfectly plastic, and yielding occurs according to the Von Mises criterion. It has been clearly shown that the dimensionless mean contact pressure ratio is not constant at 2.8 in the plastic range but depends on modulus of elasticity whether E/Y is greater or lesser than 300. But the peak value (*i.e.* maximum mean contact pressure ratio), the dimensionless interference at which this value occurs, the trend of variation are all dependent on E/Y ratio. Dimensionless contact area, contact load also depends on modulus of elasticity. But dimensionless contact load, contact area and mean contact pressure is independent of the radius of sphere. The development of the elastic core and the transition to the plastic region within the surface for the wide range of interference is studied using Von Mises stress. It is observed that the dimensionless interference ratio at the instance when the plastic region fully covers the surface is dependent on the values of modulus of elasticity when

other properties are kept constant.

5. Nomenclature

Symbol	*Meaning*	*Unit*
P	Contact load	N
R	Radius of the sphere	mm
p	Pressure	GPa
ω	Interference	μm
A	Contact area	μm^2
E	Modulus of Elasticity	GPa
Y	Yield strength of sphere	GPa
ν	Poison's ratio	

5.1 Subscripts

c = critical values

5.2 Superscripts

/ = equivalent
* = dimensionless

6. References

[1] J. A. Greenwood and J. B. P. Williamson, "Contact of Nominally Flat Surfaces," *Proceedings of the Royal Society of London*, Vol. A295, 1966, pp. 300-319.

[2] S. Timoshenko and J. N. Goodier, "Theory of Elasticity," McGraw-Hill, New York, 1951.

[3] E. J. Abbott and F. A. Firestone, "Specifying Surface Quality－A Method Based on Accurate Measurement and Comparison," *Journal of Mechanical Engineering*, No. 55, 1933, pp. 569-572.

[4] W. R. Chang, I. Etsion and D. B. Bogy, "An Elastic-plastic Model for the Contact of Rough Surfaces," *Journal of Tribology*, Vol. 109, No. 2, 1987, pp. 257-263.

[5] Y. Zhao, D. M. Maietta and L. Chang, "An Asperity Micro Contact Model Incorporating the Transition from Elastic Deformation to Fully Plastic Flow," *Journal of Tribology*, Vol. 122, No. 1, 2000, pp. 86-93.

[6] L. Kogut and I. Etsion, "Elastic-plastic Contact Analysis of a Sphere and a Rigid Flat," *Journal of Applied Mechanics*, Vol. 69, No. 5, 2002, pp. 657-662.

[7] D. Tabor, "The Hardness of Metals," Clarendon Press, Oxford, 1951.

[8] L. Kogut and I. Etsion, "A Semi-analytical Solution for the Sliding Inception of a Spherical Contact," *Journal of Tribology*, Vol. 125, No. 3, 2003, pp. 499-506.

[9] V. Brizmer, Y. Kligerman and I. Etsion, "The Effect of Contact Conditions and Material Properties on the Elasticity Terminus of a Spherical Contact," *International Journal of Solids and Structures*, Vol. 43, 2005, pp. 5736-5749.

[10] R. L. Jackson and I. Green, "A Finite Element Study of Elasto-plastic Hemispherical Contact against a Rigid Flat," *Journal of Tribology*, Vol. 127, No. 2, 2005, pp. 343-354.

[11] J. J. Quicksall, R. L. Jackson and I. Green, "Elasto-plastic Hemispherical Contact Models for Various Mechanical Properties," *Journal of Engineering Tribology*, Vol. 218, No. 4, 2004, pp. 313-322.

[12] R. L. Jackson, I. Chusoipin and I. Green, "A Finite Element Study of the Residual Stress and Deformation in Hemispherical Contacts," *Journal of Tribology*, Vol. 127, No. 3, 2005, pp. 484-493.

[13] S. Shankar and M. M. Mayuram, "A Finite Element Based Study on the Elastic-plastic Transition Behavior in a Hemisphere in Contact with a Rigid Flat," *Journal of Tribology*, Vol. 130, 2008, pp. 1-6.

[14] R. Malayalamurthi and R. Marappan, "Elastic-plastic Contact Behavior of a Sphere Loaded against a Rigid Flat," *Mechanics of Advanced Materials and Structures*, Vol. 15, No. 5, 2008, pp. 364-370.

Engineering, 2010, 2, 212-219
doi:10.4236/eng.2010.24031 Published Online April 2010 (http://www.SciRP.org/journal/eng)

The Development of Self-Balancing Controller for One-Wheeled Vehicles

Chung-Neng Huang
Graduate Institute of Mechatronic System Engineering, National University of Tainan, Taiwan, China
E-mail: *kosono@mail.nutn.edu.tw*
Received November 30, 2009; *revised February* 16, 2010; *accepted February* 19, 2010

Abstract

The purpose of this study is to develop a self-balancing controller (SBC) for one-wheeled vehicles (OWVs). The composition of the OWV system includes: a DSP motion card, a wheel motor, and its driver. In addition, a tilt and a gyro, for sensing the angle and angular velocity of the body slope, are used to realize self-balancing controls. OWV, a kind of unicycle robot, can be dealt with as a mobile-inverted-pendulum system for its instability. However, for its possible applications in mobile carriers or robots, it is worth being further developed. In this study, first, the OWV system model will be derived. Next, through the simulations based on the mathematical model, the analysis of system stability and controllability can be evaluated. Last, a concise and realizable method, through system pole-placement and linear quadratic regulator (LQR), will be proposed to design the SBC. The effectiveness, reliability, and feasibility of the proposal will be confirmed through simulation studies and experimenting on a physical OWV.

Keywords: Self-balancing Controller, One-wheeled Vehicle, Mobile-inverted-pendulum, Pole-placement, Linear Quadratic Regulator (LQR)

1. Introduction

In recent years, because of the surging consciousness of global pollution and energy-shortage crises, automobiles and motorcycles are no longer the best for transportation. In order to fit the daily required and improve above problems, exploring new energy or developing lighter and innovative mobile carriers are beginning to be known as new trends. The earliest two-wheeled balancing robot was published in 1987 by Prof. Yamafuji [1]. From then on, the concerning researches with this topic have been increasing [2-6] and have even been a commercialized product. For example, the Human Transporter, was developed by Segway Co., U.S.A., which is a very famous two-wheeled balancing vehicle [7,8]. In addition, NASA's Robonaut, Segway platform puts robots in motion, is now aim in the military projects [9].

However, the balancing mechanism of a two-wheeled system is rather complicated. Whereas, for the problems, the two-wheeled synchronization and body balancing should be considered simultaneously, making a lot of sensors a requirement. It does not only complicate the system, but also increases the cost. For the reasons above, how to simplify the two-wheeled system has become one of the studying motives of OWV. By this motive, not only can it maintain the advantages of a two-wheeled system, but it can also simplify the system mechanism further, decreasing the cost.

Nowadays, although a lot of references engaging in the studies of two-wheeled balancing carriers can be found [2-6], the ones for OWV studies are still insufficient [10,11]. Trevor Blackwell [12], an American engineer, has proposed an OWV design on his personal website, and the concept OWV, EMBRIO, is published by BRP [13], a motorcycle manufacturer in Canada. Besides, [10] is the newest one based on fuzzy controls for balancing.

According to the above studies, one can find that the proposed OWV is rather new and is a worthy topic in studies on modern robots and carriers. However, most of the studies on robot-balancing subjects are often adopting the fuzzy control theory to handle those balancing control problems [4,14,15], but carrying out system modeling and analysis, and confirming the effectiveness and feasibility through experiment studies [14,15]. For fuzzy control, using linguistic information, can model complex systems without employing precise quantitative analyses, particularly for the controlled plant with in-

Identify applicable sponsor/s here. (*sponsors*)

complete knowledge [4,14]. However, it has not been viewed as rigorous due to lack of formal synthesis technologies, which guarantee the basic requirements for control systems such as global stability [15]. That is, it is not only difficult to precisely know the mutual influence between each system state but also might be difficult and expensive to design the controller for its complexity highly depending on the number of fuzzy rules [16].

Consequently, finishing system modeling and analysis for proposed SBC is set as the first step of this study. Next, by linearizing the system model, pole-placement and state-feedback controls can be found and designed. Finally, through human-computer interaction, a DSP card featured with motion control is adopted to handle the real-time computation of digital signals.

However, from above studies found that only using the pole-placement and state-feedback controls, the feedback gains can not be adjusted easily. It is difficult to lead the system in a better stability. Here, LQR is used to improve the above problems. For comparison, both the numerical and experiment studies on SBC, basing on pole-placement and LQR controls, respectively, are made. The studies have proved that the proposed SBC is able to perform higher controllability and stability.

2. Modeling for OWV

The concept of the OWV prototype is simply constructed by a wheel motor and two sensors as a tilt and gyro. Here, the wheel motor is adopted as the driving wheel of the OWV that uses the feedback signals from sensors to balance the system body. **Figure 1** shows the outward appearance of OWV prototype where the box on the upper side of wheel motor can be treated as the balancing weight of inverted-pendulum, and in which the motor driver, sensors are set. **Figure 2** shows the free body diagram of OWV in **Figure 1**.

According to the free body diagram in **Figure 2**, the kinetic energy E and potential energy U can be expressed as follows, respectively.

$$E = \frac{1}{2}M_w \dot{X}_w^2 + \frac{1}{2}m(\dot{X}_w + \dot{\theta} l\cos\theta)^2 + \frac{1}{2}m(-\dot{\theta} l\sin\theta)^2 + \frac{1}{2}J_m \dot{\theta}^2 + \frac{1}{2}J_w(\frac{\dot{X}_M}{R})^2 \quad (1)$$

$$U = -mgl + mgl\cos\theta \quad (2)$$

Basing on Lagrange's equation as well as the coefficient transformation for deriving mathematic model of OWV, the Lagrange equation can be written as:

$$\frac{d}{dt}\left(\frac{\partial L}{\partial \dot{X}_w}\right) - \frac{\partial L}{\partial X_w} = \frac{T_w}{R}$$

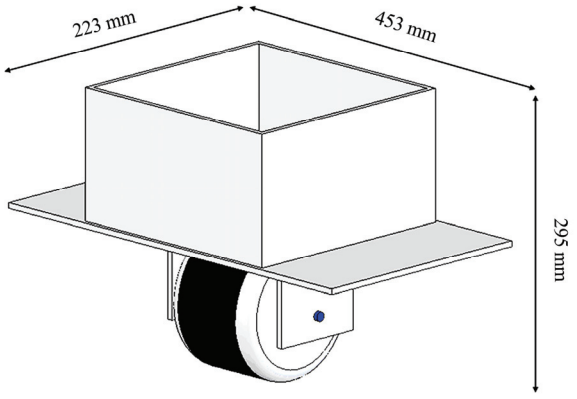

Figure 1. OWV prototype.

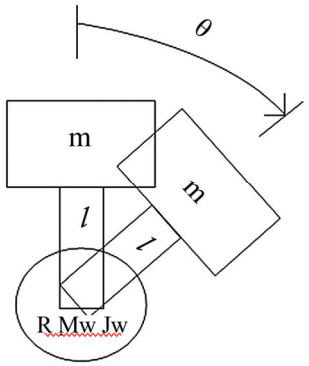

Figure 2. Free body diagram of OWV.

$$\frac{d}{dt}\left(\frac{\partial L}{\partial \dot{\theta}}\right) - \frac{\partial L}{\partial \theta} = 0 \quad (3)$$

where $L = E - U$

From (3), the accelerations of body movement and included angle between vertical axis and body can be found as follows.

$$\ddot{X}_w = \frac{\frac{T_w}{R} + ml\sin\theta\dot{\theta}^2 - \frac{m^2l^2g\sin\theta\cos\theta}{ml^2 + J_m}}{M_w + m + \frac{J_w}{R^2} - \frac{m^2l^2\cos^2\theta}{ml^2 + J_m}} \quad (4)$$

$$\ddot{\theta} = \frac{\frac{-ml\cos\theta(\frac{T_w}{R} + ml\sin\theta\dot{\theta}^2)}{M_w + m + \frac{J_w}{R^2}} + mgl\sin\theta}{ml^2 + J_m - \frac{m^2l^2\cos^2\theta}{M_w + m + \frac{J_w}{R^2}}} \quad (5)$$

Since (4) and (5) are nonlinear equations, for simplifying and modeling, let them be represented on the balanced point $\theta = 0°$ and given $M_e = M_w + m + \frac{J_w}{R^2}$, then

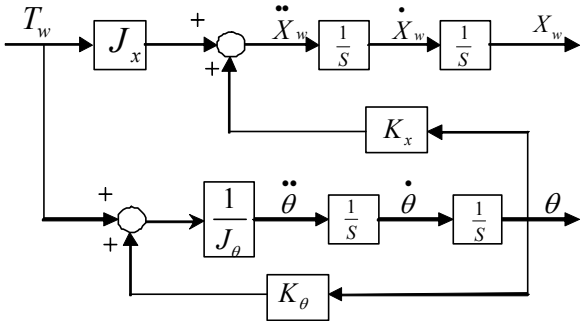

Figure 3. OWV control (linear).

the equations can be rewritten as

$$\ddot{X}_w = \frac{-m^2l^2g\theta}{M_e(ml^2+J_m)-m^2l^2} + \frac{(ml^2+J_m)T_m}{M_eR(ml^2+J_m)-m^2l^2R} \tag{6}$$

$$\ddot{\theta} = \frac{mglM_e\theta}{M_e(ml^2+J_m)-m^2l^2} + \frac{-mlT_m}{M_eR(ml^2+J_m)-m^2l^2R} \tag{7}$$

By using (6) and (7), the block diagram for OWV control can be illustrated as shown in **Figure 3**. Where,

$$J_x = \frac{ml^2+J_m}{R[M_e(ml^2+J_m)-m^2l^2]},$$

$$K_x = \frac{-m^2l^2g}{M_e(ml^2+J_m)-m^2l^2}$$

$$J_\theta = \frac{-ml}{M_eR(ml^2+J_m)-m^2l^2R},\quad K_\theta = -M_egR$$

From **Figure 3**, it can be found that OWV is a single input and multiple output system (SIMO). Besides, OWV is similar to the inverted-pendulum vehicle, belonging to the non-minimum phase system [3,17].

3. Analysis and Design for State Variables

3.1. Performance of System Instability

Since a system can be represented in state space by following equations:

$$\dot{X} = AX + Bu \tag{8}$$

$$y = CX + Du \tag{9}$$

for $t \geq t_0$ and initial conditions with respect to the equilibrium point, $X(t_0) = (0,0,0,0)$, where

X : state vector

$\dot{X}$: derivative of the state vector with respect to time

y : output vector

u : input or control vector

A: system matrix

B: input matrix

C: output matrix

D: feed forward matrix

(8) is called the state equation, and the vector X, the state vector, contains the state variables. It can be solved for the state variables. Besides, (9) is called the output equation. This equation is used to calculate any other system variables.

For the linear, time-invariant, second-order system as OWV, its system dynamics can be transformed and expressed by state equations; the state space of OWV can be taken on the following form by (6) and (7).

$$\begin{bmatrix} \dot{X}_w \\ \ddot{X}_w \\ \dot{\theta} \\ \ddot{\theta} \end{bmatrix} = \begin{bmatrix} 0 & 1 & 0 & 0 \\ 0 & 0 & \frac{-m^2l^2g}{M_e(ml^2+J_m)-m^2l^2} & 0 \\ 0 & 0 & 0 & 1 \\ 0 & 0 & \frac{M_emgl}{M_e(ml^2+J_m)-m^2l^2} & 0 \end{bmatrix} \begin{bmatrix} X_w \\ \dot{X}_w \\ \theta \\ \dot{\theta} \end{bmatrix} + \begin{bmatrix} 0 \\ \frac{ml^2+J_e}{M_eR(ml^2+J_m)-m^2l^2R} \\ 0 \\ \frac{-ml}{M_eR(ml^2+J_m)-m^2l^2R} \end{bmatrix} [T_w] \tag{10}$$

$$\begin{bmatrix} X_w \\ \theta \end{bmatrix} = \begin{bmatrix} 1 & 0 & 0 & 0 \\ 0 & 0 & 1 & 0 \end{bmatrix} \begin{bmatrix} X_w \\ \dot{X}_w \\ \theta \\ \dot{\theta} \end{bmatrix} \tag{11}$$

In order to confirm the effectiveness of the derived model, through the simulation by mechanical design software Solidworks, or CATIA, system analysis and estimation of system coefficients are done.

Table 1 and **Figure 4** show the estimated system coefficients of OWV by Solidworks' analysis.

Based on above, system coefficients and system stability, the analysis finds that for OWV it is not a stable system. Initially, it would fall down by an outside disturbance. This phenomenon can be confirmed by the root locus as shown in **Figure 4**. Where, for one of the poles locating in the right of s-plane, it can be judged that it is an unstable system. Besides, this result also can be confirmed by finding out the eigenvalues of system matrix in (10) as $S = 0,\ 0,\ 4.4116,\ -4.4116$.

Table 1. System coefficients of OWV.

m	4.31 kg
J_m	0.1984 kg/m^2
l	0.1 m
R	0.07 m
M_w	5.1819 kg
J_w	0.0123 kg/m^2

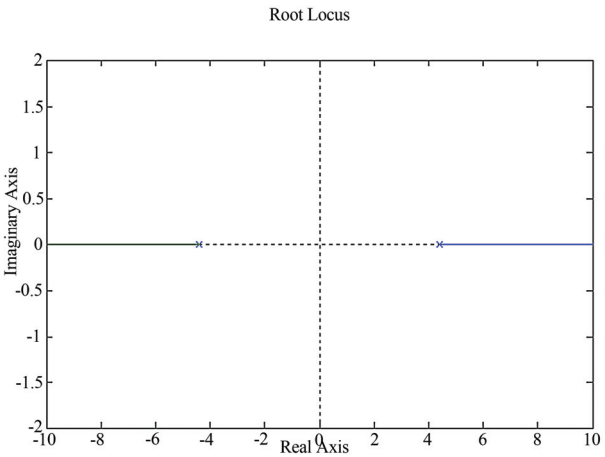

Figure 4. Root-locus diagram.

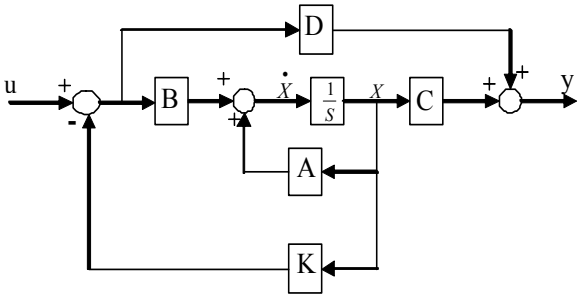

Figure 5. State-feedback block diagram.

In order to improve the system instability, the state feedback as well as the pole-placement design is adopted to make the system stable and balanced. By which, the block diagram of the system state feedback is shown as **Figure 5**. Where, the feedback is given as $u = -Kx(t)$.

3.2. Analysis for the Controllability of OWV

Accepting to discuss the system stability in state-space analysis, the controllability of system is also an important index. That is, before designing state-feedback controllers, the analysis for controllability should be done in advance to make sure the system is able to achieve the desired responses through state-feedback control and observing.

Pole-placement is a viable design technique only for systems that are controllable. In order to be able to determine controllability or, alternatively, to design state feedback for a plant under any representation or choice of state variables, a matrix can be derived that must have a particular property if all state variables are to be controlled by the plant input, u. For an nth-order plant whose state equation is (8), which is completely controllable if the matrix

$$Q_c = \begin{bmatrix} B & AB & A^2B & \cdots & A^{n-1}B \end{bmatrix} \tag{12}$$

is of rank n, where Q_c is called the controllability matrix. Now, by substituting the coefficients of **Table 1** to the system and inputting matrices in (10) and using (12), then $rank[Q_c] = 4$ can be found. That is, OWV is completely controllable on the balancing point. Its closed-loop system's poles can be placed at desired locations on the s-plane through using the state feedback $u(t) = -Kx(t)$.

3.3 State-Feedback Control

In **Figure 5,** for the system feedback $u = -Kx(t) = [k_1 \quad k_2 \quad k_3 \quad k_4]$, the closed-loop system matrix can be expressed as

$$A - BK = \begin{bmatrix} 0 & -1 & 0 & 0 \\ 1.2717\,k_1 & 1.2717\,k_2 & 0.6987 + 1.2717\,k_3 & 1.2717\,k_4 \\ 0 & 0 & 0 & -1 \\ -2.2696\,k_1 & -2.2696\,k_2 & -19.4625 - 2.2696\,k_3 & -2.2696\,k_4 \end{bmatrix} \tag{13}$$

Thus, the transfer function of the closed-loop system $\det[sI - (A - BK)] = 0$, is

$$\begin{bmatrix} s & 1 & 0 & 0 \\ -1.2717k_1 & s - 1.2717k_2 & -0.6987 - 1.2717k_3 & -1.2717k_4 \\ 0 & 0 & s & 1 \\ 2.2696k_1 & 2.2696k_2 & 19.4625 + 2.2696k_3 & s + 2.2696k_4 \end{bmatrix} = 0$$

Here, assume an example for placing the system's poles at s = 0, 0, -4.5, -4, since the system transfer function should satisfy the condition $s^2(s+4.5)(s+4) = 0$, the feedback gains of system state can be found as $K = [k_1 \quad k_2 \quad k_3 \quad k_4] = [0 \quad 0 \quad -16.5062 \quad -3.7452]$. In order to confirm the effectiveness of pole-placement, a simulation study on OWV by using the results (feedback gains) of the above example is done. **Figure 6** shows that through system feedback control, all system's poles of OWV have located in the left of s-plane. In addition, the feed-back system, being disturbed by a continuous impulse motion,

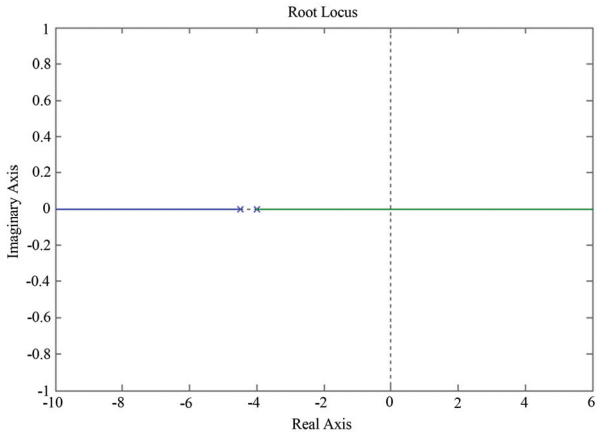

Figure 6. Root-locus diagram.

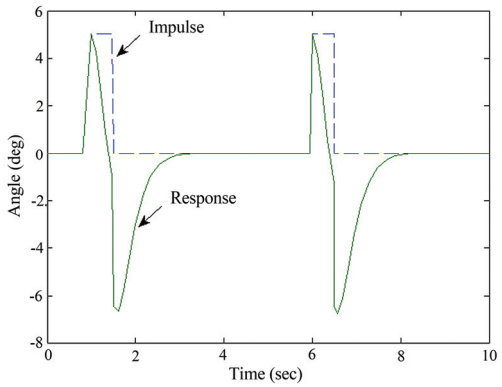

Figure 7. Impulse and system response.

still can return to the desired balancing state as shown in **Figure 7**.

3.4 LQR Control

In above section, it shows that pole-placement and state-feedback controls used for SBC are available and realizable. However, if the unstable pole could only be placed in the left of s-plane by using assignments (experienced studies), then adjusting the feedback gains to a better stability for OWV would be difficult.

In order to improve above problem, LQR, the continuous time infinite horizon linear quadratic regular with control constraints, is adopted to design SBC. Deterministic LQR theory was first introduced by Kalman, and has been playing a central role in modern control theory as well as various engineering practices; the reader can be referred to the well-known book [18], as the following problem:

Minimize quadratic performance index

$$J = \int_0^{+\infty} \left[X^T(t) Q X(t) + u^T(t) R u(t) \right] dt \qquad (14)$$

subject to linear dynamics (8), (9) and a constraint on the input $u(t) \in U$, for all $t \in [0,+\infty)$.

Here, the state vector $X : [0,+\infty) \to IR^n$ is locally absolutely continuous, and the minimization is carried out over all locally integrable controls $u : [0,+\infty) \to IR^k$. Throughout the note, the standing assumptions are

1) Q and R, the weighting matrices of $X(t)$ and $u(t)$, are symmetric and with positive semi-definite and positive definite, respectively.

2) The pair (A, B) is controllable. The pair (A, C) is observable.

3) The set U is closed, convex, and $0 \in \text{int}\, U$.

For the unconstrained problem (8), (9) and (14), the optimal solution of the problem is the following state-feedback control.

$$u(t) = -K(t) X(t) \qquad (15)$$

where, $K(t) = R^{-1} B^T P(t)$, and P, the unique symmetric and positive definite matrix, is the solution of the Riccati differential equation as

$$\dot{P}(t) = -P(t)A + A^T P(t) + P(t) B R^{-1} B^T P(t) - Q \qquad (16)$$

Since there is only stable state considered for OWV system, that is $\dot{P}(t) = 0$, (16) can be rewritten as

$$PA + A^T P - P B R^{-1} B^T P = -Q \qquad (17)$$

By substituting (17) into (15) with system coefficients, $K(t)$, the optimal feedback gains, can be found as

$K = \begin{bmatrix} k_1 & k_2 & k_3 & k_4 \end{bmatrix} = \begin{bmatrix} -3.1623 & -3.9851 & -32.5896 & -7.5687 \end{bmatrix}$, by giving matrices $R = [1]$, and $Q = diag([10 \quad 1 \quad 1 \quad 1])$. The R and Q are provided to have constraint of control action satisfied.

Figure 8 shows the comparison of stability responses by using pole-placement and LQR, respectively. Where, SBC, basing on LQR control, let OWV have a better system stability is confirmed.

4. Physical Demonstration of OWV

For further confirming above numerical studies and the feasibility of OWV, the testing setup is accomplished and pictured in **Figure 9**.

A motor driver and sensors (SSY0090 tilt and CRS03-02 gyro) are set in the box and a 24-V 250-W wheel motor (SA176-6) [19] is used as the driving wheel. All the algorithms for pole-placement, feedback-gain calculation, and LQR etc. are developed with C language and implemented in an ITRI PMC32-6000 DSP board with a clock frequency of 40MHz (**Figure 10**).

Figure 11 illustrates that when the instability of body is detected by those sensors, the angular signals, through A/D transformation, transfer to DSP for real-time digital

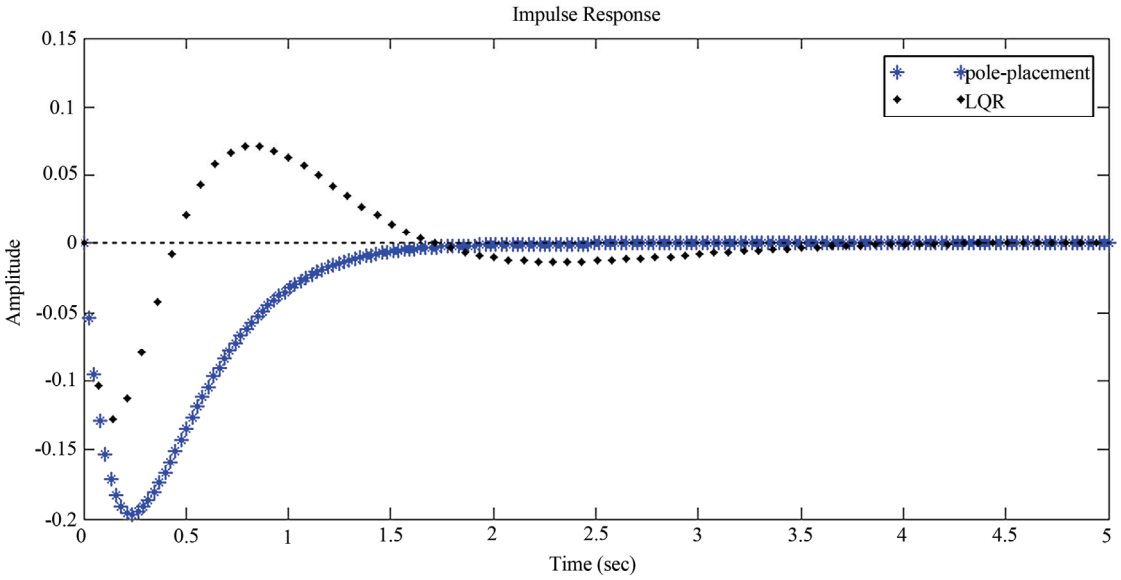

Figure 8. Comparison of stability responses.

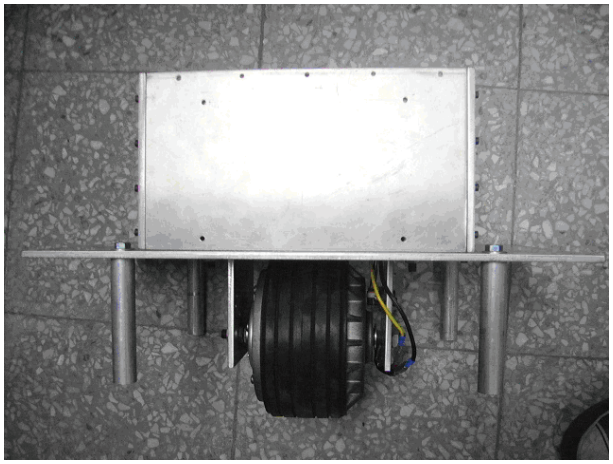

Figure 9. OWV setup.

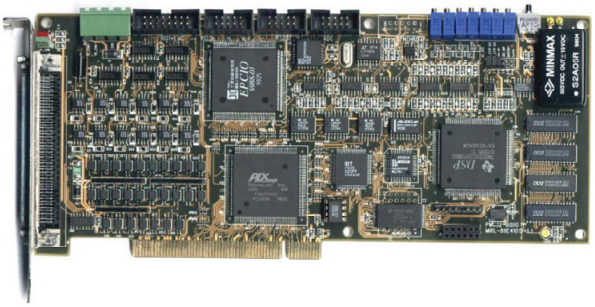

Figure 10. DSP board.

computation and decision. Then, the decision signal from DSP will send to motor driver via D/A transformation. Here, the sampling period is set to 1 ms. That is, the interrupting algorithm is executed by every 1 ms.

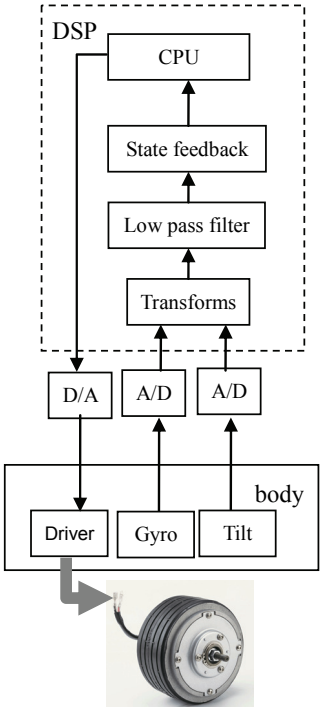

Figure 11. Control block diagram of OWV.

Figure 12 shows the voltage outputs of motor control, angular signals of OWV's body from gyro and tilt while SBC bases on pole-placement and LQR controls, respectively. Here, by examining angular velocity (**Figure 12(b)**), since it, the derivatives of body tilt angle can be taken as the estimation of next-state body falls, the

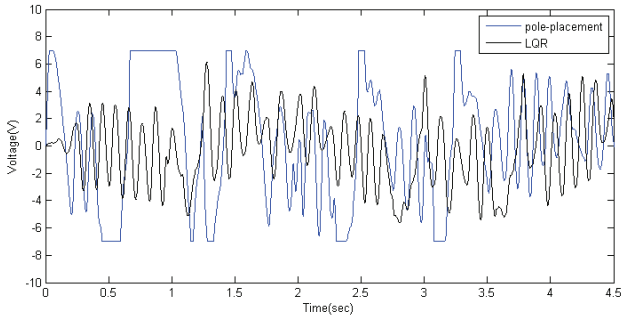

(a) voltage outputs

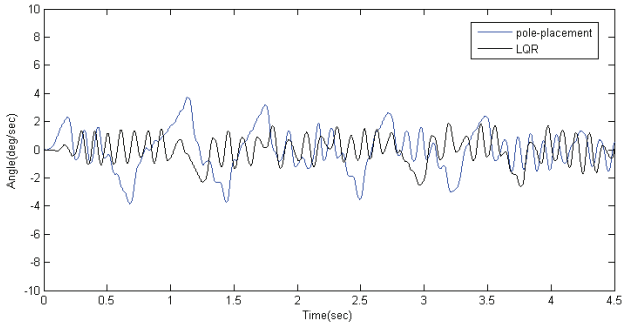

(b) angular velocity

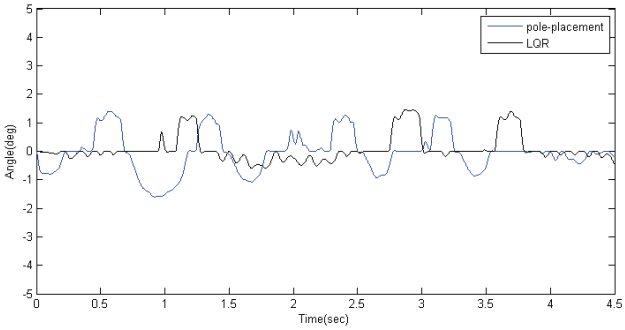

(c) tilt angle

Figure 12. Control signals.

voltage signal (**Figure 12(a)**) is approximately inverse to angular velocity for falling-preventive control. Besides, in **Figure 12(c)**, even through some tiny oscillations within ± 2 degree occur when the body of OWV is starting to swing up by the wheel-motor driving a horizontal force to move OWV back and forth, after 3.75 seconds it can return to the desired balancing state. Consequently, it proves that SBC is able to be realized by both above controls. Moreover, through the comparisons of the signals in **Figure 12**, finds that the magnitude of the state signals by LQR control is smaller than those by pole-placement control. It is not only shows LQR with better system stability performance but also corresponding to the objective of LQR control in (14).

5. Conclusions

This study has proposed a SBC, based on concise construction and control theories for OWV. Only based on state-space modeling and real-time sensing, the SBC is attractive for its conciseness and feasibility. Studied results show that the real-time SBC is not only can be realized but also can let OWV with optimal stability by LQR control.

By further developing OWV technologies, such as SBC etc., the benefits not only can serve the handling problems, existing in present electrical mobile-robots, welfare carriers, or two-wheel entertainment vehicles as large steering radius (angle), differential gear, or synchronization control etc., but also with advantages on cost, setup, light quantity, and saving energy, etc.

6. References

[1] Z. Sheng and K. Yamafuji, "Postural Stability of a Human Riding a Unicycle and Its Emulation by a Robot," *IEEE Transactions on Robotics and Automation*, Vol. 13, No. 5, 1997, pp. 709-720.

[2] Y.-S. Ha and S. Yuta, "Trajectory Tracking Control for Navigation of the Inverse Pendulum Type Self-contained Mobile Robot," *Robotics and Autonomous Systems*, Vol. 17, No. 1-2, 1996, pp. 65-80.

[3] F. Grasser, A. D'Arrigo, S. Colombi and A. C. Ruffer, "JOE: A Mobile, Inverted Pendulum," *IEEE Transactions on Industrial Electronics*, Vol. 49, No. 1, 2002, pp. 107-114.

[4] S. Jung and S. S. Kim, "Control Experiment of a Wheel-Driven Mobile Inverted Pendulum Using Neural Network," *IEEE Transactions on Control Systems Technology*, Vol. 16, No. 2, 2008, pp. 297-303.

[5] K. Pathak, J. Franch and S. K. Agrawal, "Velocity and Position Control of a Wheeled Inverted Pendulum by Partial Feedback Linearization," *IEEE Transactions on Robotics*, Vol. 21, No. 3, 2005, pp. 505-513.

[6] Y. Kim, "Dynamic Analysis of a Nonholonomic Two-Wheeled Inverted Pendulum Robot," *Journal of Intelligent and Robotic Systems*, Vol. 44, No. 1, 2005, pp. 25-46.

[7] H. Tirmant, M. Baloh, L. Vermeiren, T. M. Guerra and M. Parent, "B2, an Alternative Two Wheeled Vehicle for an Automated Urban Transportation System," *Proceedings of IEEE Intelligent Vehicles Symposium*, Vol. 2, 2002, pp. 594-603.

[8] D. Voth, "Segway to the Future [autonomous mobile robot]," *IEEE Intelligent Systems*, Vol. 20, 2005, pp. 5-8.

[9] R. O. Ambrose, R. T. Savely, S. M. Goza, P. Strawser, M. A. Diftler, I. Spain and N. Radford, "Mobile Manipulation using NASA's Robonaut," *Proceedings of IEEE International Conference on Robotics and Automation*, New Orleans, 2004, pp. 2104-2109.

[10] K. Hofer, "Electric Vehicle on One Wheel," *IEEE Vehicle Power and Propulsion Conference*, Dearborn, September 7,

2005, pp. 517-521.

[11] K. Hofer, "Observer-Based Drive-Control for Self-Balanced Vehicles," *Proceedings of IEEE/IECON* 32*nd Annual Conference on Industrial Electronics*, 2006, pp. 3951-3956.

[12] The Electric Unicycle, http://tlb.org/eunicycle.html

[13] EMBRIO, http://www.brp.com/en-CA/

[14] C. W. Tao, J. S. Taur, T. W. Hsieh and C. L. Tsai, "Design of a Fuzzy Controller with Fuzzy Swing-Up and Parallel Distributed Pole Assignment Schemes for an Inverted Pendulum and Cart System," *IEEE Transactions on Control Systems Technology*, Vol. 16, 2008, pp. 1277-1288.

[15] R. J. Wai, M. A. Kuo and J. D. Lee, "Cascade Direct Adaptive Fuzzy Control Design for a Nonlinear Two-Axis Inverted-Pendulum Servomechanism," *IEEE Transactions on Systems*, *Man and Cybernetics*, *Part B*, Vol. 38, 2008, pp. 439-454.

[16] C. W. Tao and J.-S. Taur, "Flexible Complexity Reduced PID-like Fuzzy Controllers," *IEEE Transactions on Systems*, *Man and Cybernetics*, *Part B*, Vol. 30, No. 4, 2000, pp. 510-516.

[17] M. I. El-Hawwary, A. L. Elshafei, H. M. Emara and H. A. Abdel Fattah, "Adaptive Fuzzy Control of the Inverted Pendulum Problem," *IEEE Transactions on Control Systems Technology*, Vol. 14, No. 6, 2006, pp. 1135-1144.

[18] B. Anderson and J. Moore, "Optimal Control-Linear Quadratic Methods," Prentice-Hall, Upper Saddle River, 1990.

[19] Y.-P. Yang and D. S. Chuang, "Optimal Design and Control of a Wheel Motor for Electric Passenger Cars," *IEEE Transactions on Magnetics*, Vol. 43, No. 1, 2007, pp. 51-61.

Appendix A

Nomenclature

m : pendulum payload mass

J_m : pendulum moment of inertia

l : Pendulum length

R : wheel radius

M_w : single wheel mass

J_w : single wheel moment of inertia

X_w : center cart trajectory

θ : pendulum tilt angle

T_w : driving torque

Engineering, 2010, 2, 220-227
doi:10.4236/eng.2010.24032 Published Online April 2010 (http://www.SciRP.org/journal/eng)

Algorithms for Masking Pixel Defects at Low Exposure Conditions for CMOS Image Sensors

***Vinesh Sukumar, Jason Tanner, Atif Sarwari, *Herbert L Hess**
**Microelectronics Research and Communications Institut-MRCI, University of Idaho, Moscow, U.S.A.*
E-mail: vsukumar@ieee.org
Received November 20, 2009; *revised January* 27, 2010; *accepted February* 4, 2010

Abstract

This paper introduces certain innovative algorithms to mask for pixel defects seen in image sensors. Pixel defectivity rates scale with pixel architecture and process nodes. Smaller pixel and process nodes introduce more defects in manufacturing. Brief introduction to causes for pixel defectivity at lower pixel nodes is explained. Later in the paper, popular defect correction schemes used in image processing applications are discussed. A new approach for defect correction is presented and evaluated using images captured from an 8M Bayer image sensor. Experimentation for threshold evaluation is done and presented with practical results for better optimization of proposed algorithms. Experimental data shows that proposed defect corrections preserves a lot of edge details and corrects for bright and hot pixels/clusters, which are evaluated using histogram analysis.

Keywords: Hot Pixels, Pixel Clusters, Defect Correction, Cluster Correction

1. Introduction

Digital imaging systems (including digital still camera, digital video camera etc) capture the spectrum or color information of physical stimuli by filtering the object image through color filters with different spectral transmittances, and transform the photon signal into electronic signal which finally is quantized into digital counts with electronic sensors [1]. Electronic sensors generally are based on Charge-Coupled Device (CCD) or Active Pixel Sensor (APS) Complimentary MOS technology. This digital information produced by these electronic sensors, ignoring all non-idealities of CMOS/CCD imager optics and pixels, must undergo some image processing functions prior to display on any visual media or data storage in Red Green Blue (RGB) format. The resolving power of the imaging system to present details of the viewing object can be presented in terms of system MTF (Modulation Transfer Function) [1].

Pixel architecture is always a crucial element of any imaging system design, which can be quantified in MTF terms. Pixel designers always have to make a fundamental tradeoff when choice comes to selecting a pixel size. Reducing pixel size improves the imaging system performance by increasing spatial resolution for fixed sensor die size. Increasing pixel size improves the imaging system performance by increasing dynamic range and signal-to-noise ratio. Pixel scaling has been very aggressive in the APS CMOS domain when compared to that of CCD as illustrated in **Figure 1**. These solid-state image sensors develop in-field defects in all common APS CMOS manufacturing environments. This is more challenging for smaller pixel geometries. Many experiments have demonstrated the growth of significant quantities of pixel defects that degrade the dynamic range of an image sensor and potentially limit low-light imaging performance. Existing image processing techniques used in several imaging applications used for suppressing hot-pixels are inadequate because these defective pixels saturate at relatively low illumination levels.

In this paper, an 8M CMOS APS sensor, which has plenty of hot-pixels, is used for analysis. A correction algorithm repairs the final image by certain unique processing algorithms which are discussed in this paper. Performance metrics and tradeoffs are presented in the latter half of the paper.

2. Hot Pixel Characteristics

As pixels are made smaller to improve on image resolution, pixel elements get located closer together, resulting in increased risk of cross-talk between adjacent pixels. Shallow trench isolation (STI) regions, which may be dielectric-filled trenches formed in the substrate of the

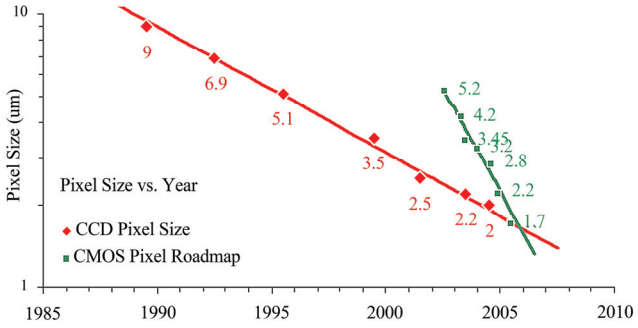

Figure 1. CCD and CMOS pixel scaling trends.

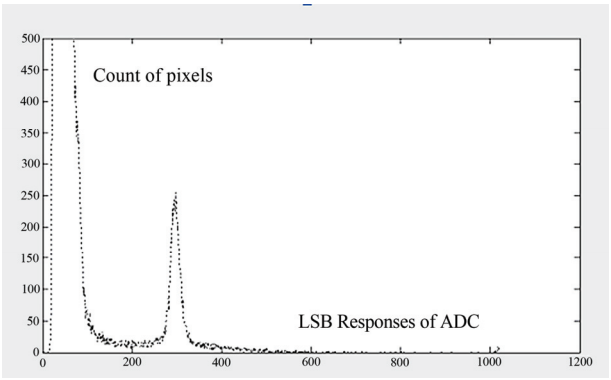

Figure 2. Histogram response of very hot pixels for a 1.3 M dark image capture presented for a 10bit ADC.

image sensor, may be used to isolate pixels and pixel elements from each other but STI boundaries have a higher defect density than the substrate, creating a higher density of "trap sites" along the STI boundaries as compared to the silicon/gate oxide interface or silicon surface that can "trap" electrons or holes. Trap sites may result from defects along the silicon dioxide/silicon interface between the STI boundaries and the silicon substrate. Trapped electrons or holes may generate a proportional current at the trap site. The current generation from trap sites inside or near the photosensor contributes to dark current (*i.e.*, electrical current in the photo sensor in the absence of light) in CMOS image sensors since a constant charge may be leaking in the photodiode. Because the readout circuitry of the image sensor may not distinguish between sources of charge in the photosensitive element, dark current may be added to the magnitude of the signal output from the pixel, thus making the pixel appear brighter in the produced image than that point actually appeared in the scene. Such a pixel may be referred to as a hot pixel. This issue becomes more of a challenge as process nodes shrink along with pixel architecture. These hot pixels manifest as bright pixels in an image taken at dark or low light conditions. The problem can be seen as a hump in the histogram to the right of the main peak as illustrated in **Figure 2**. With increasing integration time and temperature, the hump

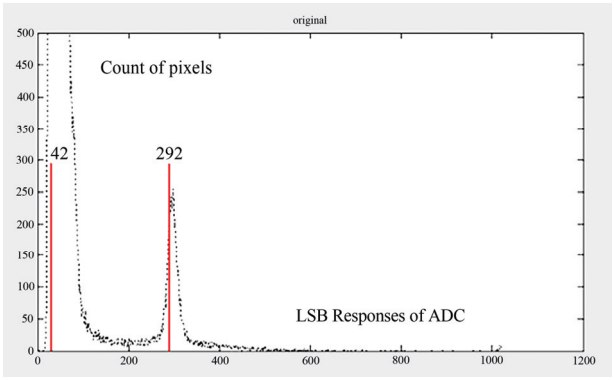

Figure 3. Histogram response highlighting the normal pixel response and very hot pixel for a dark image capture.

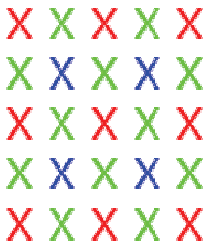

Figure 4. 5 × 5 window kernel used for defect correction in many image processing systems.

moves further to the right and decreases in size as pixels become brighter [2].

This paper talks in details on algorithms which can be implemented in the image pipeline to mask these defects with minimum to no loss in image details and resolution.

3. Defect Correction Schemes

Over the years, several image processing scientists have been very innovative is masking these hot pixels. One of the popular approaches towards defect correction in the past was to determine if the center pixel of a 5 × 5 window kernel is outside the range of the neighboring pixels. It was then checked to see if it was within an X (X = 250) LSB counts of the median value in Bayer space. In a dark image capture, the median of the normal pixels in 10 bit domain would be about 42 LSB counts. So 292(X = 250 + 42) LSB counts and lower are pixels that would not be removed since they are within 250 LSB counts of the median pixel value (presenting with an example because past approaches worked with a window as well) [3]. As can be seen from **Figure 3**, about half of the pixels would pass, when they should all be fails. These dice would render a poor image in all the dark regions. Lowering the limit of X = 250 LSB counts down to X = 200 LSB counts or lower would remove more of the worst case hot pixels, but even pixels as low as 140 LSB counts would be visible in a dark image. In addition,

removing clusters is important since the likelihood of failing pixels in the same window is more likely as pixel size shrink in lower process nodes. Better solutions to resolve this issue are presented below.

Approach 1: In earlier implementations, if the pixel of a 5 × 5 window kernel as presented in **Figure 4** lies within the range of the six nearest neighbors, the pixel under test was automatically considered a good pixel. In this new approach, if it is assumed that any two red pixels are completely exposed to maximum 1023 LSB counts (for a 10 bit ADC domain) and are located next to each other. Other assumption is that the rest of the pixels have a response portfolio of 100 LSB counts. Checking one of the 1023LSB count pixel would show that it does lie within the range of 1023 LSB counts and pass quality monitor before being checked to be within a threshold of the median. This new approach allows an indicated number of pixels to be removed from the 5 × 5 window kernel before the range is checked.

In MATLAB simulations, two thresholds are used: 200 and 150 LSB counts. In these simulations, (one at 150 and one at 200 LSB counts) the highest pixel of the six neighbors was removed from the list of eligible pixels. Several dice from the different production lots were tested. From the data below, throwing out the high pixel from the nearest neighbors removed more bright pixels. At the same time, the lower threshold replaced more pixels [4].

The option of removing defective pixels from any defect analysis kernel is essential to eliminate any pixel clusters. During experimental analysis, using images with known defects, the visually best images removed only one defective pixel. Removing two defective pixels created false colors in some images and noticeably removed detail. This approach also removed the most defects. The test image used in this study is presented in **Figure 5**, which is captured using a digital SLR. Image 5a shows none of the brightest pixels from the analysis kernel being removed. Image 5b is with one pixel removed from the kernel. Image 5b is with two pixels and lastly Image 5c is with three pixels removed from the defect correction kernel. It is clear that when more pixels are removed from the analysis kernel, borders tend to become more blurred leading to loss of fine detail. This would be unacceptable in many high end mobile camera applications where importance is given to preserving details.

A potential improvement to Approach 1 will be to use a dynamic distance option rather than a static distance option from the median of the kernel. This option creates a dynamic threshold by calculating the difference from the MAX pixel value (with an option of removing certain number of pixels from the window of analysis) and then multiplying it by a set constant. A MIN and MAX value is set for this threshold. For example, if the threshold T_d < 50 LSB counts, the value is automatically set to 50 and

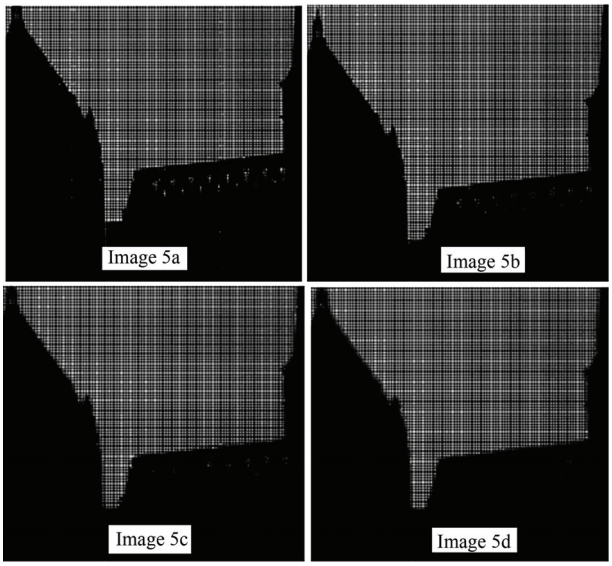

Figure 5. Effect of eliminating different amount of defective pixels from the defect analysis kernel on a digital SLR captured test image [5].

if T_d > 400 LSB counts, the value is set to the difference from the MAX to the median. This allows flat areas of the image to be flat and to check for edges of the image. Experimental analysis using this improved Approach 1 is preserved for future analysis.

Approach 2: In this approach, instead of comparing the center pixel to its neighbors, this approach checked to see if the center pixel has any neighbors within its range. The pixels from the analysis kernel are also forced to have two of their neighbors in that threshold. The neighbors were forced to lie within a group of predetermined shapes as illustrated in **Figure 6** (three horizontal rows, three vertical rows, two diagonals, and four corners-only one is illustrated for simplicity).

This approach forced regions to have context with relation to the area under test. So if no shape is found in the neighborhood, the center pixel failed and was assigned the median value. If any shape(s) is to be found, the pixels lying within the shape(s) were summed to find the mean. The center pixel has to be within a set threshold of the mean to be valid. This way multiple pixels can be ignored to identify a defective pixel. The image regions, where the kernel passes over edges or other shapes can judge a pixel by the context of the pixels in its neighborhood rather than all eight surrounding pixels from the kernel. For example in **Figure 7**, if there is a vertical edge in an image, where the transition happens from black to white. All of the horizontal shapes will fail as none of the three pixels are on the black plane. For the vertical shapes, the first column will pass as while the last column will not as they are not in the neighborhood of the center pixel. In a similar fashion, the diagonal shapes test will both fail and two of the four corner shape tests will pass. So all the pixels in the two columns and

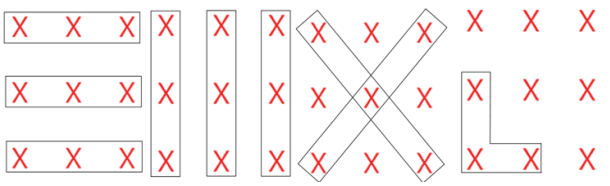

Figure 6. Predetermined shapes used in Approach 2 defect correction analysis.

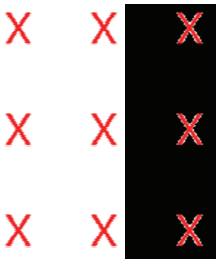

Figure 7. A 3 × 3 kernel showing transition from white to black region in a test image. This is done to gauge performance of Approach 2.

two corner shapes will be used to compute an average. If the center pixel is found to lie within a threshold of the

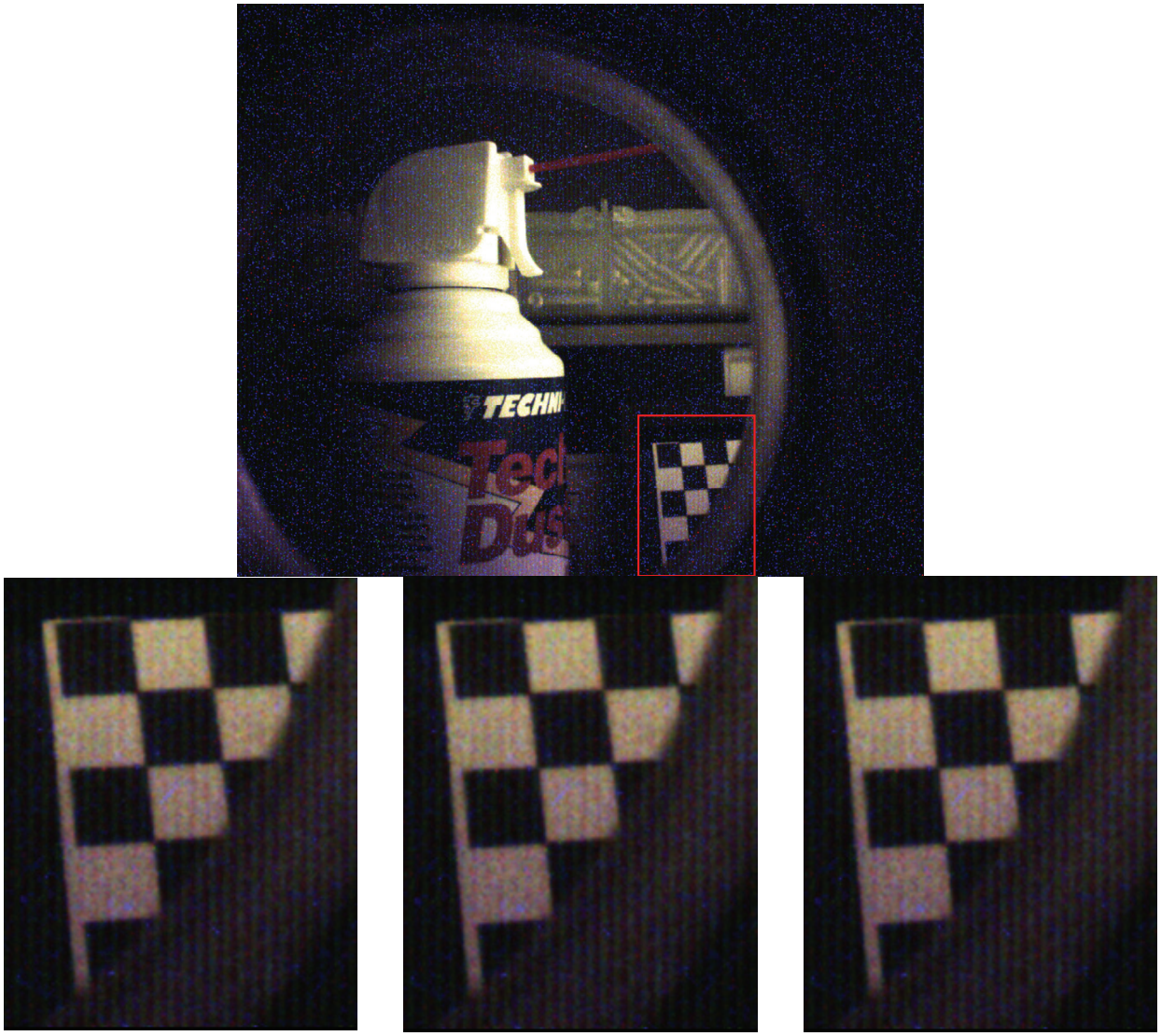

Approach 2–310 Approach 2–351 Approach 2–251

Approach 2–310: First threshold of 300 and a second threshold of 100.
Approach 2–351: First threshold of 300 and a dynamic second threshold of 50.
Approach 2–251: First threshold of 200 and a dynamic second threshold of 50.

Figure 8. Different versions of Approach 2 are tested on an 8 M captured image to visually understand improvements expected. The red box image indicates the region being tested from the original image. Note the ability of the different implementations to remove the noise in the upper left corner of the checkerboard pattern. Approach 2 clearly does the best job of presenting details and not mixing together the square with the neighboring white regions. Definitions for each of the approaches are presented below.

Approach 2–310: First threshold of 300 and a second threshold of 100.
Approach 2–351: First threshold of 300 and a dynamic second threshold of 50.
Approach 2–251: First threshold of 200 and a dynamic second threshold of 50.

Figure 9. Different versions of Approach 2 are tested on a different section of the image to understand detail preservation. Each of the approaches used does a good job with elimination of defects and avoid any smearing artifacts.

computed value, the pixel under test is a good pixel. If it is to be a defective pixel, the computed average value of the neighbors or the median of the neighbors will now be the new pixel value. In this test case, five pixels instead of eight pixels will compute the new value of the pixels in the analysis kernel [6].

This algorithm will be able to handle anything lower than three pixel clusters that lay within one of the pre-defined shapes. Also, this approach takes advantage of the random noise patterns. There is always a point, where the noise overrides the ability to detect any shapes. Such die would be failed as gross fails [7]. As a minor adjustment to Approach 2, the threshold of the neighbors in the analysis kernel is also dynamically adjusted. This is based on the number of pixels that are counted to be as neighbors. If a given pixel has all eight neighbors, it is considered a possibility that the pixel under test lies within a region of subtle transition. This expanded the threshold by a set factor. This approach is tested by multiplying by scale two if there are more than three pixels and multiplied by scale three if there are more than six pixels.

4. Experimental Results

In the experimental test results section, multiple versions of Approach 2 are tested to narrow down the optimal thresholds and other settings. Unless otherwise mentioned, all test images used are taken from an 8 M CMOS image sensor. This sensor supports 1.75 um pixel, 4WS

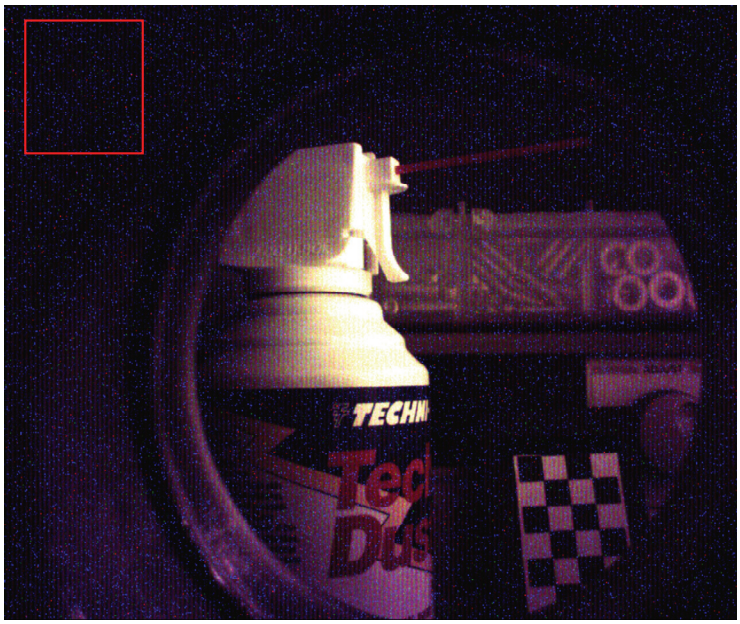

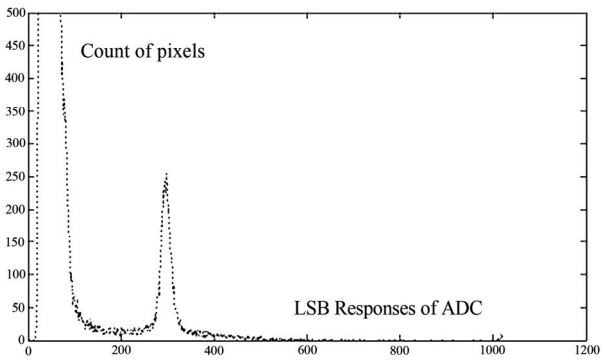

Histogram response: Original image

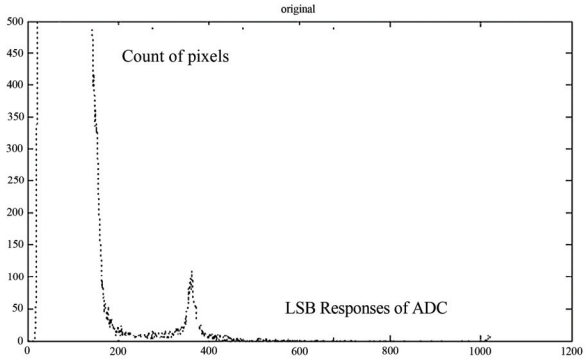

Histogram response: Approach 2–310

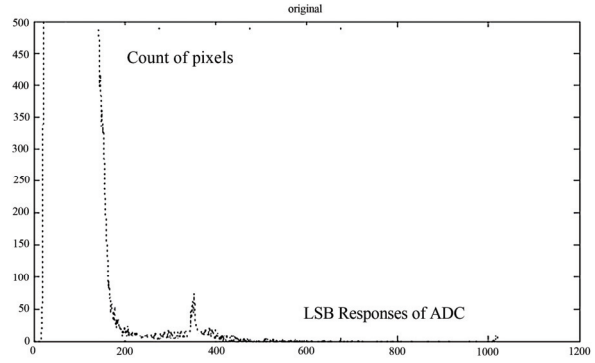

Histogram response: Approach 2–351

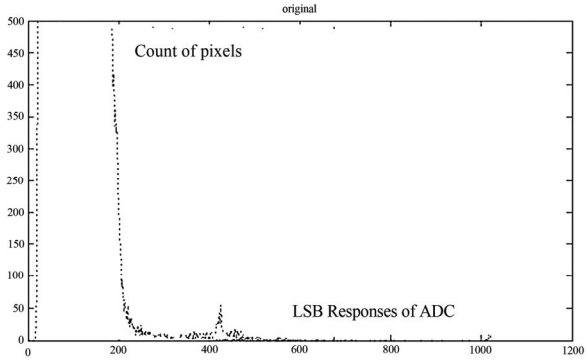

Histogram response: Approach 2–251

Figure 10. Using a statistical analysis tool, it was found that the region highlighted in the red box of the test image has the highest number of pixel defectivities or response deviation from the ideal pixel mean. Using different implementations of Approach 2, histogram responses are computed to understand pixel responses. Approach 2-251 does show the lowest second peak response and as expected the first peak response has shifted toward the right because of more averaging done on the original image.

architecture and cropped to the center 1 M region. All test images are BAYER 10 data to apply the correction

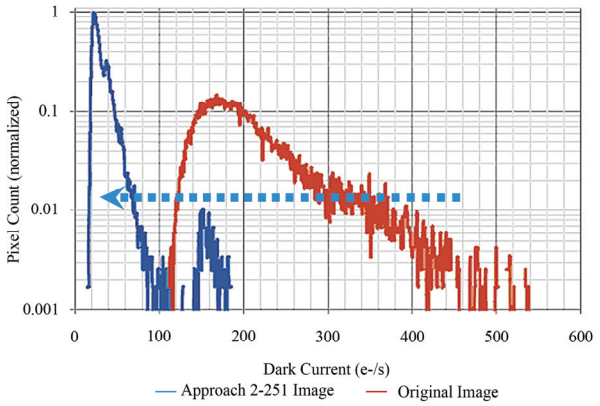

Figure 11. Log plot presenting the dark current data in electrons/second for the original image (red window in Figure 10) to processed image (Approach 2-251).

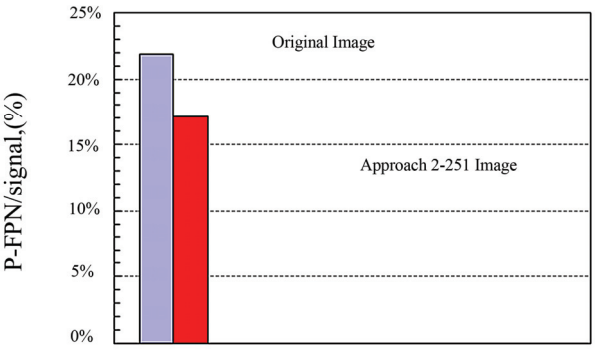

Figure 12. SNR plots for original image (red window in Figure 10) to processed image (Approach 2-251).

schemes and then interpolated to RGB color space using a simple bilinear algorithm. Region of analysis used in each of the image used for evaluation is highlighted for convenience to the reader.

From the results provided above, it is very evidently seen that dark current or defectivity counts of the processed image has significantly gone down. This is clearly reflected on test images, which are presented in **Figures 8** and **9**. In order to narrow down the optimal threshold usage for Approach 2, histogram analysis is done on select dark regions of the test image. The region chosen for analysis has the maximum pixel defectivity count. This is done to better understand shift in histogram response. Histogram profiles pre and post correction are presented for comparison in **Figure 10**. In **Figure 10**, using Approach 2, the second peak of the histogram plot for each of the thresholds is much lower in comparison with the original image. This highlights that the pixels of varying amplitudes are much lower in occurrence and get faded into the normal distribution. This helps maintain a tight mean value and sigma deviation for the entire statistical window of analysis. Approach 2–251 is optimal in threshold usage leading to good masking of pixel defects with little to no loss in resolution details. This is also better presented in **Figure 11** using dark current analysis. **Figure 11** shows that the dark current distribution (metric using in the imaging world to present pixel defectivity behavior) has moved left post processing making the image visually more appealing.

All versions of Approach 2 are also able to remove noise and elevate Signal to Noise Ratio's (SNR) as the computed from the window of analysis used in **Figure 10**.

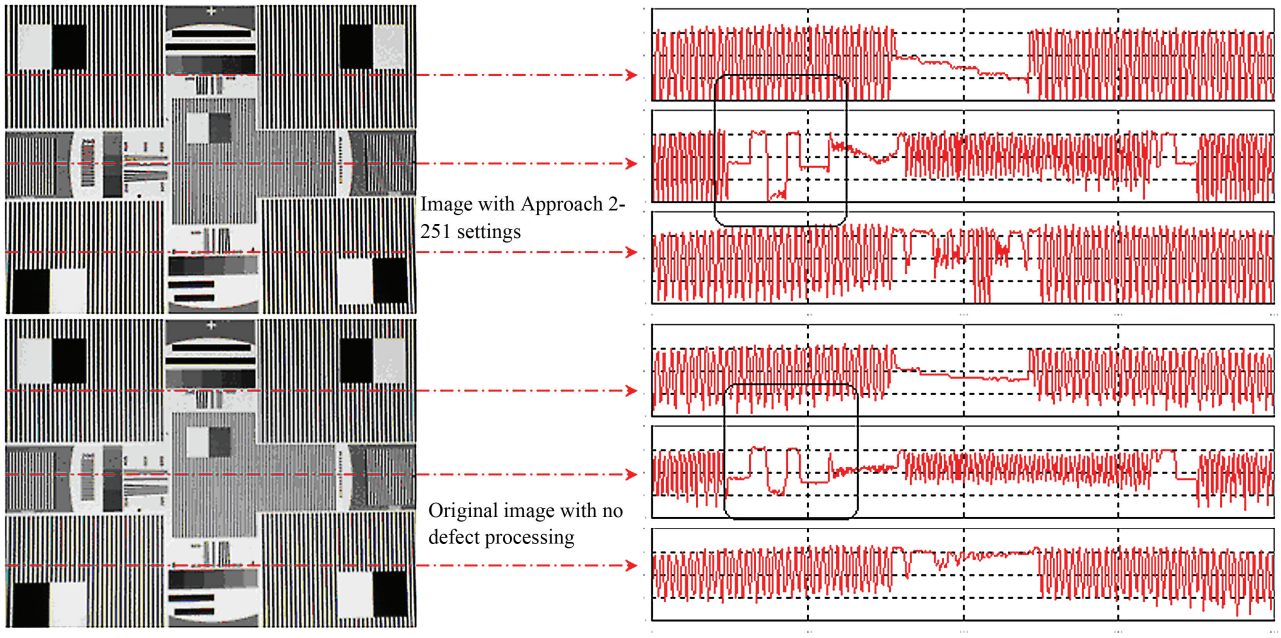

Figure 13. MTF charts captured using the original image to processed image (Approach 2-251 used on original image). Row profile illustrates details along the x-axis.

This is done for both the original image and processed image (Approach 2-251). The data indicates that the SNR for the processed image has increased by 7% for the same signal strength of the image. This indicates that Approach 2-251 is better.

Sharpness score is also captured using Modulation Transfer Function (MTF) charts to gauge preservation of details. In this test, the original 8M CMOS image sensor is used to capture the sharpness chart and Approach 2-251 code is used on the entire frame of the original image to understand sharpness details. As illustrated in **Figure 13**, little to no loss in transitional details is seen. This further validates Approach 2-251 usage.

5. Conclusions and Future Work

In conclusion, Approach 2 preserves shapes and edges and gives a greatly improved final image. As seen from the analysis done on the test image, Approach 2 is capable of catching most of the true fails. The false fails corrected by Approach 2 do not leave any visible defects. The different variations of Approach 2 are capable of being scaled to fit the appropriate imaging application. In the case study conducted by the author, Approach 2-251 gives in optimal results. As pixel size decreases, correction for hot pixels and clusters will become very critical.

As part of future work, this research work will be extended to consider potential dynamic calculation of the-multiplier used in Approach 2. At the same time, explore possibilities of extending the range used for dynamic threshold or shrink by a percentage ratio.

5. References

[1] R. C. Gonzalez and R. E. Woods, "Digital Image Processing," Addison-Wesley, Massachusetts, 1992.

[2] H. Wach, *et al*., "Noise Modeling for Design and Simulation of Computational Imaging Systems," *Optical Pattern Recognition*, XVI, *Proceedings of SPIE*, Vol. 5438, No. 159, 2004, pp. 159-170.

[3] Jean-Marc, Leger, Dominique, *et al*., "Modulation Transfer Function Measurement Using Non Specific View," *Optical Engineering*, Vol. 43, 2004, pp. 1355-1365.

[4] O. Hadar, M. Huber, R. Huber and A. Stern, "MTF as a Quality Measure for Compressed Images Transmitted Over Lossy Packet Network," *Optical Engineering*, Vol. 40, No. 10, 2001, pp. 2134-2142.

[5] J. S. Lee and R. I. Hornsey, "Photoresponse of Photodiode Arrays for Solid State Image Sensors," *Journal of Vacuum Science and Technology*, Vol. 18, No.2, 2000, pp. 621-625.

[6] Yadid-Pecht, "Geometrical Modulation Transfer Function for Different Pixel Active Area Shapes," *Optical Engineering*, Vol. 39, No. 4, 2000, pp. 859-865.

[7] G. D. Boreman and A. Plogstedt, "Spatial Filtering by a Nonrectangular Detector," *Applications of Optical Engineering*, Vol. 28, No. 6, 1994, pp. 3063-3071.

Engineering, 2010, 2, 228-236
doi:10.4236/eng.2010.24033 Published Online April 2010 (http://www.SciRP.org/journal/eng)

The Stability of Cylindrical Shells Containing an FGM Layer Subjected to Axial Load on the Pasternak Foundation

Abdullah Heydaroglu Sofiyev, Mehmet Avcar
Department of Civil Engineering of Suleyman Demirel University, *Isparta*, *Turkey*
E-mail: *asofiyev@mmf.sdu.edu.tr*, *mavcar@mmf.sdu.edu.tr*
Received July 7, 2009; *revised November* 4, 2009; *accepted November* 12, 2009

Abstract

In this study, the stability of cylindrical shells that composed of ceramic, FGM, and metal layers subjected to axial load and resting on Winkler-Pasternak foundations is investigated. Material properties of FGM layer are varied continuously in thickness direction according to a simple power distribution in terms of the ceramic and metal volume fractions. The modified Donnell type stability and compatibility equations on the Pasternak foundation are obtained. Applying Galerkin's method analytic solutions are obtained for the critical axial load of three-layered cylindrical shells containing an FGM layer with and without elastic foundation. The detailed parametric studies are carried out to study the influences of thickness variations of the FGM layer, radius-to-thickness ratio, material composition and material profile index, Winkler and Pasternak foundations on the critical axial load of three-layered cylindrical shells. Comparing results with those in the literature validates the present analysis.

Keywords: FGM Layer, Stability, Cylindrical Shell, Critical Axial Load, Winkler and Pasternak Foundations

1. Introduction

Functionally graded materials (FGM) are characterized by a gradual change in properties within the specimen as a function of the position coordinates. The property gradient in the material is typically caused by a position-dependent chemical composition, micro structure or atomic order. There are several studies about the processing of FGM, and an overview of the different manufacturing methods can be found in Koizumi [1] and Kieback *et al*. [2]. The mechanical behavior of FGMs shells, such as bending due to mechanical loads, free vibration, stability and buckling, etc., have been studied by many scientists [3-8]. However, the literature on the investigation of vibration and stability problems of composite structures that composed of ceramic, FGM, and metal layers is scarce. A self-consistent constitutive framework is proposed to describe the behaviour of a generic three-layered system containing an FGM layer subjected to thermal loading given by Pitakthapanaphong and Busso [9]. Na and Kim [10] investigated three dimensional thermo-mechanical buckling analysis for FG composite plates that composed of ceramic, FGM, and metal layers by using the finite element methods. Liew *et al*. [11] presented the non-linear vibration analysis for layered cylindrical panels containing FGMs and subjected to a temperature gradient arising from steady heat conduction through the panel thickness. Lia and Batra [12] investigated buckling of axially compressed thin cylindrical shells with the functionally graded middle layer. Sofiyev *et al*. [13] and Sofiyev [14] studied vibration and stability of three-layered truncated conical and cylindrical shells containing an FGM layer subjected to an axial compressive load, respectively.

For some cases, these shells are embedded in an elastic medium. There are different approaches to analyze the interaction between a structure and an ambient medium. Most earthen soils can be appropriately represented by a mathematical model from Pasternak, whereas sandy soils and liquids can be represented by Winkler's model [15].

Despite the evident importance of practical applications cylindrical shells, the investigations on vibration and stability of homogeneous and FGM shells on elastic foundations are limited in the literature [16-23]. The stability problem of composite cylindrical shells that composed of ceramic-FGM-metal layers embedded in an elastic medium, subjected to an axial compressive load

have not been studied yet. In the present work, an attempt is made to address this problem. Therefore, it is very important to develop an accurate, reliable analysis towards the understanding of the stability characteristics of the layered FGM structures with the effect of an elastic medium.

2. Formulation of the Problem

Figure 1(a) shows a composite cylindrical shell with simply supported edge conditions, composed of ceramic, FGM, and metal layers, of length L, radius R and total thickness $h = h_1 + h_2$. The ceramic and metal layers are assumed to be homogeneous and isotropic. The shell is referred to a coordinate system xyz in which x and y is in the axial and circumferential directions of the shell and z is in the direction of the inward normal to the middle surface. The origin of the coordinate system is located at the end of the shell, on the reference surface of the FGM layer. The three layered cylindrical shell containing an FGM layer is subjected to an axial compressive load T (**Figure 4**):

$$N_x^0 = -T\,, \quad N_y^0 = 0\,, \quad N_{xy}^0 = 0 \tag{1}$$

The in plane geometry of the layered structure is shown in **Figure 1(b)**. The FGM layer extends from $z = -a$ to $z = +a$ and, for continuous property assumptions to be valid; the thickness of this layer must be significantly larger than dominant micro structural length scale (e.g. grain size). The interfaces between the different layers are assumed to be perfectly bonded at all times and the multilayer system behaviour to be linear elastic.

We assume that the composition is varied from the bottom to top surface, *i.e.* the bottom surface ($z = -a$) of the layer is metal-rich whereas the top surface ($z = a$) is ceramic-rich. In such a way, the effective material properties P, like Young's modulus E or Poisson's ratio can be expressed as

$$P = P_c V_c + P_m V_m \tag{2}$$

in which P_c and P_m denote the temperature-dependent properties of the ceramic and metal surfaces of the FGM layer, respectively.

V_c and V_m are the ceramic and metal volume fractions of the FGM layer and are related by

$$V_c + V_m = 1 \tag{3}$$

Following Reddy and his co-workers, the ceramic volume fraction V_c is assumed as

$$V_c = \left(\frac{z + a}{2a} \right)^N \tag{4}$$

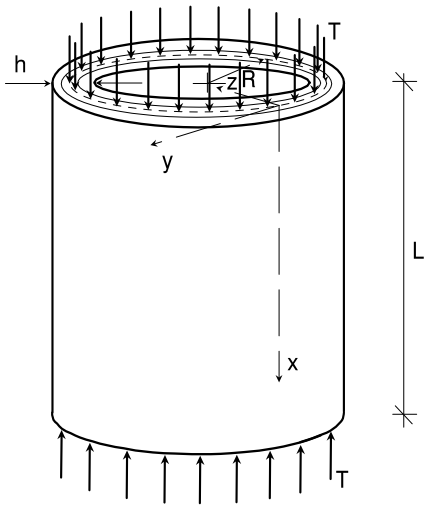

(a)

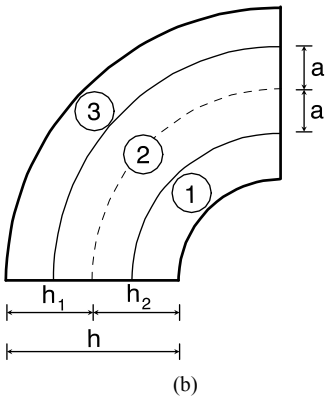

(b)

Figure 1. Schematic representation of (a) a three layered cylindrical shell and coordinate axes; (b) dimensions of the three-layered system.

where N is the volume fraction index $0 \le N < \infty$.

V_c is satisfying the following conditions at homogeneous layers interfaces [9],

$$V_c = \begin{cases} 0 & at \;\; z = -a \\ 1 & at \;\; z = a \end{cases} \tag{5}$$

Variation of volume fraction V_c in the thickness direction of composite cylindrical shell composed of Ceramic-FGM-Metal layers is shown in **Figure 2**. The top surface is fully ceramic and bottom surface is fully metal of the FGM layer. The horizontal-axis stands for the volumetric percentage of ceramic while vertical-axis represents the position along the thickness of shell. Metal is the dominant constituent at the bottom layer and its volume fraction is increased continually from the bottom to the top of FGM layer. At the top layer, ceramic is the dominant constituent.

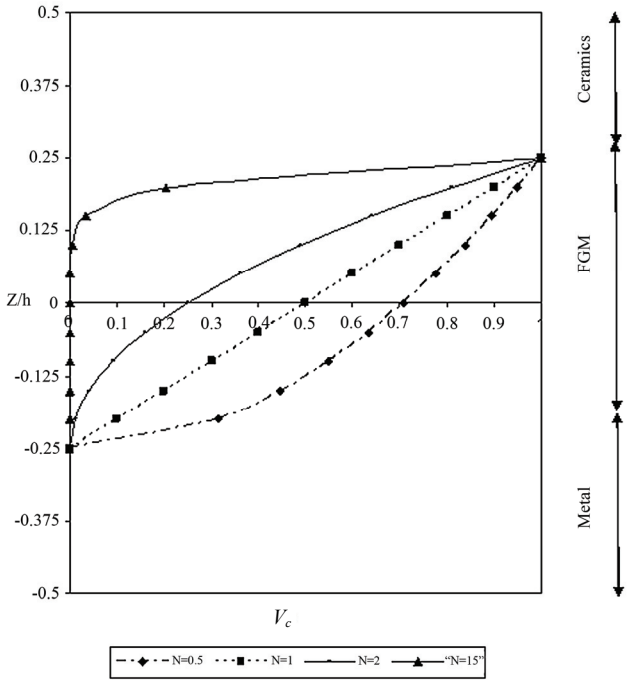

Figure 2. Variation of volume fraction V_c in thickness direction of the Ceramic-FGM-Metal three layered shell.

From Equations (2)–(5), the Young's modulus $\hat{E}$ and the Poisson's ratio $\hat{\nu}$ of an FGM layer can be written as

$$\hat{E} = (E_c - E_m)V_c + E_m; \quad \hat{\nu} = (\nu_c - \nu_m)V_c + \nu_m \qquad (6)$$

where E_m, ν_m and E_c, ν_c are the Young's modulus and Poisson's ratio of the metal and ceramic surfaces of homogeneous metal and ceramic materials, respectively.

$$E(z) = \begin{cases} E_{0m} \\ E_m + (E_c - E_m)V_c \\ E_{0c} \end{cases}$$

$$\nu(z) = \begin{cases} \nu_{0m} \\ \nu_m + (\nu_c - \nu_m)V_c \\ \nu_{0c} \end{cases}$$

3. Basic Equations

The stress-strain relations for three layered shells containing an FGM layer are given as follows [11, 14]:

$$\begin{Bmatrix} \sigma_x^{(k)} \\ \sigma_y^{(k)} \\ \sigma_{xy}^{(k)} \end{Bmatrix} = \begin{bmatrix} Q_{11}^{(k)} & Q_{12}^{(k)} & 0 \\ Q_{12}^{(k)} & Q_{11}^{(k)} & 0 \\ 0 & 0 & Q_{66}^{(k)} \end{bmatrix} \begin{Bmatrix} e_x - z\dfrac{\partial^2 w}{\partial x^2} \\ e_y - z\dfrac{\partial^2 w}{\partial y^2} \\ e_{xy} - z\dfrac{\partial^2 w}{\partial x \partial y} \end{Bmatrix} \qquad (9)$$

the FGM layer, respectively.

In the majority of practical applications involving FGMs, they are used as interlayer between two homogeneous materials. For such cases, the through-thickness variation of the Young's modulus and Poisson's ratio in the three-layered system are (7) and (8). where E_{0m}, ν_{0mo} and E_{0c}, ν_{0c} are the Young's modulus and Poisson's ratio of the

$$\begin{array}{ll} \text{for} & -h_1 \le z \le -a \\ \text{for} & -a \le z \le a \\ \text{for} & a \le z \le h_2 \end{array} \qquad (7)$$

$$\begin{array}{ll} \text{for} & -h_1 \le z \le -a \\ \text{for} & -a \le z \le a \\ \text{for} & a \le z \le h_2 \end{array} \qquad (8)$$

where $\sigma_x^{(k)}, \sigma_y^{(k)}$ and $\sigma_{xy}^{(k)}$ are the stresses in the layers, e_x and e_y are the normal strains in the curvilinear coordinate directions x and y on the reference surface, respectively, whereas e_{xy} is the corresponding shear strain; w is the displacement of the reference surface in the normal direction, positive towards the axis of the cylinder and assumed to be much smaller than the thickness, a comma denotes partial differentiation with respect to the corresponding coordinates.

The quantities $Q_{ij}^{(k)}$, $i, j = 1, 2, 6; k = 1,2,3$ for lamina are

$$Q_{11}^{(1)}=Q_{22}^{(1)}=\frac{E_{0m}}{1-\nu_{0m}^2},\ \ Q_{12}^{(1)}=\frac{\nu_{0m}E_{0m}}{1-\nu_{0m}^2},\ Q_{66}^{(1)}=\frac{E_{0m}}{1+\nu_{0m}}$$

$$Q_{11}^{(2)}=Q_{22}^{(2)}=\frac{(E_c-E_m)V_c+E_m}{1-\left[(\nu_c-\nu_m)V_c+\nu_m\right]^2}$$

$$Q_{12}^{(2)}=\frac{\left[(E_c-E_m)V_c+E_m\right]\left[(\nu_c-\nu_m)V_c+\nu_m\right]}{1-\left[(\nu_c-\nu_m)V_c+\nu_m\right]^2}$$

$$Q_{66}^{(2)}=\frac{(E_c-E_m)V_c+E_m}{1+(\nu_c-\nu_m)V_c+\nu_m}$$

$$Q_{11}^{(3)}=Q_{22}^{(3)}=\frac{E_{0c}}{1-\nu_{0c}^2},\ \ Q_{12}^{(3)}=\frac{\nu_{0c}E_{0c}}{1-\nu_{0c}^2},\ Q_{66}^{(3)}=\frac{E_{0c}}{1+\nu_{0c}} \quad (10)$$

The well-known force and moment resultants are expressed by [14,25]

$$\left[\left(N_x,N_y,N_{xy}\right),\left(M_x,M_y,M_{xy}\right)\right]=\sum_{k=1}^{3}\int_{z_k}^{z_{k+1}}\left(1,\mathrm{z}\right)\left[\sigma_x^{(k)},\sigma_y^{(k)},\sigma_{xy}^{(k)}\right]\mathrm{d}z \quad (11)$$

The relations between the forces N_x, N_y, N_{xy} and the Airy stress function $\overline{\Phi}=\Phi/h$ are given by

$$\left\{N_x,\mathrm{N}_y,\mathrm{N}_{xy}\right\}=\left\{\frac{\partial^2\Phi}{\partial y^2},\ \frac{\partial^2\Phi}{\partial x^2},\ -\frac{\partial^2\Phi}{\partial x\partial y}\right\} \quad (12)$$

For the elastic foundation, one assumes the two-parameter elastic foundation model proposed by Pasternak [15]. The foundation medium is assumed to be linear, homogenous and isotropic. The bonding between the truncated conical shell and the foundation is perfect and frictionless. If the effects of damping and inertia force in the foundation are neglected, the foundation interface pressure p may be expressed as

$$p=K_w w-K_p\left(\frac{\partial^2 w}{\partial x^2}+\frac{\partial^2 w}{\partial y^2}\right) \quad (13)$$

where K_w is the modulus of subgrade reaction for the foundation and K_p the shear modulus of the subgrade. Note that by setting $K_p=0$, the Pasternak model becomes that of the Winkler foundation model.

When the above assumptions are taken into consideration, the modified Donnell type stability and compatibility equations of composite cylindrical shells that composed of ceramic, FGM, and metal layers, subjected axial compressive load and resting on the Pasternak foundation are given, respectively by

$$\frac{\partial^2 M_x}{\partial x^2}+2\frac{\partial^2 M_{xy}}{\partial x\,\partial y}+\frac{\partial^2 M_y}{\partial y^2}+\frac{N_y}{R}-T\frac{\partial^2 w}{\partial x^2}$$

$$-K_w w+K_p\left(\frac{\partial^2 w}{\partial x^2}+\frac{\partial^2 w}{\partial y^2}\right)=0 \quad (14)$$

$$\frac{\partial^2 e_x}{\partial y^2}+\frac{\partial^2 e_y}{\partial x^2}-2\frac{\partial^2 e_{xy}}{\partial x\,\partial y}=-\frac{1}{R}\frac{\partial^2 w}{\partial x^2} \quad (15)$$

where M_x, M_{xy}, M_y are moment resultants.

Substitute expressions (9)-(13) in Equations (14) and (15). A system of differential equations for the stress function and the normal displacement can be obtained in form as

$$\begin{bmatrix} L_{11} & \mathrm{L}_{12} \\ L_{21} & \mathrm{L}_{22} \end{bmatrix}\begin{bmatrix} \Phi \\ w \end{bmatrix}=0 \quad (16)$$

where the following definitions apply:

$$L_{11}=A_2\left(\frac{\partial^4}{\partial x^4}+\frac{\partial^4}{\partial y^4}\right)+2\left(A_1-A_5\right)\frac{\partial^4}{\partial x^2\partial y^2}+\frac{1}{R}\frac{\partial^2}{\partial x^2} \quad (17)$$

$$L_{12}=-A_3\left(\frac{\partial^4}{\partial x^4}+\frac{\partial^4}{\partial y^4}\right)-2\left(A_4+A_6\right)\frac{\partial^4}{\partial x^2\partial y^2}$$

$$-T\frac{\partial^2}{\partial x^2}-K_w+K_p\left(\frac{\partial^2}{\partial x^2}+\frac{\partial^2}{\partial y^2}\right) \quad (18)$$

$$\mathrm{L}_{21}=\mathrm{B}_1\left(\frac{\partial^4}{\partial x^4}+\frac{\partial^4}{\partial y^4}\right)+2\left(B_2+B_5\right)\frac{\partial^4}{\partial x^2\partial y^2} \quad (19)$$

$$\mathrm{L}_{22}=\frac{1}{\mathrm{R}}\frac{\partial^2}{\partial x^2}-B_4\left(\frac{\partial^4}{\partial x^4}+\frac{\partial^4}{\partial y^4}\right)-2\left(B_3+B_6\right)\frac{\partial^4}{\partial x^2\partial y^2} \quad (20)$$

in which expressions A_i, $B_i\,(i=1-6)$ are defined as follows:

$$A_1=C_{11}B_1+C_{21}B_2,$$

$$A_2=C_{11}B_2+C_{21}B_1,$$

$$A_3=C_{11}B_3+C_{21}B_4+C_{12},$$

$$A_4=C_{11}B_4+C_{21}B_3+C_{22},$$

$$A_5=C_{61}B_5,\quad A_6=C_{61}B_6+C_{62},$$

$$B_1=C_{10}D,$$

$$B_2=-C_{20}D,$$

$$B_3=\left(C_{20}C_{21}-C_{11}C_{10}\right)D,$$

$$B_4=\left(C_{20}C_{11}-C_{21}C_{10}\right)D,$$

$$B_5=1/C_{60},$$

$$B_6=C_{61}/C_{60},$$

$$D=1/\left[\left(C_{10}\right)^2-\left(C_{20}\right)^2\right] \quad (21)$$

in which expressions C_{1k_1}, C_{2k_1} and C_{6k_1} $(k_1 = 0,\ 1,\ 2)$ are defined as follows:

$$C_{1k_1} = \frac{E_{0m}}{1-\nu_{0m}^2}\int_{-h_1}^{-a} z^{k_1}\mathrm{d}z + \int_{-a}^{a} z^{k_1}\ \frac{(E_c - E_m)V_c + E_m}{1-\left[(\nu_c - \nu_m)V_c + \nu_m\right]^2}\mathrm{d}z + \frac{E_{0c}}{1-\nu_{0c}^2}\int_{a}^{h_2} z^{k_1}\mathrm{d}z \tag{22}$$

$$C_{2k_1} = \int_{-a}^{a} z^{k_1}\ \frac{\left[(E_c - E_m)V_c + E_m\right]\left[(\nu_c - \nu_m)V_c + \nu_m\right]}{1-\left[(\nu_c - \nu_m)V_c + \nu_m\right]^2}\mathrm{d}z + \frac{E_{0m}}{1-\nu_{0m}^2}\int_{-h_1}^{-a} z^{k_1}\mathrm{d}z + \frac{E_{0c}}{1-\nu_{0c}^2}\int_{a}^{h_2} z^{k_1}\mathrm{d}z \tag{23}$$

$$C_{6k_1} = \frac{E_{0m}}{1+\nu_{0m}}\int_{-h_1}^{-a} z^{k_1}\mathrm{d}z + \int_{-a}^{a} z^{k_1}\ \frac{(E_c - E_m)V_c + E_m}{1+(\nu_c - \nu_m)V_c + \nu_m}\mathrm{d}z + \frac{E_{0c}}{1+\nu_{0c}}\int_{a}^{h_2} z^{k_1}\mathrm{d}z \tag{24}$$

Equation (16) is the basic differential equations for the vibration and stability of generic composite cylindrical shells containing an FGM layer resting on a Pasternak foundation.

4. Solution of Basic Equations

Consider a cylindrical shell with simply supported edge conditions. The solution of the system of Equation (16) is sought as follows [24]:

$$w = \xi \sin\frac{m_1 x}{R}\sin\frac{ny}{R},\quad \Phi = \zeta \sin\frac{m_1 x}{R}\sin\frac{ny}{R} \tag{25}$$

where $m_1 = m\pi R/L$, m is the half wave length in the direction of the x-axis, n is the wave number in the direction of the y-axis, ξ and ζ are the amplitudes.

Substituting Expression (25) in the Equation set (16), applying Galerkin's method in the ranges $0 \le x \le L$ and $0 \le y \le 2\pi R$ and eliminating ζ from the equations, the following equation for the critical axial load is obtained:

$$T_{wp}^{cr} = \frac{1}{m_1^2 R^2}\left\{\left[A_3\left(m_1^4 + n^4\right) + 2\left(A_4 + A_6\right)m_1^2 n^2\right] + \left[m_1^2 R - A_2\left(m_1^4 + n^4\right) - 2\left(A_1 - A_5\right)m_1^2 n^2\right] \times \frac{\left[m_1^2 R + B_4\left(m_1^4 + n^4\right) + 2\left(B_3 + B_6\right)m_1^2 n^2\right]}{B_1\left(m_1^4 + n^4\right) + 2\left(B_2 + B_5\right)m_1^2 n^2}\right\} + \frac{R^2\left[K_w + K_p(m_1^2 + n^2)R^{-2}\right]}{m_1^2} \tag{26}$$

The minimum values of the critical axial load (T_{wp}^{cr}) are obtained by minimizing Equation (26) with respect to m and n, the number of longitudinal and circumferential buckling waves.

As $K_p = 0$, from Equation (26), in special case for the critical axial load (T_w^{cr}) of three layered cylindrical shells containing an FGM layer on the Winkler foundation is obtained.

As $K_w = K_p = 0$, from Equation (26), in special case for the critical axial load (T^{cr}) of three layered cylindrical shells containing an FGM layer without an elastic foundation is obtained.

5. Numerical Results and Discussions

The buckling loads of single-layer orthotropic and ($0^o/90^o/0^o$) cross-ply laminated graphite/epoxy circular cylindrical shells under pure axial load are compared in **Table 1** with results of the Jones and Morgan [25], using their material properties, *i.e.*, $E_1 = 30 \times 10^6$ psi; $E_2 = 0.75 \times 10^6$ psi; $G_{12} = 0.375 \times 10^6$ psi; $\nu_1 = 0.25$; $\nu_2 = 0.0625$, and cylindrical shell parameters $L = 34.64$ in; $R = 10.0$ in; $h = 0.12$ in. It can be seen that the present results are in very good agreement with results of Jones and Morgan [25].

As there are presently no results in the open literature for the buckling of cylindrical shells under an axial load and resting on elastic foundations, comparison of results in this study is made with those of Paliwal *et al*. [17] for the free vibration analysis of homogenous isotropic cylindrical shells resting on a Winkler foundation. The comparison is shown in **Table 2**.

When the inertial term is added into the left side of Equation (14), after integrating and after some mathematical operations for the dimensionless frequency parame-

Table 1. Comparisons of dimensionless critical axial loads for single-layer orthotropic and ($0^o/90^o/0^o$) cross-ply laminated cylindrical shells.

	Jones and Morgan [25]	Present study
Lay-up	$T^{cr}L^2/E_2h^3$	$T^{cr}L^2/E_2h^3$
(0^o)	1482	1482.0 (3,7)
($0^o/90^o/0^o$)	1859.8	1859.8 (3,6)

Table 2. Comparison of the dimensionless frequency parameter ω_{1w} for a cylindrical shell resting on the Winkler foundation ($R/h = 100$; $L/R = 2$; $K_w = 10^{-4}$ N/m^3).

Paliwal *et al*. [17]	Present study
0.6788(1)	0.6792(1)
0.3639(2)	0.3646 (2)
0.2053(3)	0.2080(3)
0.1275(4)	0.1382(4)

ter w_{1w} of the free vibration of FGM cylindrical shells resting on the Winkler-Pasternak foundations, the following expression is obtained in Equation (27), where the mass density per unit length defined as

$$\rho_t = \rho_{0m}(h_1 - a) + \int_{-a}^{a}\left[(\rho_c - \rho_m)V_c + \rho_m\right]\mathrm{d}z + \rho_{0c}(h_2 - a) \quad (28)$$

This comparison is to ensure that the elastic foundation effects have been correctly integrated into the present formulation.

Based on the above comparisons of **Tables 1** and **2**, the accuracy of the present study is validated.

5.1. Numerical Results

The buckling analysis of three layered cylindrical shells containing an FGM layer was conducted for ceramic and metal combinations. The FGM material considered was Zirconium oxide and Titanium alloy, referred to as $ZrO_2/Ti\text{–}6Al\text{–}4V$ or FGM. The temperature dependence

$$\omega_{1w} = \sqrt{\frac{1}{\rho_t}\left\{\frac{1}{R^4}\left\{\begin{bmatrix} A_3\left(m_1^4+n^4\right)+2\left(A_4+A_6\right)m_1^2n^2 \end{bmatrix}+\begin{bmatrix} m_1^2R-A_2\left(m_1^4+n^4\right) \\ -2\left(A_1-A_5\right)m_1^2n^2 \end{bmatrix}\right.\right.} \\ \left.\left.\times\frac{\left[m_1^2R+B_4\left(m_1^4+n^4\right)+2\left(B_3+B_6\right)m_1^2n^2\right]}{B_1\left(m_1^4+n^4\right)+2\left(B_2+B_5\right)m_1^2n^2}\right\}+K_w+K_p(m_1^2+n^2)/R^2\right\} \quad (27)$$

of FGM material properties can be expressed as

$$P = P_0(P_{-1}T^{-1}+1+P_1T+P_2T^2+P_3T^3) \quad (29)$$

in which $T = 300$ K (room temperature), P_0, P_{-1}, P_1, P_2, P_3 are the coefficients of temperature T (K) expressed in Kelvin and are unique to the constituent materials Reddy and Chin [4].

Typical values for ZrO_2 and $Ti\text{–}6Al\text{–}4V$ listed in **Table 3**. The materials are assumed to be perfectly elastic throughout the deformation. E_{0c}, E_{0m}, ν_{0c}, ν_{0m}, are the Young's modulus and Poisson's ratio of the metal and ceramic materials of the cylindrical shell, respectively.

Numerical computations, for pure metal, pure ceramic and three layered cylindrical shells containing an FGM layer with or without the Pasternak-Winkler foundations have been carried out using expression (26). The results are presented in **Table 4** and **Figures 4-7**. The results given in all tables below for the values of the critical axial load, corresponding to the numbers of longitudinal and circumferential waves (m, n) are presented in parentheses.

In **Table 4** variations of the critical axial load and corresponding wave numbers for pure metal, pure ceramic and three layered cylindrical shells containing an FGM layer with different compositional profiles (N = 0.5; 1; 2; 15), versus the Winkler foundation stiffness K_w and the shear subgrade modulus K_p are presented. It is observed that the critical axial load of three layered cylindrical shells containing an FGM layer increases gradually with increasing K_w or K_p separately or together for all compositional profiles. The effect of the composi ional profiles on the critical axial loads reduce, as the considering affect of elastic foundations. Further more, for the small values of K_w and K_p the variations of volume fractions of the FGM has a considerable influence on the values of the critical axial load. When the volume fraction index N increases, the values of the critical axial loads with and without elastic foundation decrease. When the volume fraction index N increases, the effect to the critical axial loads with and without elastic foundation increases.

When the shear subgrade modulus K_p is zero and the Winkler foundation stiffness K_w is changed, the effect on the critical axial load (T_w^{cr}) are 5.95%, 11.62%; 49.08% for $K_w = 5\times10^7;\ 1\times10^8;\ 5\times10^8$ (N/m^3), respectively, for $N = 0.5$ of the FGM layer of three layered cylindrical shells.

When K_p is keep constant ($K_p = 10^6$ N/m) and the Winkler foundation stiffness K_w is changed the effect on the critical axial load (T_{wp}^{cr}) are 25.82%, 31.48%; 69% for $K_w = 5\times10^7;\ 1\times10^8;\ 5\times10^8$ (N/m^3), respectively, for $N = 0.5$ of the FGM layer of three layered cylindrical shells.

Table 3. Temperature-dependent coefficients of Young's modulus E (MPa) and Poisson's ratio ν for ceramics and metals (Reddy and Chin [4]).

Coefficients	Zirconia (ZrO_2)		Titanium alloy (Ti-6Al-4V)	
	E_c (Pa)	ν_c	E_m (Pa)	ν_m
P_0	2.4427×10^{11}	0.2882	1.2256×10^{11}	0.2884
P_{-1}	0	0	0	0
P_1	-1.371×10^{-3}	1.133×10^{-4}	-4.586×10^{-4}	-1.121×10^{-4}
P_2	1.214×10^{-6}	0	0	0
P_3	-3.681×10^{-10}	0	0	0
P	1.68063×10^{11}	0.2980	1.05698×10^{11}	0.2981

Table 4. Variations of critical axial loads and corresponding circumferential wave numbers for pure metal, pure ceramic and three layered FGM cylindrical shells versus the foundations moduli K_w and K_p ($h/h_1 = h/h_2 = 2$, $h/a = 4$, $L/R = 3$; $R/h = 200$).

K_w	K_p	ZrO_2	ZrO_2–FGM-Ti-6Al-4V				Ti-6Al-4V
			$N = 0.5$	$N = 1$	$N = 2$	$N = 15$	
0	0	7.364(24,4)	5.062(6,11)	4.969(16,12)	4.873(22,7)	4.684(19,10)	3.695(24,4)
5×10^7	0	7.663(25,2)	5.363(25,2)	5.275(25,2)	5.184(25,2)	5.001(25,2)	3.990(25,2)
	10^5	7.764(25,2)	5.464(25,2)	5.375(25,2)	5.284(25,2)	5.101(25,2)	4.091(25,2)
	10^6	8.669(25,2)	6.369(25,2)	6.281(25,2)	6.190(25,2)	6.007(25,2)	4.996(25,2)
1×10^8	0	7.955(25,2)	5.650(25,2)	5.566(26,2)	5.475(25,2)	5.293(25,2)	4.262(26,2)
	10^5	8.055(25,2)	5.751(26,2)	5.667(26,2)	5.576(25,2)	5.393(25,2)	4.363(26,2)
	10^6	8.961(25,2)	6.656(26,2)	6.572(26,2)	6.481(25,2)	6.298(25,2)	5.267(26,2)
5×10^8	0	9.957(28,2)	7.547(30,2)	7.475(30,2)	7.399(30,2)	7.226(30,2)	6.009(31,2)
	10^5	10.058(28,2)	7.647(30,2)	7.575(30,2)	7.500(30,2)	7.327(30,2)	6.110(31,2)
	10^6	10.962(29,2)	8.551(30,2)	8.479(30,2)	8.403(30,2)	8.230(30,2)	7.013(31,2)

When K_w is keep constant ($K_w = 10^8$ N/m^3) and the shear subgrade modulus K_p is changed the effect on the critical axial load (T_{wp}^{cr}) are 13.61%, 31.48% for $K_p = 10^5$; 10^6 (N/m), respectively, for $N = 0.5$ of the FGM layer of three layered cylindrical shells.

Note, the following expression is used for percents:

$$\left[(T_{wp}^{cr} - T^{cr})/T^{cr}\right]\times 100\%$$

Figure 3 shows the variations of the values of critical axial loads for the cylindrical shell composed of ZrO_2–FGM-Ti-6Al-4V layers with and without elastic foundation with respect to $h/2a$. When $h/2a = 1$, the three layered cylindrical shell containing an FGM layer transformed to the pure FGM cylindrical shell.

When the ratio, $h/2a$, increases, the values of the critical axial loads for the composite cylindrical shells composed of ZrO_2–FGM-Ti-6Al-4V layers with and without elastic foundations increase. On the other hand, when FGM layer thickness is increased, the values of the critical axial loads with and without elastic foundation for the three layered cylindrical shells degrease.

Figure 4 shows the variations of the values of critical axial loads for the composite cylindrical shell composed of ZrO_2–FGM-Ti-6Al-4V layers with respect to $h/2a$.

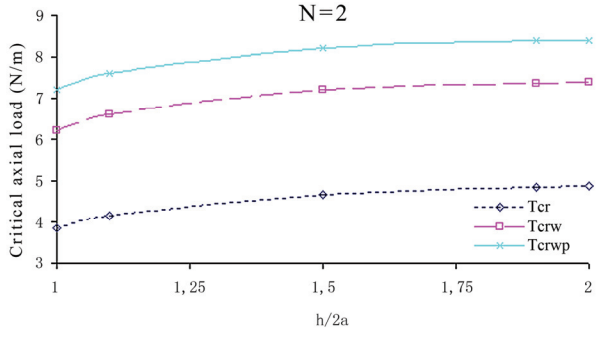

Figure 3. Variations of critical axial loads for three layered FGM cylindrical shells with and without elastic foundations for N = 2, versus $h/2a$ ($h_1 = h_2$, R/h = 200, L/R = 3; $K_w = 5\times10^8$ N/m^3; $K_p = 10^6$ N/m).

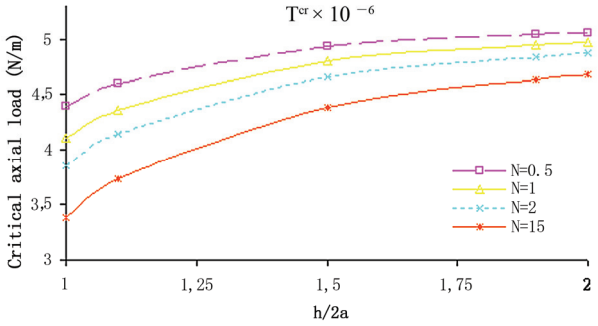

Figure 4. Variations of critical axial loads for three layered FGM cylindrical shells without elastic foundations versus h/2a; ($h_1 = h_2$; R/h = 200; L/R = 3).

The effects of compositional profiles on the critical axial load of three layered cylindrical shells containing an FGM layer are decreased, as the ratio $h/2a$ increase. For example, comparing the values of the critical axial load of three layered cylindrical shells containing an FGM layer with the values for pure ceramic cylindrical shells, at $N = 2$; $h/2a = 1$; 1.5; 2.0, the effects are 47.7%; 36.7%; 33.8% as $K_w = 5\times10^8 N/m^3, K_p = 0$, respectively.

Figure 5 shows the variations of the values of critical axial loads for the composite cylindrical shell composed of ZrO2–FGM-Ti-6Al-4V layers on a Winkler foundation with respect to $h/2a$. The effects of compositional profiles on the critical axial load of three layered cylindrical shells containing an FGM layer resting on a Winkler foundation are decreased, as the ratio $h/2a$ increase. For example, comparing the values of the critical axial loads of three layered cylindrical shells containing an FGM layer with the values for pure ceramic cylindrical shells, at N = 2; h/2a = 1; 1.5; 2.0, the effects are 37.8%; 27.6%; 25.7% as $K_w = 5\times10^8$ N/m^3, $K_p = 0$, respectively.

Figure 6 shows the variations of the values of critical axial loads for the composite cylindrical shell composed of ZrO_2–FGM-Ti-6Al-4V layers on a Pasternak foundation with respect to $h/2a$ ratios. As the ratio $h/2a$ increase, the effects of compositional profiles on the critical axial

load of three layered cylindrical shells containing an FGM layer resting on a Winkler foundation are decreased. For example, comparing the values of the critical axial loads of three layered cylindrical shells containing an FGM layer with the values for pure ceramic cylindrical shells, at $N = 2$; $h/2a = 1$; 1.5; 2.0, the effects are 34.3%; 25.1%; 23.3% as $K_w = 5\times10^8$ N/m^3, $K_p = 10^6$ N/m, respectively.

In **Figure 7** are illustrated variations of critical axial loads for three layered FGM cylindrical shells with and without elastic foundation versus R/h. When the ratio R/h increases, the values of the critical axial loads for cylindrical shells composed of ZrO_2–FGM-Ti-$6Al$-$4V$ layers with and without elastic foundation decrease. The effect of the elastic foundation on the values of the critical axial load of three layered cylindrical shells containing an FGM layer are increased, as the ratio R/h increase. For example, comparing the values of the critical axial load of three layered cylindrical shells containing an FGM layer with the values for pure ceramic cylindrical shells, at N = 2; R/h = 100; 200; 300, the effects are 15.34%; 51.8%; 91.1% as $K_w = 5\times10^8$ N/m^3, $K_p = 0$, 25.7%; 72.4%; 128.9% as $K_w = 5\times10^8$ N/m^3, $K_p = 10^6$ N/m respectively.

6. Conclusions

In this study, the stability of cylindrical shells that composed of ceramic, FGM, and metal layers subjected to axial load and resting on a Pasternak foundation is investigated. Material properties of an FGM layer are varied continuously in thickness direction according to a simple power distribution in terms of the ceramic and metal volume fractions. The modified Donnell type stability and compatibility equations on a Pasternak foundation are obtained. Applying Galerkin's method analytic solutions are obtained for the critical axial load of three-layered cylindrical shells containing an FGM layer with and without elastic foundations. The detailed parametric studies are carried out to study the influences of thickness variations of the FGM layer, radius-to-thickness ratio, material composition and material profile index, Winkler and Pasternak foundations on the critical axial load of three-layered cylindrical shells. Comparing results with those in the literature validates the present analysis.

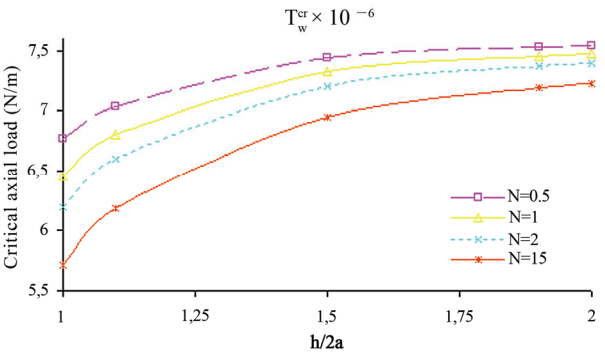

Figure 5. Variations of critical axial loads for three layered FGM cylindrical shells on a Winkler foundation versus h/2a ($h_1 = h_2$; R/h = 200; L/R = 3; $K_w = 5\times10^8$ N/m^3).

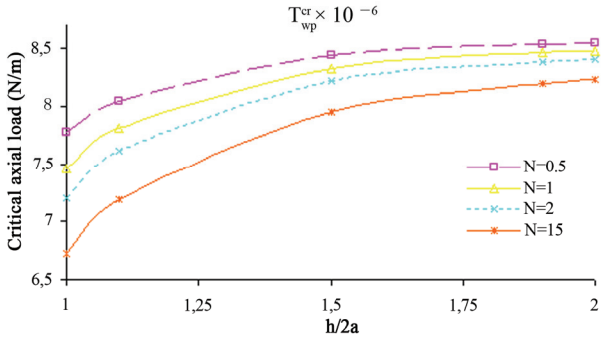

Figure 6. Variations of critical axial loads for three layered FGM cylindrical shells on a Pasternak foundation versus h/2a ($h_1 = h_2$; R/h = 200; L/R = 3; $K_w = 5\times10^8$ N/m^3; $K_p = 10^6$ N/m).

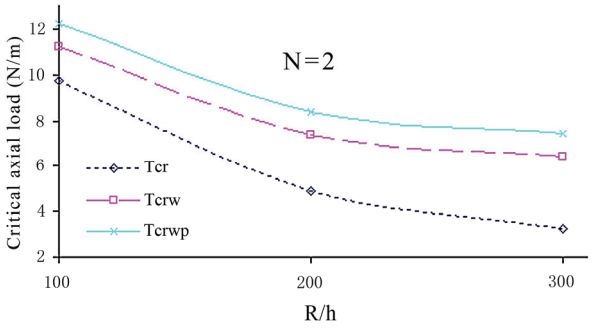

Figure 7. Variations of critical axial loads for three layered FGM cylindrical shells with and without elastic foundations versus R/h ($h_1 = h_2$; L/R = 3; $K_w = 5\times10^8$ N/m^3; $K_p = 10^6$ N/m).

7. Acknowledgements

This study is supported by the Scientific and Technical Research Council of Turkey (TUBITAK) under Project Number 108M322. The authors thank to TUBITAK for the support of the project.

8. References

[1] M. Koizumi, "The Concept of FGM," *Ceramic Transactions*, *Functionally Gradient Materials*, Vol. 34, 1993, pp. 3-10.

[2] B. Kieback, A. Neubrand and H. Riedel, "Processing techniques for Functionally Graded Materials," *Mate-*

rials Science and Engineering A, *Structural Materials*: *Properties*, *Microstructure and Processing*, Vol. 362, No. 1-2, 2003, pp. 81-105.

[3] V. Birman, "Buckling of Functionally Graded Hybrid Composite Plates," *Proceedings of the* 10*th Conference on Engineering Mechanics*, Boulder, USA, 1995.

[4] J. N. Reddy and C. D. Chin, "Thermomechanical Analysis of Functionally Graded Cylinders and Plates," *Journal of Thermal Stresses*, Vol. 21, 1998, pp. 593-602.

[5] T. Y. Ng, K. Y. Lam, K. M. Liew and J. N. Reddy, "Dynamic Stability Analysis of Functionally Graded Cylindrical Shells under Periodic Axial Loading," *International Journal of Solids Structures*, Vol. 38, No. 8, 2001, pp. 1295-1309.

[6] A. H. Sofiyev, "Dynamic Buckling of Functionally Graded Cylindrical Shells under Non-periodic Impulsive Loading," *Acta Mechanica*, Vol. 165, No. 3-4, 2003, pp. 153-162.

[7] H. S. Shen and N. Noda, "Post-buckling of FGM Cylindrical Shell under Combined Axial and Radial Mechanical Loads in Thermal Environments," *International Journal of Solids Structures*, Vol. 42, No. 16, 2005, pp. 4641- 4662.

[8] H. S. Shen, "Functionally Graded Materials: Nonlinear Analysis of Plates and Shells," CRC Press, Boca Raton, 2009.

[9] S. Pitakthapanaphong and E. P. Busso, "Self-consistent Elasto-plastic Stress Solutions for Functionally Graded Material Systems Subjected to Thermal Transients," *Journal of Mechanics and Physics of Solids*, Vol. 50, No. 4, 2002, pp. 695-716.

[10] K. S. Na and J. H. Kim, "Three-dimensional Thermomechanical Buckling Analysis for Functionally Graded Composite Plates," *Composite Structures*, Vol. 73, No. 4, 2006, pp. 413-422.

[11] K. M. Liew, J. Yang and Y. F. Wu, "Nonlinear Vibration of a Coating-FGM-substrate Cylindrical Panel Subjected to a Temperature Gradient," *Computer Methods in Applied Mechanics and Engineering*, Vol. 195, No. 9-12, 2006, pp. 1007-1026.

[12] S. R. Lia and R. C. Batra, "Buckling of Axially Compressed Thin Cylindrical Shells with Functionally Graded Middle Layer," *Thin Walled Structures*, Vol. 44, No. 10, 2006, pp. 1039-1047.

[13] A. H. Sofiyev, A. Deniz, I. H. Akcay and E. Yusufoglu, "The Vibration and Stability of a Three-layered Conical Shell Containing a FGM Layer Subjected to Axial Compressive Load," *Acta Mechanica*, Vol. 183, No. 3-4, 2006, pp. 129-144.

[14] A. H. Sofiyev, "Vibration and Stability of Composite Cylindrical Shells Containing a FG Layer Subjected to Various Loads," *Structural Engineering and Mechanics an International Journal*, Vol. 27, No. 3, 2007, pp. 365-391.

[15] P. L. Pasternak, "On a New Method of Analysis of an Elastic Foundation by Means of Two Foundation Constants," Gosudarstvennoe Izdatelstvo Literaturi po Stroitelstvu I Arkhitekture, Moscow, 1954.

[16] V. A. Bajenov, "The Bending of the Cylindrical Shells in an Elastic Medium," Visha Shkola, Kiev, 1975.

[17] D. N. Paliwal, R. K. Pandey and T. Nath, "Free Vibration of Circular Cylindrical Shell on Winkler and Pasternak Foundation," *International Journal of Pressure Vessels and Piping*, Vol. 69, 1996, pp. 79-89.

[18] T. Y. Ng and K. Y. Lam, "Free Vibrations Analysis of Rotating Circular Cylindrical Shells on an Elastic Foundation," *Journal of Vibration and Acoustics*, Vol. 122, No. 1, 2000, pp. 85-89.

[19] H. G. Tj, T. Mikami, S. Kanie and M. Sato, "Free Vibration Characteristics of Cylindrical Shells Partially Buried in Elastic Foundations," *Journal of Sound and Vibration*, Vol. 290, No. 3, 2006, pp. 785-793.

[20] A. H. Sofiyev, S. N. Keskin and A. H. Sofiyev, "Effects of Elastic Foundation on the Vibration of Laminated Nonhomogeneous Orthotropic Circular Cylindrical Shells," *Journal of Shock and Vibration*, Vol. 11, 2004, pp. 89-101.

[21] Z. Q. Cheng and S. Kitipornchai, "Membrane Analogy of Buckling and Vibration of Inhomogeneous Plates," *Journal of Engineering Mechanics–ASCE*, Vol. 125, No. 11, 1999, pp. 1293-1297.

[22] Z. Y. Huang, C. F. Lu and W. Q. Chen, "Benchmark Solutions for Functionally Graded Thick Plates Resting on Winkler–Pasternak Elastic Foundations," *Composite Structures*, Vol. 85, No. 2, 2008, pp. 95-104.

[23] P. Malekzadeh, "Three-dimensional Free Vibration Analysis of Thick Functionally Graded Plates on Elastic Foundations," *Composite Structures*, Vol. 89, No. 3, 2009, pp. 367-373.

[24] V. L. Agamirov, "Dynamic problems of nonlinear shells theory", Nauka, Moscow, 1990.

[25] R. M. Jones and H. S. Morgan, "Buckling and Vibration of Cross-ply Laminated Circular Cylindrical Shells," *American Institute of Aeronautics and Astronautics Journal*, Vol. 13, No. 5, 1975, pp. 664-671.

Engineering, **2010, 2, 237-256**
doi:10.4236/eng.2010.24034 Published Online April 2010 (http://www.SciRP.org/journal/eng)

The Stretch, Limit and Path Forward for Particle Reinforced Metal Matrix Composites of 7075 Al-Alloys

Rupa Dasgupta
Advanced Materials & Processes Research Institute, *CSIR*, *Bhopal*, *India*
E-mail: *dasguptarupa@gmail.com*
Received November 30, 2009; *revised February* 8, 2010; *accepted February* 12, 2010

Abstract

Al-based metal matrix composites [MMCs] have been the research interest of a wide spectrum of material scientists throughout the world for some over two decades now. The present paper has chosen one alloy system namely the 7xxx series and from an extensive literature review concluded that since the beginning of the new millennium nothing note worthy has been added to the knowledge already gained in the last quarter of the last century except confirm the earlier findings that MMCs if properly fabricated by choosing the processing route and with appropriate size and volume fraction of dispersoids can improve most of the mechanical, corrosion and wear resistant properties of the base alloy. The author's own research activities using this alloy system for making MMCs that include attempts to improve upon the properties by making composites, ageing and also secondary processing have been included. An attempt has been made to establish the stretch to which improvement is possible in the alloy system by making composites and trying all other routes known for meaningful improvement in properties. Further, the way forward for such particulate composites has been drawn to realise the material scientists' dream of seeing such MMCs as engineering components. For this, the areas which now need research include mass production of composites, focus on its machining, joining, processing as also reduction in the size of dispersoids are some of the areas that have been identified and discussed in the paper.

Keywords: Al-based MMCs, 7xxx Series, 7075 Alloy, Tempering, Ageing, Retrogression and Reageing, Hardness, Mechanical Properties, Wear Properties, Extrusion, Corrosion, Machining, Joining, Mass Production

1. Introduction

Material scientists and researchers in this area have been fulfilling the demand of the engineering sector in synthesizing materials to attain the demanded properties to enhance efficiency and cost savings in the manufacturing sector. In fulfilling this demand a certain trend has been followed, the materials presently been used is tried for improvement through known methods of alloy additions, heat treatment, grain modification and the like. Once the limit is reached through these methods either due to economic constraint or difficulty in mass production or further improvement is ruled out, does a different line of thought emerge in further improving the properties or decreasing cost and increasing efficiency. At times, a completely new system takes over, like was done around three decades back when due to the limits reached in alloy systems, metal matrix composites were thought of and after some two decades of experimental research the economically feasible routes, dispersoids and alloy system that can give meaningful improvement have been narrowed down. Alongside, basic understanding of mixing between the alloy and dispersoid has also now been reached. In the last decade though research continues in this field yet the results obtained were a mere confirmation of the previously attained results and a plateau in the improvement possible has been reached. But before the clogging takes place, it was essential to change the direction of research once again and it is only obvious that further improvement could be obtained in any system by adopting another route of fabrication. In this line secondary processing was the obvious choice, though much work has not been reported in this direction.

The present paper has made an attempt of finding the

Table 1. Chemical composition limits of 7075 alloy.

Weight	Cu	Mg	Mn	Si	Fe	Cr	Zn	Ti	Others	
									Each	Total
Minimum	1.2	2.1	-	-	-	0.18	5.1	-	-	-
Maximum	2.0	2.9	0.30	0.40	0.50	0.28	6.1	0.20	0.05	0.15

limit of enhancing the mechanical and wear resistance properties of a commonly used Aluminium alloy, the 7075 alloy by different routs; by making 1) composites 2) heat treatment of the alloy and composite and also 3) extruding the alloy and composite to rods. A comparison in the properties attained by the different routes would help find the limit upto which the properties in this alloy system can be stretched. Further research in this area after this would not have anything much to add and this type of an activity to be used as a tool for 'stretching to the limit' any system before they see the light of the day as an engineering component.

2. The Al-Zn-Cu-Mg Alloy System

2.1. Alloying Additions

The main alloying element in the 7xxx series of Al-alloys is Zinc and is known for its high specific strength. In this series the 7075 alloy is the most commonly used by the engineering sector especially the aerospace industry. The chemical composition limit of 7075 alloy is as follows [1-4]:

The presence of Mn in the alloy is responsible for the uniform deformation through cross slip, for retarding fatigue damage accumulation and enhancing fatigue life.

The addition of Cu results in an increases in the stability of Guinier-Preston zones formed at room temperature together with a decreases in the nucleation temperature and also results in an increase in the strengthening ability and a lower sensitivity to the heating rate of ageing temperature, however, the higher super saturation of the Cu bearing alloy results in a higher quench higher sensitivity and at slow quench rates of the ternary alloy shows a higher strengthening potential. Again when the reinforcement particle size is decreased, tensile strength of the composite increases but fracture toughness follows the opposite trend-it increase as the particle size increases.

In addition to Zn, Mn and Cu which are the two major constituents of the 7075 alloys, Zr is added. Its presence results in grain refinement and diffusion of Cu relatively quickly to grain boundaries and due to in consequence of non equilibrium segregation during quenching a solute depleted layer develops near the grain boundaries

2.2. Phase Diagram and Phase Precipitation

The phase diagram for the 7075 alloy is given in

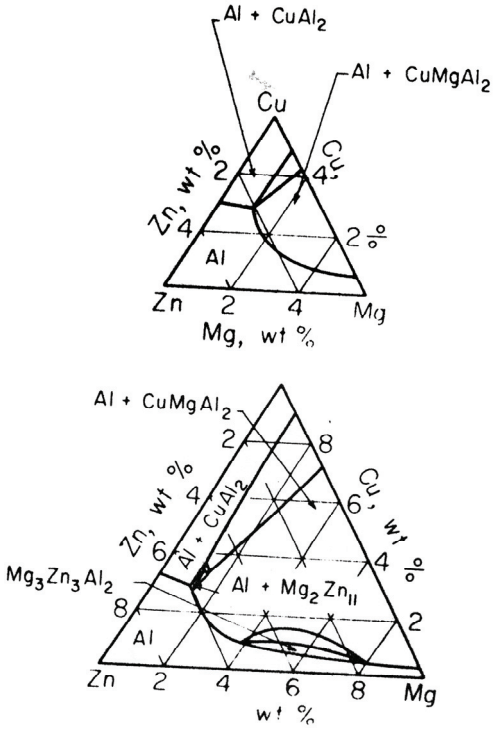

Figure 1. Phase diagram for the Al-Zn-Cu-Mg system.

Figure 1 [1].

The phase in equilibrium with an Aluminium matrix in commercial alloys are designated $MgZn_2$ [M-Phase], $Mg_3Zn_3Al_2$ [T-Phase] and Mg_5Al_3 [β-Phase]. The first phase ranges in composition from $MgZn_2$ to Mg_4Zn_7Al. The T-Phase has a wide range of composition, from 74% Zinc-16% Magnesium to 20% Zinc-31% Magnesium. The β-phase appears only when the magnesium content is considerably greater than the Zn content. Such alloys are strengthened primarily by Mg in solid solution. Precipitation hardening of alloys with Zn in excess of Mg occurs in the sequence zones through coherent precipitates to the M-Phase. Quaternary alloys contain copper, magnesium and zinc. The M-Phase composition ranges in the quaternary system from $MgZn_2$ to CuMgAl and may be described as $Mg[Al,Cu,Zn]_2$. The range of composition for the T-Phase is from that of Al-Mg-Zn ternary to that of Phase designated $CuMg_4Al_6$ and may be described as $Mg_3[Al,Cu,Zn]_5$. A third phase is $CuMgAl_2$ [S-Phase], with a small range of composition. The $CuAl_2$ phase appears only if copper is considerably in excess of Mg. Several nonequilibrium invariant melting reactions are encountered in the high strength quaternary alloys. A

reaction at 475℃ involving M, T, and S phases is usually encountered, but as copper content increases melting may be encountered down to 460℃. Usually the J-Phase has the highest solvus temperature and is slow to dissapear during ingot homogenization. Precipitation hardening in high strength alloys is by the sequence leading to M-Phase. Zones and coherent precipitates are low in copper content and precipitates increase in copper content in the overageing regime. Additions of iron, manganese and silicon interact with one another and with copper and magnesium. Chromium reacts with aluminium and magnesium to form a dispersoid.

The ageing of rapidly quenched Al-Zn-Mg alloys [5-10] from room temperature to relatively low ageing temperatures is accompanied by the generation of GP zones having an approximately spherical shape. With increasing ageing time, GP zones increase in size and the strength of the alloy increases. Extended ageing at temperatures above room temperature transforms the GP zones in alloys with relatively high Zn-Mg ratios into the transition precipitate known as η′ or M′, the precursor of the equilibrium $MgZn_2$, η or M phase precipitate. Ageing time and temperatures that develop the highest strength characteristics of the T6 temper produce zones to have an average diameter of 2 to 3.5 nm.

The addition of higher copper contents affords greater precipitation hardening, with some contribution of Cu atoms to zone formation. Crystallographic arguments indicate that copper and aluminium atoms substitute for zinc in the $MgZn_2$ transition and the phase $MgZn_2$ and MgAlCu form an isomorphous series in which an aluminium atom and a copper atom substitutes for two Zn atoms. Electropotential measurement and X-ray analysis indicate that copper atoms enter into the η′ phase during ageing temperatures above about 150°C [300°F], thus ageing these alloys above this temperature substantially increase their resistance to stress corrosion cracking.

In cast ingot form, alloy 7075 forms one or more variants of $[Fe,Cr]_3SiAl_{12}$, Mg_2Si and a psuedobinary eutectic made up of Al and $MgZn_2$. The latter phase contains Al+Cu as a substitute for Zn and can be written as $Mg[Zn,Cu,Al]_2$. Subsequent heating causes the iron rich phases to transform to Al_7Cu_2Fe. Mg_2Si is relatively insoluble and tends to somewhat spheroidize, $Mg[Zn,Cu,Al]_2$ rapidly begins to dissolve and at the same time some Al_2CuMg precipitates also dissolve as this phase requires high temperature and lengthy soaking to completely dissolve. Cr is precipitated from super saturated solution as $Cr_2Mg_3Al_{18}$ dispersoid concentrated heavily in the primary dendrite regions. A well solutionized wrought alloy contains only Al_7Cu_2Fe, $[Fe,Cr]_3SiAl_{12}$ and Mg_2Si, along with the dispersoid. Recrystallized grains are extremely elongated or flattened because of dispersoid bonding and unrecrystallized regions are not unusual even in sheet. The unrecrystallized regions are made up of very fine subgrains in which boundaries are decorated by hardening precipitate.

2.3. Ageing Behaviour

The 7075 alloys are used both in the un-tempered condition and tempered condition corresponding to T6 and T7 tempering [5-10]. T6 tempering is done by solution heat treatment at 466℃ to 482℃ followed by water quenching followed and ageing at between 115℃ to 130℃ for obtaining high strength in reasonably short ageing cycle. An alternate tempering known as T7 or RRA [Retrogression and Reageing] technique is also used which is a two stage treatment after T6 tempering; the samples are retrogressed at 200℃ for duration short enough to allow only dissolution of precipitates. The second stage involves reageing *i.e*. the retrogressed samples were reaged at 120℃ to fully restore the peak aged condition of the T6 temper. In the RRA treatment the maximum static tensile and compressive properties of T6 temper are combined with the resistance to stress corrosion of the T73 temper. RRA treatment results in precipitate dissolution and then re-precipitation growth of coarser equilibrium phase particles in the grain boundary regions. For short time retrogression, the hardness can be restored after reageing but almost no restoration is observed for prolonged retrogression time [> 50 min]. RRA is effective only for alloys containing coherent dispersoids but is less effective for alloys containing incoherent dispersoids. The RRA process improves the resistance of stress corrosion cracking in high strength 7xxx alloys which have the same strength of T6 temper [11-13]. The TMT process improved strength, fracture toughness, fatigue property and corrosion resistance. Also stability in property, higher strength, improved corrosion resistance and lower rate of growth of fatigue cracks are obtained by the use of elevated temperature ageing. TEM studies have shown that 75 min retrogressed 7075-T6 Al alloy has smaller grain boundary precipitated and a higher dislocation concentration than the T6 stage. The optimum retrogression time changes with material thickness.

2.4. Properties of Alloys

Density is reduced by addition of magnesium and increased by all other element. For commercial alloys it ranges between 2.740 kg/m^3 and 2.830 kg/m^3, with most alloys around 2.800 kg/m^3 [1].

The mechanical properties of the cast and aged alloys are shown in **Table 2** [1-4,14].

These alloys achieve their strength by precipitation through a complex sequence of Guinier Preston [GP] zones, η′ nucleating on GP zones, η′ transforming into η. In addition their processing route is rather complex, including some plastic strain followed by natural ageing

Table 2. Tensile properties of 7075 alloy.

Property	As cast	Naturally Aged	Artificially Aged
Hardness [HV]	500-700	500-800	800-1200
UTS [MPa]	100-150	150-200	180-250
YS [MPa]	50-100	80-150	120-200
Elongation [%]	1-3	2-5	0-2
Shear strength [MPa]	152 MPa	331 MPa	317 MPa
Poisson Ratio		0.33 at 20℃[68°F]	
Elastic Modulus [GPa]	Shear : 26.9	Tension: 71.0	Compression: 72.4
Fatigue Strength [MPa]		159 MPa [23 Ksi] at 5×10^8 cycles	

and a multistep artificial ageing treatment. In these alloys zinc is the major constituent.

The 7XXX alloys are typically used for aircraft structural parts and other highly stressed applications where very high strength and good resistance to corrosion is required. These alloys are widely used in aeronautics industry and aerospace structural applications

2.5. Property Improvement through Mechanical Processing

The alloy system has been moderately subjected to different types of secondary processing. The following observations have been reported on secondary processed alloys of this series:

- The grain structure of the rolled plate [15-16] was found to be comprised of high aspect ratio grains elongated in the rolling direction of the plate. The structure consisted largely of unrecrystallized material although a small volume fraction of recrystallized grain was present. The elongated grains contained an internal structure of small [1 to 5 μm] equiaxed subgrain with an average misorientation across subgrain boundaries ~ 5 deg.
- The microstructure of a forged product which is characterized by 'pan cake' unrecrystalized grain morphology [17]. Observation of unetched section revealed the presence of constituent phases with particle sizes up to 20 μm. The major constituent phase was present as fragmented rounded gray coloured particles strung out into longitudinal direction. Qualitative energy dispersive x-ray analysis of these particle identified them as Al, Cu, and Fe reached. Upon etching in Keller's reagent, these particles turned light brown conforming their identification as β[AlCuFe].
- The grains of the 7475 alloy formed sheet were longer, approx. 11.5 μm than in the as received sheet, approx 9.5 μm [18]. Addition the original grain had pan cake shape, whereas the grain in the form parts appeared to be more equiaxed.
- Forming pressure corresponding to optimum super plastic condition and low back pressure result in a more uniform thickness distribution in the formed part. The average size of the originally non equiaxed grain increases 20% during initial training. Grains become more equiaxed with increasing strain while maintaining nearly constant grain size for strain in the range 1-1.4 [19].
- The compressive stress-strain response of as cast and aged 7075 alloys is found to depend strongly on both the applied strain rate and the test temperature. However, the aged material is generally found to be stronger than the as cast material. The work hardening rate is seen to decrease with increasing strain, stain rate and temperature and its value is higher in the aged material than in the as cast material [20].

3. AMMCs of the Series

3.1. From the Beginning, Since 1980s

Literature review of Al-Zn based composites show that this system has been widely investigated both in terms of understanding the mechanism of formation and property evaluation of composites [21-53]. Different routes for preparation of composite have been adopted, however for practical purposes the casting, powder and squeeze casting routes have been adopted and in some cases these have been subjected to secondary processing *i.e.* extrusion of as cast composite and consolidation followed by extrusion for composite prepared by powder metallurgy ones. Properties have been characterized for cast and aged composite.

The main dispersoid that have been investigated are SiC and Al_2O_3. Stronger matrix alloys tend to produce stronger composites although the increase in strength due to reinforcement tends to be lower when higher strength matrix alloy are used and in the case of matrix alloys with less strength reinforcement has been observed to lead to reduction in strength; it was found that composites containing 13 μm particles possesses greater toughness than those containing 5 μm particles.

The excellent flow resistance and ductility of Al 7xxx series alloys is achieved through the formation of extremely small, uniformly dispersed particles of a second phase within the original aluminium phase matrix, *i.e.* ageing process. The enhancement in strength is highly dependent on the type, distribution and size of precipitate particles present.

The microstructural studies of composite in the cast

Table 3. Best mechanical properties attained by MMCs of 7xxx alloy system.

Dispersoid [Vol.%]	Method of Formation	Ageing Condition	Hardness [HV]	UTS [MPa]	Reduction in Area [%]	0.2% Proof Stress
SiC [15%] [5 μm]	Spray deposited	Under aged	----	609	10.5	499
		Peak aged	--	630	10	570
		Over aged	--	574	12.5	510
SiC [15%] [13 μm]	Spray deposited	Under aged	--	595	6.3	502
		Peak aged	--	645	4.8	595
		Over aged	--	496	5	539
SiC [15%] [60 μm]	Spray deposited	Under aged	--	453	1.3	431
		Peak aged	--	504	1	501
		Over aged	--	493	2	484
SiC [15%] [2-3 μm]	[forming temp/press] [499/2.07]	--	--	455	--	373
	[5.4/2.07]			448		368
	[529/2.07]			420		332
SiC [5%] [2-3 μm]	[490/2.07]	--	--	448	--	391
	[505/2.07]			463		395
	[520/2.07]			432		330

condition have been widely investigated. The microstructure is dependent on a number of parameters like macro segregation of dispersoid, primary and secondary dendrite spacing, solidification rate, solidification time, dendrite ripening; the cast structure exhibits coarse dendrite grains, however in contrast small non dendritic structure was observed in the aged structure. In both materials the grain size decreases as the strain rate increases.

The tensile properties of the composite have been investigated by several investigators with a view to assessing its properties vis-à-vis conventional alloy to find commercial application of the composite. Properties have been evaluated in cast, aged and processed conditions for composites prepared by different route. The main observations are: 1) addition of 5 and 13 μm particles in 7075 alloy increased the 0.2% proof stress and UTS values in composites made by spray deposition over the monolithic material. The addition of 60 μm particle however, reduced the 0.2% proof stress and UTS of the resulting composite in the under aged stress and UTS of the resulting composites in the under aged and peak aged condition. There are only small differences in the 0.2% proof stress and UTS of 5 and 13 μm SiC particulates reinforced composite but 60 μm particulate reinforced material has much lower yield and fracture strength. 2) It has been reported that the 0.2% proof stress and tensile strength tends to increase and toughness and ductility decreases with increasing volume fraction. For a constant volume fraction of reinforcement tensile properties generally tend to increase with a decrease in particle size for a larger particle composite ductility is reduced compared with that of monolithic material. 3) The yield strength [0.2% offset] and ultimate tensile strength increased only marginally with an increase in strain rate. Increase in tensile strength is accompanied by decrease in tensile ductility. 4) Environment was found to have little influence on yield strain of the high purity alloy. However, strength increases only marginally with an increase in strain rate.

Literature on secondary processing of composites of this series of alloys is limited although extensive reports are available on the secondary processing of alloys of 7xxx series. However, these observations are not been detailed in this paper since it deals with composites only. Some studies have been carried out on the effect of alloying elements in secondary processing of this composite system; it mentions that the presence of iron produces a slight decrease in strength, elongation and fracture in wrought product. Iron together with manganese may produce a slight increase in strength with limited increase in elongation. Manganese, chromium, molybdenum and zirconium appear to have a strong strengthening effect with corresponding decrease in % elongation. The effect of silicon addition varies some what depending on Mg: Zn ratio [54,55]. The properties attained by investigators adopting different processing routes for making composites are given in **Table 3** below:

Since this series of alloys are not generally used for wear resistant purposes there is no report on the wear properties of composites prepared from this series of alloys. However there is a study in which the wear behaviour of high tensile strength aluminium alloys under dry and lubricated conditions for 7004-T6 alloys were compared with 2014 alloys. It has been observed that these alloys are easily worn out. Severe wear at high contact load have been reported. In paraffin oil, the wear rates were approx 1/10 the wear rates under dry condi-

tions 7004-T6 showed a lower friction coefficient compared to 2024-T4. For 7004-T6, wear cracks which would propagate in the sliding direction occurred and large and elongated particles were detected [48-53].

Creep resistance of the alloys and composites both are relatively low, however longer creep life can be achieved if the load is intermittently relieved and the material is allowed a period of rest. Residual stresses from working processes may reduce creep resistance and so does precipitation during creep [56-58].

3.2. The Recent Past [Since 2000]

The recent past has not since much progress in the research of this series of composites. The researchers have more or less confirmed the findings of earlier researchers and at times provided an understanding of the behaviour observed. The role of work hardening characteristics of matrix alloys in the strengthening of metal matrix composites has been shown to be associated with a high dislocation density in the matrix due to the difference in coefficient of thermal expansion between the reinforcement and the matrix. In a study where the composites were made by a pressureless infiltration method, the composite reinforced with SiC particles exhibited higher strength values than the control alloy in all aging conditions (underaged (UA), peak-aged (PA), and overaged (OA)), as well as a solution treated condition. Spontaneous infiltration was further prompted owing to the combined effect of both Mg and Zn. This may lead to an enhancement of wetting between the molten alloy and the reinforcement. Consequently, strength improvement in a composite may be attributed to good bond strength *via* enhancement of wetting. The grain size of the control alloy is greatly decreased to about 2.5 mm compared to 10 mm for the commercial alloy. In addition, the grain size in the composite is further decreased to about 2mm. These grain refinements contributed to strengthening of the control alloy and the composite [59]. In another recent study, the role of work hardening characteristics has been shown to be due to increased prismatic punching of dislocations. This relationship of decreasing work hardening rate associated with increasing prismatic punching of dislocations for different Al-based matrices is in the order 7075, 2014, 7010, 2024, 6061 and commercial purity aluminium leading to increased strength increments has been noted. From the study, it is concluded that lower the work hardening rate, higher is the strengthening and *vice versa* in particulate metal–matrix composites [60]. The corrosion behaviour of the MMCs was studied by electrochemical measurements to study the effect of the addition of silicon carbide on the corrosion behaviour of the MMC [61]. The electrochemical noise result shows that the amplitude of the potential noise of the composite is lower than that of the spray deposited 7075 alloy. The potentiodynamic polarization curves results show that both the cathodic oxygen reduction current density and the anodic dissolution current density of the 7075/SiCp MMC are less than those of the 7075 alloy. Thus, the addition of SiC particles increases the corrosion resistance of the MMC. This may be due to that the microstructure of the spray deposited MMC is compact and SiC particles are nonmetallic material, the addition of it minimizes the real corrosion area of the alloy. In another study [62], an attempt has been made to fabricate Al-SiC_p and Al-Al_2O_3 composite materials by powder metallurgy technique at different volume percentage of reinforcement (5, 10, 15, 20, and 25%). The corrosion behavior of the composites was analyzed using AC Gill potentiostat with 3.5 wt% NaCl medium. Four factors, five level, central composite, rotatable design matrix is used to optimize the required number of experiments. The mathematical models were developed by the response surface method (RSM). The developed models have been checked for their adequacy and significance by the *F*-test and *t*-test, respectively. The results obtained from the mathematical models have been optimized and also tested using conformity test runs that closely match the experimental results. A mathematical model has been successfully developed [63] to predict the wear rate of AA7075 aluminium/SiCp composite material fabricated by powder metallurgy technique at 95% confidence level within range of investigation based on the results obtained after studying the effect of reinforcement particle size, applied load and sliding speed on the dry sliding wear behaviour of AA7075 aluminium/SiCp composites fabricated by powder metallurgy technique with 5-25 vol.% SiCp with an average particle size of about 40-150 μm using the conventional powder metallurgy (*P*/*M*) process. The effect of selected process variables on the porosity of 7075 Al alloy 10% SiC composite and subsequent optimal settings of the variables have been obtained using Taguchi method [64]. The results indicate that the holding time, holding temperature and stirring speed are the significant variables. Stirring time is insignificant variable. As the holding time, holding temperature and stirring time increases the porosity decreases. When the stirring speed increases, porosity increases. The predicted optimal value of porosity is 4.71%.

Although very limited studies have been reported on processing of composites, a particular study reports in detail the effect of extrusion and rolling on a SiC_p/7075 aluminum alloy composite fabricated by squeeze casting using a vortex method [65]. The composites were hot rolled to the total rolling reduction of about 94% at temperatures between 573 K and 773 K and at a rolling strain per pass of 0.10. Superplastic characteristics such as microstructure and apparent activation energy were compared with these of the composites made by other processes in order to clarify the superplastic deformation mechanism. Fine grain size of about 1 μm was attained

in the composite rolled at a temperature of 573 K and at the strain per pass of 0.1. In the case of rolling at 573 K, the composite obtained exhibited high strain rate superplasticity with a maximum elongation of about 230% at strain rate of 7×10^{-1} s and at 798 K. Plots between ε^1 and σ showed linear relation when exponent of $n = 2$ was assumed. Threshold stresses obtained from the linear relations were largely dependent on the testing temperature. Apparent activation energy determined from relationship between strain rate and testing temperatures was 244 kJ/mol, which was smaller than that for the powder metallurgical and mechanically alloyed Aluminium composite. It seems that there is no substantial difference of high strain rate superplastic mechanism between the composite fabricated by a vortex method and powder metallurgical aluminum alloy composites.

3.3. What Has Seldom Been Tried

Inspite of the enormous amount of R&D that has gone into Al-based MMCs of every possible alloy with different dispersoids establishing beyond doubt the usefulness of making composites that can be competitive on a production scale to Al-alloys and steels in some cases, and although some of these have already been in commercial use now, a few areas still remained to be explored. These areas have seldom been researched on or reported in the literature though all researchers would agree that these areas needs to be addressed to before Al-base composites are freely available in the market as an alternative to commercial alloys for engineering applications. The areas in which very little or no work has been done/reported include the following:

- Machining of Composites: Particulate MMCs are invariably harder than the base alloy and more abrasive due to the incorporation of the second phase. Hence machining of these poses difficulty as tools used for Al-based alloys are generally used even for the MMCs; the tools wear out fast and needs frequent replacement that adds to the cost of processing of these materials. Most of the times when conventional tools used for Al do not work properly or are blunted tools for machining harder materials like diamond tip tools are used which are costly. But a systematic study has not been done in trying to fabricate/design tools especially for MMCs.
- Joining of Composites: This aspect has not at all been reported though it is a very important area as making components will require joining of two pieces quite frequently. Welding could be the most apt method of joining but welding rods for the purpose needs to be developed. The other known methods of joining similar and dissimilar metals needs to be assessed and researched on.
- Primary/Secondary Processing: The literature available on primary processing including forging, extrusion and rolling is very limited and scanty. Most of the work is on extrusion of only MMCs made from powder metallurgy route in which small samples have been extruded. But before thinking of engineering applications for MMCs, the difficulties in processing these materials needs to be addressed to and parameters optimised. The present paper reports some of the authors' experience in this field.
- Equi Channel Angular Pressing: Equi Channel Angular Pressing [ECAP] is emerging as a competitive route of processing Al-based alloys wherein the grain size is drastically decreased by passing billets through a die containing two channels, equal in cross section, intersecting at a certain angle introducing large shear strain without any reduction in the cross section of the material. Since the process is applicable to large samples, it appears to have the potential for significantly changing the material properties by effective grain size reduction even in a bulk form. This area has never been reported to have been tried for MMCs. It is felt that Al-based MMCs will respond positively to ECAP adding to the benefits of composite making.
- Ultrafine Dispersoids: Dispersoid size, shape, volume fraction, wettability and distribution play the most important role in the properties attained in MMCs. A lot of research has centered on optimizing these parameters and based on the results property designing of composites is possible. However, all the experimentation has stopped at decreasing the dispersoid level below 10μm, possibly due to the difficulty in dispersing uniformly and without coagulation finer particles in the matrix especially when the liquid metallurgy route is adopted for making the composites. If the coagulation problem cannot be addressed on decreasing the particle size below 10 μm, alternate methods of fabrication have to be attempted at like in-situ composites, which has been a modern trend of research for making MMCs. Again, in the present age of nano materials methods of dispersion or making composites with nano sized dispersoids holds a lot of potential for commercial exploitation in the future.
- Bulk Production: One of the causes could be the most important cause as to why Al-based MMCs inspite of all its advantages are yet to see the light of the day extensively as engineering components is the level of production. Researchers are content with the high quality yet small quantities that they can repetitively produce in their laboratories, but the engineering sector is not convinced that the same benefits can be replicated on up scaling. Either party is not ready to bridge the gap by producing the material in bulk due to a number of reasons different for either party. But unless the fear in the mind of the users is removed as to the property improvement even when produced in bulk quantity by the researchers, their dream to see their research product in the market will be difficult to realise. So also, the manufacturing units should be entrepreneurial enough to take some risk in this matter, as certain changes might be

needed in their production line up when alloys are replaced by composites. Somewhere by some groups are needed to take up the challenge of bridging the gap if Al-MMCs are to see the light of the day in the near future.

4. Our Results

The present paper has made an attempt of finding the limit of enhancing the mechanical and wear resistance properties of a commonly used Aluminium alloy, the 7075 alloy by different routs; by making 1) composites 2) heat treatment of the alloy and composite and also 3) extruding the alloy and composite to rods. A comparison in the properties attained by the different routes would help find the limit upto which the properties in this alloy system can be stretched. The experimental setups and results obtained are detailed below.

4.1. Experimental Details

4.1.1. Making of Alloy and Composite

The Al-based alloy confirming to the 7075 composition with 1.6 Cu, 2.5 Mg, 5.6 Zn, 0.3 Cr was selected for the present study. The chemical composition of the alloy was analysed using SPARKMET optical spectrometer [Model: SPECTRA] for confirmation.

For preparing composites from these alloys; 10 volume % of dispersoids of SiC of were used with size between 20-40 μm. The composites were prepared by the liquid metallurgy technique. For preparing the composites, the alloys were melted in a gas fired furnace in a graphite crucible. The melted alloy was fluxed with Coveral 11 and degassed with dry nitrogen gas. The pre weighed quantity and preheated dispersoids were poured into the melt after passing through a sieve. During insertion of the dispersoid the melt was stirred constantly by means of a stirrer placed in the melt operated by a motor. The stirrer speed was controlled as required. After complete insertion of the dispersoids in the molten alloy, the alloy was simultaneously stirred and heated for some time for uniform mixing and temperature. The melt with the dispersoids were then poured into preheated permanent moulds of required size and shape.

4.1.2. Ageing and Tempering

The alloys and composites were aged under T6 tempering and adopting retrogression and re-ageing method [RRA]. In the RRA method, the samples were quenched and aged as per the following steps:

- The alloys and composites were aged at 490℃ for 8 hours and water quenched. The quenched samples were heat treated at 120℃ for 24 hours and were furnace cooled. This corresponds to T6 ageing.
- The T6 aged samples were retrogressed at 200℃ for 45 minutes.
- The retrogressed samples were re-aged at 120℃ for 24 hours.

4.1.3. Extrusion

A 400 tonne hydraulic press with extrusion facility was used for extrusion experimentation. The alloy and composites were sized to a diameter of 50 mm diameter and ~60mm length for extrusion to rods at an extrusion ratio of 10:1. The billets were homogenised under at 480℃ for 12 hours. A pressing speed of 0.4 mm/sec was used and billets were soaked at 350℃ for two hours before extrusion. The container, liner and billet were maintained at the extrusion temperature by externally heating the complete setup, to prevent heat loss during extrusion. The pressure required for successful extrusion was compared for optimizing the extrusion process.

4.1.4. Laboratory Tests

For microstructural studies, samples from the cast and aged alloys and composites of size approximately 20 mm diameters were metallographically polished and etched in Kellar's reagent. The microstructure of the sample was observed in the optical microscope at lower magnifications upto X500 and in the JEOL scanning electron microscope operating at 20 KV at higher magnifications for a better understanding of the constituent phases in the microstructures. The secondary mode of electron emission was initially used for the microstructural investigations. However, when the precipitates expected to be precipitated at the grain boundaries was not properly visible with this mode, the back scattered electron emission mode of the scanning electron microscope was used for observing the precipitation of phases.

Bulk hardness was determined using the EQUOTIP SN 716-1159, Vers-1.16 hardness tester in which the indentation was produced using the Tungsten carbide ball indenter of 20mm diameter with a test tip of 3 mm diameter.

The tensile properties *i.e.* ultimate tensile strength [UTS] and % elongation were determined in the Shimadzu make Universal Testing Machine [UTM] of capacity 100 tonne. Tests were carried out at a load of 4 tonne with load increment of 0.4 tonne. Fractographic analysis of the fractured tensile samples was carried out in which the fractured surface was observed in the scanning electron microscope in order to understand the mechanism of material failure and changes in the mode of failure, if any, as a result of adding particulates to the alloy and extruding them.

The specimens were subjected to dry sliding wear tests under dry conditions using a pin-on-disc wear testing [Figure] [Cameron Plint make]. The test specimen in this case were in the form of cylindrical pins of length 53mm and 8 mm in diameter and the disc counterpart was of AISI 304 grade stainless steel [Fe 0.08-C 2.0-Mn 1.0-Si 8.0-Ni 18.0 Cr] having a hardness of 194 HV. The specimen was held against the rotating steel disc and this

sliding motion results in wear of the pin. The weight of the specimen was taken after every 500 m, sliding distance. The weight loss was calculated from the difference in weight between the initial weight and weight after a specified number of rotations. Dividing the weight loss by the density of the material [calculated by Archimedes principle] gives the volume loss. This volume loss was taken for comparing the wear behaviour. Further, the wear rate was calculated by dividing the volume loss by the total distance traversed. Experiments were conducted in the present study at two speeds of rotation, one low at 200 rpm and the other high at 750 rpm corresponding to linear speeds of 1.04 m/s and 3.92 m/s respectively. Tests were carried out under three applied pressures, *i.e*. 1, 3 and 5 MPa; wear loss was measured at distance corresponding to a sliding distance of 2500 m at intervals of 500 m and the corresponding volume loss calculated. Temperature rise of the specimen was not noted under the present study. The worn surface was studied under the scanning electron microscope [SEM] to study the nature of material removal and surface damage and to compare between material removal mechanism between the cast, aged and extruded conditions and between the alloy and composites under identical conditions.

4.2. Results and Discussion

4.2.1. Microstructural Observations

The microstructure of the cast, aged under T6 and RRA conditions and extruded rods for the alloy and composite is shown in **Figure 2**.

In the as cast state, the 7075 alloy shows heterogeneous precipitation along the grain boundaries as well as inside the grain boundaries **Figure 2(a)**. The alloy exhibits a black filigree of MgZn [18]. Under T6 conditions, there is heavy precipitation in the grains although the grain boundaries are not very clearly defined **Figure 2(b)**, and under RRA conditions dissolution of grain boundaries was observed **Figure 2(c)** and shows a granular structure with grains of varying size and distribution of very fine phases in the grains in the Al-matrix resulting from non uniform solidification rates during casting **Figure 2(a)**. On extrusion directionality is seen along the longitudinal direction and the grain structure is completely broken down **Figure 2(d)**. The transverse section exhibits a granular structure **Figure 2(e)** but the phases are not much resolved. The cast composite exhibits **Figure 2(f)** a near uniform distribution of the particulates within the matrix and clear dendrites are seen in the matrix of Aluminium; grain boundaries are clearly defined with some precipitates in the grains. On ageing the 7075 composite, dissolution of grain boundaries was observed together with coagulation of precipitates around the SiC dispersoids **Figure 2(g)**. Again on extrusion directionality **Figure 2(h)** is seen and distribution of particulates uniformly is also observed. In the transverse section of the extruded composite, studs of the particle heads can be seen uniformly distributed in the matrix **Figure 2(i)**. A few particles [dispersoids] are seen to have been conglomerated in the extruded condition.

4.2.2. Hardness

The bulk hardness [HB] was measured on at least ten locations on the polished and etched sample and the average of the values with standard deviation are tabulated in **Table 4.**

It is seen from the above table that making composites drastically increases the hardness of the alloy by nearly 40% and extruding them further increases the value by some 25% **Table 2**; the latter improvement is due to strain induced strengthening during the processes involved.

4.2.3. Tensile Properties and Fractographic Studies

The stress-strain graph for the extruded alloy and composite is shown in **Figures 3(a)** and **(b)** respectively.

From the nature of the graph it is seen that the alloy exhibits a ductile behaviour but the composite shows a brittle failure. This is possibly due to the incorporation of the SiC particles that are uniformly distributed in the matrix giving the composite a brittle nature. The fractographic studies of the alloy and composite in the cast condition **Figures 4(a)** and **(b)** respectively confirm the loss of ductility on forming composites as the former shows cup and cone type of fracture relating to ductile nature and the latter shows cleavage facets, voids with inclusions [marked by *] and micro cracks [marked by arrow] which are characteristic features of brittle nature of failure. The deep voids with inclusions are the possible cause of fracture in this case.

The Ultimate Tensile strength [UTS] of the cast, homogenised and extruded alloys and composites are shown in **Table 5** and plotted in **Figure 5** for comparison. It is seen that homogenisation increases the UTS for both the alloy and composite resulting possibly from uniformity in the distribution of phases. Extrusion further improves the UTS in the case of alloy though marginally; however for composites a slight decrease has been recorded. The reported results are an average of three sam ples tested in each case.

The fractographs of the tested samples reveals the nature of failure and the effect of homogenisation and/or extrusion on the nature of the sample if any. The fractograph of the homogenised alloy **Figure 6(a)** is very similar to the cast alloy **Figure 6(a)** exhibiting uniform dim-

Table 4. Hardness of alloy and composite under different conditions.

System	As Cast	RRA	Extruded
Alloy	50.06±7.22	71.0±3	96.6±3
Composite	79.6±8.35	72.1±3	101.2±4

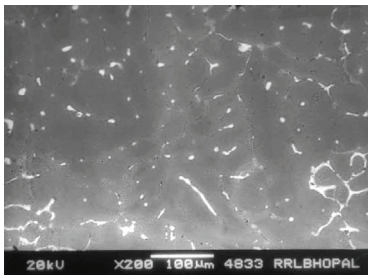

a: Cast Alloy

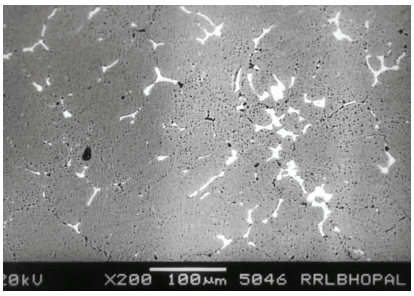

b: Aged Alloy –T6

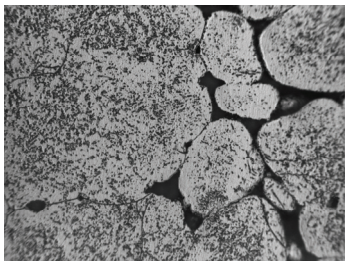

c: Aged Alloy - RRA

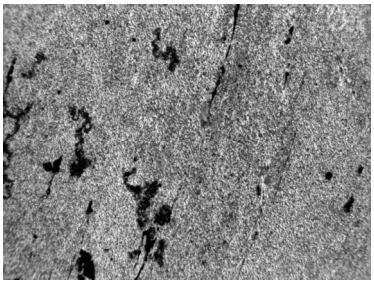

d: Extruded Alloy- longitudinal direction

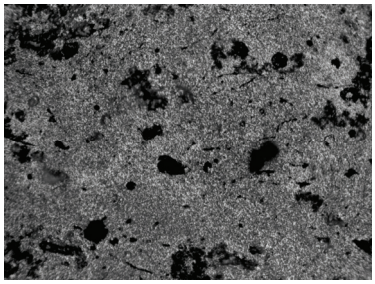

e: Extruded Alloy- transverse direction

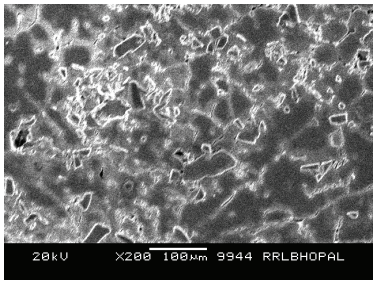

f: Cast Composite

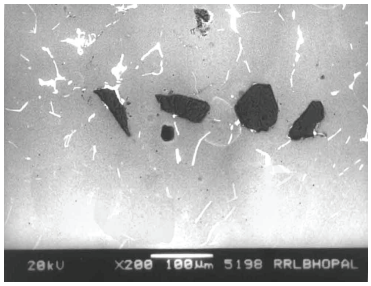

g: Aged Composite –T6

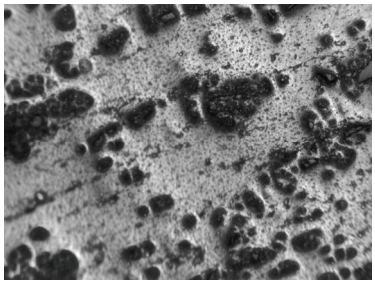

h: Extruded Composite-longitudinal direction

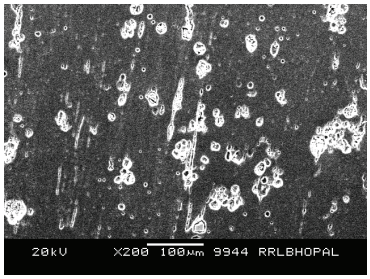

i: Extruded Composite- transverse direction

Figure 2. Microstructure under different conditions.

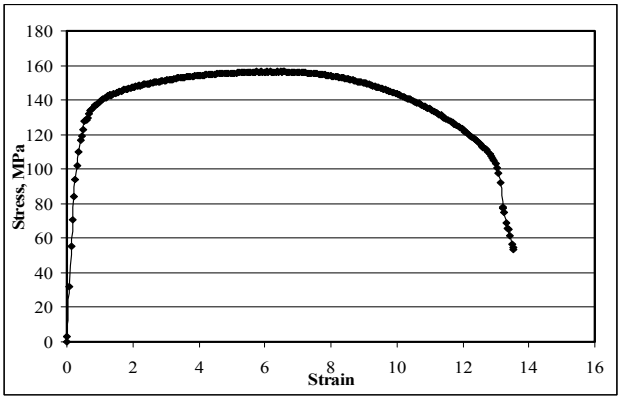

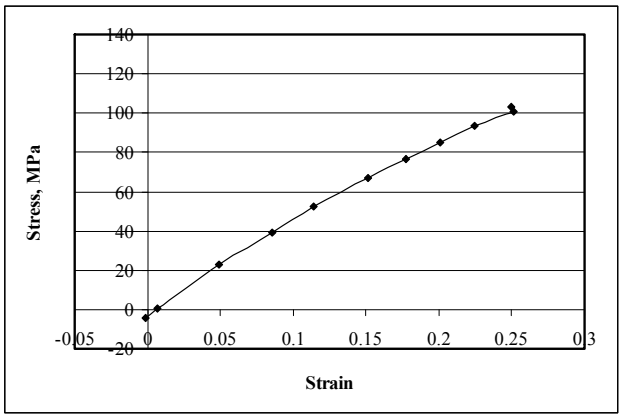

Figure 3. (a) Stress-Strain graph for extruded alloy; (b) Stress-Strain graph for extruded composite.

ples [marked A], with tear ridges indicative of cup and cone type of fracture [marked B] and large number of voids [marked C] indicating ductile fracture [66]. The smooth and fibrous region with proper neck formation at lower magnifications **Figures 6(b)** and **(c)** confirms a pure ductile mode of fracture in both the homogenised and extruded samples. The broken surface of the extruded alloy also exhibit similar structure [**Figure 6(d)**] with a high

Table 5. UTS of Samples.

Sample	UTS, MPa
Cast Alloy	87.57 ± 5.23
Homogenised alloy	159.09 ± 1.88
Extruded alloy	165.59 ± 2.08
Cast Composite	81.85 ± 6.77
Homogenised Composite	112.08 ± 1.48
Extruded Composite	103.10 ± 3.15

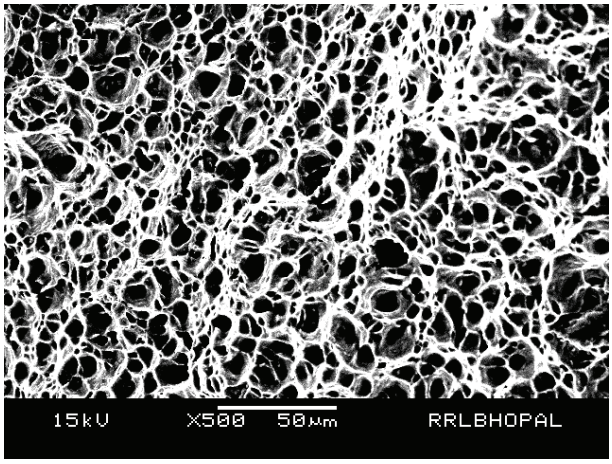

(a)

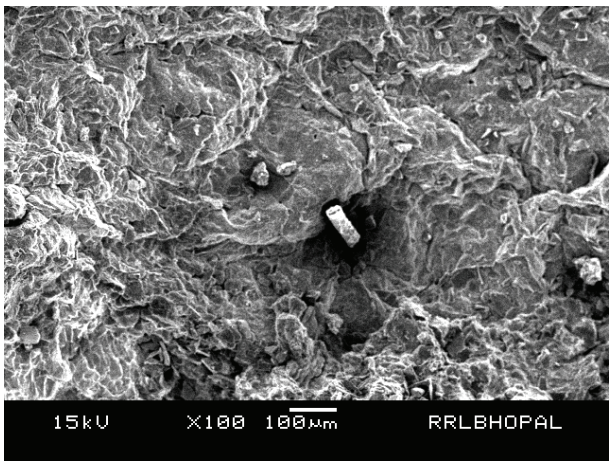

(b)

Figure 4. Fractured surface (a) ductile failure for alloy (b) brittle failure of composites.

density of equiaxed dimples that is found mainly in ductile materials. Fracture by micro void coalescence [67] is the only mode of fracture to be confirmed. No other physical parameter can be seen in the fractographs of the alloys.

In the case of composites, the fractured surface exhibits a slight modification on homogenisation in which voids are seen along with the cleavage in a very scattered manner **Figure 7(a)** unlike the cast condition where only cleavage facets indicative of brittleness is observed **Figure 7(b)**. The river patterns on the facets can also be seen **Figure 7(b)** a clear indication of the brittle mode of the fracture in the homogenised samples [68]. Extrusion however increases the number of voids in the fractographs to a considerable extent; certain portions reveal a smoother surface of fracture, revealing numerous equiaxed dimples, suggestive of ductile tensile fracture **Figure 7(c)**; at times incomplete material removal processes are also seen [marked by arrow]. Higher magnification fractographs **Figure 7(d)** shows dimples with an inclusion, which could have been the cause of fracture along with some stretched cleavage facets and majority of shallow dimples. This indicates a mixed mode of fracture *i.e.* ductile and brittle fracture in the extruded composites.

4.2.4. Sliding Wear Behaviour and Worn Surface Studies

Sliding wear tests were carried out on the cast, homogenised and extruded alloy and composite under two speeds of rotation 200 and 750rpm and under three pressures corresponding to 1, 3 and 5 MPa and the volume loss against sliding distance plotted. It was found that the alloy in all the conditions seized at 5 MPa pressure at both the speeds of rotation, whereas composites sustained the pressure at the lower speed of rotation. Again, alloys seized even at 3MPa pressure at the higher speed of rotation whereas the composites could sustain the conditions upto the sliding distance tested *i.e.* 2500 m. Seizure of the material can be understood from the machine stopping and also from the surface being tested which shows material movement; the scanning electron micrographs of seized samples **Figure 8** shows complete overlapping of material and material movement cutting across wear tracks **Figure 8(a)**; the seized material in turn do not show any structure and looks like a lump of mass on the surface adhered to the surface and material from the inner surface are also exposed **Figure 8(b)**.

In order to compare the behaviour between the alloy and composite for a particular experimental condition, the volume loss against sliding distance is plotted as in **Figure 9**, shown below. It is seen that under all the experimental conditions, the composite exhibits lesser volume loss as compared to the alloy through the duration of the test. Moreover, homogenisation of alloy or composite doesnot have any significant bearing in reducing the volume loss and this is probably due to softening of the matrix as a result of homogenisation and volume loss is directly dependant on the hardness and stiffness of the material. The volume loss for composites is significantly lower than the alloy under a particular experimental condition, especially under the same sample condition. Extrusion has a significant effect in decreasing the volume loss for both alloy and compositeand under a pressure of 3 MPa and 200 rpm,

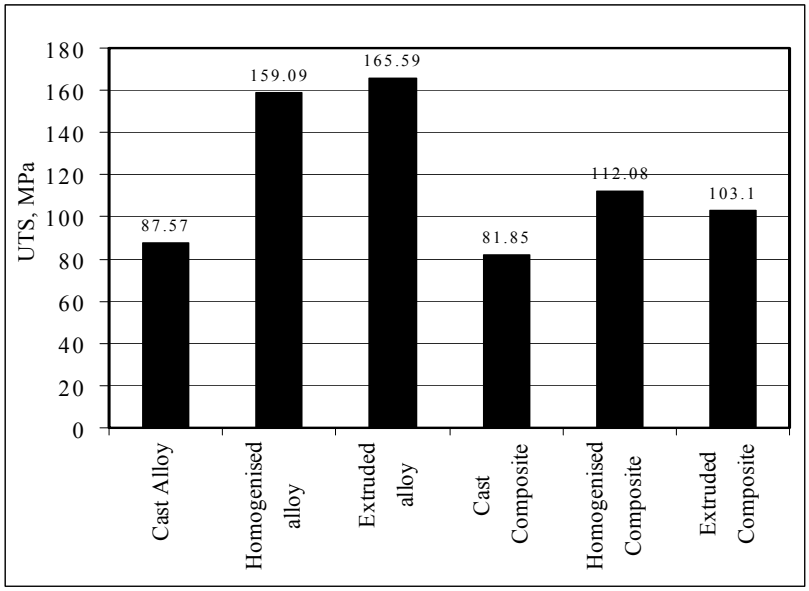

Figure 5. Comparative plot of UTS of the samples.

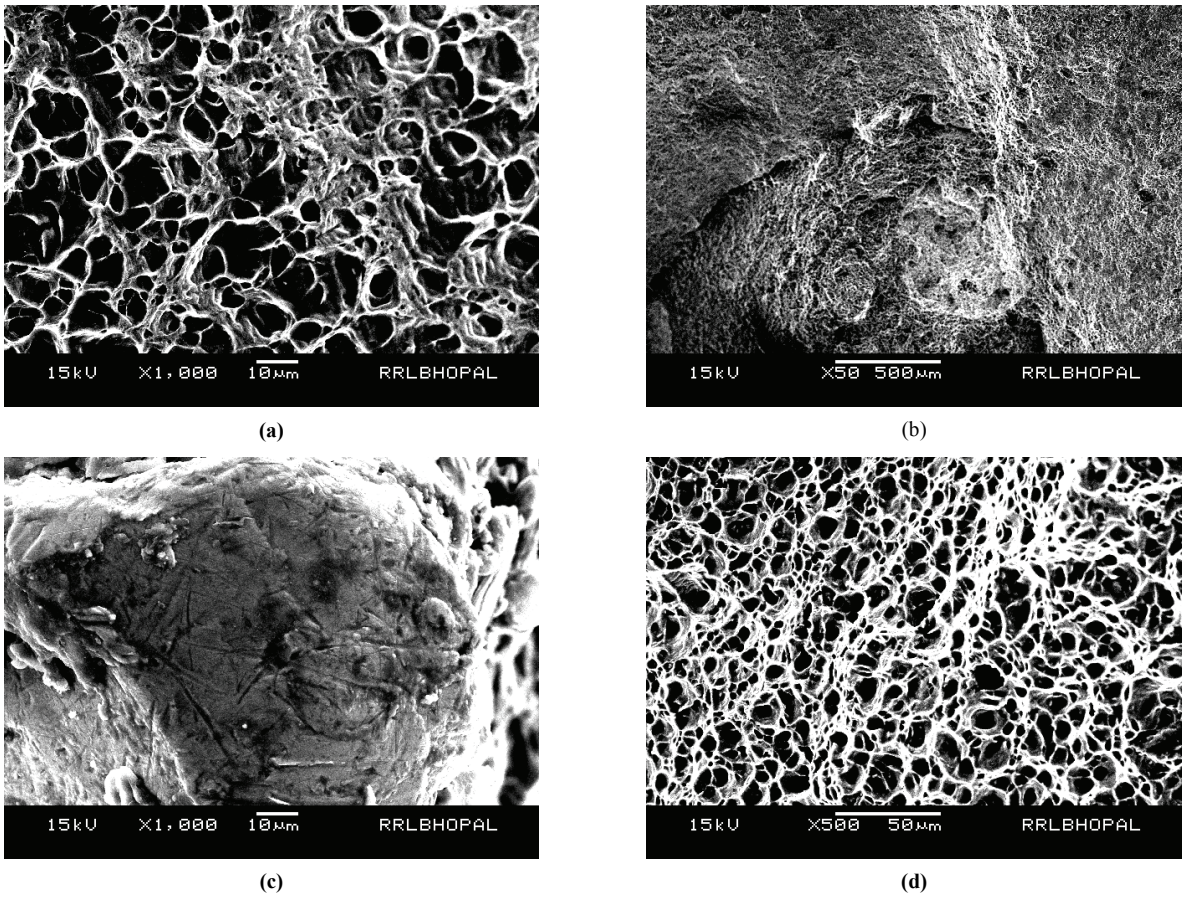

(a) (b)

(c) **(d)**

Figure 6. Fractographs of alloys under different conditions. (a) Homogenised alloy; (b) neck formation at lower magnifications for homogenised and extruded alloys; (d) extruded alloy.

the extruded alloy even exhibits less volume loss *i.e.* better wear resistance than the cast and homogenised composite. It is interesting to note that higher speeds of rotation results in lesser volume loss which is probably

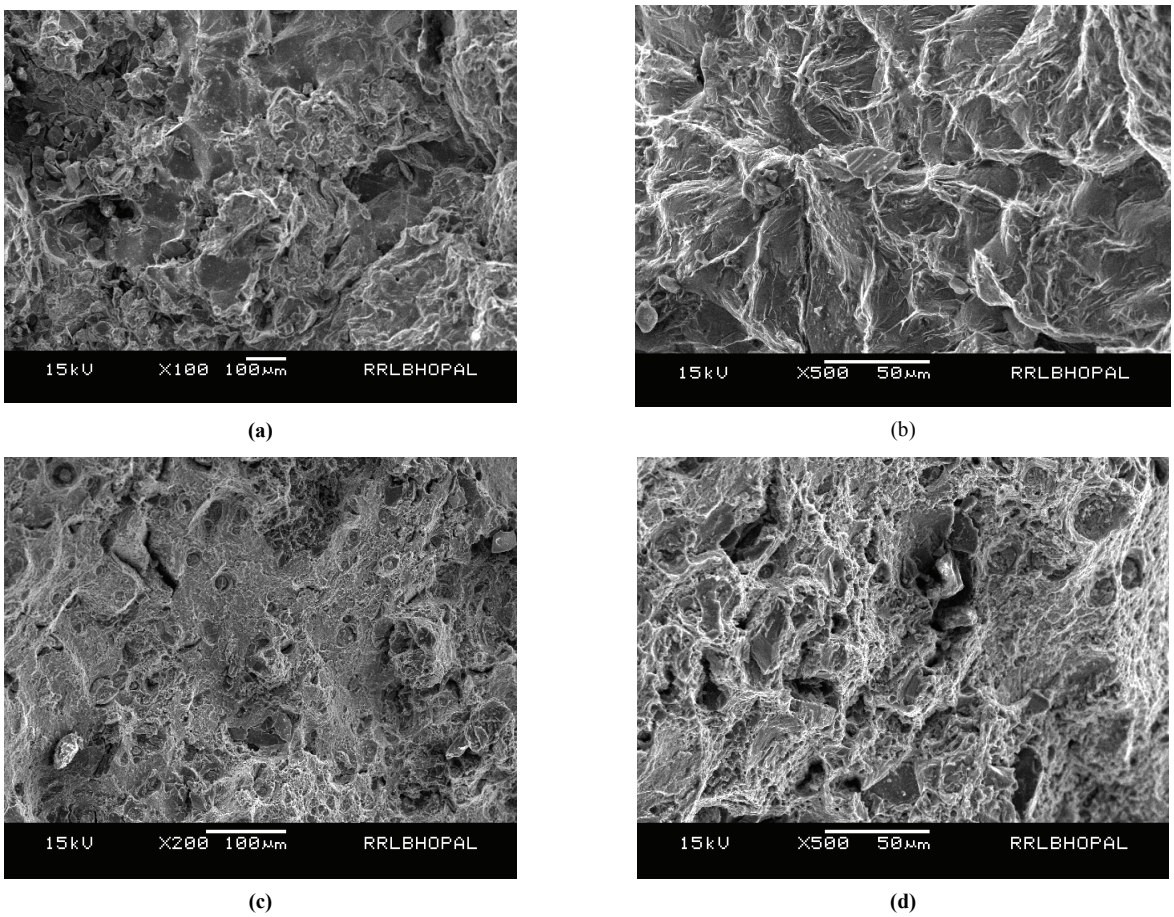

(a) (b)

(c) **(d)**

Figure 7. Fractographs of composites under different conditions.(a) Homogenised composite; (b) homogenised composite showing river patterns on the cleavage facets; (c) extruded composite showing incomplete material removal processes marked by arrow; (d) magnified view of 'c' showing stretched cleavage facets and shallow dimples.

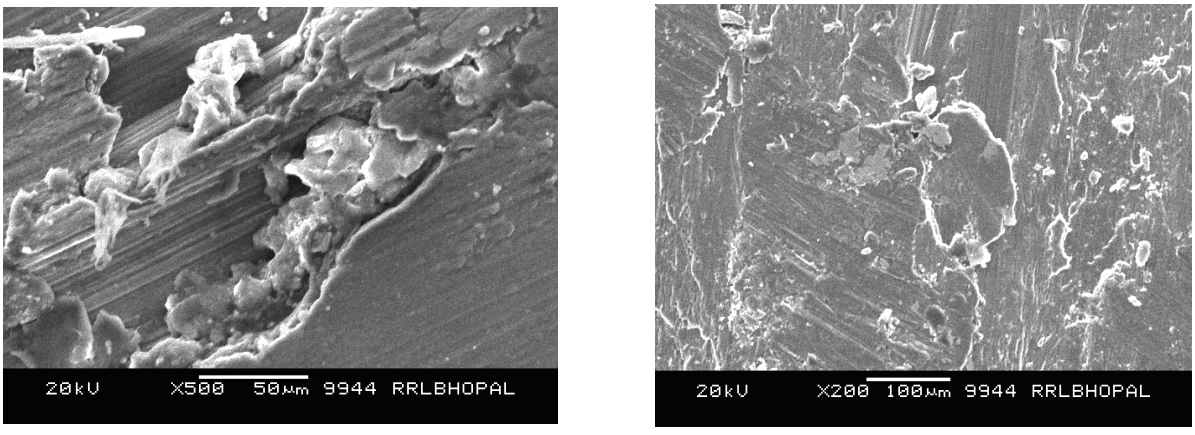

(a) (b)

Figure 8. Micrographs of seized samples.

due to less time that the surfaces get to slide against each other due to the enhanced speed; the material damage is also less in such cases as seen from comparing its worn surfaces at a particular load at different speeds **Figure10**. The effect of load on volume loss is more predominant in the cast condition that in the extruded condition as can be seen on comparing **Figures 9(a)** and (**b)**.

Unlike alloys, which have seized even under a pressure of 3 MPa at higher speeds of rotation, composites have not experienced seizure under a pressure of 3 MPa

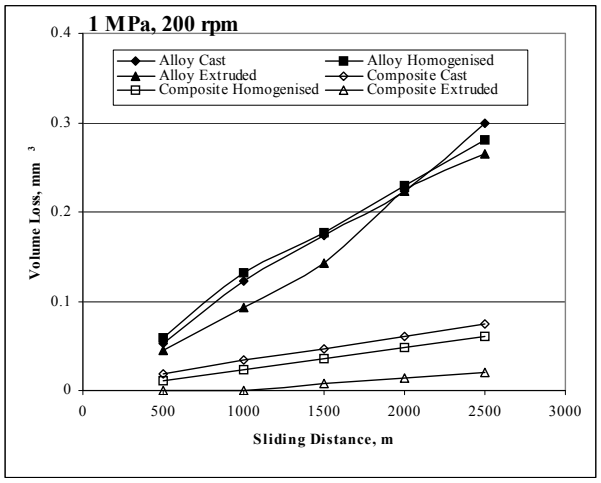

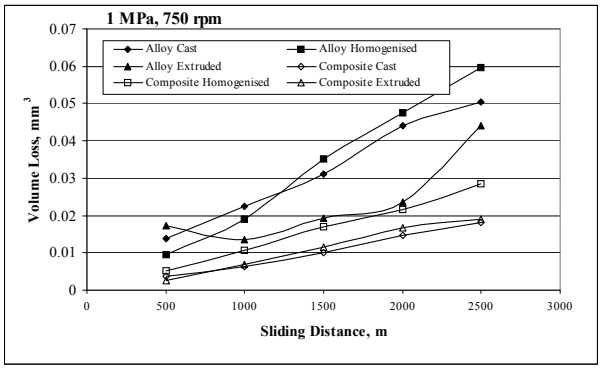

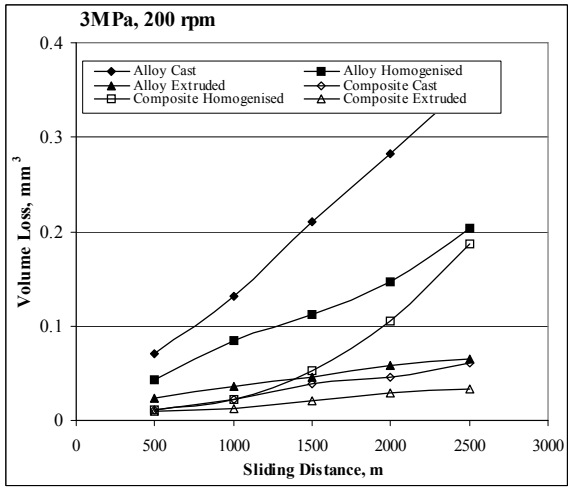

Figure 9. Comparison of volume loss with sliding distance between alloy and composite under different conditions.

under any condition; however the cast and homogenised composites have seized after traversing a minimal distance when the pressure was increased to 5MPa, but even in this condition at both the speeds of rotation they could complete the duration of the test in the extruded condition without any signs of seizure on its worn surface [**Figure 11**]. The advantage of making composites even

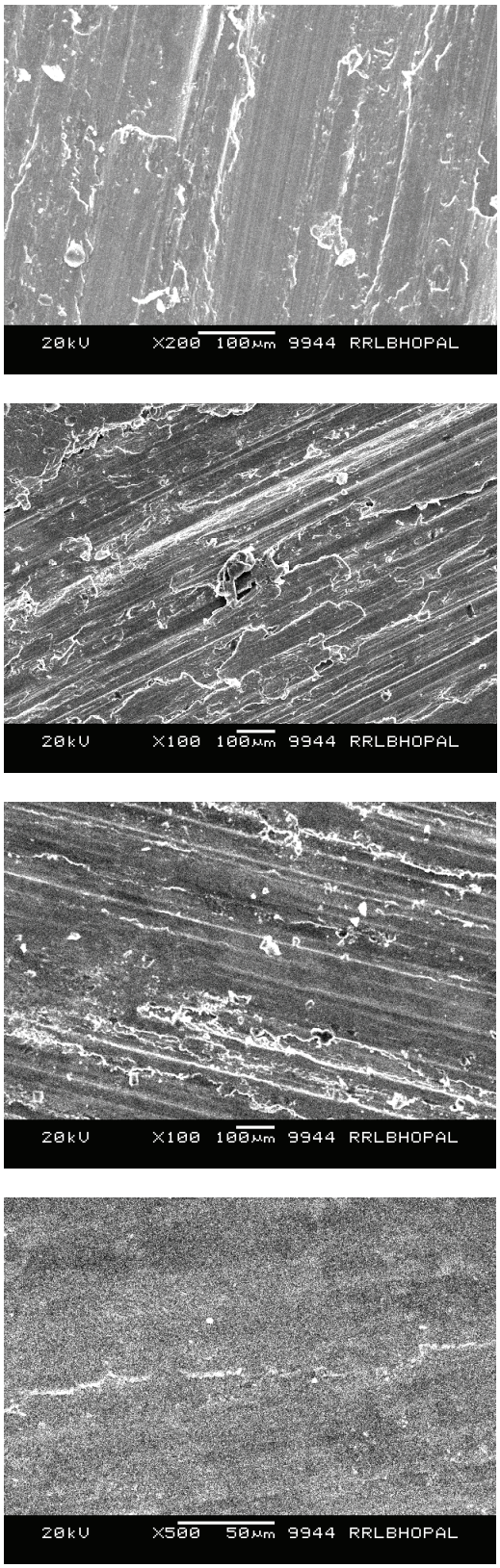

Figure10. Worn surface showing effect of speed at a pressure of 1 MPa. (a) alloy at 200 rpm; (b) alloy at 750 rpm; (c) composite at 200 rpm; (d) composite at 750 rpm.

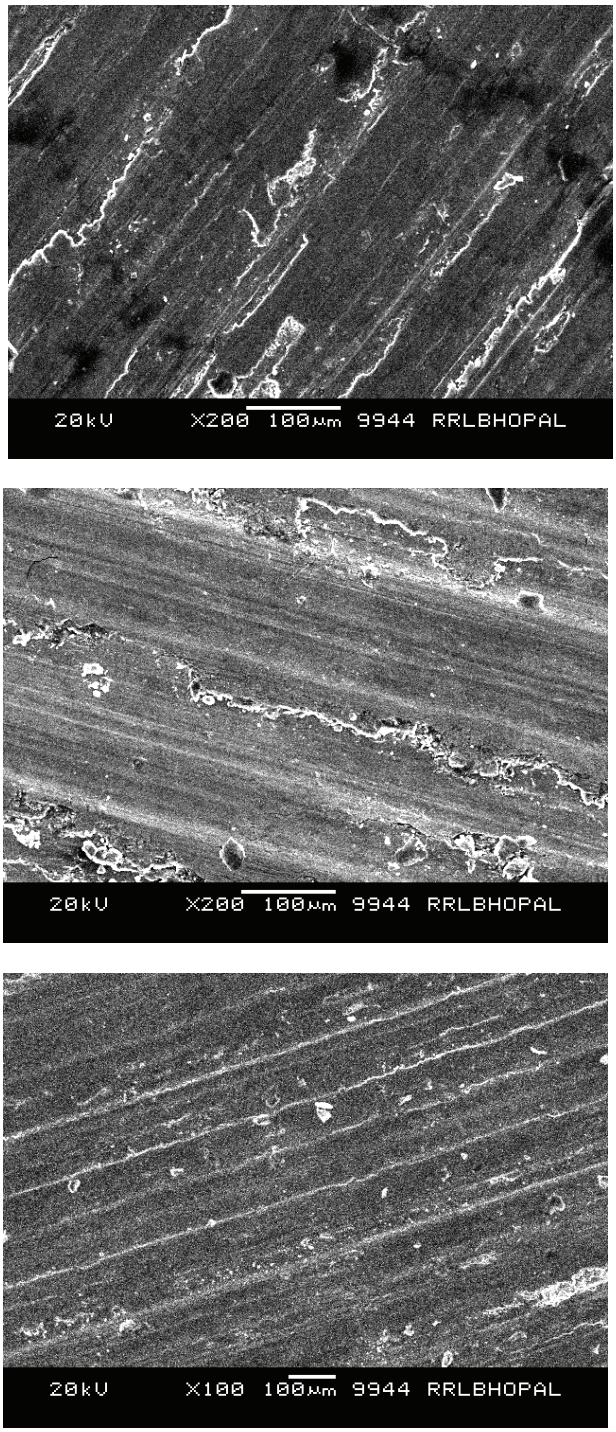

Figure 11. Worn surface of composites at 5MPa pressure. (a) Cast at 200 rpm; (b) Extruded at 200 rpm; (c) Extruded at 750 rpm.

from a non conventional wear resistant alloy like the one being discussed is thus established from the above studies and it brings home the point that extrusion improves the sliding wear resistance properties in both the alloy and composite.

In order to compare the effect of extrusion on wear behaviour of composites, the variation for composites under experimental conditions where alloys have seized is plotted in **Figure 12**. In the Figure, the nature of lines represents the pressure applied like dashed lines represents a pressure of 3 MPa and a filled line a pressure of 5 MPa; again filled symbols represents a sliding speed of 200 rpm and unfilled symbols a speed of rotation of 700 rpm; likewise the letters A, D and G is the cast, B, E and H the homogenised and C, F and I the extruded conditions. From the graph it is seen that the 1) under conditions where the cast and homogenised composites seize at 5 MPa pressure when the speed of rotation is 750 rpm but the extruded composites do not seize 2) homogenisation or heat treatment softens the material leading to more volume loss under the same experimental conditions even over the cast condition 3) extruded composites exhibits better wear resistance [as measured from inverse of volume loss] than the cast condition at high pressures; however at lower pressures the cast condition performs marginally better or it can be said that there is no beneficial effect of extrusion when the load is comparatively less, that is to say that extrusion makes the composites more versatile to withstand harsher conditions of wear related damage.

5. Achievements in a Nutshell

Al-Zn based composites prepared through different routes like casting, powder and squeeze casting routes have been extensively reported and have been extensively been characterised on a laboratory scale and in very rare cases have these been subjected to secondary processing. However any engineering component from the composites has still not been reported. The main dispersoid that have been investigated are SiC and Al_2O_3. The main findings and best results obtained as a result of forming MMCs are as follows:

- Stronger matrix alloys tend to produce stronger composites although the increase in strength due to reinforcement tends to be lower when higher strength matrix alloy; it was found that composites containing 13 μm particles possesses greater toughness than those containing 5 μm particles.
- The microstructural studies of composite in the cast condition is dependent on a number of parameters like macro segregation of dispersoid, primary and secondary dendrite spacing, solidification rate, solidification time, dendrite ripening; the cast structure exhibits coarse dendrite grains, however in contrast small non dendritic structure was observed in the aged structure. In both materials the grain size decreases as the strain rate increases.
- The tensile properties of the composite have been investigated by several investigators with a view to assessing its properties vis-à-vis conventional alloy to find

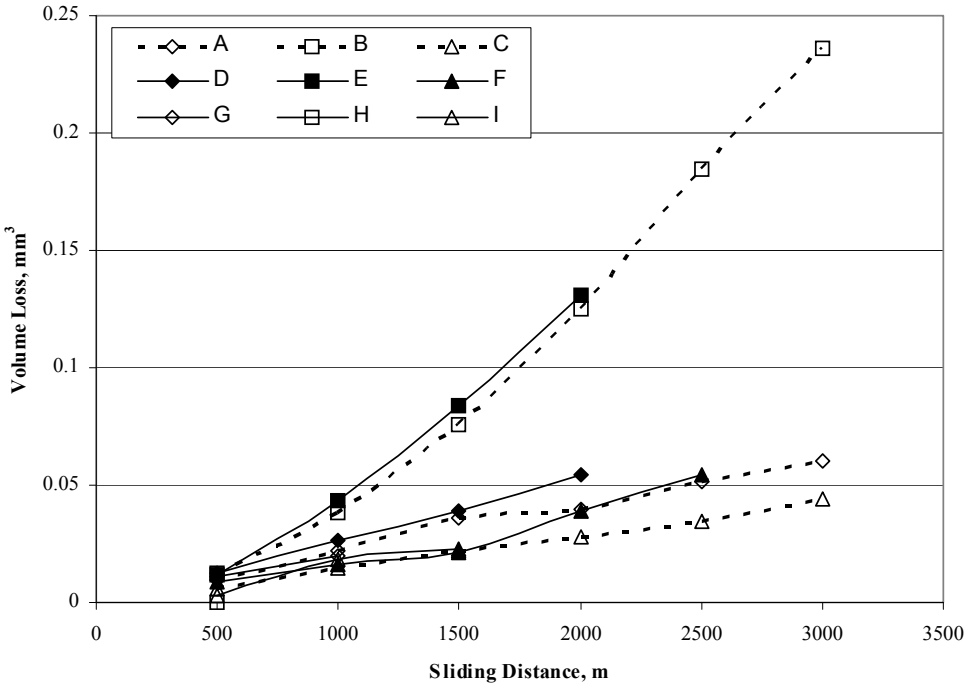

A: Cast, 3MPa, 750 rpm; B: Homogenised, 3MPa, 750 rpm; C: Extruded, 3MPa, 750 rpm
D: Cast, 5MPa, 200 rpm; E: Homogenised, 5MPa, 200 rpm; F: Extruded, 5MPa, 200 rpm
G: Cast, 5MPa, 750 rpm; H: Homogenised, 5MPa, 750 rpm; I: Extruded, 5MPa, 750 rpm

Figure 12. Comparison of wear behaviour under different conditions for composites.

commercial application of the composite. It was found that the properties are dependant on several factors like particle size and volume fraction and there is a peak in the properties attained limiting the size and volume of dispersoids possible for better properties over the monolithic material.

- The best mechanical properties attained in MMCs of this class are made through powder metallurgy routes though this route is not practical for large components and is not economical.
- Strength improvement in a composite may be attributed to good bond strength *via* enhancement of wetting; also presence of the combination of Mg and Zn helps in wetting in this alloy system. This again is dependant on the forming technique and spontaneous infiltration has been found to give the best properties due to an enhancement of wetting between the molten alloy and the reinforcement.
- Effect of alloying elements has an effect even on the properties even after secondary processing of this composite system; the presence of iron produces a slight decrease in strength, elongation and fracture in wrought product. Iron together with manganese may produce a slight increase in strength with limited increase in elongation. Manganese, chromium, molybdenum and zirconium appear to have a strong strengthening effect with corresponding decrease in % elongation. The effect of silicon addition varies some what depending on Mg: Zn ratio.
- It has been observed that these alloys are easily worn out. Severe wear at high contact load have been reported. In paraffin oil, the wear rates were approx 1/10 the wear rates under dry conditions; however 7004-T6 showed a lower friction coefficient compared to 2024-T4.
- Creep resistance of the alloys is relatively low, especially for high strength alloys. However, such studies have not been reported for composites of these alloys.
- The role of work hardening characteristics has been shown to be associated with a high dislocation density in the matrix due to the difference in coefficient of thermal expansion between the reinforcement and the matrix.
- The corrosion behaviour of the MMCs was studied by electrochemical measurements to study the effect of the addition of silicon carbide on the corrosion behaviour of the MMC. The corrosion behaviour of the metal matrix composite show that both the cathodic oxygen reduction current density and the anodic dissolution current density are less than those of the alloy. Thus, the addition of SiC particles increases the corrosion resistance of the MMC.
- Very limited studies have been reported on processing of composites. In a study, the composites were hot rolled to the total rolling reduction of about 94% at temperatures between 573 K and 773 K and at a rolling strain per pass of 0.10.
- Inspite of the enormous amount of R&D that has

gone into Al-based MMCs of this alloy establishing beyond doubt the usefulness of making composites they are yet to produced at competitive rates on a production scale. Until this is done the possibility of making components from the composites inspite of all its advantages will remain a dream.

- Again, before components are thought of some areas needs address. Till now conventional methods/tools as used for the alloys have been used for the purpose but further development and exclusive research on composites per se needs to be addressed to. These include:
- Machining of Composites
- Joining of Composites
- Primary/Secondary Processing
- Equi Channel Angular Pressing
- Composites from Ultrafine Dispersoids

6. The Stretch, Limit and the Future

The contributions made towards increasing the state of knowledge in enhancing the physical, mechanical, wear and corrosion resistance has established the efficacy of making composites with better properties than the alloy; the conditions under which the improvements can be best realised have also been established by different researchers throughout the world mainly through laboratory scale studies. It is seen that the properties attained has been stretched to the maximum possible and there is no much scope of further improvement in the properties as the methods and materials used have all been optimised; and since the last decade no further improvement in terms of properties have been recorded. This in a way has put a limiting factor for further improvement.

The next step would be to mass produce these composites adopting the techniques and adhering to parameters that have been established to give the best results and establish feasibility of making composites on a mass scale retaining the improved properties. Until this is done the ultimate aim of making meaningful engineering components from the composites will never be realised.

Together with mass production and making components for the engineering sector, certain aspects specifically for composites need to be addressed like machining, joining, primary and secondary processing.

Further some basic research is also needed like decreasing the size of the dispersoid further to nano- or micro-size and to establish the parameters for uniform distribution; this definitely will further enhance the properties. Also computer simulation and mathematical modeling of composite fabrication is an area where some scattered work has been done; this area would also need to be addressed to that would cut down on actual experimentation and prediction of properties attainable if the nature, shape, size, volume fraction and processing techniques are known.

Some twenty years of research has gone into making composites and with that we till date know so much. Another ten to fifteen years of research in certain areas still not addressed to as mentioned above would help see the composites in the market readily available. It is time instead of reinventing the wheel and treading known paths of property evaluation and improvement that are now more or less guaranteed, the critical issues as mentioned above are taken up for research that would help in taking the laboratory scale composites a step further and a step closer to the engineering sector.

7. References

[1] J. E. Hatch, "Aluminium, Properties, Physical Metallurgy and Phase Diagrams," American Society for Metals, Metals Park, Ohio, 1971.

[2] I .J. Polmear, "Light Metal Age, Metallurgy of the Light Metals," Edword Arnold Publishers Ltd, London, 1981, p.69.

[3] I. J. Polmear, "Light Metal Age, Metallurgy of the Light Metals," Edword Arnold Publishers Ltd, London, 1981, p.73.

[4] L. F. Mondolfo, "Grain Refinement in Aluminum Alloyed with Titanium and Boron," *Metallurgical and Materials Transactions B*, Vol. 2, No. 2, 1971, pp. 465-471.

[5] R. C. Dorward, "Precipitate Coarsening during Overaging of Al-Zn-Mg-Cu Alloy," *Materials Science and Technology*, Vol. 15, No. 10, 1999, pp. 1133-1138.

[6] S. Suresh, T. Christman and Y. Sugimurlan, "Accelerated Ageing in Cast Al Alloy-SiC Particulate Composites," *Scripta Metallurgica*, Vol. 23, No.9, 1989, pp. 1599-1602.

[7] J. S. Robinson, S. D. Whelena and R. L. Cudd, "Retrogression and Reaging of 7010 Open Die Forgings," *Materials Science and Technology*, Vol. 15, No. 6, 1999, pp. 717-724.

[8] A. Deschamps, Y .Brechet and F. Livet, "Influence of Copper Addition on Precipitation Kinetics and Hardening in Al-Zn-Mg alloy," *Materials Science and Technology*, Vol. 15, No. 99, 1999, pp. 993-1000.

[9] W. S. Lee, W. C. Sue, C. F. Lin and C. J. Wu, "Effect of Aging on High Strain Rate and High Temperature Properties of 7075 Aluminum Alloy," *Materials Science and Technology*, Vol. 15, 1999, pp. 1379-1386.

[10] Yi-Lei Wu, F. H. [Sam] Froes, Chenggong Li and Alex Alvarez, "Microalloying of Sc, Ni and Ce in an Advanced Al-Zn-Mg-Cu Alloy," *Metallurgical and Materials Transactions A*, Vol. 30A, No. 4, 1999, pp. 1017-1024.

[11] K. Ural, "A Study of Optimization of Heat Treatment Conditions in Retrogression and Reaging Treatment of 7075-T6 Al alloy," *Journal of Materials Science Letters*, Vol. 13, No. 5, 1994, pp. 383-385.

[12] M. Kanno, I. Araki and Q. Cui, "Precipitation Behavior

of 7000 Alloys during Retrogressional and Reaging Treatment," *Materials Science and Technology*, Vol. 10, 1994, pp. 599-603.

[13] M. Furukawa, P. B. Berbon, Z. Horita, M. Nemoto, N. K. Tsenev, R. Z. Valiev and T. G. Langdon, "Age Hardening and the Potential for Superplasticity in a Fine Grained Al-Mg-Li-Zr Alloy," *Metallurgical and Materials Transactions A*, Vol. 29A, No. 1, 1998, pp. 169-177.

[14] J. E. Hatch, "Aluminium Properties and Physical Metallurgy," American Society for Metals, Metals Park, Ohio, 1984, p. 2.

[15] Y. Huang, F. J. Hummpberys, N. Ridley and Z. C. Wang, "Diffusion Bonding of Hot Rolled 7075 Al alloys," *Materials Science and Technology*, Vol. 14, 1998, pp. 405-410.

[16] J. M. Zhang, M. A. Przystuna and A. J. Luevano, "Characterization of Pore and Constituent Particle Populations in 7050-T7451 Al Plate Alloys," *Metallurgical and Materials Transactions A*, Vol. 29A, No. 3, 1998, pp. 727-737.

[17] M. G. Zelin and S. Guillard, "Microstructure and Properties of Superplastically Formed Al Alloy 7475 Pans," *Materials Science and Technology*, Vol. 15, 1999, pp. 309-315.

[18] H. Iwasaki, T. Mori, M. Mabuchi and K. Higashi, "Microstructural Evolution and Plastic Stability during Superplastic Flow in A 7475 Aluminum Alloy," *Materials Science and Technology*, Vol. 15, 1999, pp. 180-184.

[19] D. N. Hanlon and W. M. Rainforth, "Some Observations on Cyclic Deformation Structures in the High Strength Commercial Aluminum Alloy AA 7150," *Metallurgical and Materials Transactions A*, Vol. 29A, No. 11, 1998, pp. 2727-2736.

[20] Y. N. Kwon and Y. W. C. Hang, "The Effect of Grain Size and Temperature on the Superplastic Behavior of a 7075 Al Alloy," *Metallurgical and Materials Transactions A*, Vol. 30A, 1999, pp. 2037-2047.

[21] W. S. Miller and F. J. Humphreys, "Fundamental Relationship between Microstructures and Mechanical Properties of Metal Matrix Composites," In: M. N. Gungar and P. K. Liaw, Ed., 517.

[22] Nuesbaum, "New Application for Al. Based MMC," *Light Metal Age*, Vol. 55, February 1997, p. 54.

[23] R. Asthana, "Reinforced Cast Metals Part I-Solidification Microstructure," *Journal of Material Science*, Vol. 33, No. 7, 1998, pp. 1679-1698.

[24] M. S. Zedalis, P. S. Cilman and S. K. Das, "In High Performance Composites for the 1990's," In: S. D. Das, *et al*. Ed., *The Metallurgy Society of AIME*, Warrendale PA, 1990, pp. 61-81.

[25] T. J. A. Doel and P. Bowen, "Effect of Particle Size and Matrix Aging Conditions on Toughness of Particle Reinforced Aluminum Based Metal Matrix Composites," *Materials Science and Technology*, Vol. 12, No. 7, 1996, pp. 586-594.

[26] E. M. Taleff, G. A. Henshall, T. G. Nieh, D. R. Lesuer and J. Wadsworth, "Warm Temperature Tensile Testing Ductility in Al-Mg Alloys," *Metallurgical and Materials Transactions A*, Vol. 29A, No. 13, 1998, pp. 1081-1091.

[27] M. J. Hadianford and Y. W. Mai, "In Situ SEM Studies on the Effect of Particulate Reinforcement on Fatigue Crack Growth Mechanism of Aluminum Based Metal Matrix Composites," *Journal of Materials Science*, Vol. 30, No. 21, 1995, pp. 5335-5346.

[28] Y. C. Zhou, Z. P. Duan and Q. B. Yang, "Failure of SiC Particulate Reinforced Metal Matrix composites Induced by Laser Thermal Shock," *Metallurgical and Materials Transactions A*, Vol. 29A, No. 2, 1998, pp. 685-692.

[29] O. P. Modi, M. Saxena, B. K. Prasad, A. K. Jha, S. Das and A. H. Yegneswaran, "Role of Alloy Matrix and Dispersoid on Corrosion Behaviour of Cast Al alloy Composite," *Corrosion*, Vol. 54, No. 2, 1998, pp. 129-134.

[30] P. K. Rohatgi, S. Das and R. Asthana, "Science, Technology and Industrial Potential of Cast Metal Ceramic Particle Composites," Materials Science and Technology in the future, CSIR, Bhopal, 1985, pp. 123-184.

[31] P. K. Rohatgi, R. Asthana and S. Das, "Solidification, Structure and Properties of Cast Metal-ceramic Particle Composites," *International Metals Reviews*, Vol. 31, No. 3, 1986, pp. 115-139.

[32] T. S. Srivatsan, "Microstructure, Tensile Properties and Fracture Behaviour of Al_2O_3 Particulate Reinforced Aluminium Alloy Metal Matrix Composites," *Journal of Materials Science*, Vol. 31, No. 5, 1996, pp. 1375-1388.

[33] S. Sriram, C. Daniels and T. S. Srivatsan, "Influence of Al_2O_3 Particulate Reinforcement on Tensile Fracture of an Aluminium Alloy Metal Matrix Composite," *Meatls Materials and Processes*, Vol. 17, No. 3, 1995, pp. 183-199.

[34] A. M. Gokhale, N. U. Deshpande, D. K. Denzer and J. Liu, "Relationship between Fracture Toughness, Fracture Path, Microstructure of 7050 Aluminium Alloy: Part II. Multiple Micromechanisms-Based Fracture Toughness Model," *Metallurgical and Materials Transactions A*, Vol. 29A, No. 4, 1998, pp. 1203-1210.

[35] M. J. Hadianford, J. Healy and Y. W. Mai, "Fracture Characteristics of a Particulate Reinforced Metal Matrix Composite," *Journal of Materials Sciences*, Vol. 29, No. 9, 1994, pp. 2321-2327.

[36] T. S. Srivatsan, "Microstructure, Tensile Properties and Fracture Behaviour of Aluminium Alloy 7150," *Journal of Materials Science*, Vol. 27, No. 17, 1992, pp. 4772-4781.

[37] A. M. Murphy, S. J. Howard and T. W. Clyne, "Characterisation of Severity of Particle Clustering and Its effect on Fracture of Particulate Metal matrix composites," *Material Science and Technology*, Vol. 14, 1998, pp. 959-968.

[38] A. J. Shakesheff and G. Purdue, "Designing Metal Matrix Composites to Meet Their Target: Particulate Reinforced Al Alloys for Missile Applications," *Material Science and Technology*, Vol. 14, 1998, pp.

851-856.

[39] P. D. Pitcher, A. J. Shakesheff and J. D. Lord, "Aluminum Based Metal Matrix Composites for Improved Elevated Temperature Performance," *Material Science and Technology*, Vol. 14, 1998, pp. 1015-1023.

[40] C. M. Styles, I. Sinclair, K. Foster and P. J. Gregson, "Work Hardening Effects on SiC Particle Reinforced Aluminum Alloys," *Material Science and Technology*, Vol. 14, 1998, pp. 1053-1056.

[41] A. Deschamps, Y. Brechet and F. Livet, "Influence of Copper Addition on Precipitation Kinetics and Hardening in Al-Zn-Mg Alloy," *Materials Science and Technology*, Vol. 15, 1999, pp. 993-1000.

[42] W. S. Miller and F. J. Humphreys, "Strengthening Mechanisms in Particulate Metal Matrix Composites," *Scripta Metall*, Vol. 25, 1991, pp. 33-38.

[43] D. J. Lloyd, "Aspects of Fracture in Particulate Reinforced Metal Matrix Composites," *Acta Metall*, Vol. 39, No. 1, 1991, pp. 59-71.

[44] N. J. Hurd, "Fatigue Performance of Alumina Reinforced Meatal Matrix Composites," *Materials Science and Technology*, Vol. 4, 1988, pp. 513-517.

[45] R. P. Wei, C.-M. Liao and M. Gao, "A Transmission Electron Microscopy Study of Constituent-particle-induced Corrosion in 7075-T6 and 2024-T3 Aluminum Alloys," *Metallurgical and Materials Transactions A*, Vol. 29A, 1998, pp. 1153-1160.

[46] M. Gao, C. R. Feng and R. P. Wei, "An Analytical Electron Microscopy Study of Constituent Particles in Commercial 7075-T6 and 2024-T3 Alloys," *Metallurgical and Materials Transactions A*, Vol. 29A, No. 4, 1998, pp. 1145-1151.

[47] D. J. Lloyd and B. Chamberlin, "In Cast Reinforced Composites," American Society for Metals, Metals Park, 1988, pp. 263-268.

[48] F. M. Hosking, F. F. Portillo, R. Wunderlin and R. Mehrabian, "Composite of Aluminium Alloys: Fabrication and Wear Behaviour," *Journal of Materials Science*, Vol. 17, No. 2, 1982, pp. 477-498.

[49] A. Wang and H. J. Rack "Abrasive Wear of Silicon Carbide Particulate and Whisker Reinforced 7091 Aluminum Matrix composites," *Wear*, Vol. 146, No. 2, 1991, pp. 337-348.

[50] S. Turenne, Y. Chatigny, D. Simard, S. Caron and J. Masounave, "The Effect of Abrasive Particle Size on the Slurry Erosion Resistance of Particulate Reinforced Aluminium Alloy," *Wear*, Vol. 141, No. 1, 1990, pp. 147-158.

[51] L. H. Chen and D. A. Rigney, "Transfer during Unlubricated Sliding Wear of Selected Metal Systems," *Wear*, Vol. 105, No. 1, 1985, pp. 47-61.

[52] R. L. Devis, C. Subramaniam and J. M. Yellup, "Abrasive Wear of Aluminium Composites-A Review," *Wear*, Vol. 201, No. 2, 1996, pp. 132-144.

[53] B. Venkataraman and G. Sundararajan, "Corellation between the Characteristics of the Mechanically Mixed Layer and Wear Behaviour of Aluminium, Al-7075 alloy and Al-Metal Matrix Composites," *Wear*, Vol. 245, No. 1, 2000, pp. 22-38.

[54] A. K. Mukhopadhyay, "On the Nature of Fe Bearing Particles Influencing Hard Anodizing Behavior of AA7075 Extrusion Products," *Metallurgical And Materials Transactions A*, Vol. 29A, 1998, pp. 979-987.

[55] C. M. Styles, "Superplastic Forming Behavior of Complex Shapes and Post Forming Mechanical Properties of Aluminum Based SiCp Reinforced Metal Matrix Composites," *Materials Science and Technology*, Vol. 16, 2000, pp. 759-764.

[56] F. A. Mohamed, "On the Creep Strengthening of SiC Particulate in SiC-Al Composites," *Metallurgical and Materials Transactions A*, Vol. 28A, No. 12, 1997, pp. 2780-2782.

[57] Y. Li and T. G. Langdon, "An Examination of Creep Data for an Al-Mg Composite," *Metallurgical and Materials Transactions A*, Vol. 28, No. 5, 1997, pp. 1271-1273.

[58] K. T. Park, E. J. Lavernia and F. A. Mohamed, "High Temperature Creep of Silicon Carbide Particulate Reinforced Aluminium," *Acta Metallurgica et Materialia*, Vol. 38, No.11, 1990, pp. 2149-2159.

[59] K. B. Lee and H. Kwon, "Strength of Al-Zn-Mg-Cu Matrix Composite Reinforced with SiC Particles," *Metallurgical and Materials Transactions A*, Vol. 33A, No. 2, 2002, pp. 455-465.

[60] K. T. Kashyap, C. Ramachandra, C. Dutta and B. Chatterji, "Role of Work Hardening Characteristics of Matrix Alloys in the Strengthening of Metal Matrix Composites," *Bulletin of Materials Science*, Vol. 23, No. 1, 2000, pp. 47-49.

[61] Y. L. Cheng, Z. H. Chen, H. L. Wu and H. M. Wang, "The Corrosion Behaviour of the Aluminum Alloy 7075/SiCp Metal Matrix Composite Prepared by Spray Deposition," *Materials and Corrosion*, Vol. 58, No. 4, 2007, pp. 280-284.

[62] V. Balasubramanian, J. Senthilkumar, M. Balasubramanian, "Optimization of the Corrosion Behavior of AA7075 Al/SiC_P and Al/Al_2O_3 Composites Fabricated by Powder Metallurgy," *Journal of Reinforced Plastics and Composites*, Vol. 27, No. 15, 2008, pp. 1603-1613.

[63] S. Kumar and V. Balasubramanian, "Developing a Mathematical Model to Evaluate Wear Rate of AA7075/SiCp Powder Metallurgy Composites," *Wear*, Vol. 264, No. 11-12, 2008, pp. 1026-1034.

[64] R. K. Bhushan S. Kumar and S. Das, "Optimisation of porosity of 7075 Al Alloy 10% SiC Composite Produced by Stir Casting Process through Taguchi Method," *International Journal of Materials Engineering Innovation*, Vol. 1, No. 1, 2009.

[65] H. Takeo, I. Tsunemichi, K. Toshiro and T. Hiroyuki, "High Strain Rate Superplasticity of the SiC_p/7075 Aluminum Alloy Composite Made by a Vortex Method," *Keikinzoku*, Vol. 51, No. 3, 2001, pp. 169-174.

[66] O. C. Wells, "Interpretation of scanning electron microscope fractographs," John A Fellows, 8th Edition, *Metals Handbook*, ASM Committee on Fractography by

electron microscopy, ASM, Vol. 9, 1974, pp. 64-67.

[67] O. C. Wells, "Scanning electron microscope fractographs," John A Fellows, 8th Edition, *Metals Handbook*, ASM Committee on Fractography by Electron Micros-Copy, ASM, Vol. 9, 1974, pp. 64-78.

[68] O. C. Wells, "Interpretation of scanning electron microscope fractographs," John A Fellows, 8th Edition, *Metals Handbook*, ASM Committee on Fractography by Electron Microscopy, ASM, Vol. 9, 1974, pp. 64-78.

Engineering, **2010, 2, 257-262**
doi:10.4236/eng.2010.24035 Published Online April 2010 (http://www.SciRP.org/journal/eng)

Scientific Research

Optimum Shape of High Speed Impactor for Concrete Targets Using PSOA Heuristic

Francesco Ragnedda, Mauro Serra
Department of Mathematics and Computer Science, *University of Cagliari*, *Cagliari*, *Italy*
Department of Structural Engineering, *University of Cagliari*, *Cagliari*, *Italy*
E-mail: *ragnedda@ unica.it*, *serrama@unica.it*
Received November 16, 2009; *revised January* 20, 2010; *accepted February* 4, 2010

Abstract

The present paper deals with the optimum shape design of an absolutely rigid impactor which penetrates into a semi-infinite concrete shield. The objective function to maximize is the depth of penetration (DOP for short) of the impactor; in the case of impactors with axisymmetric shapes DOP is calculated using formulas obtained by Ben-Dor *et al*. [1-3] with the method of local variations [4] and based on the mechanical model proposed by Forrestal and Tzou [5]. In the present paper we show that using a different class of admissible functions, more general than the axisymmetric one, better results can be obtained. To solve the formulated optimization problem we used a custom version of the particle swarm optimization method (briefly denoted by PSOA), a very recent numerical optimization algorithm of guided random global search. Numerical results show the optimal shape for various types of shields and corresponding DOP; some Ben-Dor *et al*. [1-3] results are compared to solutions obtained.

Keywords: Impactor; Optimization; Particle Swarm; Global Search

1. Introduction

A problem important both for the civil world as well as for military research is to evaluate the depth of penetration (DOP) of a high-speed impactor when it penetrates a shield. A quite general solution to such problem was proposed by Forrestal *et al*. [5-7] in the case of concrete targets. Four different models for the shield material are considered: incompressible elastic-plastic (Model 1), incompressible elastic-cracked-plastic (Model 2), compressible elastic-plastic (Model 3) and compressible elastic-cracked-plastic (Model 4). Supposing the impactor's shape is axysimmetric with an unknown starting radius (flat nose), given length and final radius, (we call K_0 such class of shapes) and using the Forrestal *et al*. [5-7] model, Ben-Dor *et al.* [1-3,8] we investigated the maximum depth of penetration and found corresponding numerical solutions. From a mathematical point of view, the problem is reduced to a non-classical variational one for a functional that is a function of integrals of the unknown impactor's shape; the technique used to solve it is that of local variations, proposed by Banichuk *et al*.[4]. In the following we shall define a new class of impactors and show how to get corresponding formulas.

It is worth noting that in the current literature, some penetration problems for three-dimensional bodies of optimal shape are also present [9-12] and very recently Banichuk and Ivanova [13] obtained new results applying the Forrestal and Tzou model to pyramidal impactors.

2. Model Building

Let us consider an impactor whose impact velocity is normal to the concrete shield and has modulus v_{imp}. The impactor has a shape built in the following manner: consider a body of revolution obtained revolving a curve of function $y = y(z)$ in the Cartesian coordinates (Oxy) around z axis by 2π and let $0 \le z \le L$, where L is the length of the impactor; we suppose also that $y(z) \ge zL/R$ The function $y(z)$ has the unknown value $y(0) = y_0$ for $z = 0$ and the fixed value R for $z = L$ (**Figure 1**). Next we cut such body with two planes passing through y axis and crossing the zx plane respectively through $(0,0)$, (L,R) and $(0,0)$, $(L,–R)$. Excluding the two external parts of the body we get a new non-axisymmetric shape called

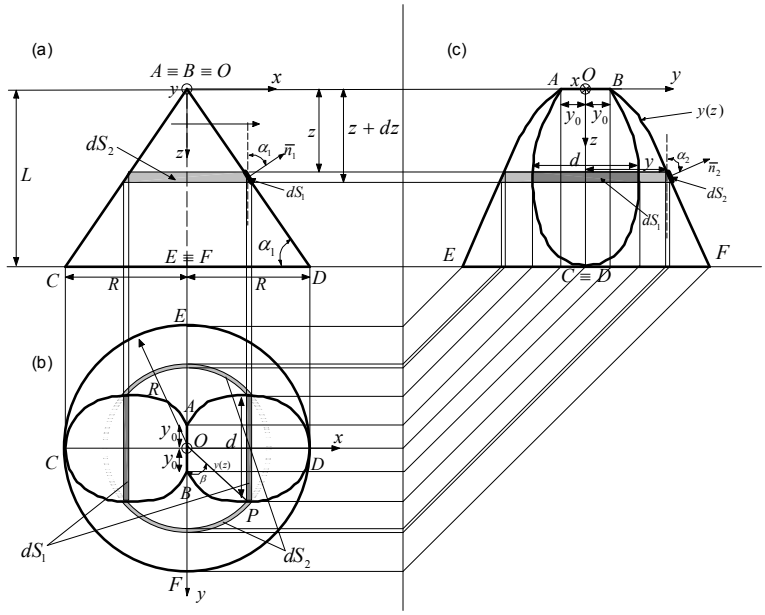

Figure 1. Screwdriver impactor.

"screwdriver shape" or shape of class K_1 (**Figure 1**). In the shape so obtained we can distinguish two distinct surfaces: S_1, corresponding to the plane part, and S_2 corresponding to the curved (remaining) one, that is S = S_1 + S_2.

Using the model of Forrestal and Tzou (1997) and Ben-Dor *et al*. [3] the drag force D of an axisymmetric striker of class K_1 of given length L and final radius R has two different expressions depending on the current penetration length h:

$$D = \begin{cases} \eta h & \text{if } 0 \le h \le 4R \\ \int_S t_z dS & \text{if } h \ge 4R \end{cases} \quad (1)$$

where $\eta > 0$ is an experimental constant; dS is the elementary surface of the impactor and t_z the component along z of the normal stress σ acting on dS (see **Figure 1**). According to Forrestal and Tzou [5], σ is equal to the following parabolic expression

$$\sigma(v) = \sigma_* \left[A_0 + A_1 k v_n + A_2 (k v_n)^2 \right] \ , \ k = \sqrt{\frac{\rho_m}{\sigma_*}} \quad (2)$$

where ρ_m is the density of the shield, σ_* its uniaxial compressive strength and A_0, A_1, A_2 are given positive dimensionless constants shown in **Table 1** (see [5]): The drag force D when $h \ge 4R$ (second stage of penetration), is caused by the force D_1 applied to the plane lateral surface S_1, and D_2, applied to the curved lateral surface S_2 of the impactor; so the total drag force D is expressed by the following formula

Table 1. Coefficients for different models of the shield.

Number of the model	Characteristec of the model	A_0	A_1	A_2
1	Incompressible, elastic-plastic	5.18	0.00	3.88
2	Incompressible, elastic-cracked-plastic	4.05	1.36	3.51
3	Compressible, elastic-plastic	4.50	0.75	1.29
4	Compressible, elastic-cracked-plastic	3.45	1.60	1.12

$$D = D_1 + D_2 \quad (3)$$

Let us consider now a thin strip of impactor realized by cutting it with two planes distant one from the other dz and orthogonal to z axis (see **Figure 1**). The surface dS between such planes is decomposed in two parts: dS_1 (plane part) shown in dark grey and dS_0 (curved part) showed in light grey. The elementary surface dS_1 has the following expression

$$dS_1 = 2d \frac{dz}{\sin(\alpha_1)}$$

where α_1 is the angle between the negative direction of z axis and the outer unit vector $\overline{n_1}$ normal to S_1 and d is the segment shown in **Figure 1(b)** and **(c)**. Taking into account that $\tan(\alpha_1) = R/L = p$ we can write

$$dS_1 = 4\sqrt{1+p^2}\sqrt{y^2 - (pz)^2}\,dz \quad (4)$$

Whereas from **Figure 1 (b)** and **(c)** we have

$$dS_2 = 4\overline{OP}\beta\sqrt{1+y'^2}\,dz$$

where prime denotes derivation with respect to z ; moreover $\overline{OP} = y(z)$ and $\beta = \text{asin}(pz/y)$ so

$$dS_2 = 4y\sqrt{1+y'^2}\,\text{asin}\left(\frac{pz}{y}\right)dz \tag{5}$$

Remembering that only the normal component t_z of σ is responsible for the drag force, we can write

$$D = D_1 + D_2 = \int_{S_1} t_z dS_1 + \int_{S_2} t_z dS_2 \tag{6}$$

but

$$t_z = \begin{cases} \sigma\cos(\alpha_1) = \sigma\dfrac{p}{\sqrt{1+p^2}} & \text{on } S_1 \\ \sigma\cos(\alpha_2) = \sigma\dfrac{y'}{\sqrt{1+y'^2}} & \text{on } S_2 \end{cases} \tag{7}$$

so

$$D = \int_{S_1} t_z dS_1 + \int_{S_2} t_z dS_2 = 4\int_0^L \sigma p\sqrt{y^2-(pz)^2}\,dz + 4\int_0^L \sigma yy'\text{asin}\left(\frac{pz}{y}\right)dz \tag{8}$$

Substituting (2) in (8) we have

$$D = 4\sigma_*\int_0^L (A_0 + A_1 kv_n + A_2(kv_n)^2)p\sqrt{y^2-(pz)^2}\,dz + 4\sigma_*\int_0^L (A_0 + A_1 kv_n + A_2(kv_n)^2)yy'\text{asin}\left(\frac{pz}{y}\right)dz \tag{9}$$

where v_n has the expression

$$v_n = \begin{cases} v\cos(\alpha_1) = v\dfrac{p}{\sqrt{1+p^2}} & \text{on } S_1 \\ v\cos(\alpha_2) = v\dfrac{y'}{\sqrt{1+y'^2}} & \text{on } S_2 \end{cases} \tag{10}$$

Introducing the following dimensionless variables:

$$\tilde{D} = \frac{D}{\pi\sigma_* R^2}\ ,\ \tilde{z} = \frac{z}{L}\ ,\ \tilde{y} = \frac{y}{L}$$
$$\tilde{y}' = y'\ ,\ \tau = \frac{R}{L}\ ,\ V = kv \tag{11}$$

(from now on tilde is omitted)
we get the following quadratic expression for D:

$$D = a_0 + a_1 V + a_2 V^2 \tag{12}$$

where

$$\begin{aligned} a_0 &= A_0(B_0 I_1 + B_1 I_2) \\ a_1 &= A_1(B_0 B_2 I_1 + B_1 I_3) \\ a_2 &= A_2(B_0 B_2^2 I_1 + B_1 I_4) \end{aligned} \tag{13}$$

$$\begin{aligned} B_0 &= \frac{4p}{\pi\tau^2} \\ B_1 &= \frac{4}{\pi\tau^2} \\ B_2 &= \frac{p}{\sqrt{1+p_2}} \end{aligned} \tag{14}$$

$$\begin{aligned} I_1 &= \int_0^1 \sqrt{y^2-(pz)^2}\,dz \\ I_2 &= \int_0^1 \beta yy'dz \\ I_3 &= \int_0^1 \beta\frac{yy'^2}{\sqrt{1+y'^2}}dz \\ I_4 &= \int_0^1 \beta\frac{yy'^3}{1+y'^2}dz \end{aligned} \tag{15}$$

Now applying the equation of motion of the impactor (for details see [3] we find the following expression

$$P = 1 + \omega\int_0^{V^*} \frac{V}{a_0 + a_1 V + a_2 V^2}dV \tag{16}$$

where

$P = \dfrac{DOP}{4R}$ is the dimensionless expression of DOP

$\omega = \dfrac{m}{4R^3\pi k}$ is an dimensionless coefficient

V^* is the adimensional velocity of the impactor for $h = 4R$ found imposing that for $h = 4R$ the expression of the drag force D in the first stage of penetration has the same value of D in the second stage of penetration [3]:

$$V^* = \frac{-a_1 + \sqrt{a_1^2 - 4(a_0-\omega)W^2}\,(a_2+\omega)}{2(a_2+\omega)} \tag{17}$$

where $W = kv_{imp}$ is the dimensionless impact velocity. Of course to get real values of V^* the discriminant in (17) must be nonnegative.

3. Building a Better Solution

In the case of shape of revolution of class K_0 Ben-Dor *et al*. [3] found the solution for a large set of problem parameters and showed that the optimal shape has a flat nose and is concave. Let us now show with an example that using a shape of class K_1 a better solution than that corresponding to class K_0 is obtained. To begin, we consider the following problem parameters: model number: 3(compressible elastic-plastic shield); ω = 14; τ =0.5; W = 3.5. The optimum DOP value for a body of class K_0 is $P = 14.1$ [3]. Using the same problem parameters, let

us now build a shape of class K_1 choosing a generatrix of the form

$$y(z) = az^b + c \tag{18}$$

where $a = 0.491$; $b = 0.38$; $c = 5.616 \times 10^{-3}$ (**Figure 2**).

Now, applying Equations (13)-(17) we found that P = 14.4 > 14.1. This is sufficient to show that class K_1 can give better solutions than class K_0. We note that several theoretical and numerical considerations about screw-driver shapes can be found in [14] and the references given there, although applied to the Newton problem of optimal aerodynamic bodies.

4. Formulation of the Optimum Design

Our task is not only to show that class K_1 can give better solutions than class K_0 as we have seen in the previous section, but also to find the generatrix $y(z)$ for which the corresponding impactor shape belonging to K_1 maximizes DOP:

$$\begin{gathered} DOP = DOP(y) \to \max_y \\ \text{with } y(0) = y_0(\text{free}) \text{ and } y(1) = \tau(\text{fixed}) \end{gathered} \tag{19}$$

We shall show in the following part of the paper one possible strategy of solution.

5. Psoa Algorithm

To solve this problem we will use the method PSOA (Particle Swarm Optimization Algorithm), a recent heuristic suitable for finding global optima solutions. PSOA was introduced about one decade ago [15,16], inspired by the behaviour of school of fish, flocks of birds or swarm of bees observed in nature. Like genetic algorithms (GA) and ant colony optimization methods (ACO), PSOA is also a stochastic, population-based global search algorithm. In a natural swarm each individual or particle changes position toward better places, to reach food or to escape from predators, exchanging information with the neighbourhood and without any central control. In the mathematical model at each individual corresponds a particle i and at every particle i is associated a position vector $\overline{x}_i$ in a n-dimensional space, to which corresponds a certain value of the objective function $f(\overline{x}_i)$ that represents the quality of $\overline{x}_i$; of course $\overline{x}_i$ should be a feasible solution to the problem under study . If some constraints must be considered, the objective function can be modified using the penalty technique. When the algorithm starts, a collection (swarm) of m particles is randomly chosen using a uniform probability distribution. Then the vector position of each particle is updated at every iteration adding a displace

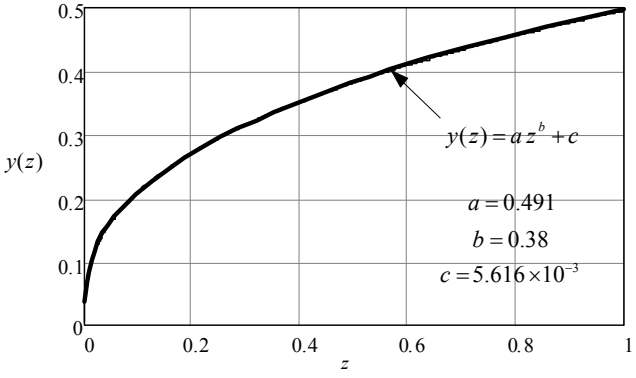

Figure 2. A solution on class K_1.

ment based on the information about the previous swarm positions; the knowledge of the gradient of f is not needed. So the iteration rule is the following

$$\overline{x}_i^{(k+1)} = \overline{x}_i^{(k)} + \overline{s}_i^{(k+1)} \tag{20}$$

where $\overline{x}_i^{(k)}$ and $\overline{x}_i^{(k+1)}$ = positions of particle i at $k-th$ and $k+1$-iteration, $\overline{s}_i^{(k+1)}$ = displacement of particle i at $k+1$-iteration.The formula for $\overline{s}_i^{(k+1)}$ is

$$\overline{s}_i^{(k+1)} = w\overline{s}_i^{(k)} + c_1 r_1(\overline{p}_i - \overline{s}_i^{(k)}) + c_2 r_2(\overline{p}_g - \overline{s}_i^{(k)}) \tag{21}$$

Formula (21) is the core of the algorithm and contains some fundamental information about the neighbourhood of particle *i*: w is called inertia and serves to control the influence of the previous displacement on the new one. Recommended values of w range from 0 to 1.4; $\overline{p}_i$ is the best position found for the particle i to iteration k, whereas $\overline{p}_g$ is the best position inside the swarm up to iteration k; c_1 and c_2 are two positive constants used to balance the cognitive and social aspect: usually $c_1 = c_2 = 2$. r_1 and r_2 are random parameters in the range [0,1], sampled from a uniform distribution. The algorithm stops when a prescribed number of consecutive iterations without improvement in the objective function is reached. From (20) and (21) it is clear that PSOA takes account of the previous random walks of particles. During iterations typically two main problems can arise: the first is the explosion of the swarm: it means that the maximum distance between two particles grows indefinitely and consequently an overflow error occurs; the second is the stagnation of the swarm which means that all the particles occupy the same position, leading to a suboptimal-solution. To try to avoid such inconveniences the two following additional rules are included in the algorithm: the first rule is the limitation of the maximum displacement: $\left|\overline{s}_i^{(k)}\right| \le s_{\max}$ where $s_{\max}$ is a constant which is

problem dependent; the second one is called craziness: with an assigned probability P_{cr} (for example 0.005), the displacement $\overline{s_i}^{(k+1)}$ is not calculated with (21) but completely randomly, with the only condition that its modulus must be $\leq s_{\max}$. The PSOA algorithm preposed has several advantages with respect to classical optimization algorithms: 1) it is able to find the true optimum solution in the entire search space (global optimum); 2) it is easy to implement; 3) it can handle non-differentiable function and no calculation of derivatives is required. The main disadvantage is that it can be quite time-consuming. The PSOA algorithm so far described is only one among many others possible that can be found in the current literature [15,17-19]. For the problem under consideration the swarm is formed by m particles and each particle is a generatrix $y_i(z)$ to which corresponds an impactor shape of class K_1 and a certain value of the objective function f (DOP); each generatrix is approximated by the vector $\overline{y_i}$ where every component of $\overline{y_i}$ is a value of y_i; the z axis has been discretized into n-1 intervals so we have n points in which to calculate the generatrix; as a consequence the vector y_i belongs to an n-dimensional space; because we know in advance that the most critical zone of the impactor shape in near z = 0, the n-1 intervals of z axis are not equals, but shorter near z = 0 and longer as we go toward z = 1. In our calculations n (which corresponds to the swarm size) has been fixed to 30. In **Figure 3** some generatrices of optimum impactors of class K_1 are shown using the following common parameters: Model n.3, τ = 0.5, ω = 14 for different impactor's speed W = 1.0, 2.0, 3.0, 3.5.

In **Table 2** the comparison of DOP of impactors of class K_1 illustrated in **Figure 3**, and the corresponding impactors of class K_0 (surfaces of revolution) with the same problem parameters Model n.3, τ = 0.5, ω = 14, is shown for W = 1.0, 2.0, 3.0, 3.5.

Table 2 shows clearly that the classical and intuitive search space of axisymmetric high speed impactors does not guarantee the best solution (*i.e.* the maximum DOP). In fact in the cases studied show that an impactor shape belonging to a more general class K_1 (non-axisymmetric shape called "screwdriver shape"), can give better results.

6. Concluding Remarks

Starting from the mechanical model proposed by Forrestal et al. and using formulas obtained by Ben-Dor *et al*. for finding the best impactor shape in the class K_0 of axisymmetric bodies, we presented a different shape of impactors in the new class K_1 which is different from the standard axisymmetric shape, and show that bodies belonging to class K_1 can give better results compared to corresponding K_0 bodies. We also finalized a code based on PSOA heuristic algorithm to find the best generatrix in class K_0 once some problem parameters are fixed. Some results are also given in a tabular form. We must emphasize that the class K_1 is not the most general class of impactors we can imagine so the problem of the best impactor remains open.

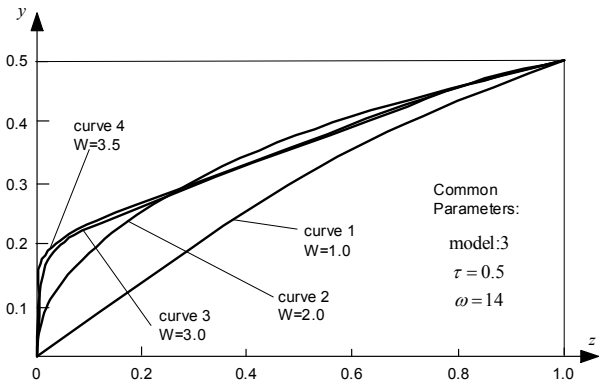

Figure 3. Some generatrices of optimum impactors.

Table 2. Comparison of DOP of impactors.

DOP of impactors of class class K_1 with the following common parameters: Model n.3, τ = 0.5, ω = 14		Corresponding DOP of impactors of class K_0 using the same parameters: Model n.3, τ = 0.5, ω = 14	
Impaactor's speed	DOP of impactor of class K_1	Impactor's speed	DOP of impactor of class K_0
W = 1.0 (curve 1 on figure.3)	2.0	W = 1.0	2.0
W = 2.0 (curve 2 on figure.3)	6.0	W = 2.0	5.8
W = 3.0 (curve 3 on figure.3)	11.6	W = 3.0	11.2
W = 3.5 (curve 4 on figure.3)	14.7	W = 3.5	14.1

7. References

[1] G. Ben-Dor, A. Dubinsky and T. Elperin, "Numerical Solutions for Shape Optimization of an Impactor Penetrating into a Semi-infinite Target," *Computers and Structures*, Vol. 81, No. 1, 2003, pp. 9-14.

[2] G. Ben-Dor, A. Dubinsky and T. Elperin, "Shape Optimization of an Impactor Penetrating into a Concrete or a Limestone Target," *International Journal of Solids and Structures*, Vol. 40, No. 17, 2003, pp. 4487-4500.

[3] G. Ben-Dor, A. Dubinsky and T. Elperin, "Modeling of High-speed Penetration into Concrete Shields and Shape Optimization of Impactors," *Mechanics Based Design of Structures and Machines*, Vol. 34, No. 2, 2006, pp. 139-156.

[4] N. V. Banichuk, V. M. Petrov and F. L. Chernousko, "The Method of Local Variations for Variational Prob-

lems Involving Non-additive Functionals," *USSR Computational Mathematics and Mathematical Physics*, Vol. 9, No. 3, 1969, pp. 66-76.

[5] M. J. Forrestal and D. Y. Tzou, "A Spherical Cavity-expansion Penetration Model for Concrete Targets," *International Journal of Solids and Structures*, Vol. 34, No. 31-32, 1997, pp. 4127-4146.

[6] M. J. Forrestal, B. S. Altman, J. D. Cargile and S. J. Hanchak, "An Empirical Equation for Penetration Depth of Ogive-nose Projectiles into Concrete Targets," *International Journal of Impact Engineering*, Vol. 15, No. 4, 1994, pp. 396-405.

[7] M. J. Forrestal, D. J. Frew, S. J. Hanchak and S. Brar, "Penetration of Grout and Concrete Targets with Ogive-nose Steel Projectiles," *International Journal of Impact Engineering*, Vol. 18, No. 5, 1996, pp. 465-476.

[8] G. Ben-Dor, A. Dubinsky and T. Elperin, "Applied High-speed Plate Penetration Dynamics," Springer, Berlin, 2006.

[9] A. I. Bunimovich and G. E. Yakunina, "On the Shape of Minimum-resistance Solids of Revolution Moving in Plastically Compressible and Elastic-Plastic Media," *Journal of Applied Mathematics and Mechanics*, Vol. 51, No. 2, 1987, pp. 386-392.

[10] N. A. Ostapenko and G. E. Yakunina, "The Shape of Slender Three Dimensional Bodies with Maximum Depth of Penetration into Dense Media," *Journal of Applied Mathematics and Mechanics*, Vol. 63, 1999, pp. 953-967.

[11] G. E. Yakunina, "On Body Shapes Providing Maximum Penetration Depth in Dense Media," *Doklady Physics*, Vol. 46, No. 2, 2001, pp. 140-143.

[12] G. E. Yakunina, "On the Optimal Shapes of Bodies Moving in Dense Media," *Doklady Physics*, Vol. 50, No. 12, 2005, pp. 650-654.

[13] N. V. Banichuk and S. Y. Ivanova, "Shape Optimization of Rigid 3-D High-speed Impactor Penetrating into Concrete Shields," *Mechanics Based Design of Structures and Machines*, Vol. 36, 2008, pp. 249-259.

[14] D. Bucur and G. Buttazzo, "Variational Methods in Shape Optimization Problems," Birkhauser, Boston, 2005.

[15] R. C. Eberhart and J. Kennedy, "A New Optimizer Using Particle Swarm Theory," *Proceedings of the 6th International Symposium on Micromachine and Human Science*, Nagoya, 1995, pp. 39-43.

[16] J. Kennedy and R. C. Eberhart, "Particle Swarm Optimization," *Proceedings of the IEEE International Joint Conference on Neural Networks*, Perth, 1995, pp. 1942-1948.

[17] M. Clerc, "Particle Swarm Optimization," ISTE, London, 2006.

[18] M. M. Ali and P. Kaelo, "Improved Particle Swarm Algorithms for Global Optimization," *Applied Mathematics and Computation*, Vol. 196, 2008, pp. 578-593.

[19] P. C. Fourie and A. A. Groenwold, "The Particle Swarm Optimization Algorithm in Size and Shape Optimization," *Structural and Multidisciplinary Optimization*, Vol. 23, No. 4, 2002, pp. 259-267.

[20] A. P. Engelbrecht, "Fundamentals of Computational Swarm Intelligence," Wiley, Chichester, 2005.

Engineering, 2010, 2, 263-269
doi:10.4236/eng.2010.24036 Published Online April 2010 (http://www.SciRP.org/journal/eng)

Electrical Performance Study of a Large Area Multicrystalline Silicon Solar Cell Using a Current Shunt and a Micropotentiometer

Hala Mohamed Abdel Mageed[1], Ahmed Faheem Zobaa[2], Ahmed Ghitas[3], Mohamed Helmy Abdel Raouf[1], Mohamed Sabry[3], Abla Hosni Abd El-Rahman[1], Mohamed Mamdouh Abdel Aziz[4]
[1]*National Institute for Standards*, *Giza*, *Egypt*
[2]*University of Exeter*, *Exeter*, *UK*
[3]*National Research Institute of Astronomy and Geophysics*, *Helwan*, *Egypt*
[4]*Cairo University*, *Cairo*, *Egypt*
E-mail:{*halaabdelmegeed*, *mohammed_makka*}*@yahoo.com*, *aghitas@hotmail.com*, *mohamed.ma.sabry@gmail.com*
Received November 30, 2009; *revised February* 12, 2010; *accepted February* 19, 2010

Abstract

In this paper, a new technique using a Current Shunt and a Micropotentiometer has been used to study the electrical performance of a large area multicrystalline silicon solar cell at outdoor conditions. The electrical performance is mainly described by measuring both cell short circuit current and open circuit voltage. The measurements of this cell by using multimeters suffer from some problems because the cell has high current intensity with low output voltage. So, the solar cell short circuit current values are obtained by measuring the voltage developed across a known resistance Current Shunt. Samples of the obtained current values are accurately calibrated by using a Micropotentiometer (μpot) thermal element (TE) to validate this new measuring technique. Moreover, the solar cell open circuit voltage has been measured. Besides, the cell output power has been calculated and can be correlated with the measured incident radiation.

Keywords: Large Area Multicrystalline Silicon Solar Cell; Current Measurements; Calibration; Current Shunt; Micropotentiometer; Short Circuit Current; Open Circuit Voltage

1. Introduction

There are many types of the solar cells that are used in different life applications. The main important types of the solar cells are manufactured by some back-contact techniques [1-3]. Back-contact solar cells have some advantages over ordinary solar cells due to their lower cost and their higher efficiency [4,5]. Moreover, characteristics of these back-contact solar cells are studied to enhance their performance [6,7].

Short circuit current and open circuit voltage are two main electrical parameters usually used to characterise solar cells. Typically, these quantities are measured by multimeters. During the solar cell current measurements some troubles appeared, because the solar cell under test produces high current intensity with low output voltage. So, the multimeters are not suitable for the solar cell output current measurements [8]. In that study, a Hall sensor technique is applied in order to overcome the problem of the effect of multimeters internal resistance in these measurements. However, the Hall sensor has some limitations and precautions; such as the dependence of its performance on operating ambient temperature, the quality and stability of the supply voltage and the linearity limitations through a specified current range [8]. It is also very sensitive to external magnetic fields and its offset is not stable and may vary with temperature and time [9].

Current sensors play a vital role in our life. At present, comprehensive research concerned current sensing technology has been conducted, including current shunts [10]. They are used in many applications to measure current by measuring the voltage developed across known impedance [11].

In this paper, a current shunt is simply used as a sensor to get the solar cell current values by measuring the voltage developed across its known resistance. Hence, a new technique using Holt HCS-1 current shunt is applied to get the short circuit currents of a multicrystalline silicon solar cell with back contact technology. Then, accurate calibra-

tions are carried out using a μpot thermal element to get the actual precise values of the measured currents.

A comparison between computed versus experimentally corrected and calibrated values of the cell short circuit currents is carried out; hence, the new current measurement system is confirmed and verified. This study is extended to measure the cell open circuit voltage; then, the cell output power is computed to be correlated with the incident radiation profile. All results are carefully studied through some representing mathematical curves.

2. Solar Cell Under Test

The multicrystalline silicon solar cell with back contact technology is shown in **Figure 1.** It has a large area of 21 cm × 21 cm. The module was installed in a tilted position at the optimum tilt angle of the location of study [12], in the outdoor. The cell current is collected by the fine finger grid which is led to the back side through 25 holes. On the back side there are 25 soldering pads for each polarity.

The outdoor cell electrical performance is studied by measuring both short circuit current and open circuit voltage in the tilted position at Helwan, Egypt.

3. Measurements and Calibrations

Measurement is a set of operations performed on a physical object or system according to an established documented procedure, for determining some physical property of the object or system. Science and technology progress is based on the development of measurements. Calibration is achieved by comparing a measurement device (unknown) against an equal or better standard.

3.1. Current Shunt Characteristics

In order to measure current with high accuracy, a current shunt is commonly used. Four-terminal resistors' current shunts are in wide use in the metrology community and in industrial measurement applications. Such applications include the measurement of DC, and AC electric currents [13].

They are commonly used in high current low voltage applications. Shunts often have low resistance value and low temperature coefficient of resistance and use Kelvin terminals for improving measurement accuracy [10]. They are the most cost effective sensing elements, having compact package profiles, suitable for DC or AC measurement. These shunts have as their major design goals adequate power dissipation and minimal resistance changes with temperature. Also considerations are taken to minimize thermoelectric errors of the 4-terminal resistance [13].

Special resistance alloys, such as Constantan, Manganin, and Zeranin, have been formulated to have very small temperature coefficients of resistance to combat the rise of temperature in shunts [14].

Figure 1. Multicrystalline silicon solar cell in the outdoor located at optimum tilt angle with the radiation sensor.

One feature of the current shunts is that it converts the applied current to voltage drop across its terminals in a linear manner [13].

3.2. Solar Cell Current Measurements Using a Current Shunt Linearity Curve

The cell current measurements are obtained by using a data logger and a current shunt linearity curve. Then a μpot thermal element is used to get the actual calibrated current values accurately.

Different current shunt products, like Fluke Model (A40, A40A, A40B) and Holt Model HCS-1 current shunts are used to simplify the task of making precise current measurements in the laboratory.

For this task, Holt HCS-1 current shunt 20 Ampere range shown in **Figure 2**, is used to measure the cell short circuit current (ISC). It is of a coaxial design; the resistor being a web of wire arranged coaxially about the axis of the shunt. The input terminal is a female UHF connector at one end, and the potential terminal is a male UHF at the other [15].

This device is used to obtain the equivalent voltage drop across its resistance structure when the short circuit current is applied. Then, this equivalent voltage is applied to a 14 bit data logger, which is in turn connected to a PC to compute the corresponding current using the shunt linearity curve. **Figure 3** illustrates the linearity curve of the 20A HCS-1 current shunt, which shows that its output voltage is linearly proportional to its input current.

The linearity equation that relates the input current to the output voltage is:

$$V_{out} = 0.0518 \times I_{in} + 5 \times 10^{-5} \quad (1)$$

Where V_{out} is the output voltage drop across the

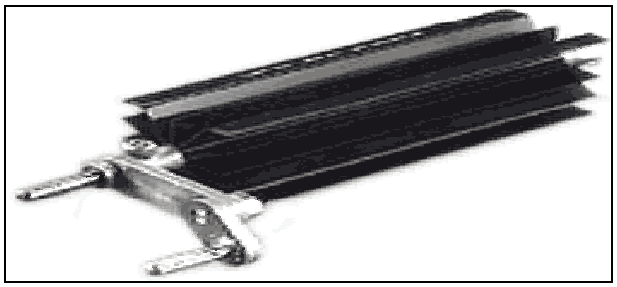

Figure 2. Holt HCS-1 current shunt with 20 A range.

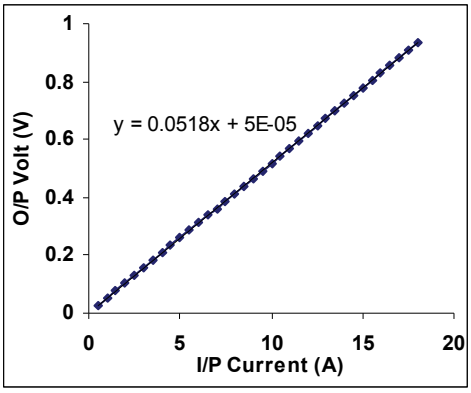

Figure 3. Linearity curve of the 20A HCS-1 current shunt.

current shunt resulted from applying input current source I_{in}.

The cell short circuit current (I_{SC}) can be computed by using the previously estimated linearity equation with the voltage drop across the shunt element V_{out} as an input to the equation. Computed daily profile of the solar cell short circuit current I_{SC} is depicted in **Figure 4**.

This current curve is obtained in terms of the shunt voltage signals transferred to the PC through a 14 Bit data logger. These voltage signals are accurately measured to get the actual voltage values experimentally, which are used to obtain the corresponding actual current values using the µpot thermal element.

Practically, samples of the voltages, which present the short circuit currents of the cell, is measured experimentally by using a precise digital multimeter (Fluke 8508A-DMM) to get their actual calibrated values accurately.

Table 1 illustrates the voltage results obtained from data logger and the actual calibrated results which measured at the same time by using the DMM.

Figure 5 shows the two voltage patterns, one of them is for the data logger voltages and the other is for the actual calibrated voltages with respect to the calculated short circuit currents obtained from the current shunt linearity equation.

The actual values of the cell short circuit currents can be obtained accurately by calibrating them by using a µpot thermal element and the calibrated voltages. Therefore, the computed current values obtained in **Figure 5**, are calibrated by the actual current values that obtained by using the µpot thermal element.

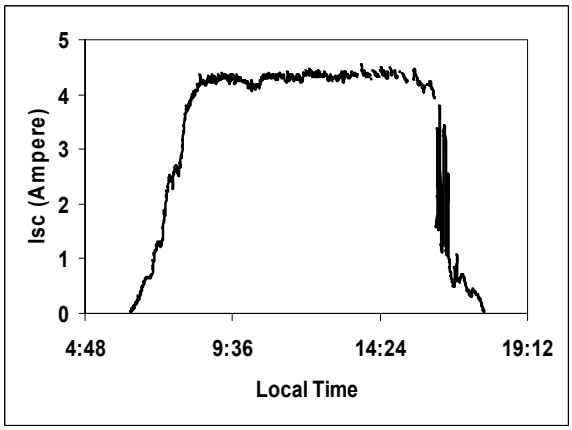

Figure 4. Computed cell short circuit current.

Table 1. Actual calibrated and data logger voltages.

Actual Calibrated Voltage (V)	Data Logger (V)
0.03300	0.02905
0.09720	0.09253
0.12320	0.11645
0.15940	0.15310
0.16000	0.15601
0.16130	0.16060
0.18645	0.18042
0.18745	0.18240
0.18845	0.18280
0.21845	0.21069
0.21940	0.21480
0.22550	0.21655
0.22850	0.22168
0.23655	0.22973
0.23745	0.23730
0.24445	0.23802

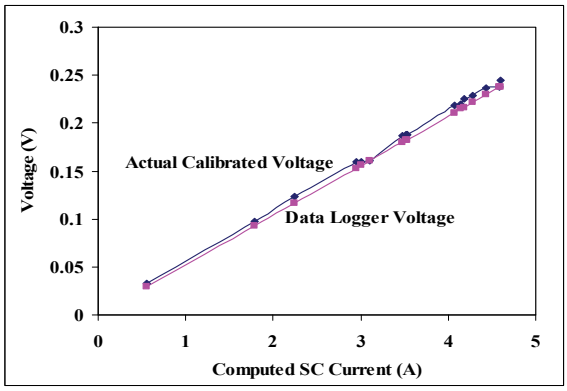

Figure 5. Data logger voltages and calibrated voltages used to obtain I_{SC}.

3.3.Solar Cell Current Calibration Using a µpot thermal element

The schematic diagram of the µpot which consists of a thermal element in series with a non reactive radial resistor is shown in **Figure 6**. The radial resistor is securely soldered into the output N-type coaxial connector and screwed into the µpot case. It has two outputs, one for the output thermal electromotive force (e.m.f), and the other for the output voltage where as in National Metrology Institutes µPots are basically voltage sources [16].

The µpot with single-range output resistor can be connected as a µpot, as a thermal voltage converter (TVC), or as a thermal current converter (TCC) when attached with a current shunt as demonstrated in **Figure 7**. Actually, this flexibility broadens the range of useful applications of this device because its rated current is almost 5 mA.

The core of the µpot is the thermal element that is shown in **Figure 8**. It consists of a thin filament-heater and a thermocouple inserted in an evacuated glass bulb. The thermocouple thermally contacts the heater at its midpoint using a bead made of electrically insulating material such as glass or ceramics [17].

The basic measurement principle of the thermal element is based on converting the electrical signal to a heat power. In such converters, energy dissipated by a current flowing through a heater resistor, raising its temperature above the ambient, is compared to the energy dissipated by the voltage flowing through the same heater.

The increase in the temperature of the heater at voltage and current, proportional to the dissipated energy, is measured using a thermocouple. Therefore, when voltage or current is applied to the input of a thermal element it gives e.m.f. At the same output e.m.f.s for both of the two inputs, we can say that this applied input current is corresponding to the applied input voltage.

Accordingly, the actual values of the voltages corresponding to the cell short circuit currents that listed in **Table 1** are applied to the µpot thermal element by using the Wavetek 9100-Calibrator. It is used in the voltage mode as a traceable standard DC source. Then, the thermal element output e.m.f.s are measured by using a precise digital multimeter (Fluke 8508A-DMM) as shown in **Figure 9**.

In the second step, the current is applied from the same calibrator, but in the current mode, to the µpot thermal element through the 20 A current shunt to attain the same output e.m.f.s obtained in the first step as demonstrated in **Figure 10**.

Therefore, these currents represent the actual calibrated values of the corrected short circuit currents of the solar cell as listed in **Table 2**.

The actual calibrated short circuit currents, the corre-

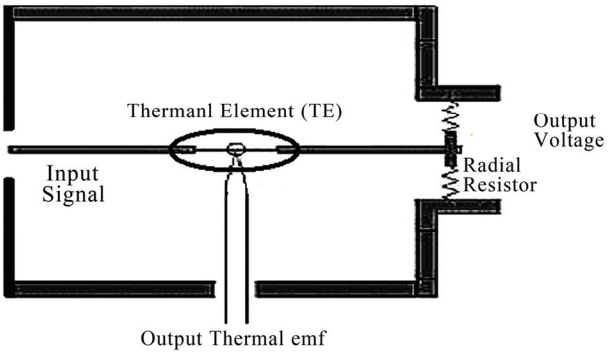

Figure 6. A Simple construction of the µ pot.

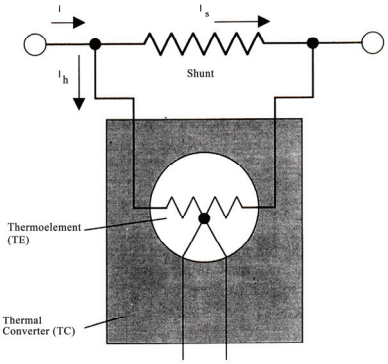

Figure 7. Thermal current converter (TCC) attached with a current shunt.

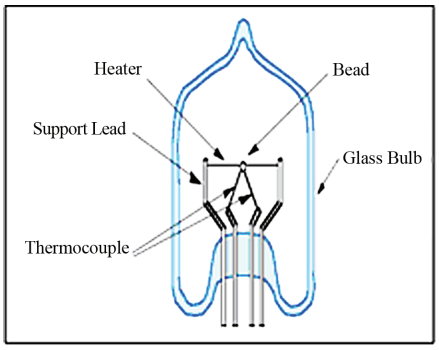

Figure 8. Structure of a Thermal Element (TE).

Figure 9. Measurements of the thermal element output emfs for the voltages corresponding to the I_{SC}.

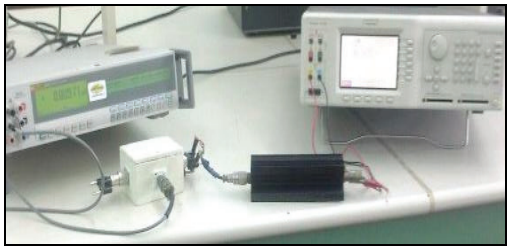

Figure 10. Calibration System of the Short Circuit Current.

Table 2. Actual calibrated short circuit currents against actual calibrated equivalent voltages of the shunt at the same output e.m.f.s.

Actual calibrated Voltage (V)	O/P emf (mV)	Actual calibrated Current (A)
0.03300	0.01778	0.54810
0.09720	0.09492	1.83410
0.12320	0.14780	2.33680
0.15940	0.24196	3.03520
0.16000	0.24360	3.04660
0.16130	0.24705	3.07040
0.18645	0.32716	3.55440
0.18745	0.33570	3.57420
0.18845	0.33390	3.59380
0.21845	0.44532	4.17147
0.21940	0.44897	4.18907
0.22550	0.47372	4.30827
0.22850	0.48601	4.36527
0.23655	0.51979	4.51737
0.23745	0.52342	4.53517
0.24445	0.55364	4.66757

sponding computed short circuit currents (obtained from data logger and current shunt linearity equation) and the computed relative error between them in percentage are recorded in **Table 3** and are illustrated in **Figure 11**.

The percentage errors between actual and computed short circuit currents don't exceed 0.04% which means that the computed results of the short circuit current are closed to the actual calibrated results.

The consistency between the actual and the computed current curves is clearly demonstrated in **Figure 11**. Therefore, the system that consists of the current shunt and the data logger is accurate, precise and reliable in the solar cell current measurements, especially at such high currents with low voltages.

4. Accurately Measured Solar Cell Electrical Output

The cell open circuit voltage signals are received by the data logger to be transferred to the PC through the prepared computer program. After the previously discussed measurement calibration techniques, accurate solar cell output power could be obtained. A daily variation of

Table 3. The actual calibrated short circuit currents and the corresponding computed short circuit currents of the cell.

Actual calibrated Short Circuit Currents (A)	Computed Short Circuit Currents (A)	Relative Error (%)
0.54810	0.55985	- 0.02143
1.83410	1.78533	0.02659
2.33680	2.24710	0.03838
3.03520	2.95463	0.02654
3.04660	3.01081	0.01175
3.07040	3.09942	- 0.00945
3.55440	3.48205	0.02035
3.57420	3.52027	0.01509
3.59380	3.52799	0.01831
4.17147	4.06641	0.02518
4.18907	4.14575	0.01034
4.30827	4.17954	0.02988
4.36527	4.27857	0.01986
4.51737	4.43397	0.01846
4.53517	4.58011	- 0.00991
4.66757	4.59415	0.01572

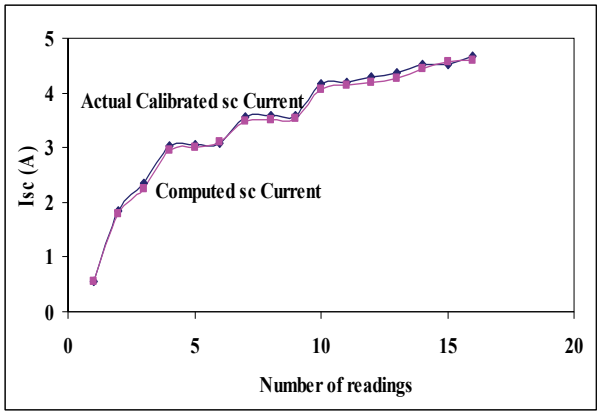

Figure 11. Actual calibrated and computed short circuit currents I_{SC}.

large area 21 cm × 21 cm multicrystalline silicon solar cell short circuit current, open circuit voltage and power are plotted in **Figure 12**.

As seen in this figure, the maximum open circuit voltage value is nearly 0.5V, while the maximum short circuit current at the same time is nearly 4.6A. This is the main distinguishing property of this solar cell.

Figure 13 shows the cell electrical output power along with the solar radiation intensity incident on its surface in case of the optimum tilted orientation. The data has been recorded in 8th March 2009 which corresponds to a tilted angle 30^{o}.

The incident radiation is recorded by using CMP3 Kipp&Zonen, which is also connected to the data logger after signal amplification.

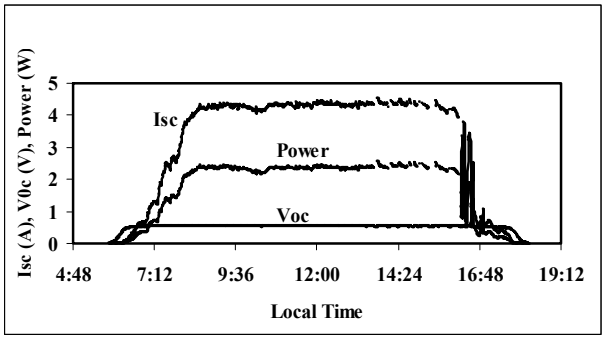

Figure 12. Daily variation of I_{SC}, V_{OC} and Power of the solar cell.

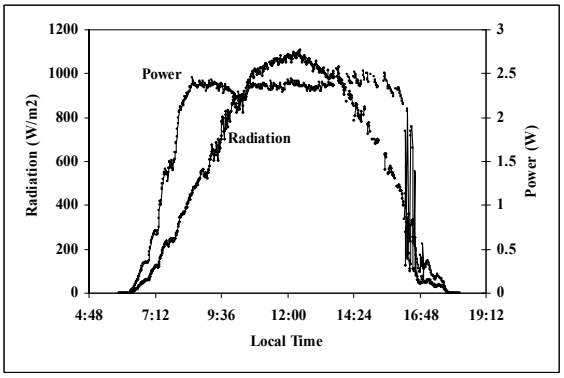

Figure 13. Daily variation of the incident solar radiation against the solar cell output power.

5. Conclusions

A new current measurement technique of a back contact large area multicrystalline silicon solar cell in outdoor conditions is introduced. The 20 Ampere, Holt HCS-1 current shunt is used for this aim to avoid the other measuring techniques' problems. It represents accurate, easy, cheap, and reliable way to get high current values at low voltages. The concept of this current shunts; is obtaining the current values by using the corresponding measured voltages developed across its known resistance.

In order to validate this new current measuring technique, samples of short circuit current values are accurately obtained and practically calibrated to get their actual precise values by using a μpot thermal element. A comparison between the accurate calibrated short circuit current results and the computed results demonstrates an excellent agreement between them to about 0.04% relative error. Then the cell electrical output power could be computed easily.

5. References

[1] W. Jooss, K. Blaschek, R. Toelle, T.M. Bruton, P. Fath and E. Bucher, "17% Back Contact Buried Contact Solar Cells," *Proceedings of the* 16*th EPVSC*, Glasgow, 2000, pp. 1124-1127.

[2] D.L. Meier, H. P. Dabis, A. Shibata, T. Abe, K. Kinoshita, C. Bishop, S. Mahajan, A. Rohatgi, P. Doshi and M. Finnegan, "Self Doping Contacts and Associated Solar Cell Structures," *Proceedings of the* 2*nd WCPSEC*, Vienna, 1998, pp. 1491-1494.

[3] K. Faika, M. Wagner, P. Fath and E. Bucher, "Simplification of EWT (Emitter-wrap Through) Solar Cell Fabrication Using Al-P-Codiffusion," *Proceedings of the* 28*th IEEE PVSC*, Anchorage, 2000, pp. 176-179.

[4] A. Kress, P. Fath, G. Willeke and E. Bucher, "Low-cost Back Contact Silicon Solar Cells Applying the Emitter-wrap Through (EWT) Concept," *Proceedings of the* 2*nd WCPSEC*, Vienna, 1998, pp. 1547-1550.

[5] W. Neu, A. Kress, W. Jooss, P. Fath and E. Bucher, "Low-cost Multicrystalline Back-contact Silicon Solar Cells with Screen Printed Metallization," *Solar Energy Materials & Solar Cells*, 2002, pp. 139-146.

[6] J. H. Bultman, A. W. Weeber, M. W. Brieko, J. Hoonstra, J. A. Dijkstra, A. C. Tip and F. M. Schuurmans, "Pin Up Module: A Design for Higher Efficiency, Easy Module Fabrication and Attractive Appearance," *Proceedings of the* 16*th EPVSC*, Glasgow, 2000, pp. 1210-1213.

[7] A. Schonecker, A. Weeber, W. Sinke, C. Zechner, A. Kress and P. Fath, "Attacking Limiting Factors in 10 × 10 cm^2 Multicrystalline Silicon, Emitter Wrap-through Solar Cell Design and Processing," *Proceedings of the* 2*nd WCPSEC*, Vienna, 1998, pp. 1677-1680.

[8] A. Ghitas and M. Sabry, "Performance of a Large Area Back Contact Silicon Solar Cell in a Desert Zone," *Proceedings of the Cairo* 11*th International Conference on Energy and Environment*, Hurghada, 2009.

[9] J. Trontelj, "Optimization of Integrated Magnetic Sensor by Mixed Signal Processing," *Proceedings of the* 16*th IEEE Instrumentation and Measurement Technology Conference*, Vol. 1, 1999, pp. 299-302.

[10] C. C. Xiao, L. Y. Zhao, T. Asada, W. G. Odendaal and J. D. van Wyk, "An Overview of Integratable Current Sensor Technologies," *IEEE Industry Application Conference*, Vol. 2, 2003, pp. 1251- 1258.

[11] R. G. Jones, P. Clarkson and A. J. Wheaton, "Calibration of Ac Current Shunts," *Precision Electromagnetic Measurements Digest Conference*, Sydney, 2000, pp. 492-493.

[12] H. K. Elminir, A. E. Ghitas, F. El-Hussainy, R. Hamid, M. M. Beheary and K. M. Abdel-Moneim, "Optimum Solar Flat-plate Collector Slope: Case Study for Helwan, Egypt," *Energy Conversion & Management*, Vol. 47, 2006, pp. 624-637.

[13] D. E. Destefan, R. S. Stant, "AC and DC Shunts—Can You Believe Their Specs?" *IEEE Instrumentation and Measurement Technology Conference*, Vol. 2, 2003, pp. 1577-1582.

[14] M. Handbook, "Stainless Steel Materials and Special Purpose Metals," 9th Edition, American Society for Metals, Detroit, pp. 640-645.

[15] T. E. Lipe, "Operation and Reference Manual for the NIST Automated AC-DC Calibration Systems and Software," National Institute of Standards and Technology Special Publication, May 2004.

[16] M. Klonz, G. Schliestedt, T. Funck, M. Stojanovic and B. Stojanovic, "Millivolt Calibrations Using Micropotentiometers with New Disc Resistors and Planar MJTCS Aided by New Millivolt Amplifiers," *IEEE Transactions on Instrumentation and Measurement*, Vol. 54, No. 2, April 2005, pp.787-790.

[17] H. Sasaki, K. Takahashi, B. D. Inglis and M. Klonz, "A Numerical Simulation of Thermoelectric Effects in Single-Junction Thermal Converters," *IEEE Transactions on Instrumentation and Measurement*, Vol. 48, No. 2, April 1999, pp. 408-411.

Engineering, 2010, 2, 270-289
doi:10.4236/eng.2010.24037 Published Online April 2010 (http://www.SciRP.org/journal/eng)

A Framework for Intelligent Decision Support System for Traffic Congestion Management System

Mohamad K. Hasan
Department of Quantitative Methods and Information Systems, *College of Business Administration*, *Kuwait University*, *Kuwait City*, *Kuwait*
E-mail: *mkamal@cba.edu.kw*
Received November 18, 2009; *revised January* 22, 2010; *accepted* February 4, 2010

Abstract

Traffic congestion problem is one of the major problems that face many transportation decision makers for urban areas. The problem has many impacts on social, economical and development aspects of urban areas. Hence the solution to this problem is not straight forward. It requires a lot of effort, expertise, time and cost that sometime are not available. Most of the existing transportation planning software, specially the most advanced ones, requires personnel with lots practical transportation planning experience and with high level of education and training. In this paper we propose a comprehensive framework for an Intelligent Decision Support System (IDSS) for Traffic Congestion Management System that utilizes a state of the art transportation network equilibrium modeling and providing an easy to use GIS-based interaction environment. The developed IDSS reduces the dependability on the expertise and level of education of the transportation planners, transportation engineers, or any transportation decision makers.

Keywords: Traffic Congestion Management System; Transportation System Management; Intelligent Decision Support System; Urban Transportation Systems Analysis; Multiclass Simultaneous Transportation Equilibrium Models; Intelligent Scenario Creation Assistance Agent

1. Introduction

Over the last few decades the dimensions of the transportation system and the interaction between these dimensions and the socioeconomic system, have increased by many folds. And despite the fact that significant advancements have occurred in Information and Communication Technologies (ICT)-based transportation systems and many network equilibrium models have been developed, comprehending this dynamic environment, identifying its critical issues, and responding to them by selecting the right alternative at the right time is still an immensely demanding and difficult task to accomplish even for well trained and experienced transportation expertise.

Urban transport problem can be understood in relation to land use and other socio-economic activities which the transportation network serves. A relationship exists between trip frequencies and socioeconomic characterristics of trip makers and the purpose for which the trip is made (such as journey to work, to school, to shopping, to social activities, etc. Each of these types of trips is spatially distributed over the city between the residential areas and places of interest and activities. Trip purposes, also influence the volume of trip generation in various land use in the city [1]. This is because the volume of journeys made from origin to destination is functionally related to the ability of respective areas to generate or attract movement. Reasons such as inadequate transport infrastructure, rapid increase in urban population, income and automobile ownership etc., had been noted to contribute to traffic congestion in many of the urban areas [2]. Traffic congestion is a critical problem in urban areas. It is not always fruitful to expand the transportation systems, if the demand is not satisfactorily met by the existing capacity. As such it is prudent to optimize the use of existing transportation system by certain management techniques.

Gazis [3] proposed a way to control closely spaced and oversaturated intersections. Gordon [4] suggested that an intersection control scheme should be aimed at controlling the relative queue lengths on the phases. Longley [5] identified two types of congestion and proposed a signal control and queue management procedure that aims at reducing secondary congestion. Pignataro *et al.* [6] described a queue management procedure. Gart-

ner *et al.* [7] presented a procedure with multi-level design for real time, traffic-adaptive control. Other work on queue management appeared in the literature [8-10]. Reddy *et al.* [11], Reddy [12], described the Transportation System Management (TSM) actions to improve vehicular movements with the help of a case study. Thomson [13] described the traffic management problem faced by highly urbanized cities of developing world due to the rapid urbanization relating to traffic congestion. This effort at reducing traffic congestion without providing for more road capacity is expected to shift the trip pattern of motorists in various ways, notably to redistribute trips spatially, temporarily, and modally. Other studies on urban traffic management emanating from non commissioned studies include that of Adefolalu [14], on traffic congestion in the city of Lagos; Oyefesobi [15] on accident reduction: Orioke [16], on traffic education: Ogunbondede [1], on the contribution of land use to traffic congestion.

These above studies show that traffic congestion problem is a common phenomenon in urban and part of TSM actions to improve the existing transportation system for the better serviceability and efficiency by taking various measures. Transportation Systems Management (TSM) measures, originally conceived as a tool applicable on a region-wide scale, can be successfully applied at major activity centers to avoid, minimize or postpone the need for more capital-intensive transportation improvements [17]. A transportation management system (TSM) is intended to provide information on transportation system performance and identify alternative actions to alleviate congested roadway conditions. Although a TSM can use data obtained from a traffic operation surveillance and control system, in general a TSM is considered to be more a planning tool than an operations tool [18].

The main objectives of TSM actions are to coordinate all individual elements of transportation systems through operating, regulatory and control policies, so as to achieve the maximum efficiency and productivity and minimize environmental pollution and energy consumption. TSM actions, whether applied on a corridor or at city network level, aim at maximizing the expected output of the transportation systems as whole and achieve the specific objectives [11].

TSM actions include:

- Assuring the safety and the efficiency flow of passenger vehicles and trucks along urban and rural transportation networks [19].
- Choosing the most efficient improving alternatives solutions of the existing transportation system problem at a minimum cost [19].
- Increasing the transit system ridership by increasing the frequency of buses or trains, reducing the fair, and assuring scheduling time accuracy.
- Minimizing the air pollution, noisy, and all others undesirable environmental impacts of the existing transportation system [19]
- Banning of particular class of vehicles at certain times/certain areas.
- Auto free zones where vehicles are totally prohibited.
- Special bus lanes and streets where spaces are reserved for public buses and emergency vehicles and other improvements of facilities for buses viz. bus bays and bus stops.
- Fiscal measures like parking fee, road pricing and supplementary licensing etc. which in turn make the less vehicle usage.
- Parking Control
- Staggering of office hours
- Car pooling
- Travel Bonus
- Controlled Entry
- Banned turns
- Geometric improvements
- Improvements for slow moving traffic
- Improvements to pedestrian facilities
- Improvements in intersection circulation
- Synchronization and redesign of signals

Detailed benefits of the TSM Program can be found in [19].

To evolve TSM action plan for the selected corridor there is a need to understand and analyze the characteristics of traffic flow as well as existing transit system, land use development which generates the traffic on this corridor and their ill effects.

To integrate the entire above feature of TSM, we first defined Congestion Management System (CMS) and Intelligent Decision Support System (IDSS).

A Congestion Management System (CMS) is a systematic process of monitoring, measuring, and diagnosing the causes of current and future congestion in major travel corridors [20]; performing a detailed evaluation analysis and recommendations for different alternatives solutions strategies that can be implemented to improve management of current and future congestion [20]; and monitoring and evaluating the performance of strategies that have been implemented to manage or mitigate congestion [21]. US Federal transportation legislation requires Metropolitan Planning Organizations (MPO) to develop and implement a CMS as part of the metropolitan transportation planning process [22]. The CMS provides a consistent basis to make transportation investment decisions and ensures that travel demand management (TDM) and transportation system management (TSM) measures are considered prior to roadway capacity expansion, in accordance with goals and objectives established by any Metropolitan Planning Organization [20]. The MPO is a transportation policy-making organization made up of representatives from local government and transportation authorities.

The dynamic and complex nature of transportation en-

vironment, the complexity of the current transportation system and difficulty to comprehend the network equilibrium models and the limited availability of transportation expertise together created an extremely hard environment to deal with efficiently and effectively. However, the advancement and availability of intelligent agent-based technologies and solutions for integration within a comprehensive transportation system analysis framework, as a Traffic Congestion Management System (TCMS), provide promising solutions.

Ossowski *et al.* [23] summarized good literatures about the Decision Support Systems that include previous works of French [24], Silver [25], Klein and Methlie [26], Hernandez and Serrano [27], Hernandez and Serrano [28], Vlahavas *et al.* [29], Cuena and Ossowski [30], Ossowski *et al.* [31], Iglesias *et al.* [32], and Hoa Dam and Winikoff [33].

More details about the decision support system fundamentals and the classification of decision support systems can be found in Holsapple [34].

Recently, Zhang [35] addressed the requirements for an open and standardized environment for integrating various DSSs. He also addressed the emergence of intelligent agent technology to fulfill the requirements of developing innovative and efficient DSS applications. In his thesis he gave detailed illustrations of the intelligent agents in offering various advantages, such as mobility, flexibility, intelligence, etc., to overcome the major problems in existing DSSs.

Creating an intelligent agent-based DSS for TCMS that would enable and assist the transportation system users (operators) to identify critical transportation problem issues and to respond to them by selecting the right course of action in a timely, efficient and effective manner would be a response to this critical requirement. To this end, the objective of this paper is to provide such a framework.

The main objective of this research paper is to develop A Framework for Intelligent Decision Support System for Traffic Congestion Management System, using state of the art developments in urban transportation system modeling, that can be a useful decision support tool for transportation planners and decision makers for the analysis and evaluation of strategic transportation plans include transportation projects and policies.

The main contribution of this research is the creation of Scenario Management Subsystem (SMS) and the Intelligent Scenario Creation Assistance Agent (ISCAA) briefly discussed in Subsection 4.5 and Subsection 4.6 respectively. We will also show how these components are integrated with the impact models results where the inputs to these impact models are the result of the Multiclass Simultaneous Transportation Equilibrium Model (MSTEM) [36] that will be run for each transportation alternative solution. And finally, we have an intelligent DSS that can recognize a pattern of solution alternatives for traffic congestion problem associated with its total evaluation. This IDSS can be used by any non-transportation specialist decision makers for any transportation policy evaluations and recommendations.

This paper is organized as follow: Section 2 gives the main concept for the transportation systems analysis. Section 3 presents a more detailed framework for transportation system analysis combing the concept of the transportation planning process and the transportation system analysis concept. Section 3 presents The Multiclass Simultaneous Transportation Equilibrium Model (MSTEM)'s description, formulation as Variational Inequality (VI) and the data collection requirements. Section 4 illustrates the main Architecture of the Intelligent Decision Support System (IDSS) implementing the framework for transportation system analysis described in Section 2. And finally, the summary, conclusion and future research are presented in Section 5.

2. Transportation Systems Analysis

2.1. Transportation System

We briefly define the transportation planning as a continuous process consists of:

1) Problem definition, Generation of Alternatives
2) Building and Calibration of Transportation Models
3) Application of the Calibrated Transportation Models and Analysis of Alternatives
4) Evaluation and Choice
5) Implementation

A *transportation system* can be define as the combination of elements and their interactions, which produce the demand for travel within a given area and the supply of the transportation service to satisfy this demand. This definition is general and flexible enough to be applied to different context. The specific structure of the system is defined by the problem itself (or class of problem) for whose solution is employed.

Almost all of the components of a social and economic system in a given geographical area interact with different levels of intensity. However, it is practically impossible to take into account every interacting element to solve a transportation problem. The typical system approach is to isolate the most relevant element in the problem. These elements, and the relation among them, make up the ***analysis system***. The remaining elements which belong to the ***external environment*** are taken into account only in term of their interaction with the analysis system. The transportation system of a given area can also be seen as a sub-system of a wider territorial system with which it strongly interacts. The extent, to which these interactions are included in the analysis system, or in the external environment, depends on the specific problem.

Transportation is the process of transferring people, good and information from one place to another. To perform its function, any transportation system consists of several components which together act as a single unit that is designed and developed to provide a suitable technology for the "objects" to be transported.

Any transport technology must provide mobility, control, protection, and land access for the objects. Perhaps the most widespread transport technology is the one used for inland transport. That is vehicles and containers operating on highway or railway networks.

Components of such a transport system may be divided into two categories. The first category includes the physical components such as the network infrastructural fixed elements (*i.e.*, road and rail links, intersections, terminals, parking spaces, railway yards, maintenance shops, stations, etc.), and moving elements (*i.e.*, vehicles and containers). The second category includes the human components such as users, operators, owners, and regulators of the system, government and the society at large. The key players in system analysis are defined as follows:

1) Users: are those traveler and shipper who represent demand on the transport system.

2) Operators: are those who own the fleet of vehicles and hence, are responsible for their operation, maintenance and investment.

3) Owners: are those who own the network elements and hence, are concerned with construction, upgrading, operation and maintenance of the infrastructure.

4) Regulators: are responsible for traffic laws, ordinances and regulations.

5) Government: is responsible for creating the master plan for the city transportation systems and policies or projects that affect the transportation systems.

6) Society at large: is responsible location of residents and activities

It should be emphasized that these components should interact all together in order to provide effective and efficient "transportation". Furthermore, a transport system may be viewed as one of several components of more complex socio-economic system of the society. The interaction between the transport system and its surrounding socio-economic environment is, again, evident. Transport demand is a function of the magnitude and spatial distribution of socio-economic activities which in turn are greatly influenced by the characteristics of transport systems. Therefore, the actual performance of any transport system is a function of several interacting and interdependent factors within the system and those outside the system.

Like any other complex system, transport system may not always perform as desired and there are often problems and issues to be addressed and resolved. Traffic congestion, limited parking space, high accident rate, weak connectivity between major development centers, freight movements, public transit, and air pollution are but a few examples to mention. The range of possible remedies is enormous. Construction of new highways, building multistory garages, introducing new transport technologies, creating new organizational structures and traffic regulations are examples of actions which would be undertaken.

The "best" action (or set of actions) to be implemented in particular situation, is a question that is, often, not a simple one to resolve immediately and usually requires a systematic process of analysis that takes into consideration the interacting affects on the system, that is, transportation planning. Formally defined, planning is "a systematic analytical process that assists decision makers of a given system to achieve a specific set of goals and objectives within a given socio-economic environment in an optimum fashion".

2.2. Basic Premises

As indicated earlier any transport system consists of several physical as well as human components which interact together in order to produce "transportation". The transport system itself is, again, one of several components in the socio-economic activity system of the society when all interact produce what we call the "development" of that society. Therefore, the analysis of transportation systems should be based on two basic premises:

1) The total transport system within a given socio-economic environment must be considered and viewed as a single multimodal system.

2) The interaction between the total transport system and the surrounding socio-economic activity system must be taken into account in the analysis.

2.3. Basic Variables and Relationships

Based on the above premises, the resultant effect of the interactions between the activity and transport systems is manifested in the flow pattern distributed on the different elements of the transport system. Therefore, we can define three basic variables for the analysis:

T: The Transport System,
A: The Activity System
F: The Flow Pattern

The interrelationships among these three variables are shown on **Figure 1** and may be described as follows:

Relationship I: *T* and *A* determines *F*.

Relationship II: *F* cause changes over time in *A* (e.g., an increase of flow on a given route may induce more activities to shift along that route).

Relationship III: *F* causes changes over time in *T* (e.g., a congestion of flow may influence the decision to build a new road or to modify existing one).

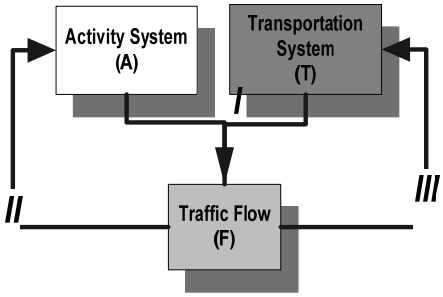

Figure 1. Basic variables and relationships in transportation system analysis.

In order to complete the description of the basic framework of the analysis it is essential to identify the major individuals, groups or institutions whose decision could influence and change any of the three basic variables of the analysis *T*, *A* and *F*. Six major groups can be identified: User, operators, owners, regulators, government, and society at large (a brief description of each group has been introduces earlier).

2.4. Basic Issues

Having defined the basic framework of analysis let us turn our attention to the basic issues involved. The first basic issue is related to the available "options" through which the six major groups can influence the system. The second basic issue is concerned with predicting the possible "impacts" of these "options" on the same groups. Thus the analysis can be described by firstly identifying the available options, secondly identifying the possible impacts, and thirdly explaining the process of predicting the set of impacts resulting from a given set of options.

2.5. Options

Options or "decision variables" are those aspects of the transport and activity systems which can directly be changed by the decision(s) of one or more individuals or groups. It is, therefore, natural to divide the available options into two categories, the first includes those related to the transport system and the second includes those related to the activity system.

1) Transportation options:

Transportation options are those decisions which can mainly influence the transport system's performance by changing aspects of the network, technology, operating policies, and/or institutional structures as follows:

a) The network may be influenced (by the owners) through the geometric and structural design of different links, intersections and terminals, the network topology and hierarchy, traffic signals, signs, markings, parking facilities, etc.

b) Technological options may include the use of electric or solar power for vehicles, the use of containers, the introduction of a new rapid transit system, etc.

c) Operating policies may include vehicle routing, scheduling, pricing, exit and entry regulations, financial regulations, laws, ordinances, etc.

d) Institutional options may include the number and types of institutions, the functions of different institutions, the domain of responsibilities, channels of communications, coordination, control, etc.

2) Activity options:

Activity options are those decisions which can mainly influence transport demand and which are, in general, not controlled by the decision makers of the transport system. People in the society have a wide range of options about how, when and where they would conduct their activities. Two types of decision should be considered:

a) long term decisions:

-The location of residence

-Employment

-Scale and pattern of activities

These decisions determine the spatial distribution of socio-economic activities and land uses in a given area. Within this context, the actual transport demand will be influenced by

b) short term decisions (travel options):

-Trip purpose

-Time of trips

-Frequency of trips

-Trip mode

-Trip route

2.6. Impacts

Impacts are those aspects of the transportation and activity systems that would be influenced by the implementation of alternative options and would consequently influenced the six major groups of the system: users, operators, owners, regulators, government, and the society at large. In order to predict and evaluate these impacts it is useful to categorize them according to the affected groups:

1) *User impacts*

Users are mainly influenced by the level of service of the transport system, and hence, their impacts variables would include:

- Travel time
- Travel cost
- Safety
- Comfort

2) *Operators impacts*

Operators are mainly concerned with maximizing their share of demand and/or their net revenues, and hence, their impact variables would include:

- The costs of several resources consumed in the op-

eration
- Maintenance and investment of their vehicle fleets
- Their shares of transport demands

3) *Owners impacts*

Owners are mainly interested in the usage and condition to their infrastructural elements, and hence their impacts would be reflected through the investment, maintenance and upgrading costs which are, in general, functions of the usage of the transport network.

4) *Regulators impacts*

Regulators are mainly interested in the safety aspects of operation.

5) *Society impacts*

The impacts on the society at large include the effects caused by the physical presence of transport facilities, such as:
- Noise
- Pollution
- Relocation of residents and activities

6) *Governmental impacts*

Governmental impacts will depend upon whether the given government institution is a user, operator, owner, regulator or representing the society at large.

It should be obvious that the above impacts will, in general, have differential effects on different groups, or even subgroups of the above six major ones. That is, some will gain while others may lose.

2.7. Prediction Process

As indicated earlier, the core of the analysis is the process of predicting the "impacts" of alternative sets of "options". A central aspect of this process is the prediction of an "equilibrium" flow pattern on the transport system resulting from a given set of options. Once this equilibrium flow is predicted, the different impacts variables can be estimated through a set of impact models. The prediction process may, then, be described as follows:

1) Specification of the transport system options T establishes performance functions, J. The function J indicates how the level of service S varies as a function of the transport options T and the volume of flow V. That is,

$$S = J(T,V)$$

2) Specification of the activity system options A establishes demand function, D. The function D indicates the volume of flow V as a function of the activity options A and the level of service S, that is,

$$V = D(A, S)$$

3) The flow pattern F consists of the volume $V$and the level of service S on the different elements of the total transport system. That is,

$$F = (V, S)$$

4) For a given set of options T^* and A^*, the resulting equilibrium flow pattern, F^*, can be computed by solving the performance and demand function. That is,

$$\left.\begin{aligned} S &= j(T^*, V) \\ V &= D(A^*, S) \end{aligned}\right\} F^* = (V^*, S^*)$$

3. The Methodological Framework for Urban Transportation Systems Analysis

Figure 2 shows the main components of the methodological framework for urban transportation systems analysis as a Traffic Congestion Management System (TCMS) that we will develop in this research paper and which depends on the transportation planning steps described earlier.

3.1. An Overview

This framework can be described as follow:

1) Socio-Economic Environment Description

This part of the frameworks represents the diagnoses and the analysis of the socio-economic environment characteristics and factors of the urban area that should be considered in the analysis and developments of the transportation system. These factors may include the population distribution, income, car ownership, and land use of the study area. In this part, we can also define the transportation problems that should be addressed and clearly and specifically determined the symptoms, cause, and consequences for each problem in addition to the objectives and goals that should be satisfied by solving these problems. Then different alternative can be generated through different options of the six groups' users, operators, owners, regulator, government, and society at large as in next parts 2 and 3. A related data collection should be performed in this part.

2) Users Characteristics and Behavior

This part represents the transportation demand side where there are, for example, the following alternatives (options or decision variables):
- Residence Locations
- Economic& Social Activities Locations
- Frequency of trip
- Destination of Trip
- Trip Purpose
- Travel Mode
-Time of Trip
- Work Locations
- Trip Route

3) Owners, Operators and Regulators Behavior

This part represents the transportation system performance side where there are, for example, the following alternatives (options or decision variables):
- Network Configuration (e.g., links, nodes, intersection, traffic signals location, waiting areas)
- Investments and maintenance Policies for the transportation network and facilities

- Vehicle fleets characteristics
- Routing, scheduling and pricing policies
- Laws, regulations and controls
- Institutions

4) Transport Demand

As a result of a combination of alternatives (options) of users characteristics and behavioral in part 2, a set transport demand functions (in fact a set of transportation demand models) can be defined. These demand functions will be functions of user behavior and system's performance.

5) Transportation System Performance

As a result of a combination of alternatives (options) of owners, operators and regulators behavior in part 3, a set transport performance functions (in fact a set of transportation performance models) can be defined. These performance functions will be functions of transportation supply and transportation demand. A combination of alternatives from part 2 and part 3 together is considered a complete scenario (alternative) that would developed (generated) to solve the problem under consideration in part 1. This is considered as step 2 in transportation planning steps. Parts 4 and 5 required building transportation demand and performance models and calibrating these models using the data collected in part 1). This is considered as part of step 3 in transportation planning steps.

6) Transportation Network Equilibrium

To analysis any completed scenario (alternative) generated by part 2 and 3, an equilibrium between the built and calibrated transportation demand models ($V = D(A,S)$) and transportation performance models ($S = J(T,V)$ should be performed. The output of this equilibrium process is the traffic pattern ($F = (V,S)$) that can be used in estimate the impacts of the given scenario on users, owners, operators, regulators, and society at large (see part 7 next). Part 4 represents, in general, the activity system Awhile part 5 represents, in general, the transportation system T at interacting together to produce the traffic pattern F. This represents Relation I in **Figure 2**. This part represents part of step 3 in transportation planning steps. To compute this equilibrium we will explain in the next subsection in detail our MSTEM model methodology.

7) Impacts on Users, Owners, Operators, Regulators, Government, and Society at large

The traffic pattern result from part 6 can be used in different impact models that should be developed for the six groups: Users, owners, operators, regulators, government, and society at large (see Subsection 1.3 part 5). This completes step 3 in transportation planning steps.

8) Evaluation and Choice

As a result of the impacts on the six groups in part 7, each alternative can be evaluated using specified evaluation criteria and the best alternative (scenario) should be chosen. (Step 4 in transportation planning steps)

9) Implementation

It is same as step 5 in transportation planning steps.

The traffic pattern F that used in the alternatives evaluation, choice and implementation will cause changes over time in activity system, A, through part 2, this represents Relation II in **Figure 1**. This traffic pattern will also cause changes over time in transportation system, T, through part 3), this represents Relation III in **Figure 1.**

3.2. The Multiclass Simultaneous Transportation Equilibrium Model (MSTEM)

Single class travel forecasting models assume that all travelers are similar in their travel-decision characteristics, such as their money-value of the time and their sensitivity to travel times in choosing their origin, destination and mode of travel, etc. To obtain more realistic models, travelers are often divided into classes, either by socio-economic attributes (e.g., income level, car availability, etc.) or by the purpose (e.g., home-based-work, non-home-based-work, home-based-shopping, etc.) of their travel, assuming that travel-decision characteristics are the same within each class, but differ among classes. However, the development of this concept of multiple classes increases the mathematical complexity of travel forecasting models. In 1986 researchers in Chile began to implement multiclass combined models emphasizing route choices in a congested transit network with several combinations of transit modes, as found in Santiago [37]. This research led to the development of ESTRAUS and related software, which has been extensively applied to Santiago as well as other Chilean cities. Florian, Wu and He [38] proposed a variant of ESTRAUS intended to be more efficient computationally.

All existing multiclass combined models including ESTRAUS, consider that the total originating and terminating flows are known, *i.e.*, the trip generation step of transportation planning process is exogenous to the combined prediction process. This deficiency is accounted in the STEM model which is the only model that combined the trip generation in the prediction process, but it is not a multiclass model. This encourage Hasan and Dashti [36] to expand STEM model to be multiple user classes model in terms of socio-economic group, trip purpose, as well as pure and combined transportation modes, interacting over a physically unique network. The developed Multiclass Simultaneous Transportation Equilibrium Model (MSTEM) will also combine explicitly the departure time as one of the main components of the prediction process for the first time and will be considered as a new generation of new Case 6 of the multiclass model classification of Boyce and Bar-Gera [39]. The MSTEM will include all the features of ESTRAUS in addition to the other features mentioned above and more flexible struc-

ture for demand models where the trip generation can depend upon the system's performance through an accessibility measure that is based on the random utility theory of users' behavior (instead of being fixed as in ESTRAUS), trip distribution is given by a more behaviorally richer Multinomial Logit (MNL) model based on the random utility theory (instead of being given by an entropy maximization model in ESTRAUS), and modal split and departure time are given by Multinomial Logit (MNL) models based on the random utility theory (instead of hierarchical Logit for modal split only in ESTRAUS). The MSTEM is formulated as a Variational Inequality problem and a diagonalization (relaxation) algorithm is proposed to solve it. The MSTEM will include all the features of ESTRAUS in performance through an accessibility measure that is based on the random utility theory of users' behavior (instead of being fixed as in ESTRAUS), trip distribution is given by a more behaviorally richer Multinomial Logit (MNL) model based on the random utility theory (instead of being given by an entropy maximization model in ESTRAUS), and modal split and departure time are given by Multinomial Logit (MNL) models based on the random utility theory (instead of hierarchical Logit for modal split only in ESTRAUS). The MSTEM is formulated as a Variational Inequality problem and a diagonalization (relaxation) algorithm is proposed to solve it.

3.2.1. MSTEM Modeling

3.2.1.1. Notation

Let $G = (N, A)$ be a multimodal network consisting of a set of N nodes and a set of A links that can represent any mode of transport m in an urban area. These modes can be grouped into different nests n that could be multiple pure and combined (combination of pure) modes. A typical user of class l with trip purpose o traveling from a given origin i at a specific departure time period t to any destination j that is accessible from i can use any of these modes for his journey. We will use the following notation for the multiclass models:

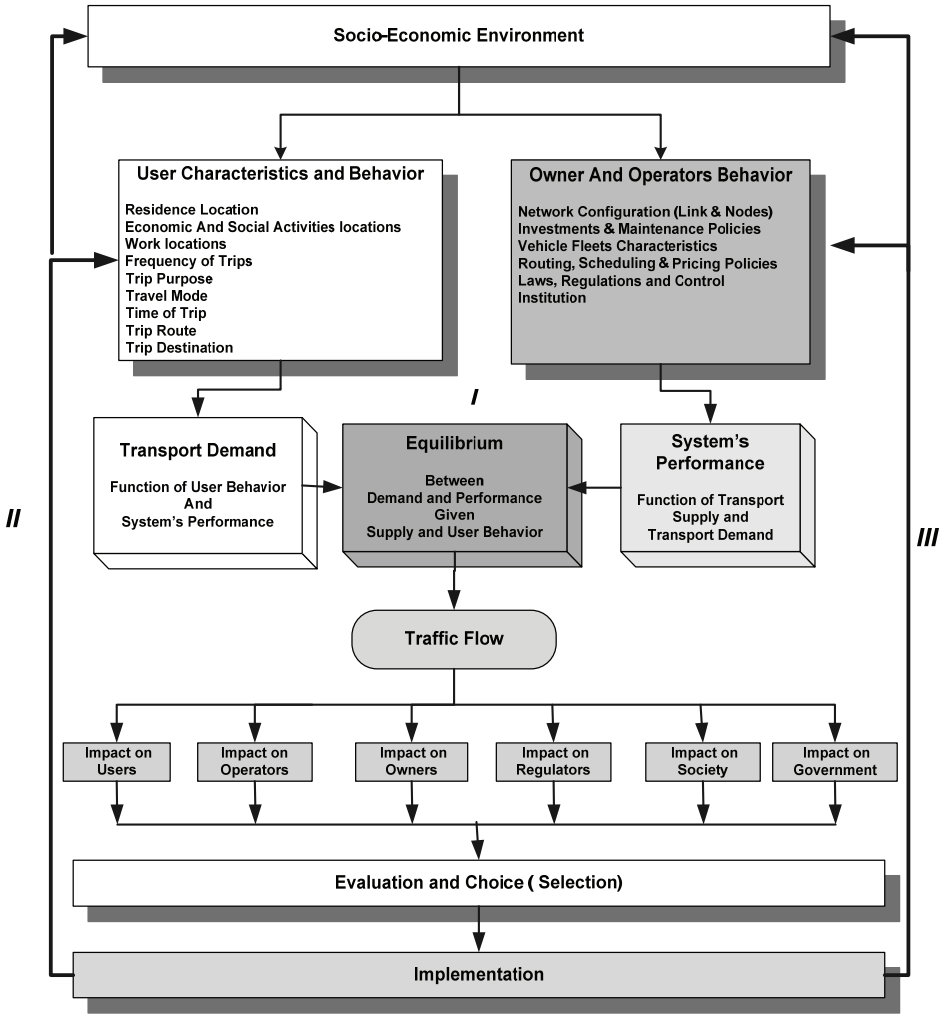

Figure 2. A framework for urban transportation system analysis as a TCMS.

G = (N,A) A multimodal network consisting of a set of N nodes and a set of A links

L = User class (e.g., income level, car availability, etc.)

L = Set of all user classes

O = Trip purpose (e.g., home-based-work, home-based-shopping, etc.)

O = Set of all trip purpose

I^{lo} = Set of origin nodes for user class l and trip purpose o

i = An origin node in the set I^{lo} for user class l with trip purpose o

D_i^{lo} = Set of destination nodes that are accessible from a given origin i for user class l with trip purpose o

j = A destination node in the set D_i^{lo} for user class l with trip purpose o

R^{lo} = Set of origin-destination pairs ij for user class l with trip purpose o, *i.e.*, the set of all origins $i \in I^{lo}$ and destinations $j \in D_i^{lo}$

M = Any transportation mode in the urban area

n = Nest of transportation modes m that has a specific characteristics (e.g., pure modes including private and public or combined modes) that are available for user class l with trip purpose o travel between origin-destination pairs ij

Λ_{ij}^{lo} = Set of all nests of modes n that are available for user class l with trip purpose o travel between origin-destination pairs ij

M_n^{lo} = Set of all transportation modes m in the nest n for user class l with trip purpose o travel between origin-destination pairs ij

t = Departure time period for user class l with trip purpose o using mode m in the nest n to travel between origin-destination pairs ij

K_m^{lo} = Time horizon of the departure time periods t for users of class l with trip purpose o using mode m between origin-destination pairs ij

p = A simple (*i.e.*, no node repeated) multimodal path (*i.e.*, it may include links with combined modes m) in the multimodal network (N, A)

P_{ij}^{lonmt} = Set of simple paths for travel from the origin node i to destination node j in the multimodal network (N, A) for users of class l with trip purpose o depart at time $t \in K_m^{lo}$ using mode $m \in M_n^{lo}$ from the nest of modes $n \in \Lambda_{ij}^{lo}$.

a = A link in the set A in the multimodal

u_{ij}^{lonmt} = the perceived minimum (generalized) cost of travel for users of class l with trip purpose o depart at time t using mode m in the nest n from the origin node i to destination node j in the set D_i^{lo}

S_i^{lo} = the accessibility of origin $i \in I^{lo}$ as perceived from user of class l with trip purpose o traveling from that origin

G_i^{lo} = the number of trips generated from origin i for users of class l with trip purpose o

A_{wj}^{lo} = the value of the w^{th} socio-economic variable that influences trip attraction at destination j for users of class l with trip purpose o

$g_w^{lo}(A_{wj}^{lo})$ = a given function specifying how the w^{th} socio-economic variable A_{wj}^{lo} influences trip attraction at destination j for users of class l with trip purpose o, and

A_j^{lo} = a composite measure of the effect that socio-economic variables, which, are exogenous to the transport system, have on trip attraction at destination j for users of class l with trip purpose o.

θ_i^{lo} and θ_{iw}^{lo} for $w = 1, 2, ..., W$ are coefficients to be estimated, where $\theta_i^{lo} > 0$.

$E_{\omega i}^{lo}$ = the value of the ω^{th} socio-economic variable that influences the number of trips generated from origin i for users of class l with trip purpose o

$q_\omega\left(E_{\omega i}^{lo}\right)$ = a given function specifying how the ω^{th} socio-economic variable, $E_{\omega i}^{lo}$, influences the number of trips generated from origin i for users of class l with trip purpose o, and

E_i^{lo} = a composite measure of the effect the socio-economic variables, which are exogenous to the transport system, have on the number of trips generated from origin i for users of class l with trip purpose o

α^{lo} and α_ω^{lo} for $\omega = 1, 2, ..., \Omega$ are coefficients to be estimated $\forall l \in L, \forall o \in O$

T_{ij}^{lonmt} = the number trips of users of class l with trip purpose o traveling from the origin node $i \in I^{lo}$ to the destination node $j \in D_i^{lo}$ and whose already chose the mode of transport $m \in M_n^{lo}$ from the nest of modes $n \in \Lambda_{ij}^{lo}$ and start their trip at the time $t \in K_m^{lo}$

T_{ij}^{lonm} = the number trips of users of class l with trip purpose o traveling from the origin node $i \in I^{lo}$ to the destination node $j \in D_i^{lo}$ and whose already chose the mode of transport $m \in M_n^{lo}$ from the nest of modes $n \in \Lambda_{ij}^{lo}$.

T_{ij}^{lon} = the number trips of users of class l with trip purpose o traveling from the origin node $i \in I^{lo}$ to the destination node $j \in D_i^{lo}$ and whose already chose the

nest of modes $n \in \Lambda_{ij}^{lo}$.

T_{ij}^{lo} = the number trips of users of class l with trip purpose o traveling from the origin node $i \in I^{lo}$ to the destination node $j \in D_i^{lo}$.

3.2.1.2. Model Assumptions and Structure

1) Travel cost functions

In single class models are often separable and symmetric, allowing for convex optimization formulation. In multi-class models travel costs of one class are affected by decisions of other classes; hence the cost structure is not separable, and in general it is not symmetric and does not allow a convex optimization formulation. We assume the following:

a) For each link $a \in A$, the link cost function, $C_a^{lonmt}, \forall t \in K_m^{lo}, \forall m \in M_n^{lo}, \forall n \in \Lambda_{ij}^{lo}, \forall ij \in R^{lo}, \forall l \in L, \forall o \in O$, will depend, in general, upon the flow over all links, the vector **f**, in the multimodal network (N, A) for all user class $l \in L$, trip propose $o \in O$, transport mode nest $n \in \Lambda_{ij}^{lo}$, transport mode $m \in M_n^{lo}$, and departure time period $t \in K_m^{lo}$, that is

$$C_a^{lonmt} = C_a^{lonmt}(\mathbf{f}) \quad \forall t \in K_m^{lo}, \forall m \in M_n^{lo}, \forall n \in \Lambda_{ij}^{lo}, \forall ij \in R^{lo}, \forall l \in L, \forall o \in O \tag{1}$$

where $\mathbf{f} = (f_a^{lonmt} : a \in A, t \in K_m^{lo}, m \in M_n^{lo}, n \in \Lambda_{ij}^{lo}, ij \in R^{lo}, l \in L, o \in O)$

We will also assume that the perceived cost of travel on any multimodal route (path) $p \in P_{ij}^{lonmt}$, is the sum of travel costs on the links that comprise that path, that is:

$$C_p^{lonmt} = \sum_{a \in A} \delta_{ap}^{lonmt} C_a^{lonmt}(\mathbf{f}), \ \forall p \in P_{ij}^{lonmt}, \forall t \in K_m^{lo}, \forall m \in M_n^{lo}, \backslash \forall n \in \Lambda_{ij}^{lo}, \forall ij \in R^{lo}, \forall l \in L, \forall o \in O \tag{2}$$

$$\delta_{ap}^{lonmt} = \begin{cases} 1 & \text{if link } a \text{ belongs to path } p \\ 0 & \text{otherwise} \end{cases}$$

$$\forall p \in P_{ij}^{lonmt}, \forall t \in K_m^{lo}, \forall m \in M_n^{lo}, \forall n \in \Lambda_{ij}^{lo}, \forall ij \in R^{lo}, \forall l \in L, \forall o \in O$$

2) The Jacobian $\nabla \mathbf{C}(\mathbf{f})$ of the link cost functions

$$\mathbf{C}(\mathbf{f}) = (C_a^{lonmt}(\mathbf{f}) : \ t \in K_m^{lo}, m \in M_n^{lo}, n \in \Lambda_{ij}^{lo}, ij \in R^{lo}, l \in L, o \in O)$$

is asymmetric

The function form specification of the link cost function in (1) depends on the application of the model and how well this link cost function represents the transport system supply in the urban area of the study. For example, if we consider only three nests of transport modes named $n_1, n_2,$ and n_3 and define them as follows:

$n_1 = \tilde{m}$ as pure private transportation modes (e.g., car, taxi, etc.)

$n_2 = \overline{m}$ as pure public transportation modes (e.g., bus, subway, metro, etc.)

$n_3 = m^c$ as combined transportation modes (e.g., car/metro, bus/metro, etc.) and used the specified link cost functions for each of the modes $\tilde{m}, \overline{m}$, and m^c that used in ESTRAUS [37] in its application to Chilean city Santiago, MSTEM model will have all the advantages of ESTRAUS from the transport system supply side representation, especially the capacity constraints for vehicles of all public transport modes, in addition to, the advantages of MSTEM model over the ESTRAUS from the transport system demand side.

That is, the link's a average operating cost $C_a^{lo\tilde{m}t}$ (operating time or generalized a cost), for users of class l, with trip purpose o, of private transportation mode $\tilde{m}$ (e.g., car, taxi, etc.) depart from his origin at time t. This is a function of the summation of vehicle flows over all private transportation modes, user classes and trip purposes ($f_a^{lo\tilde{m}t}$), as well as the fixed flow of public transportation vehicles ($\overline{F}_a^t$) on link a at time period t, all measured in equivalent vehicles (e.g., p.c.u.):

$$C_a^{lo\tilde{m}t} = C_a^{lo\tilde{m}t}\left(\sum_l \sum_o \sum_{\tilde{m}} f_a^{lo\tilde{m}t}, \overline{F}_a^t\right) \tag{3}$$

Although the Jacobian of the cost functions vector is not diagonal, it does turn out to be symmetrical, given the functional form supposed for cost functions $C_a^{lo\tilde{m}}$ (every vehicle, from whichever user class, trip purpose and private transportation mode, produces the same impact on congestion). Nevertheless, this "symmetry" of the cost functions for private modes, which is a simplification, could be relaxed without changing the problem formulation and its solution algorithm. If more general cost functions are used, considering, for instance, that different classes of users of private modes produce different impacts on road congestion, the Jacobian of these cost functions will be asymmetric just like the one associated to the public transport cost functions. Then the combined problem is asymmetric, independent of the particular characteristics of the cost functions for private modes. For every pure public transportation mode $\overline{m}$, the pure service networks can be defined as $G_{\overline{m}} = (N_{\overline{m}}, S_{\overline{m}})$ where $N_{\overline{m}}$ is the set of nodes ($N_{\overline{m}} = N$ for ground services that use the road network, such as buses, and $N_{\overline{m}} = N'$ where $N \cap N' = \varphi$ for independent public transportation services, (e.g., metro)) and $S_{\overline{m}}$ is the set of transit links (route sections) that belong to mode $\overline{m}$.

The generalized time (cost) functions of the public transportation links, considering the vehicle capacity constraints as in De Cea and Fernández [40], (sum of travel time, waiting time, transfer time, fare, etc.) depend on the vehicle flow over the road network as well as the passenger flow in the existing services, as follows:

$$C_s^{lo\bar{m}t} = \phi^{lo\bar{m}t}\left(\sum_l \sum_o \sum_{\bar{m}} f_a^{lo\bar{m}t}, \bar{F}_a^t, \forall a \in \ell, \ell \in B_{s\bar{m}t}\right) + (P_{TAR})^{lo\bar{m}t} (TAR)_s^{\bar{m}t} + (P_{WAIT})^{lo\bar{m}t}\left[\frac{\alpha^{\bar{m}t}}{d_s^{\bar{m}t}} + \beta^{\bar{m}t}\left(\frac{V_s^{lo\bar{m}t} + \tilde{V}_s^{lo\bar{m}t}}{(CAP)_s^{\bar{m}t}}\right)^{\nu^{\bar{m}t}}\right] \quad (4)$$

Where $C_s^{lo\bar{m}t}$: Average or generalized cost on link s for users of class l, with trip purpose o, of public transportation mode $\bar{m}$ (e.g. bus, subway, etc.) at time period t.

$(P_{TAR})^{lo\bar{m}t}$: Fare multiplier for users of class l, with trip purpose o, of public transportation mode $\bar{m}$ at time period t.

$(TAR)_s^{\bar{m}t}$: Fare related to public transportation link s of mode $\bar{m}$ at time period t.

$(P_{WAIT})^{lo\bar{m}t}$: Waiting time multiplier for users of class l, with trip purpose o, of public transportation mode $\bar{m}$ at time period t.

$\alpha^{\bar{m}t}$, $\beta^{\bar{m}t}$, $\nu^{\bar{m}t}$: Calibration parameters of waiting time function, for public transportation mode $\bar{m}$ at time period t.

$d_s^{\bar{m}t}$: Vehicle frequency of public transportation mode $\bar{m}$ over the pubic transportation link s at time period t.

$(CAP)_s^{\bar{m}t}$: Capacity of public transportation link s of mode $\bar{m}$ at time period t.

$V_s^{lo\bar{m}t}$: Passenger flow of class l, with trip purpose o, belonging to public transportation mode $\bar{m}$ at time period t, and which use public transportation link s.

$\tilde{V}_s^{lo\bar{m}t}$: passenger flow that competes with $V_s^{lo\bar{m}t}$ for the capacity of transit lines belonging to B_s (flow with the same trip purpose, user class, mode, and time period t that belong to other public transportation links that compete or reduce the B_s line's capacity, plus flow from other purposes, classes, modes, and time periods that also compete for the B_s lines capacity).

It is easily seen, in this case, that the Jacobian of the cost function vector is non-diagonal and asymmetric. In addition, the model considers the existence of combined modes, for example car/metro (private transportation/public transportation) or bus/metro (public transportation/public transportation). In each case, the union of the pure mode networks that compose them forms the combined mode network. The combined modes (m^c) are considered to be formed by two public transportation modes. Nevertheless, it is important to stress that this does not limit the model's general use, since there is no problem in representing combined modes such as car-public transportation (as in the application of ESTRAUS for the city of Santiago considers combined modes like car driver-metro and car passenger-metro).

b) Trip Generation (TG)

Following the same line of thought of Safwat and Magnanti [41], the accessibility S_i^{lo} of origin $i \in I^{lo}$ as perceived from user of class l with trip purpose o traveling from that origin can be defined as follows:

$$S_i^{lo} = E\left[\max_{j \in D_i^{lo}} \max_{n \in \Lambda_{ij}^{lo}} \max_{m \in M_n^{lo}} \max_{t \in K_m^{lo}} \nu_{ij}^{lonmt}\right]$$
$$\forall i \in I^{lo}, \forall l \in L, \forall o \in O$$

where E = the expectation operator.

$$S_i^{lo} = \max\left\{0, \ln \sum_{j \in D_i^{lo}} \sum_{n \in \Lambda_{ij}^{lo}} \sum_{m \in M_n^{lo}} \sum_{t \in K_m^{lo}} \exp(-\theta_i^{lo} u_{ij}^{lonmt} + A_j^{lo})\right\} \quad (5)$$
$$\forall i \in I^{lo}, \forall l \in L, \forall o \in O$$

The number of trips generated from origin i for users of class l with trip purpose o, G_i^{lo} can be expressed by:

$$G_i^{lo} = \alpha^{lo} S_i^{lo} + \sum_{\omega=1}^{\Omega} \alpha_\omega^{lo} q_\omega(E_{\omega i}^{lo})$$
$$\forall i \in I^{lo}, \forall l \in L, \forall o \in O$$

$$G_i^{lo} = \alpha^{lo} S_i^{lo} + E_i^{lo} \qquad \forall i \in I^{lo}, \forall l \in L, \forall o \in O \quad (6)$$

Similar to A_j^{lo}, E_i^{lo} is assumed to be a fixed constant during the time period required to achieve short-run equilibrium, and G_i^{lo} depends solely on the system's performance as measured by the accessibility variable S_i^{lo}.

c) Trip Distribution, Nest/Mode Split, and Departure Time Logit Models (TD/MS/DT)

Following the same line of thought of Safwat and Magnanti [41], Oppenheim [42] and Ran and Boyce [43] our distribution, nest/mode, and departure time Logit models can be given by:

$$T_{ij}^{lo} = G_i^{lo} \frac{\sum_{n \in \Lambda_{ij}^{lo}} \sum_{m \in M_n^{lo}} \sum_{t \in K_m^{lo}} \exp(-\theta_i^{lo} u_{ij}^{lonmt} + A_j^{lo})}{\sum_{j \in D_i^{lo}} \sum_{n \in \Lambda_{ij}^{lo}} \sum_{m \in M_n^{lo}} \sum_{t \in K_m^{lo}} \exp(-\theta_i^{lo} u_{ij}^{lonmt} + A_j^{lo})} \quad (7)$$
$$\forall ij \in R^{lo}, \forall l \in L, \forall o \in O$$

$$T_{ij}^{lon} = T_{ij}^{lo} \frac{\sum_{m \in M_n^{lo}} \sum_{t \in K_m^{lo}} \exp(-\theta_i^{lo} u_{ij}^{lonmt} + A_j^{lo})}{\sum_{n \in \Lambda_{ij}^{lo}} \sum_{m \in M_n^{lo}} \sum_{K_m^{lo}} \exp(-\theta_i^{lo} u_{ij}^{lonmt} + A_j^{lo})} \quad (8)$$
$$\forall n \in \Lambda_{ij}^{lo}, \forall ij \in R^{lo}, \forall l \in L, \forall o \in O$$

$$T_{ij}^{lonm} = T_{ij}^{lon} \frac{\sum_{t\in K_m^{lo}} \exp(-\theta_i^{lo} u_{ij}^{lonmt} + A_j^{lo})}{\sum_{m\in M_n^{lo}} \sum_{t\in K_m^{lo}} \exp(-\theta_i^{lo} u_{ij}^{lonmt} + A_j^{lo})} \quad (9)$$

$$\forall m \in M_n^{lo}, \forall n \in \Lambda_{ij}^{lo}, \forall ij \in R^{lo}, \forall l \in L, \forall o \in O$$

$$T_{ij}^{lonmt} = T_{ij}^{lonm} \frac{\exp(-\theta_i^{lo} u_{ij}^{lonmt} + A_j^{lo})}{\sum_{t\in K_m^{lo}} \exp(-\theta_i^{lo} u_{ij}^{lonmt} + A_j^{lo})},$$

$$\forall t \in K_m^{lo}, \forall m \in M_n^{lo}, \forall n \in \Lambda_{ij}^{lo}, \quad (10)$$

$$\forall ij \in R^{lo}, \forall l \in L, \forall o \in O$$

d) Trip Assignment (TA)

Based on the previous choices assumption, the given user will choose his or her route according to Wardrop's user equilibrium principle. That is, for all users of class l with trip purpose o traveling from the origin node $i \in I^{lo}$ to the destination node $j \in D_i^{lo}$ and whose already chose the mode of transport $m \in M_n^{lo}$ from the nest of modes $n \in \Lambda_{ij}^{lo}$ and start their trip at the time $t \in K_m^{lo}$, the perceived generalized costs on all used multimodal paths between the given origin-destination pair are equal and not grater than those on unused paths. This gives the following equilibrium conditions:

$$C_p^{lonmt} \begin{cases} = u_{ij}^{lonmt} & \text{if } h_p^{lonmt} > 0 \\ \geq u_{ij}^{lonmt} & \text{if } h_p^{lonmt} = 0 \end{cases},$$

$$\forall p \in P_{ij}^{lonmt}, \forall t \in K_m^{lo}, \forall m \in M_n^{lo},$$

$$\forall n \in \Lambda_{ij}^{lo}, \forall ij \in R^{lo}, \forall l \in L, \forall o \in O \quad (11)$$

where

$$f_a^{lonmt} = \sum_{l\in L} \sum_{o\in O} \sum_{ij\in R^{lo}} \sum_{p\in P_{ij}^{lonmt}} \delta_{ap}^{lonmt} h_p^{lonmt},$$

$$\forall a \in A, \forall t \in K_m^{lo}, \forall m \in M_n^{lo},$$

$$\forall n \in \Lambda_{ij}^{lo}, \forall ij \in R^{lo}, \forall l \in L, \forall o \in O$$

3.2.1.3. Variational Inequality Formulation for MTEM

Because of the asymmetry of the link cost functions, MSTEM cannot be cast as an equivalent optimization program as STEM. Instead, it can be formulated as the following variational inequality (VI).

$$\mathbf{C}(\mathbf{f}^*)^T(\mathbf{f}-\mathbf{f}^*) - \mathbf{U}(\mathbf{T}^*)^T(\mathbf{T}-\mathbf{T}^*) \geq \mathbf{0}$$
$$\forall \text{ feasible } \mathbf{f}, \mathbf{T} \quad (12)$$

where

$\mathbf{f}$: vector of flow on links of the multimodal network

$\mathbf{f}^*$: vector of equilibrium flow on links of the multimodal network

$\mathbf{T}$: vector of trips between origin-destination pairs of the multimodal network

$$\mathbf{T} = (\mathbf{T}^{i,lo} : i \in I^{lo}, l \in L, o \in O)$$

$\mathbf{T}^*$: vector of equilibrium trips between origin - destination pairs of the multimodal network

$\mathbf{C}(\mathbf{f}^*)$: column-vector of network link's cost functions (with non-diagonal and asymmetric Jacobian)

$\mathbf{U}(\mathbf{T}^*)$: column-vector of inverse demand functions (with non-diagonal and symmetric Jacobian), $\mathbf{U} = (\mathbf{u}^{i,lo} : i \in I^{lo}, l \in L, o \in O)$

The VI problem in (12) is Equivalent to MSTEM (see, for example, Smith [44,45] and Dafermos [46] for a formal proof of equivalency between VI and traffic equilibrium) and can be solved by the relaxation (diagonalization) algorithm (see, for example, Dafermos [47], Florian and Spiess [48], Mahmassani and Mouskos [49], and Sheffi [50])

At each iteration of the diagonalization algorithm, the cost functions C_a^{lonmt} of (1) result in diagonalized cost function $\hat{C}_a^{lonmt}$, which depend only on their own flows, f_a^{lonmt}, and the following VI should be solved:

$$\hat{\mathbf{C}}(\mathbf{f}^*)^T(\mathbf{f}-\mathbf{f}^*) - \mathbf{U}(\mathbf{T}^*)^T(\mathbf{T}-\mathbf{T}^*) \geq \mathbf{0}$$
$$\forall \text{ feasible } \mathbf{f}, \mathbf{T} \quad (13)$$

This VI can be formulated as the following Equivalent Optimization Program (ECP):

$$Min \quad Z(\mathbf{S},\mathbf{T},\mathbf{f}) = \sum_{l\in L} \sum_{o\in O} \sum_{i\in I^{lo}} \sum_{j\in D_i^{lo}} \sum_{n\in\Lambda_{ij}^{lo}} \sum_{m\in M_n^{lo}} \sum_{t\in K_m^{lo}}$$

$$\sum_{a\in A} \int_0^{f_a^{lonmt}} \hat{C}_a^{lonmt}(x)dx + \sum_{l\in L} \sum_{o\in O} \sum_{i\in I^{lo}} \frac{1}{\theta_i^{lo}} [\frac{\alpha^{lo}}{2}(S_i^{lo})^2$$

$$+\alpha^{lo} S_i^{lo} - (\alpha^{lo} S_i^{lo} + E_i^{lo}) \ln(\alpha^{lo} S_i^{lo} + E_i^{lo})]$$

$$+\sum_{l\in L} \sum_{o\in O} \sum_{i\in I^{lo}} \frac{1}{\theta_i^{lo}} \sum_{j\in D_i^{lo}} \sum_{n\in\Lambda_{ij}^{lo}} \sum_{m\in M_n^{lo}} \sum_{t\in K_m^{lo}} [T_{ij}^{lonmt} \ln(T_{ij}^{lonmt})$$

$$-A_j^{lo} T_{ij}^{lonmt} - T_{ij}^{lonmt}]$$

s.t.

$$\sum_{j\in D_i^{lo}} T_{ij}^{lo} = \alpha^{lo} S_i^{lo} + E_i^{lo} \quad \forall i \in I^{lo}, \forall l \in L, \forall o \in O$$

$$T_{ij}^{lo} = \sum_{n\in\Lambda_{ij}^{lo}} T_{ij}^{lon} \quad \forall i \in I^{lo}, \forall j \in D_i^{lo}, \forall l \in L, \forall o \in O$$

$$T_{ij}^{lon} = \sum_{m\in M_n^{lo}} T_{ij}^{lonm}$$

$$\forall i \in I^{lo}, \forall j \in D_i^{lo}, \forall n \in \Lambda_{ij}^{lo}, \forall l \in L, \forall o \in O$$

$$T_{ij}^{lonm} = \sum_{t\in K_m^{lo}} T_{ij}^{lonmt} \quad \forall i \in I^{lo}, \forall j \in D_i^{lo},$$

$$\forall m \in M_n^{lo}, \forall n \in \Lambda_{ij}^{lo}, \forall l \in L, \forall o \in O$$

$$T_{ij}^{lonmt} = \sum_{p \in P_{ij}^{lonmt}} h_p^{lonmt} \quad \forall i \in I^{lo},$$

$$\forall j \in D_i^{lo}, \forall t \in K_m^{lo}, \forall m \in M_n^{lo},$$

$$\forall n \in \Lambda_{ij}^{lo}, \forall l \in L, \forall o \in O$$

$$S_i^{lo} \geq 0 \quad \forall i \in I^{lo}, \forall l \in L, \forall o \in O$$

$$T_{ij}^{lo} \geq 0 \quad \forall i \in I^{lo}, \forall j \in D_i^{lo}, \forall l \in L, \forall o \in O$$

$$T_{ij}^{lon} \geq 0 \quad \forall i \in I^{lo}, \forall j \in D_i^{lo}, \forall n \in \Lambda_{ij}^{lo}, \forall l \in L, \forall o \in O$$

$$T_{ij}^{lonm} \geq 0 \quad \begin{matrix} \forall i \in I^{lo}, \forall j \in D_i^{lo}, \forall m \in M_n^{lo}, \\ \forall n \in \Lambda_{ij}^{lo}, \forall l \in L, \forall o \in O \end{matrix}$$

$$T_{ij}^{lonmt} \geq 0 \quad \forall i \in I^{lo}, \forall j \in D_i^{lo},$$

$$\forall t \in K_m^{lo}, \forall m \in M_n^{lo}, \forall n \in \Lambda_{ij}^{lo},$$

$$\forall l \in L, \forall o \in O$$

$$h_p^{lonmt} \geq 0 \quad \forall i \in I^{lo}, \forall j \in D_i^{lo},$$

$$\forall t \in K_m^{lo}, \forall m \in M_n^{lo}, \forall n \in \Lambda_{ij}^{lo},$$

$$\forall l \in L, \forall o \in O, p \in P_{ij}^{lonmt}$$

where

$$f_a^{lonmt} = \sum_{l \in L} \sum_{o \in O} \sum_{ij \in R^{lo}} \sum_{p \in P_{ij}^{lonmt}} \delta_{ap}^{lonmt} h_p^{lonmt},$$

$$\forall a \in A, \forall t \in K_m^{lo}, \forall m \in M_n^{lo},$$

$$\forall n \in \Lambda_{ij}^{lo}, \forall ij \in R^{lo}, \forall l \in L, \forall o \in O$$

Existence, convexity and uniqueness of ECP problem as well as equivalence between MSTEM and ECP can be followed as those of Safwat and Magnanti [41].

The Logit Distribution of Trips (LDT) algorithm that developed by Safwat and Brademeyer [51] can be modified as Multiclass Logit Distribution of Trips (MLDT) algorithm to solve the above ECP. For more details about the MSTEM methodology see Hasan and Dashti [36].

3.3. Data Collection Requirements

To apply the MSTEM to any urban transportation network we need the following data collection:

1) Household Survey

Trips mad by all household members by all modes of transport both within the study area and leaving/arriving to the area during the survey period

- Personal and household characteristics and identification

- Head of household, wife, son,…, etc.

- Sex, age, possession of a driving license, education level, and occupation

- Socio-economic information: income, car ownership, family size

- Trip data: origin, destination, purpose, start and ending times, mode used, amount of money paid for the trip, and so on

2) Traffic Counts

An actual observed traffic counts in specific locations in the city road and highways should be collected for at different time of the day (specifically in the peak hour), different day of the week, and for different kind of vehicles types.

3) Roadside Interviews

These provide useful information about trips not registered in the household survey (*i.e.* external-external in cordon survey). It involves asking a sample of drivers and passengers of vehicles (e.g. cars, public transport, goods vehicles) crossing a roadside station, a limited set of questions; these include at least origin, destination and trip purpose.

4) Network inventory

a) Road network

The following link attributes for each link:

1- From node and To node

2- Length

3- Its travel speeds-either free-flow speeds or an observed value for a given flow level

4-The capacity of the link

5- Type of road (e.g., expressway, trunk road, local street)

6- Road width, or number of lanes, or both

7- An indication of the presence or otherwise of bus lanes, or prohibitions of use by certain vehicles (e.g., Lorries)

8- Banned turns, or turns to be undertaken only when suitable gaps in the opposing traffic become available

9- Type of junction and junction details including signal timings

10- Storage capacity for queues and their presence at the start of a signal

b) Transit network

1. Lines

2. Fares'

3. Frequency

4. Travel time measurements

5) Land use inventory

a) Residential zones (housing density)

b) Commercial and industrial zones (by type of establishment)

c) Parking spaces

6) Cordon Surveys

These provide useful information about external-external and external-internal trips. Their objective is to determine the number of trips that enter, leave and/or cross the cordoned area, thus helping to complete the information coming from the household O-D survey.

7) Screen-Line Surveys

Screen lines divide the area into large natural zones

(e.g. at both sides a river or motorway), with few crossing points between them. The procedure is analogous to that of cordon survey and the data also serve to fill gaps in and validate the information coming from the household and cordon surveys.

8) Socio-economic data

To compute E_{oi}^{lo}, the value of the ω^{th} socio-economic variable that influences the number of trips generated from origin *i* for users of class *l* with trip purpose *o*, the Socio economic data for each origin *i* could be population, income, car ownership, ….etc.

To compute A_{wj}^{lo}, the value of the w^{th} socio-economic variable that influences trip attraction at destination *j* for users of class *l* with trip purpose *o*, The socio-economic data for destination node *j* could be the ground floor area of the land use type of destination *j* , employment size, …..etc.

3.4 Analysis and Evaluation of Effective Solutions for Peak-period Traffic Congestion

Peak-period traffic congestion occurs when travel demand exceeds the existing road system capacity, Sandra Rosenbloom [52]. There are two basically alter native-solutions:

I Change demand (Users Characteristics and Behavior in **Figure 2**) to meet system capability

II Change system capacity (Owners, Operators and Regulators Behavior in **Figure 2**) to meet demand.

The demand for road system capacity may be changed by:

a) Reducing the number of vehicles used to meet the existing travel demand by increasing vehicle occupancy.

b) Reorienting travel to off-peak periods.

c) Reorienting travel to less congested alternative routes.

d) Reducing the total demand for travel itself.

System capacity itself can be changed by:

a) Constructing additional roadway, either adding lanes to existing routes or providing new routes or new transportation modes.

b) Increasing the capacity of the existing road infrastructure by engineering techniques that improve traffic flow.

Sandra Rosenbloom [52] shows that 22 techniques (see **Table 1**) which appeared to have the potential to reduce or redistribute demand were fell into four major categories of approaches:

a) *social approaches* which seek to alleviate congestion utilizing techniques that change social behavior or personal interactions

b) *socio-economic* approaches which utilize techniques that induce favorable travel changes by manipulating broadly defined economic penalties and incentives

c) *socio-technical* approaches which utilize technology resources to modify social and economic behavior in ways that ultimately reduce congestion

d) *technical* approaches which use technical devices to modify directly dysfunctional travel behavior at the immediate congestion site or source.

These Twenty two techniques were grouped under these four major approaches *cover a wide range of social, behavioral and economic incentives, it* was extremely difficult to make comparisons among them. This difficulty was heightened because these techniques affected peak-period traffic congestion directly and indirectly in different ways. Sandra Rosenbloom [46] illustrated the differing impacts of these techniques in practice where most of the non-engineering techniques considered to be applicable to Peak-Period traffic congestion were not designed with the reduction of peak period traffic congestion as their primary goal; the reduction of traffic congestion was usually considered to be a secondary or indirect impact of their implementation. For such techniques to significantly affect traffic congestion, they must have first successfully met some other goal—their primary goal. However, it was often difficult to get project goals clearly articulated, and the relationship between those goals and traffic congestion identified.

Based on this analysis (see Sandra Rosenbloom [46]), the study team evaluated 17 of these techniques as both effective and feasible in a U.S. institutional context. However, none of these 17 offered more than marginal reductions in peak-period traffic congestion when applied individually. Some techniques affected so small a percent-age of travelers that reductions in congestion would not be discernible. Other techniques promised significant congestion reductions in theory but did not realize that promise in practice. It was concluded that many techniques could be implemented together with the potential for far greater combined effectiveness. An analysis was performed to determine how best to "package" or jointly implement promising techniques to optimize their combined effectiveness. It was found that all promising techniques could not be applied together because of conflicts in their impact. This analysis suggested eight sample "packages" or combinations of mutually supportive techniques. These eight packages were subjected to evaluations similar to those performed for individual techniques; while the packages are merely examples of potential combinations, the evaluation methodology employed should be of continuing use to local transportation planners.

The development of the packaging concept is consistent with the development of the Transportation System Management (TSM) concept in the U.S. The conclusions of the study should also have merit for metropolitan areas considering management schemes. They are:

- Promising congestion reduction techniques or packages must be applied to the appropriate congestion situa-

tions.

- Promising techniques have not been successful alone in significantly affecting peak-period traffic congestion
- All promising techniques cannot be implemented together because some seriously conflict with one, and - Promising congestion reduction techniques may have serious social, economic and physical side-effects which must be recognized prior to implementation

The above study summary shows the guidelines based on empirical results that can be helpful for city planner, traffic engineers or transportation authorities' decision makers. But how we help these people to perform these analysis and guidelines in some systematic or even intelligent way?

4. The Architecture of the Intelligent Decision Support System for Traffic Congestion Management System

The architecture and the information flow shown in **Figure 3** represent a high level blueprint for the implementation of the framework for an Intelligent Decision Support system Traffic Congestion Management System. The framework is derived and guided by the methodological framework for urban transportation system analysis presented in Section 3 and depicted in **Figure 2** and the adoption of the main components of the Decision Support System (DSS) is guided by standard DSS textbook such as Turban *et al*. [53]. A fourth component, the scenario management was added to package the functionally required by scenarios creation, storage, retrieval, analysis, evaluation and reporting. An Intelligent Agent for supporting scenario creation is also included in the frame-work. **Figure 3** shows the main components of the DSS, their interactions (data and control flows) with the Transportation Object Repository, with each other and with the User Interface Management Subsystem **(**UIMS) directly or indirectly. In the following section we briefly describe each of these components.

4.1. Urban Transportation Object Repository (UTOR)

The Urban Transportation Object Repository (UTOR) is an object oriented repository storing various transportation objects such as nodes, links, and zones for multimodal urban networks; equilibrium models; impact models, scenarios and user interfaces that are managed by the four subsystems discussed bellow. The four UTOR object stores are distinct but are integrated. These are:

1) Urban Transportation GIS-Data Store: This object store contains two distinct components:

Table 1. Four approaches and 22 techniques reduction of peak period traffic congestion.

Social Approaches
- Staggered Work Hours
- Shortened Work Weeks
Socio-Economic Approaches
Pricing and Regulatory Mechanisms
- Road Pricing
- Parking Controls
- Restricting Access
-Traffic Cells
- Auto-Free Zones with Facilities for Pedestrians
Land Use Planning
-New Towns
-Planned Communities
-Planned Neighborhoods
-Zoning and Building Codes
Marketing
-Incentives to Off-Peak Travel and Usage of Facilities
-Incentives to Mass Transit Usage
-Carpooling and Other Forms of Ride-Sharing Approaches
Socio-Technical Approaches
-Communications in Lieu of Travel
Technical Approaches
Traffic Engineering Techniques
-Freeway Surveillance and Control
-Traffic Simulation Models
-Maximum Use of Existing Facilities
Transit Operations
-Extended Area Services
-Priority Systems: Expressways and Freeways
-Priority Systems: Arterials Circulation Systems
Vehicle Design Factors

a) GIS Object Base: Contains various GIS Objects.

b) Transportation Data Warehouse (TDW). TDW is a multidimensional, object-oriented, nonvolatile integrated database containing various current and historical data about the transportation Objects (Inmon [54]). The TDW and GIS Objects are populated by the Extract Transform and Loading (ETL) component of Data Management subsystem (DMS) mentioned bellow.

2) Urban Transportation Model Base: contains various transportation equilibrium and impact models.

3) Scenarios Base: contains various scenarios objects that are created over times.

4) User Interface Base: contains various user interface (UI) objects created over time.

4.2. Data Management Subsystem (DMS)

The data management subsystem (DMS) is responsible for the data administration such as creation, storage, retrieval of node object, links object, and zone object for different modal network. DMS manages the Urban Transportation GIS-Data Store which contains two distinct but integrated data bases:

a) a GIS database contain the spatial data;

b) a transportation data warehouse mentioned above.

4.3. Extract, Transform and Load (ETL) Component

ETL component of the DMS extracts data from multiple sources, cleanse them and transform the data from its original to a form that could be place in TDW guided by the metadata, and then load the data into the TDW. The purpose of ETL is to populate TDW with integrated and cleansed data required by the transportation objects gathered from three main sources, the socio-economic, the demand data and the supply data.

4.4. Model Management Subsystem (MMS)

MMS is responsible for the creation, storage, retrieval of the transportation object models which are stored in the Model Object Base (MOB) for utilization or reuse. Two types of models are managed by MMS. These are:

a) The Transportation Network Equilibrium Models (MSTEM)

b) Impacts Models: such as impact on Users, impact on operators, impact on owners, impact on society, and impact on government discussed earlier in Section 3.

4.5. Scenario Management Subsystem (SMS)

Much like MMS, SMS is responsible for the creation, storage, retrieval, analysis, evaluation of scenarios. An important part of SMS is the impact evaluation component that assesses the impact models and presents the assessment results to the SMS. Objects are stored in Scenario Object Base (SOB) for future utilization or reuse by SMS and Intelligent Scenario Creation Assistance Agent (ISCAA) described bellow. SMS retrieves previously created scenarios and pass them to the User Interface Management Subsystem (UIMS) as initial scenarios on which further what-if analysis could be performed.

4.6. Intelligent Scenario Creation Assistance Agent (ISCAA)

The complexity of creating the right scenario or retrieving the right scenario from the previous created ones stored in the scenario base is a complex process requires human expertise which is scarce. An intelligent component within the DSS framework that would look at the historical scenario objects and assist and guide the decision maker in choosing the best alternatives from this pool of historical scenario object to be included in the initial scenario setup is extremely valuable. A solution for this problem is to create an Intelligent Scenario Creation. Assistance Agent (ISCAA) that would encode and encapsulates the expertise for scenario creation and would provide the necessary assistance for creating the right scenario. ISCAA would be a hybrid intelligent agent containing multiple computational intelligent tools (such as ANN, Rough Set, Fuzzy Logic, etc.) as well as a set of scenario creation rules.

4.7. User Interface Management Subsystem (UIMS)

The UIMS packages and manages the functionalities require for creating a data-rich intensive (maps, graphs, text, and structured data) with various visualization capabilities user interface. Since The DSS is to be used by users with various roles (Transportation Planners, Transportation Engineers, Transportation Decision Makers or Traffic Administrators), the complexity involves in dynamically creating the right graphical user interface (GUI) for the right role lies within the functionality of UIMS. For example, the transportation planner is responsible for creating models and capturing the right data for those models, as such he/she would directly interact with Model Management and Data Management and as such the GUI for this role would configure that would allow for that only. On the other hand, the transportation decision maker role deals with scenarios and as such the UIMS would create the proper GUI allowing various scenario related activities such as scenario creation, retrieval, storage and execution and presenting the result in a dashboard view allowing for a comprehensive, at-a-glance, GIS-Based graphical view of the solution generated. UIMS also provides various analysis tools such as what-if analysis, sensitivity analysis, reporting the result of impact evaluation and providing various Ad hoc queries and reports. The Graphical Interface Objects, that are created, are stored as UI Objects in the UTOR and managed by UIMS.

All components of CMS can be adapted through the Users Characteristics and Behavior (Activity System Options) and Owners; Operators; and Regulators Behavior (Transportation System Options) in **Figure 2**, in addition, to any roadway capacity expansion through the Transportation System Options. In other word, our framework in **Figure 2** can be adapted to any of the single 22 techniques in table one or any combinations (packages) of these techniques, but the evaluating and recommending alternative strategies for CMS will be done through the results of the total evaluation of Impact Models (the positive and negative parts) on Users, Owners, Operators, Regulators, Government, and Society at large for each alternative or packages of alternations. All the alternative can be reflected through the MSTEM model demand and performance (link cost functions) parameters and socio-economic and land use variables.

5. Summary, Conclusion and Future Research

5.1. Summary

Traffic congestion is a very complicated problem that

affects the social, economic and development aspects of many countries around the world. The relationship between the traffic congestion problem and socioeconomic characteristics of trip makers and the rapid increase of urbanization of the land use make the problem becomes much more complicated and calls of urgent solution. Many techniques for solving this problem were suggested starting from empirical studies for a single technique or packages of techniques , to advanced Transportation System Management (TSM) and finally to Congestion System Management (CSM). Most of these techniques tried to maximize the utilization of the existing transport system (Roads, Highways, and Transit systems) by certain management techniques prior to any expansion or addition to the transport system.

US Federal transportation legislation requires Metropolitan Planning Organizations (MPO) to develop and implement a CMS as part of the metropolitan transportation planning process [22]. Most of MPOs use traditional transportation planning modeling approach and a commercial specialized software as a part of this process to evaluate traffic relive and the length and cost for deferent alternative solutions prior to submitting their recommendations. This process requires highly educated, trained and expert personnel in transportation planning and engineering field. It would also require very user friendly transportation planning software that includes a state of the art transportation network equilibrium models. Models that are significantly more advanced than the traditional four steps sequential. Models that combine single class Trip Generation- Trip Distribution- Modal Split-Trip Assignment (TG-TD-MS-TA) [41], or a multiclass combined model [36] that combine TG-TD-MS-TA in addition to Departure Time for different class of traveler depend on income, car ownership, trip purpose, … etc.

As Boyce [55] says, "combined or integrated models of origin-destination, mode, route and time period choice can be implemented and solved with practitioner software systems such as CUBE, EMME/2, PTV Vision, QRS II, SATURN or TransCAD, if the travel forecaster has a detailed understanding of the models and the solution algorithm. Ongoing discussions with practitioners reveal that few practitioners have this requisite expertise. The observed inability of many practitioners to solve the sequential procedure with feedback in a convergent manner is one indication of this dilemma. An alternative approach is to design a software system which directly solves such an integrated model, including providing a number of options to the user. This approach was taken by the Chilean software vendor, MCT, in the development of its product ESTRAUS. The distinction between these two software development philosophies may be more subtle than is generally appreciated. The former approach offers the forecaster a "tool kit" with which to "build" a model. Then the practitioner must acquire the expertise to use it, an uncertain and arduous process with many pitfalls. The latter provides a "canned" model and an algorithm for solving it. When presented with a description of ESTRAUS, a typical user's comment is, "This is interesting, but I don't know how we would use it to solve our model." This comment may offer a clue to the dilemma of vastly upgrading or revolutionizing practice, which presumably is one of the aims of academics as well as software vendors. Would a standard set of models with numerous user options provide a more effective pathway to improving travel forecasting practice than attempting to upgrade practice model by model? Certainly, this option is worth considering, so long as several of the vendors can effectively participate in the software market".

5.2. Conclusions

The main conclusions of this research paper can be summarized as follows:

1) In this research paper, it was possible to integrate all of the above requirements in a unified framework of analyses that capture the concept of the interaction of the transport system with the activity system in one Transportation System Analysis (TSA) approached. Developing this TSA framework as a TCMS within an Intelligent Decision Support System (IDSS), that can be a useful decision support tool for transportation planners and transportation decision makers for the analysis and evaluation of strategic transportation plans include transportation projects and policies and utilizing the stat of the art of the Multiclass Transportation Equilibrium Model MSTEM [36] within an easy to use environment that would eliminate or reduce the necessity for highly educated and trained transportation specialists and decision makers, is the cornerstone of this paper.

2) The paper presents many transportation concepts and integrate all of them in such a comprehensive framework that is easy to follow and undetectable for practitioners transportation planners, transportation Engineers, or transportation decision makers.

3) The Intelligent Scenario Creation Assistance Agent (ISCAA) and the Scenario Management Subsystem (SMS) components of the IDSS architecture will be the most important components that will reduce the need of the expertise and high education level of the transportation planners and transportation engineers or any transportation decision makers. This IDSS will reduce the gap between the practitioners and software vendors and increase the usability of the most sophisticated and more behaviorally relevant Multiclass Transportation Equilibrium Model like MSTEM.

5.3. Future Research

The author started a development of data collection pro-

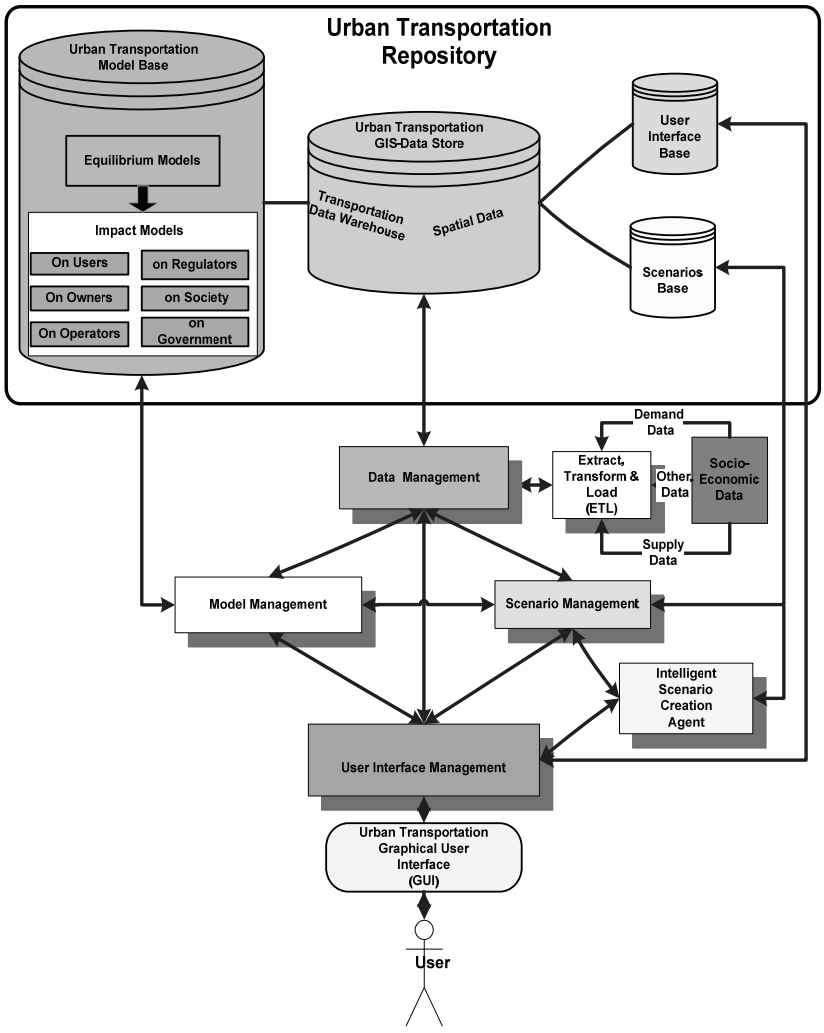

Figure 3. The architecture and information flow of the intelligent decision support system for urban transportation systems analysis as TCMS.

gram for Saint Louis Region area during his sabbatical year at University of Missouri at Saint Louis. These data will be used in the calibration and validation process for STEM, MSTEM, and ESTRAUS models for future comparisons among these models. The results of these comparisons will be reported in upcoming papers

The development of a prototype, derived from the framework described in this paper is also under way. The result of the experimentation with the prototype, in terms of its usability, degree of ease and its effectiveness in providing optimum solutions/scenarios to transportation and decision makers will be reported in upcoming papers.

6. Acknowledgements

The author wish to thank the Research Administration (RA), Kuwait University for granting the financial assistance and sponsoring this research. This research is supported by Kuwait University, Research Grant No. [IQ04/04].

7. References

[1] E. F. Ogunbodede, "Transport Management Techniques of Rapidly Changing Urban Land Use," *The Case of Akure International Journal of Environment and Development*, Vol. 1, No. 1, 1998, pp. 81-86.

[2] E. S. Mills, "Studies in the Structure of the Urban Economy," The Johns Hopkins Press, Baltimore, 1972.

[3] D. C. Gazis, "Optimum Control of a System of Oversaturated Intersections," *Operations Research*, Vol. 12, 1964, pp. 815-831.

[4] R. L. Gordon, "A Technique for Control of Traffic at Critical Intersections," *Transportation Science*, Vol. 4, 1969, pp. 279-287.

[5] D. Longley, "A Control Strategy for a Congested Computer Controlled Traffic Network," *Transportation Re-*

search, Vol. 2, 1968, pp. 391-408.

[6] L. J. Pignataro, W. R. McShane, K. W. Crowley, B. Lee and T. W. Casey, "Traffic Control in over Saturated Conditions," *NCHRP Report*, No. 194, 1978.

[7] N. H. Gartner, C. Stamatiadis and P. J. Tarnoff, "Development of Advanced Traffic Signal Control Strategies for Intelligent Transportation Systems: Multilevel Design," *Transportation Research Record*, Vol. 1494, 1995, pp. 98-105.

[8] D. J. Quinn, "A Review of Queue Management Strategies," *Traffic Engineering and Control*, Vol. 33, No. 11, 1992, pp. 600-605.

[9] A. K. Rathi, "A Control Strategy for High Traffic Density Sector," *Transportation Research B*, Vol. 22, No. 2, 1988, pp. 81-101.

[10] A. K. Rathi, "Traffic Metering: An Effectiveness Study," *Transportation Quarterly*, Vol. 45, No. 3, 1991, pp. 421-440.

[11] T. S. Reddy, E. Madhu and J. V. R. Reddy, "TSM Actions to Improve the Traffic Operations—A Case Study," *ACE*, Vol. 2, 2002, pp. 922-932.

[12] J. V. R. Reddy, "Application of TSM Actions—A Case Study on Mathura Road in Delhi," Master's Thesis, University of Baroda, Vadodra, 1998.

[13] J. M. Thomson, "Reflections on the Economics of Traffic Congestion," *Journal of Transport Economics and Policy*, Vol. 32, No. 1, 1998, pp. 93-112.

[14] Adefolalu, "Traffic Management and Enhanced Urban Environment in Nigeria: A Discussion," In: E. O. Adeniyi and I. B. Bell-Imam, Ed., 1977.

[15] S. O. Oyefesobi, "Measures to Improve Traffic Flow and Reduce Road Accidents in Nigeria," In: S. O. Onakomaiya and K. F. Ekanem, Ed., *Transportation in Nigerian. National Development Proceedings of a National Conference*, Ibadan, July 1977, pp. 4-9.

[16] J. M. A. Orioke, "Traffic Education and Flow in Ibadan City," In: S. O. Onakomaiya and N. F. Ekanm, Ed., 1981.

[17] M. A. Kennedy and K. Walter, "TSM Measures for Major Activity Centers," *Transportation Engineering Journal*, Vol. 105, No. 5, 1979, pp. 499-511.

[18] E. Lindquist, "Assessing Effectiveness Measures in the ISTEA Management Systems," Southwest Region University Transportation Center, Texas Transportation Institute, College Station, Texas, 1999.

[19] http://www.countyofkings.com/kcag/Plans_Programs/Regional%20Transportation %20Plan%20Section/Final-TS

[20] http://www.madisonareampo.org/Plan%20Elements/CongstMngt.pdf

[21] http://www.marc.org/transportation/cms/policy.pdf

[22] http://www.gvmc.org/transportation/CongestionManage

[23] S. Ossowski, J. Hernandez, M. Belmonte, A. Fernandez, A. Garcıa-Serrano, J. Pe´rez-de-la-Cruz, J. Serrano and F. Triguero, "Decision Support for Traffic Management Based on Organizational and Communicative Multiagent Abstractions," *Transportation Research Part C*, Vol. 13, 2005, pp. 272-298.

[24] S. French, "Decision Analysis and Decision Support Systems," University of Manchester, Manchester, 2000.

[25] M. Silver, "Systems that Support Decision Makers," John Wiley, Berlin, 1991.

[26] M. Klein and L. Methlie, "Knowledge-Based Decision Support Systems," John Wiley, Berlin, 1995.

[27] J. Hernandez and J. Serrano, "Environmental Emergency Management Supported by Knowledge Modelling Techniques," *AI Communications*, Vol. 14, No. 1, 2001, pp. 13-22.

[28] J. Hernandez and J. Serrano, "Reflective Knowledge Models to Support an Advanced HCI for Decision Management," *Expert Systems with Applications*, Vol. 19, No. 4, 2000, pp. 289-304.

[29] I. Vlahavas, N. Bassiliades, I. akellariou, M. Molina, S. Ossowski, I. Futo, Z. Pasztor, J. Szeredi, I. Velbitskiyi, S. Yershov and I. Netesin, "Expernet—An Intelligent multi-agent System for WAN Management," *IEEE Intelligent Systems*, Vol. 16, No. 7, 2002, p. 62.

[30] J. Cuena, S. Ossowski, "Distributed models for decision support," In: Weiss Ed., MIT Press, Cambridge, 1999, pp. 459-504.

[31] S. Ossowski, J. Hernandez, C. Iglesias and A. Fernandez, "Engineering Agent Systems for Decision Support," In: T. Zambonelli Eds., *Engineering Societies in an Agent World* III, Springer, Berlin, 2002, pp. 234-274.

[32] C. Iglesias, M. Garijo Ayestara´n and J. Gonza´lez, "A Survey of Agent-Oriented Methodologies," *Intelligent Agents* V, Springer, Berlin, 1999, pp. 317-330.

[33] K. Hoa Dam, M. Winikoff, "Comparing agent-oriented methodologies," In: Giorgini *et al.* Eds., *Agent-Oriented Information Systems*, Springer, Berlin, 2003, pp. 78-93.

[34] C. W. Holsapple, "Decision Support Systems. Encyclopedia of Information Systems," Vol. 1, 2003, pp. 551-565.

[35] H. L. Zhang, "Agent-Based Open Connectivity for Decision Support Systems," Ph.D. Thesis, School of Computer Science and Mathematics, Victoria University, 2007.

[36] M. K. Hasan and H. M. Dashti, "A Multiclass Simultaneous Transportation Equilibrium Model," *Networks and Spatial Economics*, Vol. 7, No. 3, 2007, pp. 197-211.

[37] J. De Cea, J. E. Fernandez, V. Dekock, A. Soto and T. L. Friesz, "ESTRAUS: A Computer Package for Solving Supply-Demand Equilibrium Problem on Multimodal urban Transportation Networks with Multiple User classes," *The Annual Meeting of the Transportation Research Board*, Washington, DC, 2003.

[38] M. Florian, J. H. Wu and S. He, "A Multi-Class Multi-Mode Variable Demand Network Equilibrium Model with Hierarchical Logit Structures," In: Current Trends, M. Gendreau and P. Marcotte Eds. Dordrecht, 2002, pp. 1131-1119.

[39] D. E. Boyce, H. Bar-Gera, "Multiclass Combined Models for Urban Travel Forecasting," *Networks and Spatial*

Economics, Vol. 4, 2004, pp.115-124.

[40] J. De Cea, and J. E. Fernandez, "Transit Assignment for Congested Public Transport Systems: An Equilibrium Model," *Transportation Science*, Vol. 27, No. 2, 1993, pp. 133-147.

[41] K. N. A. Safwat, and T. L. Magnanti, "A Combined Trip Generation, Trip Distribution, Modal Split and Traffic Assignment Model," *Transportation Science*, Vol. 22, No. 1, 1988, pp. 14-30.

[42] N. Oppenheim, "Urban Travel Demand Modeling: From Individual Choices to General Equilibrium," John Wiley and Sons, New York, 1995.

[43] B. Ran and D. E. Boyce, "Modeling Dynamic Transportation Networks," Springer-Verlag, Berlin, 1996.

[44] M. J. Smith, "The Existence, Uniqueness and Stability of Traffic Equilibria," *Transportation Research B*, Vol. 13, 1979, pp. 295-304.

[45] M. J. Smith, "The Existence and Calculation of Traffic Equilibria," *Transportation Research B*, Vol. 17, 1983, pp. 291-303.

[46] S. C. Dafermos, "An Iterative Scheme for Variational Inequalities," *Mathematical Programming*, Vol. 26, 1983, pp. 40-47.

[47] S. C. Dafermos, "Relaxation Algorithm for the General Asymmetric Traffic Equilibrium Problem," *Transportation Science*, Vol. 16, No. 2, 1982, pp. 231-240.

[48] M. Florian and H. Spiess, "The Convergence of Diagonalization Algorithms for Asymmetric Network Equilibrium Problems," *Transportation Research B*, Vol. 16, 1982, pp. 447-483.

[49] H. S. Mahmassani and K. C. Mouskos, "Some Numerical Results on the Diagonalization Network Assignment Algorithm with Asymmetric Interactions between Cars and Trucks," *Transportation Research B*, Vol. 22, 1988, pp. 275-290.

[50] Y. Sheffi, "Urban Transportation Networks: Equilibrium Analysis with Mathematical Programming Methods," Prentice-Hall, Englewoods Cliffs, 1985.

[51] K. N. A. Safwat and B. Brademeyer, "Proof of Global Convergence of an Efficient Algorithm for Predicting Trip Generation, Trip Distribution, Modal Split and Traffic Assignment Simultaneously on Large-Scale Networks," *International Journal of Computer and Mathematics with Applications*, Vol. 16, No. 4, 1988, pp. 269-277.

[52] S. Rosenbloom, "Peak-Period Traffic Congestion: A State-Of-The-Art Analysis and Evaluation Of Effective Solutions," *Transportation*, Vol. 7, 1978, pp. 167-191.

[53] T. Efraim, *et al.*, "Decision Support and Business Intelligence Systems," 8th Edition, Pearson Prentice Hall, New Jersey, 2007.

[54] W. Inmon, "Building the Data Warehouse, 4th Edition, Wiley, New York, 2005.

[55] D. Boyce, "Forecasting Travel on Congested Urban Transportation Networks: Review and Prospects for Network Equilibrium Models," *Networks and Spatial Economics*, Vol. 7, 2007, pp. 99-128.

Engineering, 2010, 2, 290-298
doi:10.4236/eng.2010.24038 Published Online April 2010 (http://www.SciRP.org/journal/eng)

A More Precise Computation of along Wind Dynamic Response Analysis for Tall Buildings Built in Urban Areas

Shu-Xun Chen
Guangxi University, Nanning, China
E-mail: *chenshx@gxu.edu.cn*
Received November 12, 2009; *revised January* 25, 2010; *accepted February* 4, 2010

Abstract

Modern tall buildings are generally built in urban areas, where value of the terrain roughness length is much greater than that of the general terrain areas, therefore wind-induced vibrations become more pronounced. The present formulas of numerical analysis of wind-induced response become less accurate. A more accurate expression of along-wind load spectrum matrix is proposed. On the basis of the expression, structural analysis formula of along-wind displacement and acceleration response are developed and programmed. The rationality of these formulas are illustrated in examples.

Keywords: Tall Building, Wind Load Spectrum, Wind-Induced Vibration, Response Analysis, Structural Analysis

1. Introduction

In modern cities, buildings get taller and more slender. The effects of wind-induced motions become more pronounced. Accurate prediction of structural response to wind-induced random vibrations displacement and vibration acceleration at the design stage is a basis for structural safety design and serviceability design of modern tall buildings. The wind-induced response consists of along-wind response, across-wind response and torsion response [1,2]. The paper focuses on along-wind response analysis firstly.

Several quasi-static methods in wind codes in various countries and approximate methods based on wind tunnel studies are used to predict the wind-induced response. As a building gets taller, the wind-induced random vibrations becomes more violent, these methods become less reliable. So the wind-induced response of modern tall buildings should be assessed accurately by using the theory of random vibration. Using the numerical analysis methods of random vibration response of tall buildings, people calculate structural response according to wind load spectra. According to present literatures [2-5] whose representative is literature [3], considering that the values of terrain roughness lengths are generally very small, and the turbulence densities are also very small, square items of the turbulence component are neglected in expression formula of the wind load in along-wind direction. But, for the modern tall buildings built in urban areas, the values of terrain roughness lengths are much more than ones for general buildings in general open areas. So that these items should not be neglected for tall buildings, as they are the same order values with some items that are not neglected. Otherwise, calculation results of the turbulence response of the tall buildings will have a large relative error.

To overcome the above-mentioned error, a more accurate expression of wind load spectrum matrixes is proposed in this paper. This expression is especially applicable to tall and other important buildings. Even an approximate form of the accurate expression is more precise than the present expression [3]. On the basis of this expression of wind load spectrum, structural analysis formulas of wind-induced displacement response and acceleration response in along-wind direction are developed and programmed. The expression forms of wind load spectrum and the analysis formulas proposed in this paper are especially suitable for using the models of the structural finite element analysis of tall buildings and their results of vibration modal analysis. These analysis results of wind-induced response can be directly used in member stress analysis, structural deformation analysis and structural serviceability analysis of tall buildings.

Rationality of the expression forms of wind load spectrum and the analysis formulas proposed is shown in comparison examples.

The project supported by Dr Chun-Man Chan of HKUST.

2. Expression of Wind Load Spectrum Matrix

2.1. Wind-Induced Load Vector

Wind around tall building flows in a complex and random way, so the wind is a random process. Wind loads acting on windward walls are mainly caused by the steady flow and the turbulence flow. The wind speed at node i of the windward walls can be expressed as:

$$V_i(t) = V_{oi} + V_{ri}(t) \quad (1)$$

where V_{oi} is the mean wind speed at node i, V_{oi} can be obtained with the following formulas:

$$V_{oi} = V_o (h_i/h_o)^{\alpha} \quad (2)$$

here V_0 is standard wind speed at a reference height h_o, e.g. 10 m, $\alpha = 0.12 \sim 0.30$, h_i is height of node i. $V_{ri}(t)$ in Equation (1) is the fluctuate wind speed at height h_i, its power spectrum density $S_{ri}(\omega)$ can be determined by fomulas of the present representative literature [3].

Because along-wind drag force is directly proportional to the square of relative wind speed, wind load acting vertically on node i of windward walls of a tall building can be expressed as:

$$P_{ui} = c_i a_i(\rho/2)[V_i(t) - U_i']^2 = c_i a_i(\rho/2)[V_i(t)^2 - 2V_i(t)U_i' + U_i'^2] \quad (3)$$

in which

c_i ----- c_i is the drag coefficient describing the ratio of the wind load per unit area at i node and the velocity pressure $(\rho/2)[V_i(t) - U_i']^2$.

a_i ----- area distributed at i node;

ρ ----- air density

U_i' ----- along-wind displacement speed of node i.

In Equation (3), since wind speed $V_i(t)$ is much greater than the structural displacement speed U_i', the high order small value $U_i'^2$ can be undoubtedly neglected, then we can get

$$P_{ui}(t) = c_i a_i(\rho/2)[V_i(t)^2 - 2V_i(t)U_i'] \quad (4)$$

Let

$$C_{ai} = c_i a_i (\rho/2) 2 V_i(t) \approx c_i a_i \rho V_{oi} \quad (5)$$

Adding C_{ai} to the structural damping coefficient C_{si}, a total damping coefficient C_i is obtained:

$$C_i = C_{si} + C_{ai} \quad (6)$$

It is taken as the i-th diagonal element of damping matrix $\boldsymbol{C}$ of the structural dynamic equation of the tall building shown in Equation (7):

$$\boldsymbol{K U + C U' + M U'' = P}(t) \quad (7)$$

Then the along-wind load vector of the tall building can be expressed as:

$$\boldsymbol{P_u}(t) = \{c_i a_i(\rho/2) V_i(t)^2\} \quad (i = 1, 2, ..., N) \quad (8)$$

where N is the total number of structural freedom degrees. In Equation (8), if i does not correspond to the along-wind load of the nodes of the windward walls, then c_i is taken as zero.

Place Equation (1) into Equation (8):

$$\boldsymbol{P_u}(t) = \{c_i a_i(\rho/2)[V_{oi} + V_{ri}(t)]^2\} = \{c_i a_i(\rho/2)[V_{oi}^2 + 2V_{oi}V_{ri}(t) + V_{ri}^2(t)]\} \quad (i = 1, 2, ..., N) \quad (9)$$

In the present literature, e.g. in page 76 of the present representative literature [3], $V_{ri}^2(t)$ is neglected, then

$$\overline{\boldsymbol{P}}_u(t) = \{c_i a_i(\rho/2)[V_{oi}^2 + 2V_{oi}V_{ri}(t)]\} \quad (i = 1, 2, ..., N) \quad (10)$$

The author consider that $V_{rI}^2(t)$ should not be neglected for tall buildings in urban areas. The author's reason is as follows:

In Equation (1), $V_{ri}(t)$ is the turbulent flow speed at i node. It is a random process with a zero mean value. Its variance is determined by the following equations:

$$\sigma_{ri}^2(h_i) = E[V_{ri}^2(t)] = V_{oi}^2 I_{ri}^2 \quad (11)$$

where I_{ri} is the turbulence density at i node, it can be obtained from the following equation [3]:

$$I_{ri} = \sigma_{ri}(h_i)/V_{oi} = 1/\ln(h_i/r_o) \quad (12)$$

where h_i is the height of i node, r_o is the roughness length of building terrain, $r_o = 10^{-5} \sim 10$ meter is determined by the terrain type. Because most of the modern tall buildings are usually built in urban areas, roughness length r_o of urban area is about 1-10 meter [3], which is a very great value. $V_{ri}^2(t)$ is not much less than V_{oi}^2, for instance, when $r_o = 3$ m and $h_i = 22$ m, then $I_{ri} = \sigma_{ri}(h_i)/V_{oi} = 0.5$. In Equation (11), $\sigma_{ri}^2(h_i) = E[V_{ri}^2(t)] = V_{oi}^2 I_{ri}^2 = 0.25 V_{oi}^2$. When $h_i = 22$ m, the relationship curve of I_{ri}^2 and r_o is showm in **Figure 1**:

It is shown in the The relationship curve in **Figure 1** that I_{ri}^2 of tall buildings in urban area of is much more

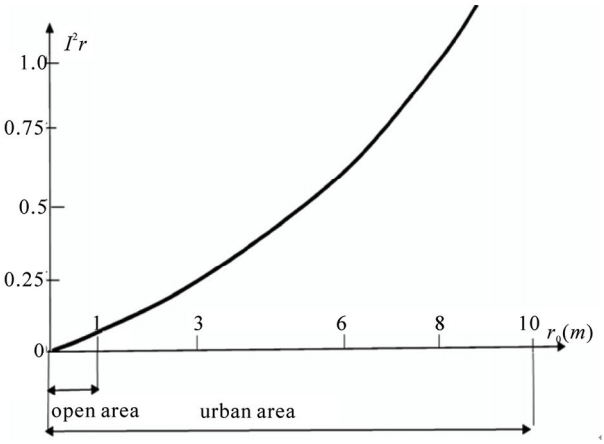

Figure 1. The relationship curve of I_{ri}^2 and r_o.

than one of general buildings in open area. Considering Equation (11), $V_{ri}^2(t)$ of Equation (9) can not be neglected, and Equation (10) with $V_{ri}^2(t)$ neglected can only be applied to buildings built in general open terrain. For modern tall buildings in urban areas, Equation (10) will cause a large relative error.

2.2. Wind Load Correlation Matrix

Correlation matrix of the wind load vector shown as Equation (9) is

$$\boldsymbol{R}_{\boldsymbol{P}u}(\tau) = E[\boldsymbol{P}_{\boldsymbol{u}}(t)\boldsymbol{P}_{\boldsymbol{u}}^{T}(t+\tau)] \quad (13)$$

Its element of row i, column j is:

$$\begin{aligned} R_{Puij}(\tau) &= c_i c_j a_i a_j (\rho/2)^2 E\{[V_{oi}+V_{ri}(t)]^2 \\ &\times [V_{oj}+V_{rj}(t+\tau)]^2\} \\ &= c_i c_j a_i a_j (\rho/2)^2 E[V_{oi}^2 V_{oj}^2 \\ &+ 2V_{oi}^2 V_{oj} V_{rj}(t+\tau) + 2V_{oi} V_{oj}^2 V_{ri}(t) \\ &+ V_{oi}^2 V_{rj}^2(t+\tau) + V_{oj}^2 V_{ri}^2(t) \\ &+ 4V_{oi} V_{oj} V_{ri}(t) V_{rj}(t+\tau) \\ &+ 2V_{oi} V_{ri}(t) V_{rj}^2(t+\tau) + 2V_{oj} V_{ri}^2(t) V_{rj}(t+\tau) \\ &+ V_{ri}^2(t) V_{rj}^2(t+\tau)] \end{aligned} \quad (14)$$

Because $V_{ri}(t)$ and $V_{rj}(t+\tau)$ are stationary ergodic normal distributive random processes [2,5,6], then

$$E[V_{ri}(t)] = E[V_{rj}(t+\tau)] = 0 \quad (15)$$

$$E[V_{ri}^2(t)] = \sigma_{ri}^2 \quad (16)$$

$$E[V_{rj}^2(t+\tau)] = \sigma_{rj}^2 \quad (17)$$

$$E[V_{ri}(t)\, V_{rj}(t+\tau)] = R_{rij}(\tau) \quad (18)$$

$$E[V_{ri}^2(t) V_{rj}(t+\tau)] = E[V_{ri}(t) V_{rj}^2(t+\tau)] = 0 \quad (19)$$

$$E[V_{ri}^2(t) V_{rj}^2(t+\tau)] = \sigma_{ri}^2\sigma_{rj}^2 + 2R_{rij}^2(\tau) \quad (20)$$

Then Equation (14) can be:

$$\begin{aligned} R_{Puij}(\tau) &= c_i c_j a_i a_j (\rho/2)^2 [V_{oi}^2 V_{oj}^2 \\ &+ V_{oi}^2\sigma_{rj}^2 + V_{oj}^2\sigma_{ri}^2 + \sigma_{ri}^2\sigma_{rj}^2 \\ &+ 4V_{oi} V_{oj} R_{rij}(\tau) + 2R_{rij}^2(\tau)] \end{aligned} \quad (21)$$

Considering Equation (12), the element of row *i*, column *j* of the correlation matrix of the wind load can be obtained:

$$\begin{aligned} R_{Puij}(\tau) &= c_i c_j a_i a_j (\rho/2)^2 [V_{oi}^2 V_{oj}^2 \\ &\times (1 + I_{ri}^2 + I_{rj}^2 + I_{ri}^2 I_{rj}^2) \\ &+ 4V_{oi} V_{oj} R_{rij}(\tau) + 2R_{rij}^2(\tau)] \end{aligned} \quad (22)$$

In the present literature [3], $V_{ri}^2(t)$ of wind load is neglected as Equation (10), then the correlation matrix shown in Equation (13) is

$$\boldsymbol{R}_{\overline{\boldsymbol{P}}u}(\tau) = E[\overline{\boldsymbol{P}}_u(t)\,\overline{\boldsymbol{P}}_u^{T}(t+\tau)] \quad (23)$$

The element of of row *i*, column *j* of the correlation matrix of the wind load is

$$\begin{aligned} R_{\overline{P}uij}(\tau) &= c_i c_j a_i a_j (\rho/2)^2 [V_{oi}^2 V_{oj}^2 \\ &+ 4V_{oi} V_{oj} R_{rij}(\tau)] \end{aligned} \quad (24)$$

Comparing Equation (24) and Equation (22), their relative error is a quite large for modern tall buildings built in urban areas.

2.3. Wind Load Spectrum Matrix

From Equation (22), a spectrum matrix of the wind load vector can be obtained:

$$S_{Pu}(\omega) = [1/(2\pi)] \int_{-\infty}^{\infty} R_{Pu}(\tau)\, e^{-j\omega\tau} d\tau \quad (25)$$

Its element of row i, column j is:

$$S_{Puij}(\omega) = [1/(2\pi)] \int_{-\infty}^{\infty} R_{Puij}(\tau)\, e^{-j\omega\tau} d\tau \quad (26)$$

Placing Equation (22) into Equation (26), the result is:

$$\begin{aligned} S_{Puij}(\omega) &= c_i c_j a_i a_j (\rho/2)^2 [V_{oi}^2 V_{oj}^2 \\ &\times (1 + I_{ri}^2 + I_{rj}^2 + I_{ri}^2 I_{rj}^2)\,\delta(\omega) \\ &+ 4V_{oi} V_{oj} S_{rij}(\omega) + 2S_{rij}(\omega) * S_{rij}(\omega)] \end{aligned} \quad (27)$$

in which the symbol $*$ expresses Duhamel integral, $\delta(\omega)$ is the δ- function:

$$\delta(\omega) = [1/(2\pi)] \int_{-\infty}^{\infty} e^{-j\omega\tau} d\tau \quad (28)$$

and

$$S_{rij}(\omega) = [1/(2\pi)] \int_{-\infty}^{\infty} R_{rij}(\tau)\, e^{-j\omega\tau} d\tau \quad (29)$$

$S_{rij}(\omega)$ is a cross-spectrum of turbulent wind velocity, which can be obtained from literature [2,12].

A good approximate expression of Equation (27) is

$$\begin{aligned} S_{Puij}(\omega) &= c_i c_j a_i a_j (\rho/2)^2 [V_{oi}^2 V_{oj}^2 (1 + I_{ri}^2 \\ &+ I_{rj}^2)\,\delta(\omega) + 4V_{oi} V_{oj} S_{rij}(\omega)] \end{aligned} \quad (30)$$

In the comparison example in this paper, relative error of Equation (30) and Equation (27) will be discussed.

If $V_{ri}^2(t)$ of Equation (9) is neglected as Equation (10), then the element of row *i*, column *j* of the wind load spectrum matrix is:

$$\begin{aligned} S_{\overline{P}uij}(\omega) &= c_i c_j a_i a_j (\rho/2)^2 [V_{oi}^2 V_{oj}^2 \delta(\omega) + 4 \\ &V_{oi} V_{oj} S_{rij}(\omega)] \end{aligned} \quad (31)$$

Comparing with Equation (31), the approximate expression Equation (30) has more items ($I_{rI}^2 + I_{rj}^2$), which is the same order value as the item corresponding to $4V_{oi}V_{oj}S_{rij}(\omega)$, and should not be neglected. Their

necessity is shown in the following formulas of wind-induced response analysis.

3. Wind-Induced Response Analysis

Wind-induced structural responses in along-wind direction include a static part, *i.e.* an along-wind translation, and a dynamic part, *i.e.* an along-wind random vibration. The along-wind translation is mainly caused by the steady flow. The along-wind vibration is caused by the turbulent flow. The along-wind random vibration includes a quasi-steady background turbulence response to low frequency component and a narrow-band resonant response.

3.1. Displacement Response Analysis

According to the analysis method of random vibration response, the calculation formula of spectrum matrix of the displacement response vector can be expressed as:

$$\boldsymbol{S}_{\boldsymbol{u}}(\omega) = \boldsymbol{H}_{\boldsymbol{u}}(\omega)\,\boldsymbol{S}_{\boldsymbol{Pu}}(\omega)\,\boldsymbol{H}_{\boldsymbol{u}}{}^{*}(\omega) \tag{32}$$

in which the spectrum matrix of wind-induced load $\boldsymbol{S}_{\boldsymbol{Pu}}(\omega)$ is shown as Equation (25), $\boldsymbol{H}_{\boldsymbol{u}}{}^{*}(\omega)$ is the conjugate matrixes of frequency response matrix $\boldsymbol{H}_{\boldsymbol{u}}(\omega)$, and

$$\boldsymbol{H}_{\boldsymbol{u}}(\omega) = \boldsymbol{\phi}_{\boldsymbol{u}}\,H_u(\omega)\,\boldsymbol{\phi}_{\boldsymbol{u}}{}^{T} \tag{33}$$

In which $\boldsymbol{\phi}_{\boldsymbol{u}}$ and $H_u(\omega)$ are the natural vibration shape and the frequency response function of the lower along-wind vibration model respectively. The relationship between the vibration shape and mass matrix is $\boldsymbol{\phi}_{\boldsymbol{u}}{}^{T}\boldsymbol{M}\,\boldsymbol{\phi}_{\boldsymbol{u}} = M_u{}^{*} = 1$. $H_u(\omega)$ can be obtained from the following formula:

$$H_u(\omega) = 1/[(\omega_u{}^2 - \omega^2) + j\,2\,\beta_u\,\omega_u\,\omega] \tag{34}$$

in which ω_u and β_u are the natural frequency and damping of the lowest along-wind vibration model.

The element of row i, column j of the displacement spectrum matrix shown in Equation (32) is:

$$S_{uij}(\omega) = \phi_{iu}\,\phi_{ju}\sum_{m=1}^{N}\sum_{n=1}^{N}\phi_{mu}\,\phi_{nu}\,|H_u(\omega)|^2\,S_{Pumn}(\omega) \tag{35}$$

In which ϕ_{iu} is the i-th element of vibration shape $\boldsymbol{\phi}_{\boldsymbol{u}}$ of the along-wind vibration mode. $S_{Pumn}(\omega)$ is shown as Equation (27). $|H_u(\omega)|$ is the absolute value of the frequency response functions of the along-wind vibration mode shown in Equation (34).

According to the response analysis theory of random vibration, the across mean square value matrix of the displacement response is:

$$E[\boldsymbol{U}_{\boldsymbol{u}}{}^{2}(t)] = \boldsymbol{R}_{u}(0) = \int_{-\infty}^{\infty}\boldsymbol{S}_{\boldsymbol{u}}(\omega)\,d\omega \tag{36}$$

Its N diagonal elements are mean square values of the displacement response of the N node freedom degrees. They are marked as a vector $\boldsymbol{\psi}_{\boldsymbol{u}}{}^{2}$. It includes the following two parts:

$$\boldsymbol{\psi}_{\boldsymbol{u}}{}^{2} = \boldsymbol{\mu}_{\boldsymbol{u}}{}^{2} + \boldsymbol{\sigma}_{\boldsymbol{u}}{}^{2} \tag{37}$$

its i-th element is the mean square value of displacement response of the i-th freedom degree. It is obtained from the following equation:

$$\psi_{ui}{}^{2} = \int_{-\infty}^{\infty}S_{uii}(\omega)\,d\omega = \phi_{iu}{}^{2}\sum_{m=1}^{N}\sum_{n=1}^{N}\phi_{mu}\,\phi_{nu}\times\int_{-\infty}^{\infty}|H_u(\omega)|^2\,S_{Pumn}(\omega)\,d\omega \tag{38}$$

in which $S_{Pumn}(\omega)$ is shown as Equation (27).

In Equation (37), $\boldsymbol{\mu}_{\boldsymbol{u}}{}^{2}$ is the square value vector of the static translation response. Its i-th element is the square value of the static translation of the i-th freedom degree. It is

$$\mu_{ui}{}^{2} = \phi_{iu}{}^{2}\sum_{m=1}^{N}\sum_{n=1}^{N}\phi_{mu}\;\phi_{nu}\;c_m c_n\;a_m a_n \times(\rho/2)^2\;V_{om}{}^{2}V_{on}{}^{2}\;/\omega_u{}^{4} \tag{39}$$

In Equation (37), $\boldsymbol{\sigma}_{\boldsymbol{u}}{}^{2}$ is the mean square value vector of the dynamic random vibration displacement response. Its i-th element is the mean square value of the random vibration displacement of the i-th freedom degree. It is

$$\sigma_{ui}{}^{2} = \phi_{iu}{}^{2}\sum_{m=1}^{N}\sum_{n=1}^{N}\phi_{mu}\;\phi_{nu}\;c_m c_n\;a_m\;a_n(\rho/2)^2 \times\{[V_{om}{}^{2}V_{on}{}^{2}(I_{rm}{}^{2}+I_{rn}{}^{2}+I_{rm}{}^{2}I_{rn}{}^{2})]/\omega_u{}^{4} + \int_{-\infty}^{\infty}|H_u(\omega)|^2[4\,V_{om}V_{on}S_{rmn}(\omega) + 2\,S_{rmn}(\omega)*S_{rmn}(\omega)]\,d\omega\} \tag{40}$$

in which $S_{rmn}(\omega)$ is shown as Equation (29).

For convenience of computation, $S_{Pumn}(\omega)$ of Equation (27) can be taken as its approximate form shown in Equation (30). So the mean square value of the random vibration displacement of the i-th freedom degree of the tall building $\sigma_{ui}{}^{2}$ becomes:

$$\sigma_{ui}{}^{2} = \phi_{iu}{}^{2}\sum_{m=1}^{N}\sum_{n=1}^{N}\phi_{mu}\,\phi_{nu}\,c_m c_n\,a_m a_n(\rho/2)^2 \times\{[V_{om}{}^{2}V_{on}{}^{2}(I_{rm}{}^{2}+I_{rn}{}^{2})]/\omega_u{}^{4} + \int_{-\infty}^{\infty}|H_u(\omega)|^2\,4\,V_{om}V_{on}S_{rmn}(\omega)\,d\omega\} \tag{41}$$

Considering:

$$\int_{-\infty}^{\infty} |H_u(\omega)|^2 S_{rmn}(\omega)\, d\omega \approx \int_{-\infty}^{\infty} |H_u(0)|^2 \times S_{rmn}(\omega)\, d\omega + \int_{\omega_u-\Delta\omega}^{\omega_u+\Delta\omega} |H_u(\omega)|^2 S_{rmn}(\omega)\, d\omega \approx r_{mn}\sigma_{rm}\sigma_{rn}/\omega_u^4 + S_{rmn}(\omega_u)[\pi/(2\beta_u\omega_u^3)] \quad (42)$$

where $|H_u(\omega_u)|^2 = 1/(2\beta_u\omega_u^2)^2$, $\Delta\omega = \pi\beta_u\omega_u$ r_{mn} is cross correlation. By convention of the present representative literature [3], σ_{ui}^2 of Equation (41) can be divided to the following two parts:

$$\sigma_{ui}^2 \approx \sigma_{ubi}^2 + \sigma_{uri}^2 \quad (43)$$

in which σ_{ubi}^2 is corresponding to the quasi-static turbulent ground displacement response of the i-th freedom degree. It is shown as follows:

$$\begin{aligned}\sigma_{ubi}^2 &= \phi_{iu}^2 \sum_{m=1}^{N}\sum_{n=1}^{N} \phi_{mu}\phi_{nu}c_m c_n a_m a_n (\rho/2)^2 \times V_{om}^2 V_{on}^2 (I_{rm}^2 + I_{rn}^2)/\omega_u^4 \\ &+ \phi_{iu}^2 \sum_{m=1}^{N}\sum_{n=1}^{N} \phi_{mu}\phi_{nu}\, c_m c_n a_m a_n (\rho/2)^2 \times 4\, V_{om}V_{on}\int_{-\infty}^{\infty} |H_u(0)|^2 S_{rmn}(\omega)\, d\omega \\ &= \phi_{iu}^2 \sum_{m=1}^{N}\sum_{n=1}^{N} \phi_{mu}\phi_{nu}c_m c_n a_m a_n (\rho/2)^2 \times V_{om}^2 V_{on}^2 (I_{rm}^2 + I_{rn}^2 + 4\, r_{mn} I_{rm} I_{rn})/\omega_u^4 \end{aligned} \quad (44)$$

In Equation (43), σ_{uri}^2 is corresponding to the dynamic turbulent resonant displacement response of the i-th freedom degree. It is shown as:

$$\begin{aligned}\sigma_{uri}^2 &= \phi_{iu}^2 \sum_{m=1}^{N}\sum_{n=1}^{N} \phi_{mu}\phi_{nu}c_m c_n a_m a_n \rho^2 \times V_{om}V_{on} \int_{\omega_u-\Delta\omega}^{\omega_u+\Delta\omega} |H_u(\omega)|^2 S_{rmn}(\omega)\, d\omega \\ &= \phi_{iu}^2 \sum_{m=1}^{N}\sum_{n=1}^{N} \phi_{mu}\phi_{nu}c_m c_n a_m a_n \rho^2 V_{om}V_{on} \times S_{rmn}(\omega_u)[\pi/(2\beta_u\omega_u^3)] \end{aligned} \quad (45)$$

If the quasi-static turbulent ground displacement response of Equation (44) is calculated according to the unreasonable approximate Equation (31) as the present representative literature [3], then it is

$$\begin{aligned}\overline{\sigma}_{ubi}^2 &= \phi_{iu}^2 \sum_{m=1}^{N}\sum_{n=1}^{N} \phi_{mu}\phi_{nu}c_m c_n a_m a_n (\rho/2)^2 \times 4\, V_{om}V_{on}\int_{-\infty}^{\infty} |H_u(0)|^2 S_{rmn}(\omega)\, d\omega \\ &= \phi_{iu}^2 \sum_{m=1}^{N}\sum_{n=1}^{N} \phi_{mu}\phi_{nu}c_m c_n a_m a_n (\rho/2)^2 \times V_{om}^2 V_{on}^2 (4\, r_{mn} I_{rm} I_{rn})/(\omega_u^4) \end{aligned} \quad (46)$$

In Equation (44), Comparing the relative values of the two items ($4\, r_{mn} I_{rm} I_{rn}$ and $I_{rm}^2 + I_{rn}^2$), it is obvious that the items corresponding to ($I_{ri}^2 + I_{rj}^2$) of Equation (30) can not be neglected as Equation (31), since the neglecting will cause a 50% or much higher relative error for the quasi-static turbulent ground displacement response.

3.2. Acceleration Response Analysis

Wind-induced acceleration response of a tall building are random values with zero mean values. Similar to Equations (37)-(40), the mean square value of acceleration response of the i-th freedom degree can be calculated as:

$$\begin{aligned}\sigma_{u''i}^2 &= \phi_{iu}^2 \sum_{m=1}^{N}\sum_{n=1}^{N} \phi_{mu}\phi_{nu}\int_{-\infty}^{\infty} \omega^4 \times |H_u(\omega)|^2 S_{Pumn}(\omega)\, d\omega \\ &= \phi_{iu}^2 \sum_{m=1}^{N}\sum_{n=1}^{N} \phi_{mu}\phi_{nu}\, c_m c_n a_m a_n (\rho/2)^2 \times \int_{-\infty}^{\infty} \omega^4 |H_u(\omega)|^2 \{ V_{om}^2 V_{on}^2 [1 + I_{rm}^2 + I_{rn}^2 + I_{rm}^2 I_{rn}^2]\, \delta(\omega) + 4\, V_{om}V_{on} S_{rmn}(\omega) + 2\, S_{rmn}(\omega) * S_{rmn}(\omega) \}\, d\omega \end{aligned} \quad (47)$$

Considering $\omega^4 |H_u(\omega)|^2 = 0$ when $\omega = 0$, can get

$$\begin{aligned}\sigma_{u''i}^2 &= \phi_{iu}^2 \sum_{m=1}^{N}\sum_{n=1}^{N} \phi_{mu}\phi_{nu}c_m c_n a_m a_n (\rho/2)^2 \times \int_{-\infty}^{\infty} \omega^4 |H_u(\omega)|^2 [4\, V_{om}V_{on} S_{rmn}(\omega) + 2\, S_{rmn}(\omega) * S_{rmn}(\omega)]\, d\omega \end{aligned} \quad (48)$$

Its approximate expression is shown as follows:

$$\sigma_{u"i}{}^2 = \phi_{iu}{}^2 \sum_{m=1}^{N} \sum_{n=1}^{N} \phi_{mu}\phi_{nu}c_m c_n a_m a_n \rho^2 \times V_{om} V_{on} \int_{-\infty}^{\infty} \omega^4 / H_u(\omega) /^2 S_{rmn}(\omega)\, d\omega \quad (49)$$

With reference to Equation (42), it can be calculated as:

$$\sigma_{u"i}{}^2 \approx \phi_{iu}{}^2 \sum_{m=1}^{N} \sum_{n=1}^{N} \phi_{mu}\phi_{nu}c_m c_n a_m a_n \rho^2 \times V_{om} V_{on} S_{rmn}(\omega_1)\,[\,\pi\omega_u/(2\beta_u)\,] \quad (50)$$

It is now widely accepted that wind-induced acceleration response has become the standard for the serviceability evaluation of motion perception in tall buildings. So Acceleration response analysis of tall buildings is of an important and practical significance

4. Example

Structure of a certain tall building is described as a 50-storey of 7-bay by 10-bay framework with 2550 nodes and 5100 members shown in **Figure 2**.

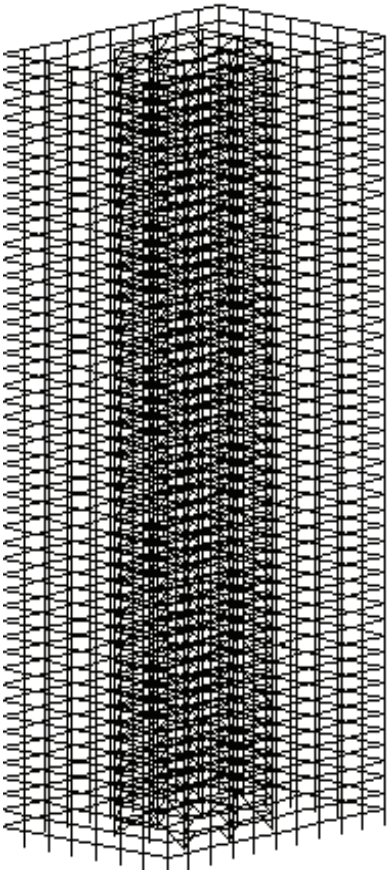

Figure 2. 3D model of the example building.

A bay width is 4.57 m and a storey height is 3.66 m. Details of the framework are shown in its plan view in **Figure 3** and elevation views in **Figures 4** and **5**.

The framework consists of exterior moment frames and a braced core, which are rectangles with the same centre. All beams and columns are rigidly connected while the diagonal braces are simply connected. Two-storey K-bracing modules are used on both the south and north faces of the core, as shown in **Figure 4**. Single-storey knee-bracing is used in the west and east faces of the core as shown in **Figure 4**.

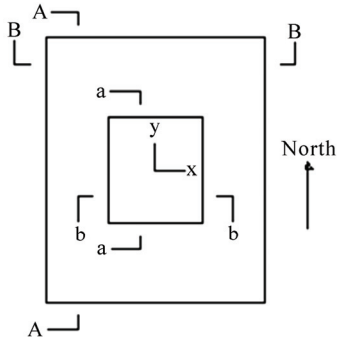

Figure 3. Plan view of the example.

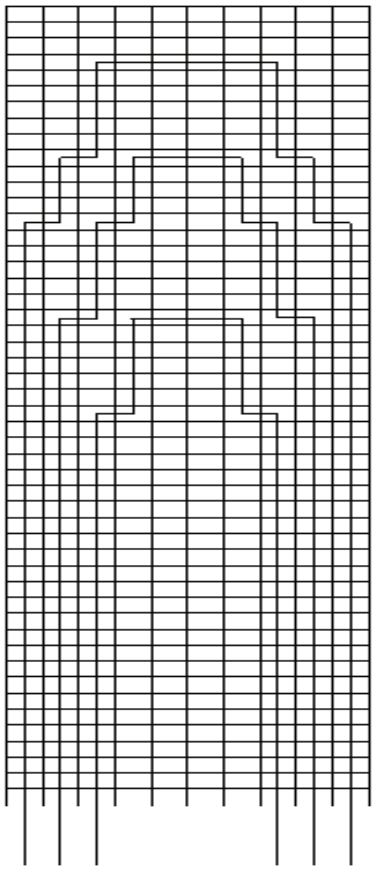

Figure 4. A-A view and drag coefficients c_i.

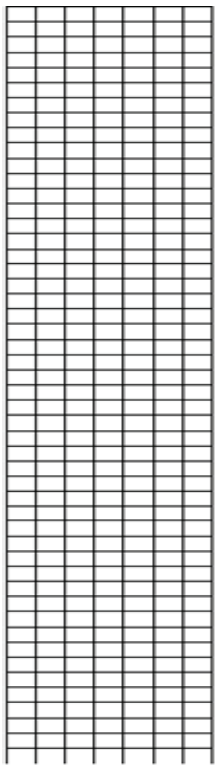

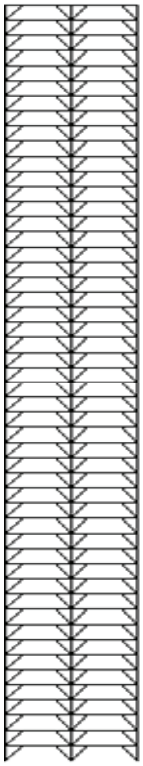

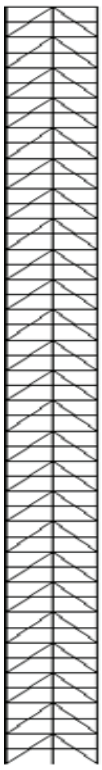

Figure. 5 B-B view. Figure 6. a-a view. Figure 7. b-b view.

The floors between the exterior frames and braced core are rigid. Mass density of the tall building is 150 kg /m^3, which is employed when node masses of this framework are calculated. American AISC standard sections are used to size the members: Beams are W24 × 103 shapes, diagonals are W14 × 90 shapes, and columns are also W14 × 233 shapes except that the cruciform columns in the core (See **Figure 3**) use pairs of two W14 × 233 shapes oriented perpendicular to each other.

The parameters about wind load are given as follows: the reference height h_0 = 10 m, the designed wind speed at the reference height V_{h0} = 30.0 m /s ^{2}, the roughness length of building terrain r_0 = 2 m, for **Equation (11)** and **Equation (12)**, $I_{ri} = \sigma_{ri}(h_i) / V_{oi} > 17.4\%$ at nodes over 22 meters. Non-dimensional decay constants C_y = C_z = 10.0 which is employed when cross-spectrums of turbulent wind are calculated, The drag coefficients c_i of surface nodes in along-wind direction are shown out as **Figure 4**.

In **Table 1**, the first, the second and third frequencies of natural vibration are given out. They are corresponding the bending vibration on X-direction, the bending vibration on Y-direction and the twist vibration of the tall building respectively.

Firstly, through the modal analysis, the lowest frequency and its vibration shape are obtained. They are corresponding to the bending vibration in along-wind direction, *i.e.* X-direction. Its circular frequency is ω_u = 0.86572 rad/s, its natural frequency is 0.13778 hertz.

In **Table 2**, the translation values of the bending vibration shapes on X-direction (along-wind direction) are listed. The relationship between the vibration shape and mass matrix are $\boldsymbol{\phi}_u^T \boldsymbol{M} \boldsymbol{\phi}_u = M_u^* = 1$. Because the floors between the exterior frames and braced core are rigid, the translation values at all nodes of the same storey are the same.

Table 1. Natural frequencies.

mode number	circular frequency	frequency (hertz)	period (sec)
1	8.6572E-01	8.6572E-01	7.2577E+00
2	9.6824E-01	1.5410E-01	6.4893E+00
3	1.2926E+00	2.0573E-01	4.8608E+00

Table 2. The bending vibration shapes in along-wind direction

Storey	X-translation	Storey	X-translation	Storey	X-translation	Storey	X-translation	Storey	X-translation
1	.14613E-05	11	.44215E-04	21	.11164E-03	31	.18569E-03	41	.25427E-03
2	.40615E-05	12	.50177E-04	22	.11898E-03	32	.19293E-03	42	.26052E-03
3	.70606E-05	13	.56396E-04	23	.12639E-03	33	.20013E-03	43	.26670E-03
4	.10390E-04	14	.62780E-04	24	.13381E-03	34	.20722E-03	44	.27271E-03
5	.14206E-04	15	.69378E-04	25	.14127E-03	35	.21426E-03	45	.27865E-03
6	.18365E-04	16	.76104E-04	26	.14871E-03	36	.22117E-03	46	.28442E-03
7	.22932E-04	17	.83006E-04	27	.15618E-03	37	.22803E-03	47	.29012E-03
8	.27790E-04	18	.90002E-04	28	.16360E-03	38	.23473E-03	48	.29567E-03
9	.33000E-04	19	.97138E-04	29	.17102E-03	39	.24137E-03	49	.30121E-03
10	.38456E-04	20	.10434E-03	30	.17836E-03	40	.24786E-03	50	.30640E-03

Table 3. The wind-induced response in along-wind direction.

Storey	μ_{ui}^2 (m^2)	σ_{ubi}^2 (m^2)	$\overline{\sigma}_{ubi}^2$ (m^2)	σ_{uri}^2 (m^2)	ψ_{ui}^2 (m^2)	$\sigma_{u''i}^2$ (m^2/Sec^4)
5	245014E-02	.533741E-03	.231407E-03	.571563E-02	.869952E-02	.321051E-02
10	.179546E-01	.391125E-02	.169575E-02	.418841E-01	.637499E-01	.235266E-01
15	.584374E-01	.127301E-01	.551921E-02	.136322E+00	.207489E+00	.765727E-01
20	.132175E+00	.287931E-01	.124835E-01	.308335E+00	.469303E+00	.173194E+00
25	.242297E+00	.527821E-01	.228841E-01	.565224E+00	.860303E+00	.317490E+00
30	.386227E+00	.841360E-01	.364778E-01	.900981E+00	.137134E+01	.506087E+00
35	.557352E+00	.121414E+00	.526400E-01	.130018E+01	.197895E+01	.730319E+00
40	.745866E+00	.162480E+00	.704444E-01	.173994E+01	.264828E+01	.977335E+00
45	.942683E+00	.205355E+00	.890331E-01	.219907E+01	.334711E+01	.123523E+01
50	.113979E+01	.248293E+00	.107649E+00	.265888E+01	.404696E+01	.149351E+01

According to Equation (39), Equation (44), Equation (46), Equation (45), Equation (38) and Equation (50), we respectively calculated the mean square value of the static translation displacement response μ_{ui}^2, the mean square value of the quasi-static turbulent ground displacement response σ_{ubi}^2, the mean square value of the unreasonable approximate quasi-static turbulent ground displacement response $\overline{\sigma}_{ubi}^2$ according to the unreasonable approximate Equation (31), the mean square value of the dynamic turbulent resonant displacement response σ_{uri}^2, the mean square value of the total displacement response ψ_{ui}^2 and the mean square value of the acceleration response $\sigma_{u''i}^2$. Considering only the response to the lowest resonant frequency, these mean square values are listed in **Table 3**.

Comparing the values of σ_{ubi}^2 and $\overline{\sigma}_{ubi}^2$ of **Table 2**, their relative error is $(\sigma_{ubi}^2 - \overline{\sigma}_{ubi}^2)/\overline{\sigma}_{ubi}^2 = 130.6\%$. Even $(\sigma_{ubi} - \overline{\sigma}_{ubi})/\overline{\sigma}_{ubi} = 51.8\%$. This fact strongly supports the above-mentioned conclusion that the items corresponding to $(I_{ri}^2 + I_{rj}^2)$ of Equation (30) can not be neglected as Equation (31) for tall buildings, since the neglecting will cause a 50% or much higher relative error for σ_{ubi}^2.

5. Conclusions

For modern tall buildings built in urban areas with a larger roughness length, the effects of wind-induced random vibrations become more pronounced. The square item of turbulence component $V_{ri}^2(t)$ of Equation (9) can not be neglected.

In this paper, a more accurate expression of along-wind load spectrum is proposed. On the basis of this expression form, analysis formula of wind-induced displacement and acceleration response in along-wind direction are developed and programmed.

As the present usual expression of along-wind load neglects the square item of turbulence component, even an approximate form of the accurate expression proposed is more accurate than the present expression. The example strongly supports this conclusion.

5. References

[1] A. G. Davenport, "Gust Loading Factors," *Journal of the Structural Divasion*, 1977, pp. 11-34.

[2] A. G. Davenport, "The Prediction Spectrum of Horizontal Gustiness Near the Ground in High Winds," 1963, pp. 194-211.

[3] C. Dyrbye and S. O. Hansen, "Wind Loads on Structures," John Wiley & Sons Inc., New York, 1996, pp. 49-106.

[4] C. H. Thorton, L. Joseph, *et al.*, "Optimization of Tall Structures for Wind Loading ," *Journal of Wind Engineering and Aerodynamics*, Vol. 36, 1990, pp. 235-244.

[5] E. Simiu and R. H. Scanlan, "Wind Effcts on Structrures: A Introduction to Wind Engineering," John Wiley & Sons Inc., New York, 1986.

[6] P. Sachs, "Wind Force in Engineering," Pergamon Press, Oxford, 1978, pp. 12-88.

[7] A. Pupleace, "Probability, Random Variable and Random Process", High Education Press, Beijing, 1983, pp. 18-48.

[8] L. G. Griffis, "Serviceability Limit States Under Wind Load," *Engineering Journal of American Institute of Steel Construction*, 1993, pp. 23-28.

[9] B. J. Vickery, *et al.*, "The Role of Damping, Mass and Stiffness in The Reduction of Wind Effects on Structures," *Journal of Wind Engineering and Industrial Aerodynamics*, Vol. 11, 1983, pp. 265-294.

[10] Ad Hoc Committee on Serviceability Research, "Structural Serviceability: A Critical Appraisal and Research Need", *Journal of Structural Engineering*, Vol. 112, No. 12, 1986, pp. 2646-2664.

[11] D. Surry and E. M. F. Stopar, "Wind Loading of Large Low Building," *Journal of Civil Engineering*, Vol. 16, 1989, pp. 526-542.

[12] F. K. Chang, "Human Response to Motions in Tall Building," *Journal of Structural Division*, Vol. 99, 1973, pp. 1259-1272.

[13] B. Blocken, *et al.*, "Wind, Rain and the Building Envelope: Studies at the Laboratory of Building Physics," KU Leuven, 2002, pp. 36-66.

[14] L. M. Fitzwater and S. R. Winterstein, "Predicting Design Wind Turbine Loads From Limited Data: Comparing Random Process and Random Peak Models," *Journal of Solar Energy Engineering*, Vol. 123, No. 4, 2001, pp. 364-371.

Engineering, 2010, 2, 299-305
doi:10.4236/eng.2010.24039 Published Online April 2010 (http://www.SciRP.org/journal/eng)

Dual Solution of MHD Stagnation-Point Flow towards a Stretching Surface

Tapas R. Mahapatra[1*], Samir K. Nandy[2], Anadi S. Gupta[3]
[1]*Department of Mathematics*, *Visva-Bharati*, *Santiniketan*, *India;*
[2]*Department of Mathematics*, *A.K.P.C Mahavidyalaya*, *Bengai*, *Hooghly*, *India;*
[3]*Department of Mathematics*, *Indian Institute of Technology*, *Kharagpur*, *India.*
[*]*E-mail*: *trmahapatra@yahoo.com*
Received September 19, 2009; *revised November* 7, 2009; *accepted November* 12, 2009

Abstract

The effect of a uniform transverse magnetic field on two-dimensional stagnation-point flow of an incompressible viscous electrically conducting fluid over a stretching surface is investigated when the surface is stretched in its own plane with a velocity proportional to the distance from the stagnation-point. This magnetohydrodynamic (MHD) flow problem is governed by the parameter b representing the ratio of the strain rate of the stagnation-point flow to that of the stretching sheet and the magnetic field parameter M. It is known from a previous paper [1] that if $b > 1$, the steady solution to the problem is monotonic increasing and the solution is also unique. But when $0 < b < b_c$ (where b_c (< 1) depends on M), there exists a dual solution which is non-monotonic in addition to a monotonic decreasing solution. It is found in this paper that bc decreases as M increases. Numerically it is shown that if $M > 0.23919$, the non-monotonic solution cannot exist and so in this case, the only solution is monotonic decreasing. A stability analysis reveals that when $0 < b < b_c$, the solutions along the upper branch corresponding to the monotonic solution are linearly stable while those along the lower branch for the non-monotonic solution are linearly unstable. It is also shown that the decay rate of a disturbance increases with increasing M for the stable solution but the growth rate of instability for the non-monotonic solution decreases with increasing M.

Keywords: Dual Solution; Magnetohydrodynamic Stagnation-Point Flow; Stretching Surface; Stability Analysis

1. Introduction

Flow of an incompressible viscous fluid over a stretching surface has important bearing on several industrial processes. For instance, in the extrusion of a polymer in a melt-spinning process, the extrudate from the die is usually drawn and simultaneously stretched into a sheet which is then cooled gradually by direct contact with water. The property of the final product depends on the rate of heat transfer at the surface of the sheet. Further the study of the flow of an electrically conducting viscous fluid caused by the deformation of the walls of the vessel containing this fluid in the presence of a magnetic field is of great interest in modern metallurgical and metal-working processes. Crane [2] obtained a similarity solution in closed analytical form for steady two dimensional flow of an incompressible viscous fluid caused solely by the stretching of an elastic sheet which moves in its own plane with a velocity varying linearly with distance from a fixed point. Pavlov [3] gave a similarity solution in exact analytical form of the MHD boundary layer equations for steady two-dimensional flow of an electrically conducting incompressible viscous fluid due to the stretching of a plane elastic surface in its own plane in the presence of a uniform transverse magnetic field. This problem was extended by Chakrabarti and Gupta [4] to include suction or injection at the stretching surface. The temperature distribution in the flow was also found by them in the case of constant surface temperature. Andersson [5] investigated the MHD flow of a viscoelastic fluid past a stretching surface in the presence of a uniform transverse magnetic field.

Recently Chiam [6] studied steady two-dimensional stagnation-point flow of an incompressible viscous fluid towards a stretching surface in the case when the parameter b representing the ratio of the strain rate of the stagnation-point flow to that of the stretching surface is

equal to unity. By removing this highly restrictive assumption (b = 1), Mahapatra and Gupta [7] analyzed the steady two dimensional orthogonal stagnation-point flow of an incompressible viscous fluid towards a stretching surface in the general case b ≠ 1. They found that the structure of the boundary layer depends crucially on the value of b. Temperature distribution in the flow was also obtained by them. Earlier Mahapatra and Gupta [8] investigated the steady two- dimensional orthogonal stagnation-point flow of an incompressible viscous electrically conducting fluid towards a stretching surface, the flow being permeated by a uniform transverse magnetic field. The steady and unsteady equations governing stagnation-point flow of an electrically nonconducting incompressible viscous fluid over a stretching surface along with the existence and uniqueness of the solutions of these equations were studied by Paullet and Weidman [9].

In this paper we investigate the dual solution of steady two-dimensional orthogonal stagnation-point flow of an incompressible viscous electrically conducting fluid towards a stretching surface in the presence of a uniform transverse magnetic field. We provided a mathematical proof in [1] that if b > 1, then the solution of this problem is monotonic increasing and further this solution is unique. But for 0 < b < 1, it was shown that there exists a dual solution which is non-monotonic in addition to a monotonic decreasing solution. We have found numerically in this paper that this dual solution exists upto a certain value of the magnetic parameter M. A linear stability analysis of these two solutions is also presented.

2. Flow Analysis

Consider the steady two-dimensional stagnation point flow of an incompressible viscous and electrically conducting fluid permeated by a uniform transverse magnetic field towards a flat stretching surface coinciding with the plane y = 0, the flow being confined to the region y > 0. Two equal and opposite forces are applied on the stretching surface along x-axis so that the surface is stretched with a velocity proportional to the distance from the stagnation-point which is taken as the origin. This is shown in **Figure 1**.

Using boundary layer approximations, the equations for steady MHD two-dimensional flow are in usual notation

$$u\frac{\partial u}{\partial x}+v\frac{\partial u}{\partial y}=-\frac{1}{\rho}\frac{\partial p}{\partial x}+\nu\frac{\partial^2 u}{\partial y^2}+\frac{1}{\rho}(\mathbf{j}\times\mathbf{B}_0)_x, \tag{1}$$

$$0=-\frac{1}{\rho}\frac{\partial p}{\partial y}, \tag{2}$$

where **j** is the electric current density, $\mathbf{B_0}$ is the imposed uniform magnetic field (acting along the y-direction). In writing (1), we have neglected the induced magnetic

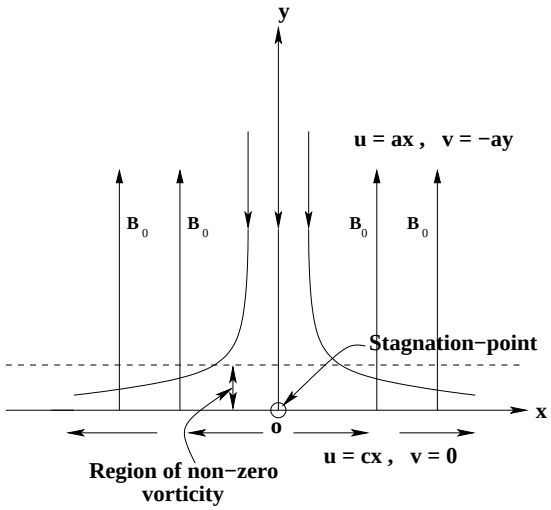

Figure 1. A sketch of the physical problem.

field since the magnetic Reynolds number R_M for the flow is assumed to be very small. Such an assumption is justified for the flow of electrically conducting fluids such as liquid metals e.g., liquid sodium, mercury etc. [10].

The equation of continuity is

$$\frac{\partial u}{\partial x}+\frac{\partial v}{\partial y}=0. \tag{3}$$

Clearly the electric current flows parallel to the z-axis which is normal to the plane of the flow. Hence by Ohm's law

$$j_x=0,\ j_y=0,\ j_z=\sigma[E_z+uB_0], \tag{4}$$

where σ is the electrical conductivity of the fluid which is assumed constant and E_z is the electric field along z-axis. It is assumed that the current lines in this two-dimensional problem close in a manner consistent with the experiment. Now since the flow is steady, Maxwell's equation gives

$$\nabla\times\mathbf{E}=\mathbf{0}, \tag{5}$$

where **E** is the electric field (which acts parallel to the z-direction). This gives

$$\frac{\partial E_z}{\partial x}=0 \quad \text{and} \quad \frac{\partial E_z}{\partial y}=0$$

so that E_z is a function of z only.

Since the induced magnetic field is neglected in view of the assumption R_M <<1, electric current in the flow is determined from Ohm's law and not from $\nabla\times\mathbf{B}=\mu_e\,\mathbf{j}$, μ_e being the magnetic permeability. But the consequence $\nabla\cdot\mathbf{j}=0$ of this equation must be satisfied [10]. Noting that the physical variables are functions of x and y, $\nabla\cdot\mathbf{j}=0$ then gives from (4), E_z = constant. Thus using (4), we find from (1),

$$u\frac{\partial u}{\partial x}+v\frac{\partial u}{\partial y}=-\frac{1}{\rho}\frac{\partial p}{\partial x}+\nu\frac{\partial^2 u}{\partial y^2} - \frac{\sigma B_0^2 u}{\rho}-\frac{\sigma B_0 E_z}{\rho}. \quad (6)$$

Since from (2), the pressure p is a function of x only, the pressure gradient $\frac{\partial p}{\partial x}$ can now be obtained from (6) in the inviscid region as

$$\frac{1}{\rho}\frac{\partial p}{\partial x}=-U(x)\frac{dU}{dx}-\frac{\sigma B_0^2 U}{\rho}-\frac{\sigma B_0 E_z}{\rho}, \quad (7)$$

where U(x) is the free stream velocity and use is made of the fact that E_z is constant. Hence eliminating $\frac{\partial p}{\partial x}$ from (6) and (7), we get

$$u\frac{\partial u}{\partial x}+v\frac{\partial u}{\partial y}=U\frac{dU}{dx}+\nu\frac{\partial^2 u}{\partial y^2}+\frac{\sigma B_0^2}{\rho}(U-u). \quad (8)$$

We note that the electric field does not directly affect the boundary layer equation although it has an influence on the relation between the free stream velocity and the pressure distribution given by (7).

Thus the governing equations for the velocity components *u* and *v* are (3) and (8). The boundary conditions are

$$u=cx,\quad v=0\quad at\quad y=0,$$
$$u\to U(x)=ax,\quad v\to -ay \quad (9)$$
$$as\ y\to\infty, \quad (10)$$

where a and c are positive constants. Under the similarity transformation

$$u=cxF'(\eta),\ v=-(c\nu)^{1/2}F(\eta),$$
$$\eta=y(c/\nu)^{1/2}, \quad (11)$$

where a prime denotes derivative with respect to the similarity variable η, we find that (3) is identically satisfied.

Substitution of (11) in (8) then gives

$$F'''(\eta)+F(\eta)F''(\eta)-F'^2(\eta)$$
$$-M^2F'(\eta)+M^2b+b^2=0, \quad (12)$$

where $b = a/c$ and M is the dimensionless magnetic parameter $B_0(\sigma/\rho c)^{1/2}$.

The boundary conditions for (12) then follow from (9) and (10) as

$$F(0)=0,\ F'(0)=1,\ F'(\infty)=b. \quad (13)$$

A detailed proof of the uniqueness of the solution for the same problem for an electrically non-conducting ($M = 0$) fluid was given by Paullet and Weidman [9]. Subsequently the present authors [1] proved the uniqueness of the solution for an electrically conducting fluid in the presence of a magnetic field ($M \neq 0$) using a similar approach as that in [9]. In [1] we have shown that if $b > 1$, the solution of the boundary value problem (BVP) given by (12) and (13) is monotonic increasing for all magnetic parameter M and further this solution is unique. But if $0 < b < 1$, there is a dual solution to the above BVP, which is non-monotonic in addition to a solution which is monotonic decreasing. Note that when $b = 1$, the above BVP admits of the exact solution $F(\eta) = \eta$, which is the inviscid solution near the stretching surface as found by Mahapatra and Gupta [8]. However this solution is not frictionless in a strict sense because in this case the friction is uniformly distributed and does not therefore affect the motion.

3. Numerical Solution

Since there is no general analytical solution of the non-linear differential equation (12) with the boundary conditions (13) for the case $b \neq 1$, so this system is solved numerically by an efficient shooting method for different values of *M* and *b*. To do this, we first transform the non-linear differential equation (12) to a system of three first order differential equations as:

$$y_1'=y_2,\ y_2'=y_3,$$
$$y_3'=y_2^2-y_1y_3+M^2(y_2-b)-b^2, \quad (14)$$

where $y_1=F(\eta),\ y_2=F'(\eta),\ y_3=F''(\eta)$ and a prime denotes differentiation with respect to the independent variable η.

The boundary conditions (13) become

$$y_1=0,\ y_2=1\ at\ \eta=0,$$
$$y_2\to b\ \ as\ \ \eta\to\infty. \quad (15)$$

The values of y_1 and y_2 are given at the starting point $\eta = 0$. But the value of y_2 as $\eta\to\infty$ is replaced by $y_2 = b$ at a finite value $\eta = \eta_\infty$ to be determined later. The value of y_3 at $\eta = 0$ is guessed in order to initiate the integration scheme. Starting from the given values of y_1 and y_2 at $\eta = 0$ and the guessed value of y_3 at $\eta = 0$, we integrate the first order Equation (14) by using a fourth-order Runge-Kutta method up to the end-point $\eta = \eta_\infty$. The computed value of y_2 at $\eta = \eta_\infty$ is then compared with $y_2 = b$. The absolute difference between this computed value and *b* should be as small as possible. To this end we use a Newton-Raphson iteration procedure to assure quadratic convergence of the iterations. The value of η_∞ is then increased till y_2 attains the value b asymptotically.

4. Dual Solution of MHD Stagnation-Point Flow

Our numerical results reveal that for $0 < b < 1$, in addition to a monotonic decreasing solution which was al-

ready found by Mahapatra and Gupta [8], there exists a dual solution which is non-monotonic. We have found that in the absence of magnetic field (M = 0), the non-monotonic solution exists in the range $0 < b \leq 0.16906$. This result in the nonmagnetic case ($M = 0$) was also obtained in [8]. For $M = 0.1$, the dual solution exists in the range $0 < b \leq 0.14845$, and for $M = 0.2$, such solution is found in the range $0 < b \leq 0.08234$. Numerically we have found that when $M \leq 0.23919$, the non-monotonic solution exists in the range $0 < b < 1$. Thus we see that as M increases, the range of b (such that $0 < b < 1$) for which the dual (*i.e.*, non-monotonic) solution exists progressively decreases. The novel result which emerges from the analysis is that when $M > 0.23919$, there is no dual solution in the range $0 < b < 1$ and the solution in this range is monotonic decreasing and unique.

Figure 2 gives the variation of the dimensionless skin-friction coefficient F"(0) with b for several values of M. Here the upper branch corresponds to the monotonic solution while the lower branch corresponds to the non-monotonic one. It can be seen that for the monotonic solution, $|F''(0)|$ increases with increase in M. This result can be physically explained as follows. It is clear from the momentum Equation (8) that when $b < 1$ (*i.e.*, a<c), the Lorentz force given by the last term is negative because the stagnation-point velocity U(= ax) is less than the stretching velocity cx of the sheet so that u > U. Hence this magnetic force decelerates the flow inside the boundary layer. Since the velocity of a fluid particle parallel to the surface is diminished relative to that of the stretching surface, the velocity gradient at the surface increases with increase in the magnetic field B_0 (characterized by the magnetic parameter M). This results in increase in the dimensionless skin-friction coefficients |F"(0)| with increase in M. Note that the above argument is valid for the monotonic solution for the velocity distribution because in this case the velocity inside the boundary layer decreases monotonically from the surface velocity cx to ax (since $a < c$) so that u > U.

Figures 3-5 display self-similar velocity profiles of F'(η) for different values of M at selected values of b. The non-monotonic behavior of the velocity distribution is evident from these figures. It is observed from these figures that for a fixed value of b, the velocity parallel to the stretching surface at a point in the boundary layer decreases with increase in M. From a physical point of view, this follows from the fact that when $b < 1$, increase in M leads to increase in the magnitude of the retarding Lorentz force acting on the fluid resulting in enhanced deceleration of the flow.

An interesting result which emerges from this analysis is that for a given value of M, the skin-friction coefficient |F"(0)| for the dual solution in the case $0 < b < 1$ is not a monotonic function of b but has a maximum at a particular value of b (see **Figure 2**). This result is to be contrasted with the corresponding result for the monotonic

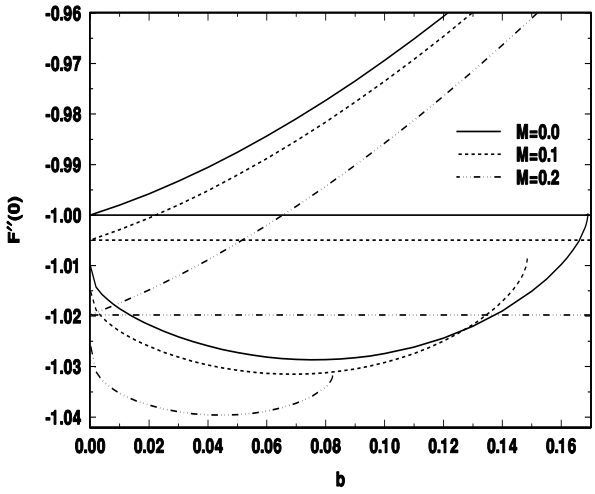

Figure 2. Reduced skin friction coefficient F''(0) with b for several values of M showing the upper and lower curves.

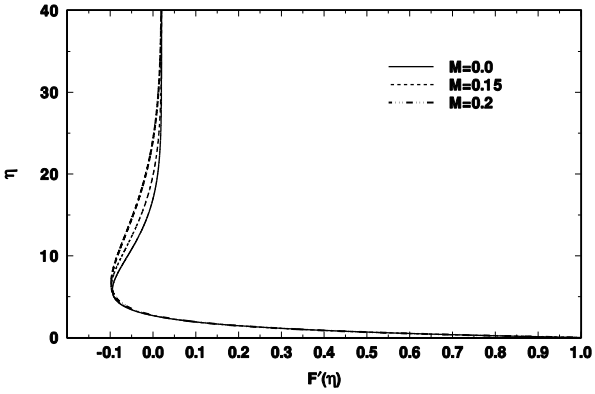

Figure 3. Self-similar velocity profiles (for non-monotonic solution) for b = 0.02 with different values of M.

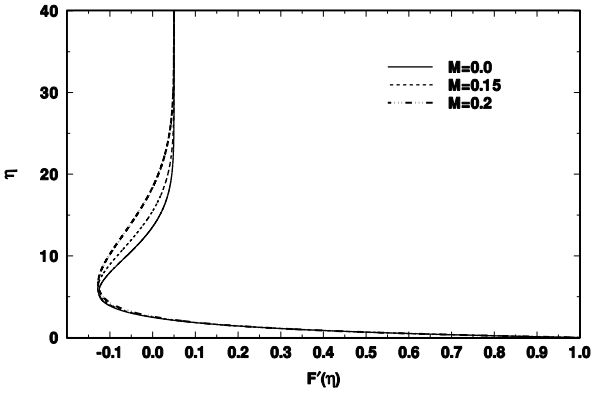

Figure 4. Self -similar velocity profiles (for non-monotonic solution) for b = 0.05 with different values of M.

solution for $0 < b < 1$, where |F"(0)| decreases monotonically with increase in b as shown in **Figure 2**. Physically this stems from the fact that for the dual solution, the

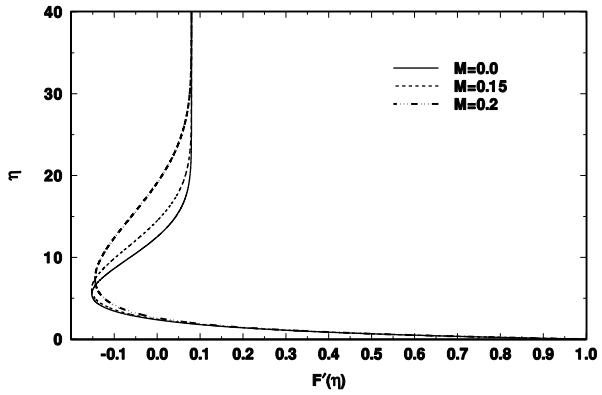

Figure 5. Self -similar velocity profiles (for non-monotonic solution) for b = 0.08 with different values of M.

self-similar velocity profiles F'(η) are non-monotonic (see **Figures 3-5**).

5. Stability Analysis

In order to ascertain which of the two solutions in the region $0 < b < b_c$ (where as shown above, b_c depends on M), is expected to appear asymptotically, we test the stability of the above two solutions.

To this end, we consider the unsteady form of the Equation (8) as

$$\frac{\partial u}{\partial t}+u\frac{\partial u}{\partial x}+v\frac{\partial u}{\partial y}=U\frac{dU}{dx}+\nu\frac{\partial^2 u}{\partial y^2} +\frac{\sigma B_0^{\,2}}{\rho}(U-u), \tag{16}$$

together with the equation of continuity (3). We seek the unsteady similarity solution in the form

$$u=cx\,f_\eta(\eta,\tau),\ \ v=-(c\nu)^{1/2}\ f(\eta,\tau), \quad \eta=y(c/\nu)^{1/2}, \tag{17}$$

where the subscript η denotes partial derivative with respect to η and τ is the dimensionless time ct. Note that with u and v given above, the equation of continuity (3) is identically satisfied. Substitution of (17) in (16) then gives

$$f_{\eta\eta\eta}+ff_{\eta\eta}-f_\eta^{\,2}-M^2f_\eta+M^2b +b^2-f_{\eta\tau}=0, \tag{18}$$

where the subscripts η and τ denote partial derivatives with respect to η and τ respectively. The boundary conditions are

$$u=cx,\quad v=0\quad at\quad y=0, \qquad u\to U(x)=ax,\ \ v\to -ay \tag{19}$$

$$as\ \ y\to\infty. \tag{20}$$

In terms of f(η,τ), these conditions are

$$f(0,\tau)=0,\ \ f_\eta(0,\tau)=1,\ f_\eta(\infty,\tau)=b. \tag{21}$$

Following Merkin [11], we put

$$f(\eta,\tau)=F(\eta)+e^{-\gamma\tau}g(\eta)\ , \tag{22}$$

where F(η) satisfies (12) subject to (13) and corresponds to the steady state solution. Further g(η) and all its derivatives are assumed small compared with the steady solution F(η) and its derivatives. Such an assumption is made because we are studying the linear stability of the basic flow F(η) so that the disturbance g(η) is small, γ being the growth (or decay) rate of the disturbance. Substituting (22) in (18) and linearizing, we get

$$g'''+Fg''+(\gamma-2F'-M^2)g'+F''g=0. \tag{23}$$

Here prime denotes derivative with respect to η. The boundary conditions for g(η) follow from (13), (21) and (22) as

$$g(0)=0,\ g'(0)=0,\ \ g'(\infty)=0. \tag{24}$$

Clearly the homogeneous linear Equation (23) subject to the homogeneous boundary conditions (24) constitutes an eigenvalue problem with γ as the eigenvalue. Without loss of generality, we can take g''(0) = 1. Solutions of (23) and (24) give an infinite set of eigenvalues $\gamma_1 < \gamma_2 < \gamma_3 <\ldots$ If the smallest eigenvalue γ_1 is negative, then there is an initial growth of disturbances and the flow is unstable. On the other hand, when γ_1 is positive, there is an initial decay and the flow is stable.

Figure 6 shows the variation of the smallest eigenvalue γ_1 for the monotonic solutions (corresponding to upper curves in **Figure 2**) with b for several values of the magnetic parameter M. Since γ_1 is real and positive for these curves, it follows that the monotonic solutions are linearly stable. Further, for a given value of b, γ_1 increases with increase in M. Thus we may say that for these stable solutions, disturbances decay more quickly with increase in M.

On the other hand, **Figure 7** gives a plot of the variation of the lowest eigenvalue γ_1 for the non-monotonic

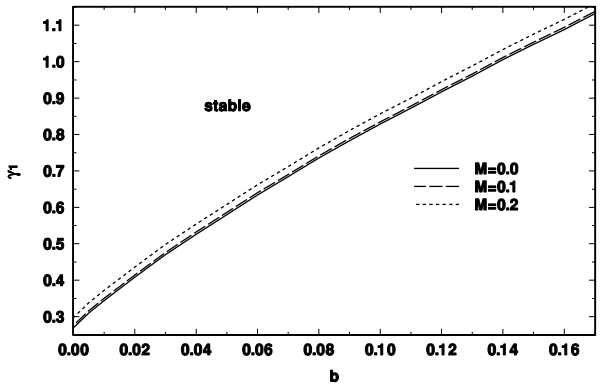

Figure 6. Plot of lowest eigenvalues γ_1 as a function of b for the upper branch solution with different values of M.

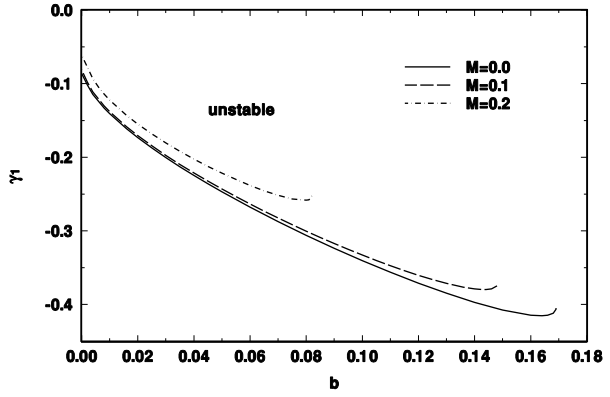

Figure 7. Plot of lowest eigenvalues γ_1 as a function of b for the lower branch solution with different values of M.

solutions (corresponding to lower curves in **Figure 2**) with b for several values of M. Since $\gamma_1 < 0$ for these curves, it is clear that the non-monotonic solutions are linearly unstable. Further for a given b, $|\gamma_1|$ decreases with increase in M for the non-monotonic solutions. Hence it follows that the growth rate of unstable disturbances decreases with increase in M. A physical interpretation of these results is that the magnetic field has a stabilizing influence on the flow. In fact a magnetic field exerts something like a viscous drag on an electrically conducting fluid and also imparts to it some degree of rigidity. Thus magnetic field can be expected to inhibit any tendency to instability. Further from an energetic point of view, a magnetic field is stabilizing since in addition to the dissipation of energy by viscosity, there is dissipation of magnetic energy in the form of Joule heating [12]. Specially, when an electrically conducting fluid is perturbed in the presence of a magnetic field, the disturbances induced by currents, whose energy is dissipated by Joule heating.

It may be noted that the result that the monotonic solution is linearly stable and the non-monotonic solution is linearly unstable in the case of an electrically nonconducting fluid with $M = 0$ was arrived at earlier in [9]. Our present stability analysis is based on the approach in [9].

6. Conclusions

An investigation is made of steady two dimensional MHD stagnation-point flow of an electrically conducting incompressible viscous fluid over a stretching surface in the presence of a uniform transverse magnetic field. The surface is stretched in its own plane with a velocity proportional to the distance from the stagnation-point. The flow problem is governed by the dimensionless parameter b representing the ratio of the strain-rate of the stagnation flow to that of the stretching surface and the magnetic parameter M. It is shown that in addition to the monotonic increasing solution (which is unique) for $b > 1$ earlier found by Mahapatra and Gupta [8], there exist two solutions in the range $0 < b < b_c$, where $b_c(< 1)$ depends on M. In this range one solution is monotonic increasing whilst the dual solution is non-monotonic. It is also found numerically that b_c decreases with increase in M and when $M > 0.23919$, the dual solution does not exist.

A linear stability analysis of the two solutions in the range $0 < b < b_c$ reveals that the monotonic decreasing solution is linearly stable but the non-monotonic solution is linearly unstable. Further the magnetic field exerts a stabilizing influence on the flow.

7. Acknowledgements

We thank the referee for his useful comments which enabled us in presenting an improved version of the paper. The work of one of the authors (T.R.M) is supported under SAP (DRS PHASE II) program of UGC, New Delhi. One of the authors (A.S.G) acknowledges the financial support of Indian National Science Academy, New Delhi for carrying out this work.

8. References

[1] T. R. Mahapatra, S. K. Nandy, and A. S. Gupta, "Magnetohydrodynamic Stagnation-point Flow of a Power-law Fluid towards a Stretching Surface," *International Journal of Non-Linear Mechanics*, Vol. 44, 2009, pp. 123-128.

[2] L. J. Crane, "Flow Past a Stretching Plate," *Zeitschrift für Angewandte Mathematik und Physik*, Vol. 21, 1970, pp. 645-647.

[3] K. B. Pavlov, "Magnetohydrodynamic Flow of an Incompressible Viscous Fluid Caused by the Deformation of a Plane Surface," *Magnitnaya Gidrodinamika*, Vol. 4, 1974, pp. 146-147.

[4] A. Chakrabarti and A. S. Gupta, "Hydromagnetic Flow and Heat Transfer over a Stretching Sheet," *Quarterly of Applied Mathematics*, Vol. 37, April 1979, pp. 73-78.

[5] H. I. Andersson, "MHD Flow of a Viscoelastic Fluid Past a Stretching Surface," *Acta Mechanica*, Vol. 95, 1992, pp. 227-230.

[6] T. C. Chiam, "Stagnation-point Flow towards a Stretching Plate," *Journal of the Physical Society of Japan*, Vol. 63, 1994, pp. 2443-2444.

[7] T. R. Mahapatra and A. S. Gupta, "Heat Transfer in Stagnation-point Flow towards a Stretching Sheet," *Heat Mass Transfer*, Vol. 38, 2002, pp. 517-521.

[8] T. R. Mahapatra and A. S. Gupta, "Magnetohydrodynamic Stagnation-point Flow towards a Stretching Sheet," *Acta Mechanica*, Vol. 152, 2001, pp. 191-196.

[9] J. Paullet and P. Weidman, "Analysis of Stagnation Point Flow towards a Stretching Sheet," *International Journal of Non-Linear Mechanics*, Vol. 42, No. 9, 2007, pp.

1084-1091.

[10] J. A. Shercliff, "A Textbook of Magnetohydrodynamics," Pergamon Press, Oxford, 1965.

[11] J. H. Merkin, "Mixed Convection Boundary Layer Flow on a Vertical Surface in a Saturated Porous Medium," *Journal of Engineering Mathematics*, Vol. 14, 1980, pp. 301-313.

[12] S. Chandrasekhar, "Hydrodynamic and Hydromagnetic Stability," Clarendon Press, Oxford, 1961.

